



Karlsruher Institut für Technologie

Molecular Engineering of Metalloporphyrins for High-Performance Energy Storage

Zur Erlangung des akademischen Grades einer
DOKTORIN DER NATURWISSENSCHAFTEN

(Dr.rer.nat.)

von der KIT-Fakultät für Chemie und Biowissenschaften des
Karlsruher Instituts für Technologie (KIT)

genehmigte

DISSERTATION

von

M.Sc. Shirin Shakouri

aus

Bergisch Gladbach

Referent: Prof. Dr. Mario Ruben
Korreferent: Prof. Dr. Helmut Ehrenberg
Tag der mündlichen Prüfung: 26.10.2023

Committee

Referent: Prof. Dr. Mario Ruben
Korreferent: Prof. Dr. Helmut Ehrenberg
1. Prüfer: PD Dr. Detlef Schooss
2. Prüfer: Prof. Dr. Olaf Deutschmann
Prüfungsvorsitz: Prof. Dr. Rolf Schuster

Tag der mündlichen Prüfung: 26.10.2023

*“Nothing in life is to be feared,
it is only to be understood.
Now is the time to understand more,
so that we may fear less.”*
- Marie Curie

Declaration

I, Shirin Shakouri, declare that this thesis entitled “Molecular Engineering of Metalloporphyrins for High-Performance Energy Storage” and the work presented in it are my own and the work was undertaken under the supervision of Prof. Mario Ruben at the Institute of Nanotechnology (INT), at the Karlsruhe Institute of Technology (KIT). I confirm that:

- This work was done wholly while in candidature for a research degree at KIT.
- The whole thesis was written by me and no other sources other than the specified were used.
- The rules for ensuring good scientific practice of the Karlsruhe Institute of Technology (KIT) have been used and the submission and archiving of the primary data, in accordance with section A(6) of the rules for ensuring good scientific practice of KIT, has been ensured.
- The electronic version of the work is consistent with the written version.
- Where I have consulted the published work of others, this is always clearly attributed.
- I have acknowledged all main sources of help.
- Where the thesis is based on work done by myself joint with others, I have made clear exactly what was done by others and what I have contributed myself.
- Furthermore, I declare that I did not undertake any previous doctoral studies and that I am currently not enrolled in any other ongoing doctoral procedure.

Signature:.....

Date:

Erklärung

Ich, Shirin Shakouri, erkläre, dass diese Arbeit mit dem Titel “Molecular Engineering of Metalloporphyrins for High-Performance Energy Storage” und die darin vorgestellten Ergebnisse meine eigenen sind. Die Arbeit wurde unter der Leitung von Prof. Dr. Mario Ruben am Institut für Nanotechnologie (INT), am Karlsruher Institut für Technologie (KIT) angefertigt. Ich bestätige:

- Diese Arbeit wurde vollständig während der Kandidatur für ein Forschungsstudium am KIT durchgeführt.
- Die gesamte Arbeit wurde von mir verfasst und es wurden keine anderen Quellen als die angegebenen verwendet.
- Es wurden Maßnahmen zur Sicherstellung einer guten wissenschaftlichen Praxis des Karlsruher Instituts für Technologie (KIT) angewendet und die Übermittlung und Archivierung der Primärdaten gemäß Abschnitt A(6) der Regeln zur Sicherstellung einer guten wissenschaftlichen Praxis des KIT sichergestellt.
- Die elektronische Fassung des Werkes entspricht der schriftlichen Fassung.
- Im Fall, dass ich die veröffentlichten Arbeiten anderer konsultiert habe, wird dies immer eindeutig zugeordnet.
- Ich habe alle wichtigen Hilfsquellen zur Kenntnis genommen.
- Wenn die Arbeit auf Arbeiten basiert, die ich gemeinsam mit anderen geleistet habe, habe ich kenntlich gemacht, was von anderen geleistet wurde und was ich selbst beigesteuert habe.
- Des Weiteren erkläre ich, dass ich kein vorheriges Promotionsstudium absolviert habe und mich derzeit nicht in einem anderen laufenden Promotionsverfahren befinde.

Unterschrift:.....

Datum:

Abstract

The demand for sustainable energy storage solutions is steadily increasing as the electrification of various sectors continues to expand. This necessity arises from the requirement to efficiently store renewable energy generated from sources such as wind or solar power. Traditional inorganic materials, such as transition metal oxides, despite their established use, are gradually approaching their limits in terms of further enhancements, particularly in energy density. Moreover, concerns related to their toxicity, elevated costs, accessibility and sustainability are motivating the exploration of alternative options. Organic materials, on the other hand, present promising avenues due to their potential for being cost-effective, environmentally friendly, and versatile. However, it's worth noting that organic materials often face challenges such as limited electrical conductivity, high solubility, and relatively low energy density.

Within this context, we introduce porphyrinoids as a class of electrode materials with great potential, owing to their impressive flexibility, extensive redox chemistry, and remarkable stability in lithium-ion battery (LIB) applications. These features, along with their b-type properties that enable their use as cathode and anode materials, high potential, and high capacities, place them as promising options for addressing the limitations typically associated with organic materials in battery applications. This study encompasses diverse approaches to design novel porphyrins and effectively modulate their properties, thereby enabling the attainment of various electrochemical characteristics tailored to specific applications: 1) A first approach involves altering the metal center within the core of the porphyrin molecule. In particular, we investigated the A2B2 porphyrin, specifically 5,15-bis(ethynyl)-10,20-diphenyl-21*H*,23*H*-porphyrin (DEPP), along with its corresponding first-row transition metal complexes spanning from Co to Zn. The objective was to gain a more comprehensive understanding of the intricate interplay between structure and performance. Notably, it was evident that the choice of metal center exerted a significant influence on both the practical voltage range and discharge capacity. During the initial cycles, specific discharge capacities of 184, 143, 114, 109, and 101 mAh g⁻¹ were achieved for CoDEPP > CuDEPP > ZnDEPP > DEPP > NiDEPP at a current density of 0.1 A g⁻¹. Furthermore, the chosen metal center also affected the overall structure of the porphyrin molecule. Factors such as the degree of planarity, intramolecular rearrangements, crystalline packing, solubility characteristics, and crystallinity were modified by this choice. These structural attributes, in turn, held the potential to impact critical features like rate capability and ion diffusion within the electrode material.

2) Another approach for tailoring material properties involves morphological considerations, encompassing factors such as crystallinity, particle shape, and size. In the case of [5,15-bis(ethynyl)-10,20-diphenylporphinato]cobalt(II) (CoDEPP), four distinct morphologies were examined, each synthesized by varying the preparation conditions. Electrochemical investigations were then conducted on these morphological variants. The outcomes demonstrated a clear correlation between material crystallinity and discharge capacities, with more crystalline forms exhibiting higher capacities. Furthermore, the interplay between surface area and particle size had a discernible impact on rate capability. This phenomenon was evident in the enhanced

performance of the flower-shaped CoDEPP morphology compared to its needle-shaped counterpart. Beyond this, the porosity of the material played a pivotal role in influencing ion diffusion, as confirmed by impedance measurements.

Moreover, a novel cathode material in the form of a pyridine-functionalized porphyrin (TPyrP) metal-organic framework (MOF) was introduced for application in advanced lithium-ion and post-lithium battery systems. This inclusion was motivated by the quest for more sustainable energy storage solutions, with particular emphasis on aluminum and calcium batteries. Furthermore, the preparation of the CuTPyrP-MOF is much more cost-efficient than the typical synthesis of A₂B₂-porphyrins due to the fewer required reaction and purification steps. These alternative systems offer considerable promise due to their potential for enhanced sustainability. In the case of calcium batteries, the pyridine-functionalized porphyrin MOF displayed remarkable cycling stability and exhibited high capacity retention over numerous cycles. This material demonstrated its competence even at elevated current densities, showcasing the ability to maintain a high specific capacity of 90 mAh g⁻¹ under a current density of 2 A g⁻¹. Unfortunately, the performance of the same material in aluminum batteries was hindered by the corrosive nature of the electrolyte employed, revealing subpar battery performance.

A detailed examination was conducted regarding the phenomenon of self-conditioning observed in porphyrinoids when utilized as cathode materials in LIBs. The irreversible oxidation events occurring at higher voltages, approximately 4 V, have previously been attributed to electrochemically induced polymerization, which has been considered a key factor contributing to the impressive cycleability of these materials. While this interpretation holds true for functional groups like ethynyl, thiophene, and 4-aminophenyl, which are recognized for their propensity to undergo polymerization, the situation is not as straightforward for other porphyrin derivatives such as [5,10,15,20-tetra(phenyl)porphinato]copper(II) (CuTPP) or [5,15-diphenylporphyrinato]copper(II) (CuDPP). In these cases, alternative forms of stabilization appear to be at play, supported by evidence of irreversible oxidation events. To further delve into the mechanism underlying electrochemically induced polymerization, computational methods such as Density Functional Theory (DFT) calculations were employed. These computational tools aimed to shed light on the intricate processes responsible for the observed polymerization phenomenon.

In summary, the study demonstrated that porphyrinoids possess substantial potential as electrode materials, and their properties can be finely adjusted through the tuning of factors like the metal center, morphology, or functional groups. This adaptability renders them highly versatile, flexible and sustainable candidates for a wide range of battery applications.

Zusammenfassung

Durch die kontinuierliche Elektrifizierung in nahezu allen Bereichen des wirtschaftlichen und alltäglichen Lebens steigt der Bedarf nach ökologischeren Energiespeichern. Die Notwendigkeit, erneuerbare Energien aus Wind- und Solarenergie effizient speichern zu können, treibt diese Anforderungen voran. Anorganische Elektrodenmaterialien, wie beispielsweise Übergangsmetalloxide, sind weit verbreitet und gut erforscht. Jedoch sind deren Möglichkeiten zur Leistungssteigerung weitgehend ausgeschöpft. Zudem erfordern Bedenken hinsichtlich ihrer Toxizität, hohen Kosten und Nachhaltigkeit die Entwicklung neuer Alternativen. Organische Materialien bieten eine vielversprechende Lösung, da sie kostengünstig, verfügbarer, nachhaltiger und flexibler sind. Dennoch sollten auch hierbei ihre Nachteile, wie beispielsweise eingeschränkte Leitfähigkeit, hohe Löslichkeit und geringe Energiedichte berücksichtigt werden.

Porphyrinoide stellen daher vielversprechende Elektrodenmaterialien in Lithium-Ionen-Batterien (LIBs) dar. Sie zeichnen sich durch außerordentliche Flexibilität, eine reiche Redoxchemie und bemerkenswerte Stabilität aus. Diese Eigenschaften, kombiniert mit dem Potenzial, sie als b-Typ-Materialien, also als Kathode und Anode einzusetzen zu können, sowie hohe Spannungen und Kapazitäten, prädestinieren Porphyrinoide als geeignete Kandidaten, um die typischen Nachteile organischer Elektrodenmaterialien zu überwinden. Meine Arbeit zeigt verschiedene Ansätze auf, um neuartige Porphyrinoide zu entwerfen und ihre Eigenschaften zu steuern, um unterschiedliche elektrochemische Merkmale für spezifische Anwendungen anzupassen. Ein Beispiel für die Beeinflussung dieser Eigenschaften ist der Austausch des Metallzentrums im Porphyrinkern. Um dies genauer zu untersuchen, wurde das A2B2-Porphyrin 5,15-Bis(ethinyl)-10,20-diphenylporphyrin (DEPP) mit den Übergangsmetallen der ersten Periode von Co bis Zn analysiert. Ziel war es, ein besseres Verständnis der Wechselwirkung zwischen Struktur und Leistung zu erlangen. Dabei wurde festgestellt, dass das gewählte Metallzentrum Einfluss auf das praktische Spannungsfenster und die Entladekapazität hat. Im ersten Zyklus wurden bei einer Laderate von 0.1 A g^{-1} Entladekapazitäten von 184, 143, 114, 109 und 101 mAh g^{-1} für CoDEPP > CuDEPP > ZnDEPP > DEPP > NiDEPP erzielt. Zusätzlich beeinflusst die Wahl des Zentralatoms die allgemeine Struktur des Porphyrins. Faktoren wie Grad der Planarität, intermolekulare Anordnung, Kristallstruktur, Löslichkeit und Kristallinität können durch die Wahl des Metalls verändert werden. Diese Eigenschaften erlauben es, Schlüsselfaktoren wie Ratenstabilität und Ionendiffusion im Elektrodenmaterial zu steuern.

Eine weitere Möglichkeit, die Eigenschaften von Materialien zu beeinflussen, besteht darin, in die Morphologie, einschließlich der Kristallinität, Partikelform und -größe einzugreifen. Im Fall von [5,15-Bis(ethinyl)-10,20-diphenylporphinato]cobalt(II) (CoDEPP) wurden verschiedene Synthesemethoden angewandt, um unterschiedliche Morphologien zu erzeugen. Der Einfluss dieser Morphologien wurde anschließend in elektrochemischen Untersuchungen analysiert. Die Ergebnisse zeigen eine deutliche Korrelation zwischen der Kristallinität des Materials und der Entladekapazität, wobei eine höhere Kristallinität zu höheren Kapazitäten führt. Die Ratenstabilität ist stark

abhängig von der Oberfläche und der Partikelgröße. Dieses Verhältnis wurde insbesondere am Beispiel des blütenförmigen CoDEPP im Vergleich zur nadelförmigen Form veranschaulicht. Die Porosität hingegen scheint die Ionendiffusion zu beeinflussen, wie durch Impedanzspektroskopie nachgewiesen werden konnte.

Das pyridin-funktionalisierte Porphyrin (TPyrP) wurde in Form eines "molecular organic framework" (MOF) für die Anwendung in Lithium-Ionen-Batterien und in neuen post-Lithium-Batteriesystemen eingeführt. Dabei lag der Fokus insbesondere auf der Untersuchung der Eignung für Aluminium- und Calcium-Batterien in Hinblick auf ihre Nachhaltigkeit. Aber auch das CuTPyrP-MOF stellt aufgrund der vergleichsweise geringen Produktionskosten, bedingt durch weniger Synthese- und Aufreinigungsschritte als bei den A2B2-Porphyrinoiden, einen großen Vorteil dar. Im Falle von Calcium-Batterien zeigte das eingeführte Porphyrin-MOF über zahlreiche Zyklen hinweg beeindruckende Zyklen- und Ratenstabilität. Selbst bei hohen Ladungsraten blieb das Material stabil und erreichte bei einer Ladungsrate von 1 A g^{-1} eine spezifische Kapazität von 90 mAh g^{-1} . Leider konnte dieses Material, vermutlich aufgrund von Instabilitäten durch den korrosiven Elektrolyten, in Aluminium-Batterien nicht genutzt werden.

Weiterhin wurde das Phänomen des "self-conditioning" untersucht, welches auftritt, wenn Porphyrinoide als Kathodenmaterial verwendet werden. Die damit einhergehende irreversible Oxidation bei etwa 4 V im ersten Zyklus wird oft mit einer elektrochemisch induzierten Polymerisation in Verbindung gebracht, die entscheidend für die bemerkenswerte Stabilität der Materialien ist. Diese Analyse erscheint für Porphyrinoide mit funktionellen Gruppen zutreffend, die für die Eingehung elektrochemischer Polymerisationen bekannt sind, wie beispielsweise Ethinyl-, Thiophen- oder 4-Aminophenylgruppen. Bei anderen Systemen wie [5,10,15,20-Tetra(phenyl)porphyrinato]kupfer(II) (CuTPP) oder [5,15-Diphenylporphyrinato]kupfer(II) (CuDPP) scheint die Erklärung komplexer zu sein. Hier könnte eine andere Form der Stabilisierung relevant sein, die sich ebenfalls durch eine irreversible Oxidation zeigt. Darüber hinaus wurde der Mechanismus der elektrochemisch induzierten Polymerisation mithilfe theoretischer Berechnungen (DFT) untersucht, um den zugrundeliegenden Mechanismus, im Falle einer Polyacetylen-Reaktion besser zu verstehen.

Zusammenfassend konnte gezeigt werden, dass Porphyrinoide ein exzellentes Elektrodenmaterial darstellen, dessen Eigenschaften durch Variation des Metallzentrums, der Morphologie und funktioneller Gruppen verändert werden können. Diese Anpassungsfähigkeit verleiht den Materialien eine bemerkenswerte Flexibilität in einer Vielzahl von Batteriesystemen.

Danksagung

An erster Stelle möchte ich mich ganz herzlich für die Bereitstellung meines Promotionsthemas, zahlreichen wissenschaftlichen Diskussionen sowie für die exzellente Betreuung bei meinem Doktorvater Prof. Dr. Mario Ruben bedanken. Prof. Dr. Helmut Ehrenberg danke ich für die Übernahme des Korreferats.

Des Weiteren möchte ich meiner Betreuerin Dr. Svetlana Klyatskaya danken, die immer an meiner Seite stand und mir immer mit guten Ratschlägen weiterhelfen konnte. Auch Dr. Ebrahim Abouzari-Lotf möchte ich für die Zusammenarbeit und all seine Hilfestellungen danken.

Ein riesiger Dank gilt all meinen Laborkollegen. Ich möchte keinen von euch missen, ihr habt mich alle auf eure Art und Weise unterstützt: Dr. Eufemio Moreno Pineda, Dr. Concepcion del Carmen Molina Jiron de Moreno, Dr. Nithin Suryadevara, Dr. Asato Mizuno, Dr. Senthil Kumar Kuppusamy, Dr. Tingting Ruan, Dr. Nico Balzer, Dr. Liang Xu, Yaorong Chen, Zhaoyang Jing, Jo Komeda, Dr. Camila Gouveia Barbosa, Patrick Lawes, Dr. Jordan Appleton, Dr. Shagor Chowdhury, Dr. Pinar Apacay, Dr. Barbora Brachnakova und Rihab Sayid.

Sören Schlittenhardt, "Söri", danke ich für all die Stunden des Zuhörens, fachlichen Diskussionen und für die Freundschaft. Ich hätte mir keinen besseren Büronachbar vorstellen können. Sai Prasanna Kumar Panguluri möchte ich danken für ebenfalls Stunden des Zuhörens und für all unsere Gespräche. Ich weiß nicht, was ich ohne dich und deine gute Laune gemacht hätte!

Hagen Sparrenberger gilt ein besonderer Dank. Ohne seine Unterstützung wäre die Laborarbeit niemals so reibungslos abgelaufen! Auch Nikolai Bartnick möchte ich danken, vor allem für die Elementaranalysen. Dr. Andreas Eichhöfer danke ich für das Messen der Pulverdiffraktogramme, leider ist er viel zu früh von uns gegangen.

Ein großer Dank gilt den zahlreichen Zusammenarbeiten mit anderen Arbeitsgruppen, die immer versucht haben, mich weiter voranzubringen. An erster Stelle ist hier der AK von Prof. Dr. Maximilian Fichtner zu nennen. Ich bin sehr dankbar, dass ich immer in den Laboren willkommen war und jeder mich freundlich begrüßt hat. Im Speziellen gilt mein Dank Thomas Smok, Dr. Sibylle Riedel und natürlich Dr. Ebrahim Abouzari-Lotf. Des Weiteren gilt mein Dank dem AK Ehrenberg, vor allem Dr. Rafael Cordoba Rojana und Dr. Sonia Dsoke, die mich bei den Versuchen zu Aluminium Batterien unterstützt haben. Dr. Torsten Scherer, Dr. Sabine Schlabach, Vanessa Wollersen, Dr. Ali Ahmadian des AK Kübel und Dr. Rafaela Debastiani danke ich für die Unterstützung bei den FIB-SEM und NanoCT Messungen. Des Weiteren gilt mein Dank Dr. Saibal Jana aus dem AK Wenzel, welcher mich bei den theoretischen Rechnungen unterstützt hat, sowie Dr. Frank Pammer aus dem AK Fichtner.

Natürlich gehört zum Schreiben einer Arbeit auch das Korrekturlesen. Hierfür möchte ich Dr. Svetlana Klyatskaya, Dr. Senthil Kumar Kuppusamy, Dr. Ebrahim Abouzari-Lotf, Dr. Sibylle Riedel, Thomas Smok und Jordan Appleton danken.

Ein weiterer großer Dank gilt der finanziellen und ideellen Förderung durch mein Promotionsstipendium der Friedrich-Ebert-Stiftung und im Speziellen der Betreuung durch Dr. Markus Trömmel.

Die Promotionszeit ist schön, aber auch fordernd. Ohne meine Freunde, meine Familie und meinen Freund, die immer an mich geglaubt haben, hätte ich das bestimmt nicht geschafft. Ich liebe euch und danke für alles!

Abbreviations

1D	One-dimension
2D	Two-dimension
3D	Three-dimension
AIB	Aluminium-ion battery
ATR	Attenuated total reflectance
BET	Brunauer-Emmett-Teller theory
BSE	Backscattered electrons
CMC	Carboxymethyl cellulose
CNT	Carbon nanotubes
CoDEPP	[5,15-bis(ethynyl)-10,20-diphenylporphinato]cobalt(II)
COF	Covalent organic framework
CoTCPP	[5,10,15,20-tetra(4-carboxylatophenyl)porphinato]cobalt(III) chloride
CPE	Constant phase element
CuDEOP	[5,15-bis(ethynyl)-10,20-difurylporphinato]copper(II)
CuDEPP	[5,15-bis(ethynyl)-10,20-diphenylporphinato]copper(II)
CuDPP	[5,15-diphenylporphyrinato]copper(II)
CuDPyrPP	[5,15-bis(4-pyridyl)-10,20-diphenylporphinato]copper(II)
CuTEP	[5,10,15,20-tetra(ethynyl)porphinato]copper(II)
CuTPP	[5,10,15,20-tetra(phenyl)porphinato]copper(II)
CuTPyrP-MOF	[5,10,15,20-tetra(4-pyridyl)porphinato]copper(II) - metal-organic framework
CuTTP	[5, 10, 15, 20-tetra(thienyl)porphinato]copper(II)
CV	Cyclic voltammetry
DCM	Dichloromethane
DDQ	2,3-dichloro-5,6-dicyano-1,4-benzoquinone
DEC	Diethyl carbonate
DEPP	5,15-bis(ethynyl)-10,20-diphenyl-21 <i>H</i> ,23 <i>H</i> -porphin
DFT	Density functional theory
DIB	Dual-ion battery
DMC	Dimethyl carbonate
DME	Dimethyl ether

DMSO	Dimethyl sulfoxide
DTT	Dibenzo[b,i]thianthrene-5,7,12,14-tetraon
EC	Ethylene carbonate
EDX	Energy-dispersive X-ray spectroscopy
EES	Electrochemical energy storage
EIS	Electrochemical impedance spectroscopy
EMF	Electromotive force
EMIm	1-Ethyl-3-methylimidazolium
FIB	Focused ion beam
FMO	Frontier molecular orbital
FTIR	Fourier-transform infrared spectroscopy
GCPL	Galvanostatic cycling with potential with limitation
GDL	Gas Diffusion Layer
H ₂ TCP	5,10,15,20-tetra(4-carboxyphenyl)-21 <i>H</i> ,23 <i>H</i> -porphyrin
H ₂ TPP	5,10,15,20-tetra(phenyl)-21 <i>H</i> ,23 <i>H</i> -porphyrin
HF	Hydrogen fluoride
HOMO	Highest occupied molecular orbital
IR	Infrared spectroscopy
KIB	Potassium-ion battery
LCO	Lithium cobalt oxide - LiCoO ₂
LFP	Lithium iron phosphate - LiFePO ₄
LIB	Lithium-ion battery
LiPF ₆	Lithium hexafluorophosphate
LiTFSI	Lithium bis(trifluoromethanesulfonyl)imide - LiC ₂ F ₆ NO ₄ S ₂
LMO	Lithium manganese oxide - Li _{1-x} Mn ₂ O ₄
LiPS	Lithium polysulfide
LUMO	Lowest unoccupied molecular orbital
MALDI	Matrix-assisted laser desorption/ionization
MDETP	[5,15-bis-(ethynyl)-10,20-dithienylporphyrinato]M(II)
MeOH	Methanol
MOF	Metal-organic framework
NanoCT	Nano-computed X-ray tomography
NCA	Lithium nickel cobalt aluminium oxide - LiNi _{0.8} Co _{0.15} Al _{0.05} O ₂
NiNC	Nickel norcorrole
NMC	Lithium nickel manganese cobalt oxides - LiNi _x Mn _y Co _{1-x-y} O ₂
NMP	<i>N</i> -Methyl-2-pyrrolidone
NMR	Nuclear magnetic resonance
OCV	Open-circuit voltage

P5Q	Poly-Pillar[5]quinone
PAN-S	Polyacrylonitrile/Sulfur
PAQS	Polyanthraquinone sulfide
PC	Propylene carbonate
PEDOT	Poly(3,4-ethylenedioxythiophene)
PNDIE	Poly[<i>N,N</i> -(ethane-1,2-diyl)-1,4,5,8-naphthalenetetracarboxiimide]
PP	propylene film
PP ₁₄ TFSI	1-butyl-1-methylpiperidinium-bis-(trifluoromethylsulfonyl)imide
PSS	poly(styrene sulfonate)
PTO	Pyrene-4,5,9,10-tetraone
PTMA	Poly(2,2,6,6-tetramethylpiperidinyloxy-4-ylmethacrylate)
PTO	Pyrene-4,5,9,10-tetraone
PVDF	Polyvinylidene fluoride
RT	Room temperature
RTIL	Room-temperature ionic liquids
SBR	Styrene-butadiene
SE	Secondary electrons
SEI	Solid electrolyte interface
SEM	Scanning electron microscope
SHE	Standard hydrogen electrode
SIB	Sodium-ion battery
SOMO	Single occupied molecular orbital
SS	Stainless Steel
TAPc	Tetraaminephthalocyanine
TAPP	5,10,15,20-tetra(4-Aminophenyl)-21 <i>H</i> ,23 <i>H</i> -porphin
TBAF	Tetrabutylammonium fluoride
TEA	Triethylamine
TEM	Transmission electron microscope
TEMPO	(2,2,6,6-tetramethylpiperidin-1-yl)oxyl
TGA-DSC	Thermogravimetric differential scanning calorimetry
THF	Tetrahydrofuran
TM	Transition metal
TMS	Trimethylsilyl
ToF	Time-of-flight mass spectrometry
TPM	Tetrapyrrolic macrocycles
TPyrP	5,10,15,20-tetra(4-pyridyl)-21 <i>H</i> ,23 <i>H</i> -porphin
TThP	5,10,15,20-tetra(4-thiophenophenyl)-21 <i>H</i> ,23 <i>H</i> -porphin
UMS	Unsaturates metal sites

Abbreviations

UV-Vis	Ultraviolet-visible spectroscopy
VOI	Volume of interest
vs	Versus
XRD	X-ray diffraction
XPS	X-ray photoelectron spectroscopy

Contents

1	Introduction	1
2	Fundamentals	5
2.1	Battery Basics	5
2.1.1	Battery nomenclature	6
2.1.2	Principle of Operation	10
2.2	Rechargeable Batteries	11
2.2.1	Lithium-ion Battery	12
2.2.2	Calcium Batteries	20
2.2.3	Aluminium Batteries	25
2.3	Organic Electrode Materials	30
2.4	Porphyrinoids	39
2.5	Porphyrinoids: Promising Battery Electrode Materials	41
2.6	CuDEPP: An Exceptional Porphyrin-based Electrode Material	45
3	Experimental methods	53
3.1	UV-Visible Spectroscopy	53
3.2	Scanning Electron Microscopy	54
3.3	FIB-SEM Tomography	55
3.4	Nano-Computed X-ray Tomography	56
3.5	Galvanostatic Cycling	57
3.6	Cyclic Voltammetry	59
3.7	Electrochemical Impedance Spectroscopy	59
4	Aim of the thesis	63
5	Central Metal Matters	65
5.1	Introduction	65
5.2	Electrochemical Experiments	66
5.2.1	Electrode Preparation	66
5.2.2	Cell Assembly	66
5.2.3	Electrochemical Measurement	67
5.3	Results and Discussion	68
5.4	Conclusion	89
6	Morphological Aspects	91
6.1	Introduction	91
6.2	Electrochemical Experiments	92
6.2.1	Electrode Preparation	92
6.2.2	Cell Assembly	93
6.2.3	Electrochemical Measurement	93
6.3	Results and Discussion	94

6.3.1	NanoCT and FIB-SEM Tomography	110
6.4	Conclusion	118
7	Pyridine-Functionalized Porphyrin MOF as Cathode Material	121
7.1	Introduction	121
7.2	Synthesis and Characterization	122
7.3	Lithium-ion Battery	131
7.3.1	Electrode Preparation and Cell Assembly	131
7.3.2	Results and Discussion	131
7.4	Aluminium Battery	134
7.4.1	Electrode Preparation and Cell Assembly	134
7.4.2	Results and Discussion	135
7.5	Calcium Battery	138
7.5.1	Electrode Preparation and Cell Assembly	138
7.5.2	Results and Discussion	139
7.6	Conclusion	145
8	The self-conditioning	147
8.1	Introduction	147
8.2	Electrochemical Experiments	149
8.2.1	Electrode Preparation	149
8.2.2	Cell Assembly	150
8.2.3	Electrochemical Measurement	150
8.3	Results and Discussion	150
8.4	Conclusion	168
9	Experimental Section	171
9.1	Materials and Equipment	171
9.2	xDEPP from Zn to Co and Free-base	176
9.2.1	Preparation of Complexes	176
9.2.2	Computational	187
9.3	Microstructure of CoDEPP	188
9.3.1	Procedure	188
9.4	Pyridine-functionalized MOF	195
9.4.1	Preparation of CuTPyrP-MOF	195
9.4.2	Computational	196
9.5	Self-conditioning	197
9.5.1	Preparation of Complexes	197
9.6	Computational	198
10	Concluding remarks	199
A	Appendix	232
A.1	Chapter 5	232
A.2	Chapter 6	237
A.3	Chapter 8	238

Chapter 1

Introduction

Batteries play a vital role in our daily lives and their importance and demand continues to grow.[1] Despite the long history of battery research, dating back to the 18th century, there is still untapped potential for further advances.[2, 3] The urgency for better and new battery technologies is clear, especially in light of climate change and the visible consequences we are experiencing. It is essential to transition to sustainable energy sources in order to significantly reduce dependence on fossil fuels. To achieve this, it is necessary to develop advanced technologies for energy storage. Renewable energy sources such as wind, solar and tidal offer great potential for clean and sustainable energy generation.[4] By harnessing these sources effectively and efficiently, we can contribute to a greener and more sustainable future. The current state of the art in energy storage technologies can be divided into several distinct categories (Fig. 1.1), including thermal (thermochemical, sensible thermal), mechanical (flywheel, compressed air), chemical (fuel cells), electrochemical (batteries, flow batteries), and electrical (capacitors, superconducting magnetic storage) storage devices.[5] Out of all, the mentioned energy storage systems, electrochemical energy storage, especially lithium-ion batteries (LIBs) with their high energy density, is the most widely used one, in particular in portable applications.[6] As the demand for electricity continues to increase due to economic growth and widespread electrification and options are required to store renewable energy, there is a pressing need for enhanced and advanced technologies.[7] Out of the many current trends in electrochemical energy storage, two can be highlighted. Firstly, there is a growing interest in exploring post-lithium systems, such as potassium (K), sodium (Na), magnesium (Mg), calcium (Ca), and aluminium (Al) batteries. These alternative systems offer the potential for higher energy densities and improved safety compared to traditional

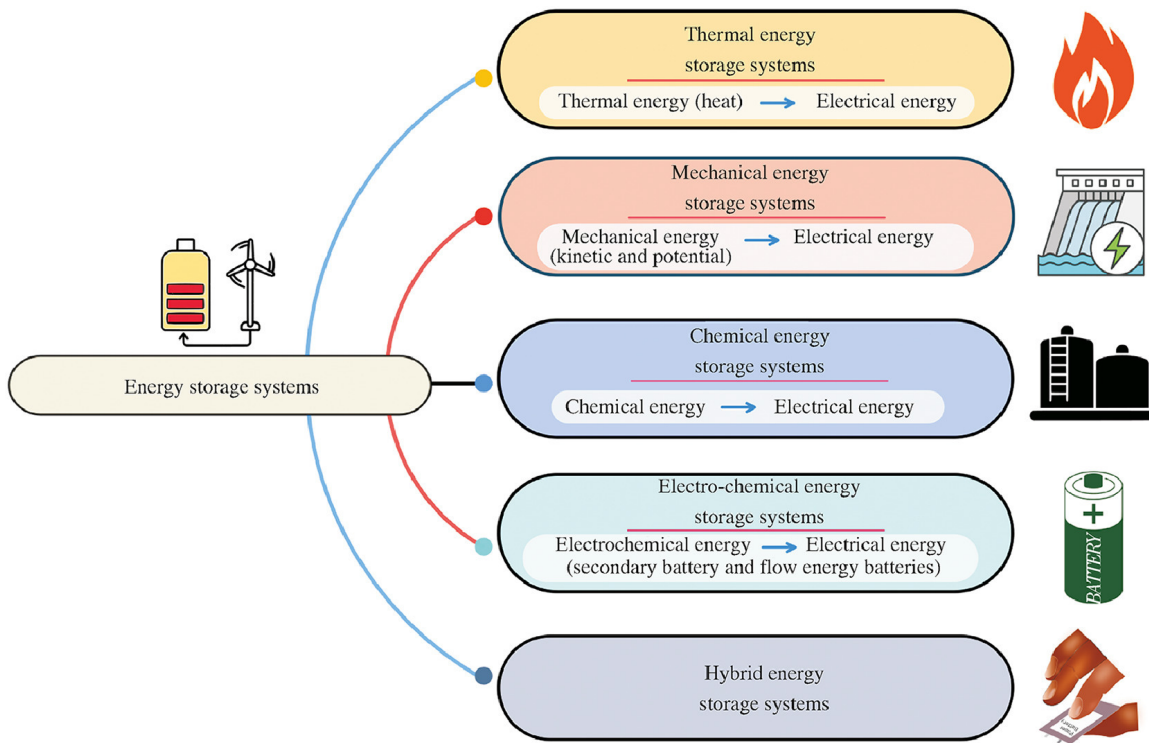


Figure 1.1: Classification of energy storage systems. Reproduced with permission[6], Copyright (2022) Elsevier.

lithium-based batteries. Secondly, there is a focus on developing new cathode materials to overcome the limitations of traditional inorganic materials such as transition metal oxides and sulfides.[8] These new cathode materials aim to enhance the performance of lithium-ion batteries.[9]

Alongside advanced technologies such as metal-air batteries, organic batteries offer more sustainable and adaptable materials for the future. They can be utilized in various systems, such as metal-ion[10], dual-ion[11] or shuttle-ion batteries.[12, 13] The redox chemistry of organic electrodes is not restricted to particular counter ions. Furthermore, the structure of organic materials can be tailored to fulfill specific application necessities. Organic electrode materials typically demonstrate high rate capability, rapid redox kinetics, and other favorable properties, such as lower costs, flexible structures, and sustainability.[14, 15]

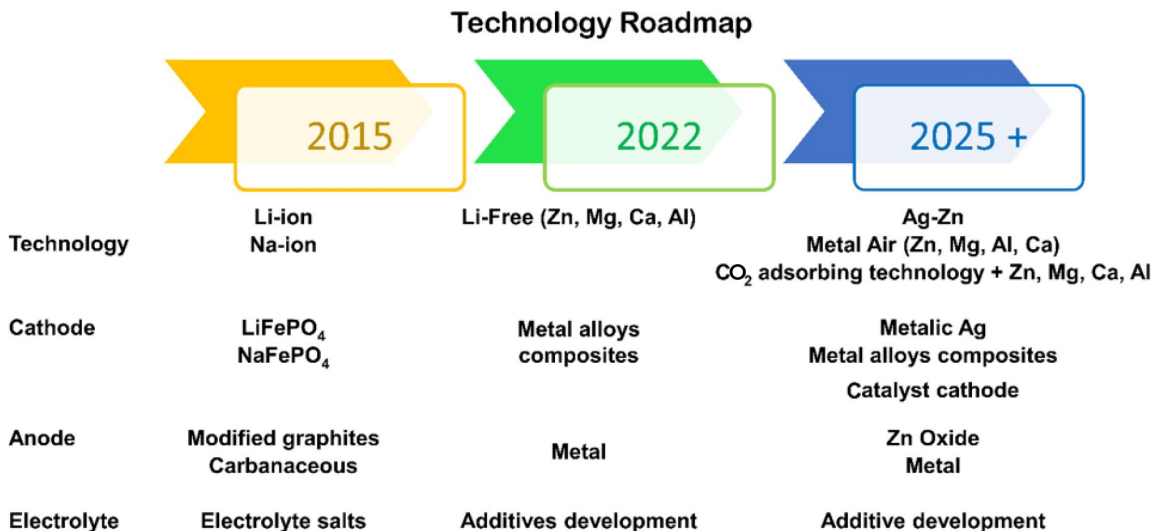


Figure 1.2: Battery technology timeline. Reproduced with permission[16], Copyright (2022) American Chemical Society.

In recent decades, there has been considerable progress in new battery technologies, indicating their vast potential (Fig. 1.2). For example, lithium-sulfur batteries can achieve four times the specific capacity of conventional cell configurations with NMC (lithium nickel manganese cobalt oxides) cathodes.[17, 18] Similarly, organic

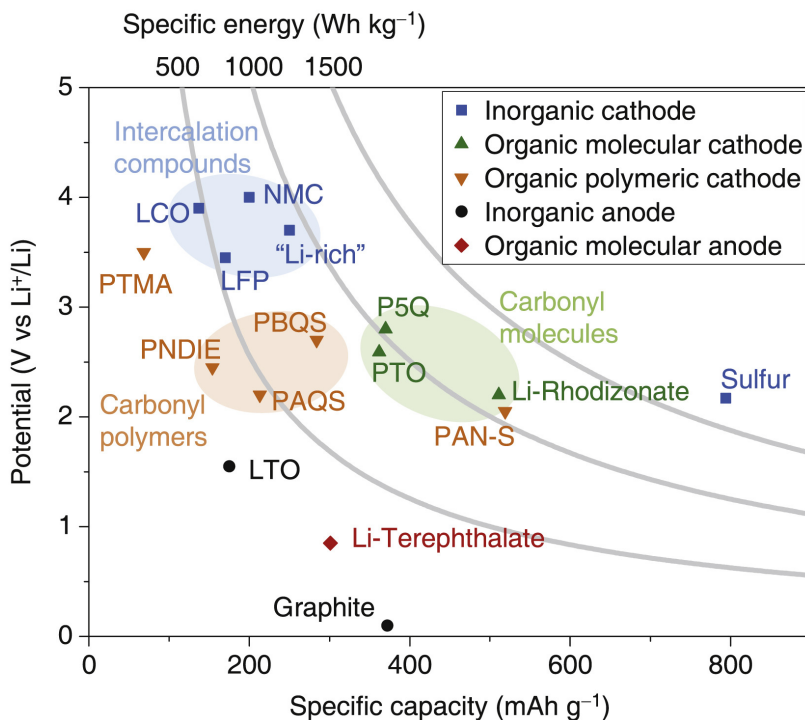


Figure 1.3: Comparison between potential and specific capacity of selected electrode materials. Reproduced with permission[18], Copyright (2018) Elsevier.

molecular cathodes exhibit nearly twice the specific capacity of NMC in lithium-ion batteries and typically offer higher energy densities.(Fig. 1.3). Moreover, the shift to post-lithium systems enhances performance and presents additional benefits such as

reduced CO₂ emissions and the use of more abundant materials, in contrast to the long-standing inorganic electrode materials.[19] In this thesis, novel organic electrode materials are developed for rechargeable battery systems. Additionally, their properties were tailored using various synthetic approaches to gain a more comprehensive understanding of the structure-performance relationship, offering fresh insights and strategies for the next generation of energy storage.

Chapter 2

Fundamentals

In this chapter, the necessary theoretical background by referencing various literature sources will be provided. The chapter aims to highlight the fundamentals and the significance of the topic. We will begin with an introduction to battery basics, covering standard definitions and presenting a comprehensive overview of the current state of the field. Although the main focus of this discussion is on lithium-ion, calcium, and aluminium batteries, the materials discussed are also potentially applicable to various post-lithium systems. Following that, we will provide an overview of organic electrode materials, discussing their advantages, disadvantages, and their potential in future battery technologies. An comprehensive discussion of porphyrinoids utilized as organic electrode materials will be presented, which serve as the foundation of this work. Lastly, this report will describe the experimental techniques used to analyse the materials utilized in this study and assess their performance in the battery system.

2.1 Battery Basics

Galvanic/voltaic cells consist of one positive and one negative electrode. The electrodes are in contact with an electrolyte and physically separated by a separator, which is typically a porous material when using liquid electrolytes. The electrolyte itself should be ionically conducting and electronically insulating.[20] Galvanic cells store electrical energy through electrochemical reactions when the electrodes are connected to an external load.[21] Fuel cells, flow batteries, and batteries are distinct forms of galvanic cells. Batteries, unlike other mentioned energy storage systems, provide a predetermined and limited amount of electricity based on the quantity of

reactants present within the closed system.[21] Another distinguishing characteristic among various types of galvanic cells is their rechargeability. Fuel cells are typically not considered rechargeable, unlike other battery types. Additionally, different types of galvanic cells can be combined, such as in the case of metal-air batteries.

Batteries can be classified into two main groups: primary batteries and secondary batteries. Primary batteries are non-rechargeable and have a limited lifespan. Secondary batteries are rechargeable and can be used multiple times. For a battery to be secondary and rechargeable, the redox reactions occurring on the electrodes must be reversible. This means that the electrochemical reactions that take place during charging and discharging can be reversed, allowing the battery to be used multiple times by alternately supplying and extracting electric energy.[22] Although primary batteries have their advantages, such as higher energy density per weight and volume and immediate full capacity, they represent only about 20% of the used batteries, including alkaline batteries.[21] In this work, focus will be on rechargeable secondary batteries, particularly lithium-ion batteries.

2.1.1 Battery nomenclature

Cathode and anode[22]: The cathode is the electrode where reduction occurs, while the anode is the electrode where oxidation of a redox reaction takes place; these reactions are spontaneous. The determination of an electrode as cathode or anode depends on whether the system is undergoing a charging or discharging process, see Table 2.1 for definitions.

Table 2.1: Definition of cathode and anode.

	Charge	Discharge
Positive electrode (+)	anode	cathode
Negative electrode (-)	cathode	anode

In the following sections, the electrodes will be used in reference to the discharge process.

Active material[23]: The active material is considered to be the material involved in the electrochemical reaction during charge and discharge. On the cathode side, this can be an organic material or transition metal oxide, while on the anode side, it can be lithium or lithium eventually intercalated within graphite. Inactive materials of

electrochemical cells include the stainless steel (SS) current collector or the separator.

Electrolyte[24]: The electrolyte serves as an ionic conductor, facilitating the transfer of charge in the form of ions between the cathode and anode. Typically, the electrolyte is a salt like LiPF_6 , which can be dissolved. It is important for the electrolyte to be ionically conductive while not being electronically conductive.

Capacity[22]: The theoretical capacity C_{theo} represents the maximum amount of electric charge that can be stored when all the active material is fully utilized. Capacity is typically measured in the unit of Coulomb, where 1C is equivalent to 1 As, or it can be expressed in Ampere-hours (Ah), where 1Ah is equal to 3600 As. To compare different electrodes, the capacity is often expressed as the specific capacity C_{spec} , which is determined by the mass of the active material used. The unit of specific capacity is Ah g^{-1} , and can be calculated using the following equation:

$$C_{\text{spec}} = \frac{n \times F}{M_w} = \frac{n \times 96485[\text{As} \cdot \text{mol}^{-1}]}{M_w[\text{g} \cdot \text{mol}^{-1}]} = \frac{n \times 26801}{M_w}[\text{mAh} \cdot \text{g}^{-1}] \quad (2.1)$$

where n represents the total number of transferred electrons during the redox reaction, F is the Faraday constant and M_w is the molecular weight of the active material. The theoretical capacity is a crucial characteristic of the electrode material as it depends on the number of electrons that can be delivered and the molecular weight, which is influenced by the chosen structure of the active material. The limiting electrode primarily determines the specific capacity.

Cell voltage[21]: The hypothetical cell voltage can be calculated using the following equation:

$$E_{\text{cell}}^{\circ} = E_{\text{red}}^{\circ}(\text{cathode}) - E_{\text{red}}^{\circ}(\text{anode}) \quad (2.2)$$

Here, the standard reduction potentials of the cathode and anode are used to determine the cell voltage, which is the difference between the two potentials. Standard conditions refer to specific parameters such as a temperature of 25 °C, an effective pressure of 1 atm, and a concentration of 1M in the solution. However, these conditions do not accurately represent all operating conditions of a battery. In such cases, the Nernst equation is used to account the non-standard conditions and calculate the cell potential:

$$E = E^{\circ} - \frac{RT}{nF} \ln Q \quad (2.3)$$

with R as universal gas constant ($8.314 \text{ J K}^{-1} \text{ mol}^{-1}$), n the number of transferred electrons per unit, F the faraday constant (96485 C mol^{-1}) and Q the reaction quotient. In order to use the Nernst equation, it is essential to have a properly balanced reaction equation. The equation should accurately represent the redox reactions occurring in the electrochemical cell.

Energy[22]: The theoretical energy \mathbf{E}_{theo} is the maximum energy that could be delivered by a given system, calculated from the theoretical capacity and theoretical voltage [V]. The theoretical voltage can be calculated by utilizing the standard potentials of the electrodes, as provided in the equation 2.2. With this, the theoretical energy can be calculated using the following equation and is given in Watt-hours (Wh):

$$E_{\text{theo}} = C_{\text{theo}} \times V \quad (2.4)$$

The gravimetric energy \mathbf{E}_{spec} is the maximum energy that can be utilized per unit mass of the active material, and it is expressed in Wh g^{-1} :

$$E_{\text{spec}} = \frac{E}{m} \quad (2.5)$$

The volumetric energy density, denoted as \mathbf{E}_{dens} , is the energy provided by the volume of the active material and is measured in Wh L^{-1} . It can be calculated using the following equation:

$$E_{\text{dens}} = \frac{E}{\text{volume}} \quad (2.6)$$

Power[23]: The gravimetric power refers to the power delivered by the cell per unit mass under specific operating conditions. The gravimetric power density represents the power output per unit mass of the cell, typically measured in W kg^{-1} . On the other hand, the volumetric power density indicates the power output per unit volume of the cell, measured in W m^{-3} .

Coulombic efficiency[23]: The coulombic efficiency η_c or faradaic efficiency, is the ratio between the number of electrons or amount of electricity delivered and the number of electrons or amount of electricity injected into the cell:

$$\eta_c = \frac{C_{\text{discharge}}}{C_{\text{charge}}} \quad (2.7)$$

The coulombic efficiency may be less than 100% as a result of side reactions, causing the loss of electrons during the reversible charge-discharge cycle of the secondary battery.

C-rate[22]: The C-rate is a parameter that measures the rate at which an electrochemical cell is charged or discharged. A C-rate of 1 C signifies that the cell can be fully charged or discharged in 1 hour.

$$C = \frac{i_{\text{applied}}}{i_{1\text{h}}} \quad (2.8)$$

with $i_{1\text{h}}$, the current to charge and discharge the cell in 1h.

Thermodynamics and kinetics[21]: The Gibbs free energy (ΔG), also known as the free energy, is a crucial thermodynamic quantity used as a criterion for predicting the direction of reactions occurring in a battery. It provides a fundamental relationship between cell voltage and energy, making it essential for understanding the behavior of batteries:

$$\Delta G^\circ = -nFE^\circ \quad (2.9)$$

The change in Gibbs free energy is determined by the multiplication of the number of electrons transferred n , the electric charge per mole of electrons (F), and the cell voltage (E°) under standard conditions. The negative sign indicates that the Gibbs free energy is negative, while the cell voltage is positive for spontaneous reactions, such as battery discharge. The negative sign indicates that the process is favoured by the change in enthalpy and entropy. The Gibbs free energy can be in this case also interpreted as the electromotive force (EMF). In real systems, equilibrium conditions are often not achieved, resulting in lower discharge potentials and higher charge potentials. This can be attributed to kinetic limitations or other factors such as physical, chemical, or electrochemical processes occurring during charge transfer and charge transport.[25] Polarization is a kinetic phenomenon that significantly impacts the performance of battery cells.[25] In lithium-ion batteries, it can lead to restricted mass transport in the electrolyte and solid phases of the electrodes, poor solid phase contact, and sluggish redox chemistry. The extent to which each of these effects contributes to the polarization depends on the thermodynamics and kinetics of the materials involved, the design of the cell, and the charging and discharging condi-

tions.[26] Three types of polarization need to be taken into account: 1) activation polarization, which occurs during charge transfer at the interfaces between the electrolyte and electrodes, 2) ohmic polarization, caused by the resistance within different components of the cell, and 3) concentration polarization, resulting from limited mass transport.[25] A comprehensive understanding of both kinetics and thermodynamics is crucial for the design of new materials.

2.1.2 Principle of Operation

The schematic representation of the working principle of secondary batteries based on cationic shuttle is shown in the Fig. 2.1. During discharge, when the cell is connected

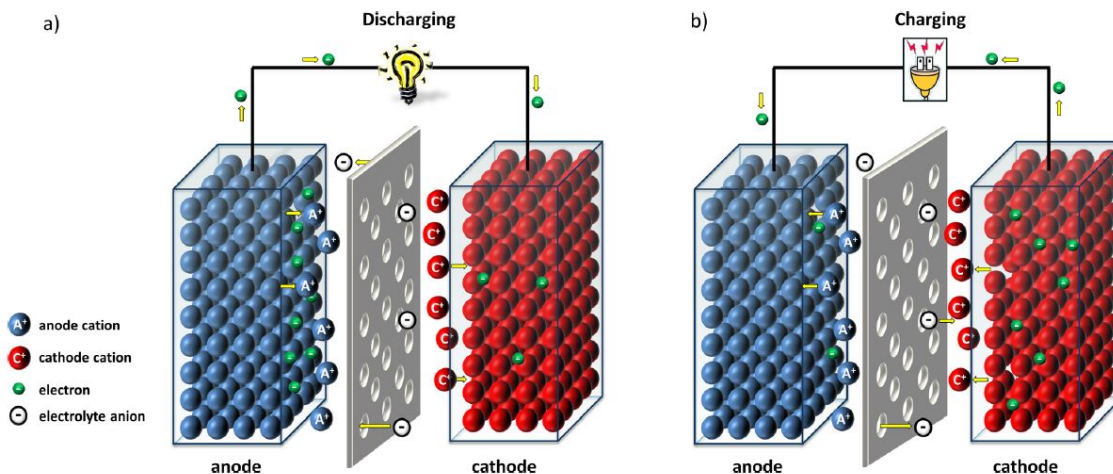


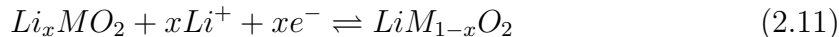
Figure 2.1: Working principle of a metal-based secondary battery. Reproduced with permission[22], Copyright (2016) American Chemical Society.

to a load, electrons flow through an external circuit from the anode to the cathode. At the anode, oxidation reactions occur, leading to the release of electrons. These electrons are then accepted at the cathode, where reduction reactions take place. The presence of the electrolyte enables the transportation of anions and cations to the anode and cathode, thereby completing the electric circuit. In the recharge process, the polarity of the electrodes is reversed, with reduction occurring at the positive electrode and oxidation at the negative electrode. The positive electrode becomes the anode, while the negative electrode becomes the cathode during the recharge process.[24] In the case of a lithium-ion battery, the redox reactions can be represented as follows:[21]

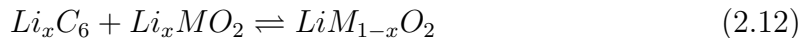
Negative electrode:



Positive electrode:



Cell:



It's crucial to emphasize that Li_xC_6 is a stoichiometric expression that indicates the makeup of the intercalated substance into the layered structure, rather than representing an individual molecule.

2.2 Rechargeable Batteries

Secondary batteries have become extensively utilized in a wide range of applications, ranging from small portable devices to powering electric vehicles. The demand for secondary batteries is continuously increasing.[27] The conversion of electrical energy to chemical energy and *vice versa* is a fundamental characteristic of secondary batteries. This process should be reversible, energy-efficient, and ideally not cause significant physical changes, as these can impact the cycle life of the battery.[24] Desired attributes of batteries include high specific energy, low internal resistance, and reliable performance under various temperature conditions. Since its introduction by Sony in 1991, there has been a growing interest in lithium-ion batteries.[28] Over the last several decades, lithium-ion technology has been predominant in the global battery market, among other technologies. However, in the future, post-lithium systems are expected to become more relevant due to their high abundance and low cost. Sodium-ion and potassium-ion batteries are already well-developed and are nearing commercialization in the coming years.[29] Additionally, multivalent systems such as magnesium, calcium, and aluminium are being intensively researched due to their ability to provide additional electrons per charge carrier. The following section will provide a description of state-of-the-art battery systems, with a primary focus on lithium-ion batteries and various post-lithium systems that are of relevance to this study.

2.2.1 Lithium-ion Battery

Three scientists, John B. Goodenough, M. Stanley Whittingham, and Akira Yoshino, were awarded the Nobel Prize in 2019 for their pioneering contributions to the development of the lithium-ion battery. Whittingham's pioneering efforts in the 1970s led to the introduction of titandisulfide as a cathode material[30], which laid the foundation for the development of rechargeable lithium-based batteries. Goodenough's subsequent breakthrough in the 1980s, with the discovery of LiCoO_2 as an improved cathode material[31], revolutionized the energy storage capabilities of LIBs. Yoshino's contributions in the 1990s, particularly his innovative use of carbon-based materials and the replacement of lithium metal with more stable alternatives[32], significantly enhanced the safety and commercial viability of LIBs. Over the past five decades, extensive research has been dedicated to further advancing battery systems, driven by the remarkable success and potential of LIBs. The continuous pursuit of higher energy densities, improved performance, and enhanced safety measures has resulted in significant advancements in battery technology.[28] As a result, LIBs have become the state-of-the-art and most widely used battery system across various applications. This section provides an overview of the significance of battery research and traces the evolution of LIBs, thus setting the stage for all subsequent explanations. It also highlights the continued interest and significance of LIBs in the context of modern energy storage requirements.

In LIBs, electrodes are used on both sides, allowing Li^+ ions to intercalate.[28] This kind of system is also known as a "rocking chair battery" because the Li^+ ions "rock" back and forth between the positive and negative electrodes.[24] Typically three categories of oxide cathode materials (Fig. 2.2) in LIBs are known: layered metal oxides like LiMO_2 ($M = \text{Co}, \text{Ni}, \text{Mn}$, and their mixtures), spinels like LiM_2O_4 ($M = \text{Mn}$ and mixtures with Co or Ni) with a tunneled structure, and olivines like LiMPO_4 ($M = \text{Fe}, \text{Mn}, \text{Ni}, \text{Co}$, and their mixtures). In modern LIBs, the cathode is pre-lithiated, meaning it already contains lithium ions, allowing the cell to be assembled in a discharged state.[28] LiCoO_2 (LCO), which was used in the first commercialized battery, consists of monovalent Li^+ ions and trivalent Co^{3+} ions arranged on the alternate (111) planes of the rock salt structure.[33] This structure is commonly referred to

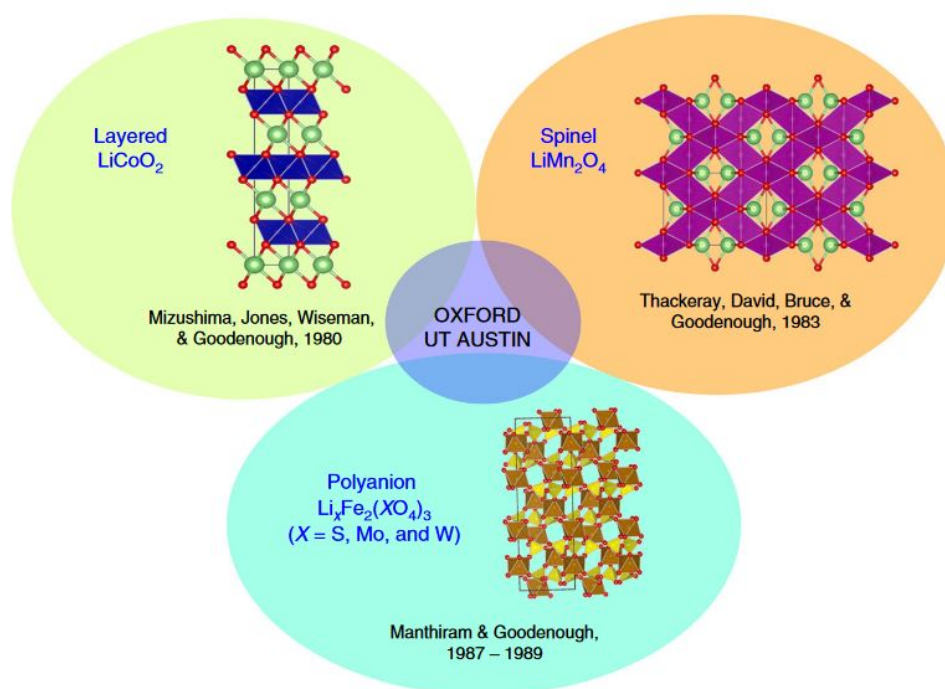


Figure 2.2: Three categories of oxide cathodes. Reproduced with permission[33], Copyright (2020) Springer Nature.

as the α - NaFeO_2 structure.[34] The significant difference in size between the cations (Li^+ and Co^{3+}) within the structure is indeed relevant for the fast intercalation of lithium ions and the intrinsic conductivity. This size disparity creates open spaces or channels within the crystal lattice, allowing for the easy movement of Li^+ ions during the intercalation process.[33] By deintercalating Li^+ ions from the LCO layers, a potential of 4 V can be achieved against Li/Li^+ .[34] LCO delivers only around 50% of the theoretical capacity ($\sim 140 \text{ mAh g}^{-1}$) at $\leq 4.2 \text{ V}$ vs. Li/Li^+ .[23] This limitation arises from chemical instability when $x < 0.5$ Li_xCoO_2 . This instability is caused by the overlap of bands in the redox-active $\text{Co}^{3+/4+}$: t_{2g} band with the O^{2-} : 2p band, leading to oxygen evolution (Fig. 2.3).[33] Based on this characteristic, one aim in designing new cathode materials was to lower the 2p oxygen bands below the Fermi level to reduce the likelihood of oxygen evolution. This goal could be achieved by incorporating aluminium into the LCO structure, such as in $\text{LiNi}_{0.8}\text{Co}_{0.15}\text{Al}_{0.05}\text{O}_2$ (Nickel Cobalt Aluminium - NCA).[34] Lowering the 2p oxygen bands by incorporating aluminum into the structure is just one approach among many other ways to optimize metal oxide structures for battery applications. One of the concerns associated with LCO is the use of cobalt, as it is a scarce and toxic material that is often linked with ethical dilemmas related to mining practices. In some countries

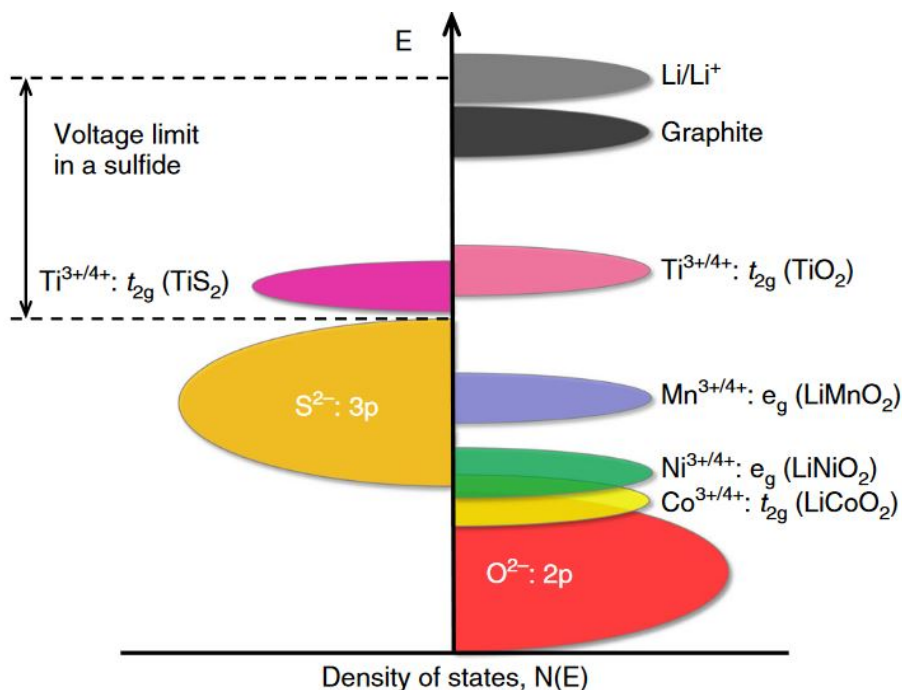


Figure 2.3: Positions of the redox energies relative to the top of the anion: p bands. Reproduced with permission[33], Copyright (2020) Springer Nature.

like the Democratic Republic of Congo, cobalt mining has been linked to issues such as child labor and poor working conditions.[35] To address these concerns, alternative approaches have been pursued, such as replacing cobalt with other 3d transition metals like Ti³⁺ or V³⁺. [33] When replacing cobalt with other transition metals like V³⁺, a potential issue that can arise is the transition from a layered structure to a spinel structure during charge and discharge cycles. This transition is caused by the low octahedral-site stabilization energy associated with V³⁺ ions.[33] LiTiO₂ operates at relatively low voltages around 1.5 V, which indeed makes it less suitable as a cathode material in typical LIBs.[33] In response to the high cost and low capacity limitations of LCO, a more successful approach was the addition of manganese and nickel to create NMC Li_{1-x}(Ni_{0,33}Mn_{0,33}Co_{0,33})O₂. However, it can utilize only 66% of the lithium ions due to the limitation that not all lithium ions can be fully deintercalated. This phenomenon is quite common for this type of oxide cathode structures.[34]

Another significant group of metal oxides in LIBs is the spinel type Li_{1-x}Mn₂O₄(LMO). Within this structure, the stable framework [Mn₂]_{16d}O₄ consists of edge-shared octahedra. This framework offers a three-dimensional pathway for the diffusion of lithium ions, facilitating fast lithium-ion conductivity within the material.[33] In the lithiated

structure of LMO, manganese exists in the oxidation state of 3+ or 4+. During delithiation, when lithium ions are extracted from the structure, Mn^{3+} undergoes oxidation to Mn^{4+} . This oxidation process results in a higher potential, and LMO can deliver a voltage of around 4.1 V against Li/Li^+ , with a capacity above 130 mAh g⁻¹[33, 34] Lithium manganese oxide often exhibits disadvantages in cycle stability, which can be attributed to several reasons. One major factor is its instability under acidic conditions. Even small impurities of water in the system can lead to the formation of hydrofluoric acid (HF) due to decomposition of LiPF_6 . As a result, Mn^{2+} ions may dissolve into the electrolyte, leading to the passivation of the electrode surface with formation of MnO or MnF_2 . [34] Another disadvantage of LMO is the Jahn-Teller distortion experienced by the Mn^{3+} ions within the $\text{MnO}_{6/3}$ octahedral structure. This distortion causes a change in the cubic symmetry to a tetragonal one, resulting in a volume change. This volume change during cycling can lead to mechanical stress and strain on the electrode, affecting its structural stability and cycling performance.[28] It is worth noting that LMO is generally considered less toxic than LCO (LiCoO_2). However, to ensure its stability, it is important to operate LMO within certain temperature limits, typically below 55 °C, and strictly avoid overcharging the battery.[23] By adhering to these conditions, LMO can serve as a stable cathode material in LIB systems.

The third group of metal oxides commonly used as cathode materials in LIBs is the olivine structure. One well-known member of this group is $\text{Li}_{1-x}\text{FePO}_4$ (LFP).[23] The distorted octahedral lithium coordination polyhedra are interconnected along the [010] edges, forming a one-dimensional diffusion pathway for lithium ions.[34] LFP is a low-cost cathode material commonly used in commercial LIBs. It exhibits excellent cycleability and has a long lifetime. However, due to its inherently low electronic conductivity, additional measures are necessary to improve its performance. One approach is to synthesize LFP as nanopowders to increase its surface area and enhance its conductivity. Another method is to deposit a carbon coating on the surface of LFP particles, which helps facilitate electron transfer within the electrode. In terms of voltage, LFP has a lower voltage against Li/Li^+ (around 3.2 V) compared to other cathode materials like LCO.[23] The specific capacity of the material is typically in

the range of 120-160 mAh g⁻¹, while the theoretical capacity is 170 mAh g⁻¹. [36] Due to the inductive effect of the phosphorus atoms, the outer electrons of the oxygen ions are polarized in strong covalent P-O bonds, weakening the covalency of the Fe-O bond. This results in a reduction in the redox energy of the Fe³⁺/Fe²⁺ redox couple and an increase in the open circuit voltage against Li/Li⁺. [34]

Table 2.2: Comparison between gravimetric capacity of lithiated metal oxides in LIBs. [23]

	Theoretical gravimetric capacity [mAh g ⁻¹]	Theoretical gravimetric capacity [mAh g ⁻¹] with account taken of the degree of insertion	Average practical gravimetric capacity [mAh g ⁻¹]	Cost
LiCoO ₂ (LCO)	274	137	120	high
LiMn ₂ O ₄ (LMO)	148	148	120	low
LiFePO ₄ (LFP)	170	150	150	low

Each electrode material has its own set of advantages and is suitable for various applications (Table 2.2). Factors like cost, toxicity, and cycle life play crucial roles for all the materials. [36] Layered oxides, despite having the highest energy density, can be quite costly in the global market due to the inclusion of cobalt, manganese, and nickel. However, in terms of cost-effectiveness, LFP emerges as a winner, primarily due to its low-cost iron component, although it does have a lower energy density compared to other materials. [34] Another significant advantage of LFP is its high thermal stability, which surpasses that of other transition metal oxides, making oxygen evolution almost impossible. Additionally, when considering lithium-ion diffusion pathways, LFP permits diffusion in only one direction, whereas other materials may allow diffusion in two or three dimensions. The disadvantages associated with LFP, such as its relatively lower energy and power density, can be mitigated by the addition of manganese, resulting in LFMP (LiFe_{1-x}Mn_xPO₄), which can increase these values by approximately 20%. [34] These arguments highlight that each material possesses its own distinct advantages and disadvantages, and the appropriate application must

be determined by considering these factors.

The design and improvement of electrode materials have become important topics due to the high demand for advancements in energy storage systems in the coming years. Beyond the familiar inorganic electrode materials, there is a revitalized field of organic electrode materials that presents compelling prospects for tackling conventional complications. These organic materials provide potential solutions for issues such as the use of unfavorable transition metals or high-temperature production methods that contribute to CO₂ emissions. Discussions about organic electrode materials will follow to explore their potential benefits and applications.

In addition to the cathode, the anode also plays a significant role in LIBs. In early attempts, lithium foil was utilized as the anode material, offering high capacities of up to 3860 mAh g⁻¹ and having a very low potential of approximately -3.04 V (vs. standard hydrogen electrode, SHE).[25] The use of Li metal as an anode provided a high theoretical capacity and excellent performance; however, challenges such as dendrite formation and safety concerns limited its practical application in commercial LIBs. Cells that are currently constructed with lithium metal as the counter electrode to investigate the performance of cathode materials are commonly referred to as half-cells. In these cells, the focus is on studying and evaluating the characteristics and behaviour of the cathode material, typically the limiting electrode when using lithium metal as an anode. Due to safety concerns associated with the use of lithium metal in commercial batteries, intercalation compounds such as graphite, hard carbons and soft carbons are commonly employed as anode materials. Graphite offers improved safety characteristics compared to lithium metal due to the uncontrollable growth of lithium dendrites.[37] Additionally, graphite anodes are cost-effective and can provide high capacities, with values of up to 372 mAh g⁻¹. [23] The intercalation of lithium into the layers of graphite can occur at low voltages, typically below 1.0 V vs. Li/Li⁺. This process leads to the formation of LiC₆ in its intercalated version. It is important to note that LiC₆ is a stoichiometric formula that represents the composition of the intercalated material, rather than a discrete molecule.

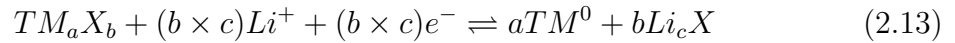
Another well-known anode material is lithium titanate oxide Li₄Ti₅O₁₂ (LTO). It features a spinel structure and can store lithium reversibly at around 1.55 V, offering

a capacity of approximately 160 mAh g^{-1} . The intercalation of lithium ions in LTO occurs without any significant volume change. Similar to graphite, the intercalation process in LTO happens in two phases. One notable advantage is that there is no visible formation of a solid electrolyte interface (SEI), contributing to the high safety of the cell. However, LTO does suffer from low electrical conductivity. To improve its performance, synthesis of LTO nanoparticles and surface coating with carbon, as done for LFP, have been explored. Unfortunately, due to its high potential against Li, LTO exhibits lower energy density. Nonetheless, LTO remains a highly useful anode material in large stationary batteries or in applications requiring high power, such as hybrid cars, where its excellent safety characteristics and power capabilities are particularly beneficial.[34]

Another class of anode materials in LIBs includes lithium alloy materials such as tin (Sn), silicon (Si), and germanium (Ge). These materials possess high theoretical capacities and operate at good voltages, around $0.4 \text{ V vs. Li/Li}^+$. Silicon, in particular, exhibits an extremely high specific capacity of up to 4212 mAh g^{-1} when fully lithiated, which is currently the highest known capacity for an alloy material.[34] However, the intercalation of lithium into Si or Sn occurs in multiple steps and results in a significant volume change. Unfortunately, this volume change leads to material amorphization and a loss of structural stability over repeated cycles. One approach to mitigate this issue is through the use of nanoparticles and embedding the alloy materials in carbon-based matrices. Although these strategies can help to alleviate volume-related issues, it is often at the expense of decreasing the exceptionally high specific capacities linked with these alloy materials.[28]

Conversion-type materials are a relatively new class of anode materials that differ from the commonly used intercalation compounds like LTO and graphite. These materials undergo a chemical reaction during lithiation, resulting in the formation of entirely new products.[38] Similar to alloy materials, conversion-type materials offer a promising route for attaining high-energy-density anodes. Various transition metal compounds, including oxides, sulfides, and phosphides, can undergo conversion reactions, leading to high capacities ranging from 500 to 1500 mAh g^{-1} . [38] The mechanism

of the conversion reaction can be represented by the following equation[38]:



where TM represents transition metals and M the anionic species. Chalcogens (S, Se) and halogens (Br, I) can also undergo conversion reactions of the following type:



Sulfur is indeed a highly attractive material for cathode applications due to its high gravimetric capacity, which can reach up to 1672 mAh g⁻¹. However, sulfur and its discharge product, Li₂S, suffer from low conductivity and the shuttle effect, where sulfur species shuttle back and forth between the cathode and anode, leading to capacity loss and cycling instability.[38] Conversion and alloy materials hold great promise as future anode materials, but there is still a need for further improvements before they can be widely implemented in commercialized batteries. The figure 2.4 gives an overview of the cathode and anode materials mentioned so far, making their strengths more visible:

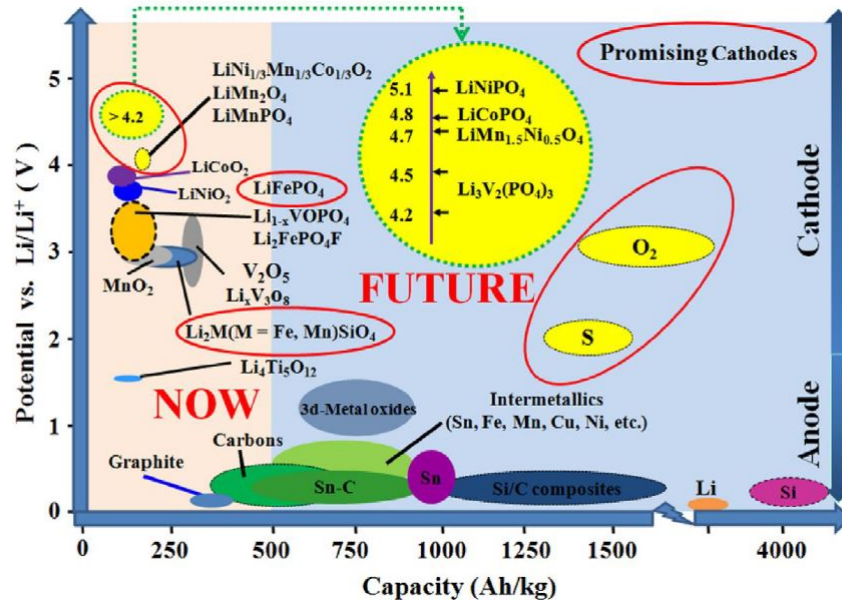


Figure 2.4: Overview of different electrode materials in current LIBs. Reproduced with permission[39], Copyright (2013) Elsevier.

2.2.2 Calcium Batteries

Calcium is the 5th most abundant metal in the Earth’s crust, even more abundant than Na, K, Mg, or Li.[40] With its low cost, it is a highly attractive material for the future battery market to meet the high demand in this field. Furthermore, owing to calcium’s high melting point and its limited propensity to develop dendrites, the substance offers a notable degree of safety.[41] Ca^{2+} ions, in contrast to Mg^{2+} and Al^{3+} ions, exhibit reduced charge density.[42, 43] This lower charge density enables more efficient charge transport while creating better mobility in the electrolyte and interfacial phenomena such as desolvation.[40] The reduction potential of calcium (-2.87 V vs. SHE) is comparable to that of Li, making it well-suited for batteries with high energy density.[40] In terms of gravimetric and volumetric capacity, calcium falls more in line with Na and K. The volumetric capacity of calcium metal (2037 mAh cm⁻³) is quite comparable to Li (2062 mAh cm⁻³).[41] However, when it comes to gravimetric capacity, there is a significant difference (Li: 3861 mAh g⁻¹ and Ca: 1337 mAh g⁻¹) (Table 9.1).[41, 42] In comparison to other multivalent systems (Al, Zn, Mg), calcium is at a disadvantage but performs better than Na. It’s important to note that these values are theoretical and actual capacities may differ, particularly depending on the cathode material used, whether it is an intercalation or conversion material. Theoretical values can decrease when considering practical discharge capacities, cell-level capacity, and energy density. Several promising cell configurations are being investigated, such as Ca//V₂O₅, Ca//LiTiO₂, and Ca//C-fiber. State-of-the-art calcium batteries can achieve energy densities up to 250 Wh kg⁻¹ and discharge capacities ranging from 60-250 mAh g⁻¹, with operating voltages between 1-4 V.[41]

Table 2.3: Comparison between material properties of different metal anodes.[42]

	Redox potentials [V vs. SHE]	Capacity [mAh g ⁻¹]	Melting point [°C]	Abundance [w%]	Density [g cm ⁻³]
Li	-3.04	3861	180	20 ppm	0.534
Na	-2.71	1164	98	2.3	0.968
K	-2.93	684	64	2.1	0.862
Mg	-2.37	2201	651	2.3	1.74
Ca	-2.87	1337	842	4.1	1.55
Zn	-0.76	818	420	75 ppm	7.14
Al	-1.66	2975	660	8.2	2.70

At the current state, there are only two feasible electrolyte salts for plating/stripping calcium at low overpotentials and room temperature (left part of Fig. 2.5): $\text{Ca}(\text{BH}_4)_2$ as demonstrated by Bruce *et al.*[44], and calcium tetrakis(hexafluoroisopropoxy)-borate, $\text{Ca}[\text{B}(\text{hfp})_4]_2$, as explored by Zhao-Karger *et al.*[45] Both salts have been tested exclusively in ether-based electrolytes.[42] The use of conventional current collectors (such as SS, Cu, Al) or calcium itself is not possible due to low coulombic efficiency and poor cycle stability. Utilization of Pt, Au or carbon-coated aluminium electrodes is necessary for calcium reversible plating and stripping.[40, 42] More common salts like $\text{Ca}(\text{OCl}_4)_2$ or $\text{Ca}(\text{BF}_4)_2$ still require a high overpotential of more than 1 V to initiate the electrodeposition and dissolution of calcium.[40, 42, 46] However, it has been observed that $\text{Ca}(\text{BF}_4)_2$ is capable of transporting calcium ions at high temperatures above 75 °C.[43] Another issue could be the strong reduction potential of Ca metal, which may induce electrolyte decomposition and the formation of an insulating layer on the electrode.[43] These challenges present two potential breakthrough approaches: 1) reducing the severe polarization hysteresis of calcium stripping/plating in electrolytes containing, for example, $\text{Ca}(\text{OCl}_4)_2$ or $\text{Ca}(\text{BF}_4)_2$, and 2) improving the utilization efficiency with conventional metal current collectors.[42]

In recent years, extensive research has been conducted on various cathode materials for calcium batteries, as depicted in Fig. 2.5. Materials such as Prussian blue and those with olivine structures have been explored towards high potential cathode materials. On the other hand, materials like S and metal sulfides are known for their high capacity characteristics.[42]

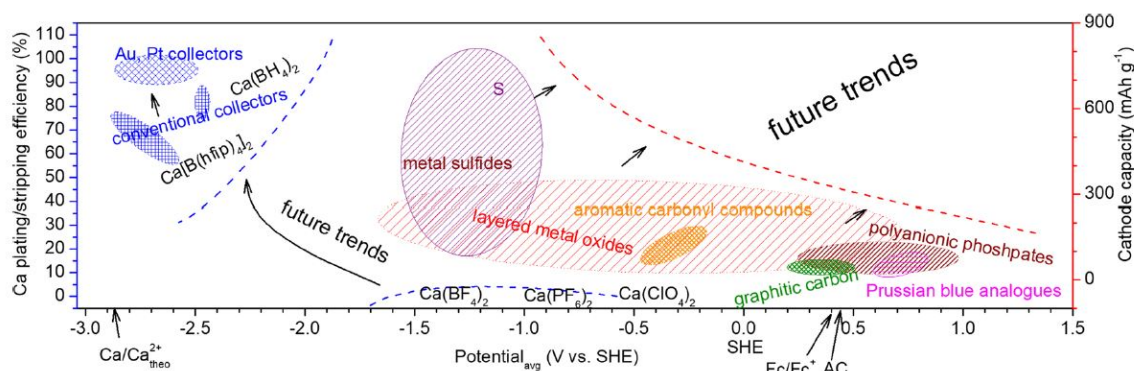


Figure 2.5: Overview of different electrode materials and future trend for Ca Batteries. Reproduced with permission[42], Copyright (2022) Wiley.

Both intercalation and conversion materials, despite their advantages, exhibit limitations in terms of cycling stability and capacity. Some promising attempts have been made with organic carbonyl compounds, but their capacity and voltage are already fixed, leaving limited room for further improvement.[42] Taking a closer look at more investigated materials like S and metal sulfides, which belong to the conversion-type materials, initial studies utilized calcium trifluoromethyl sulfonate ($\text{Ca}(\text{TFS})_2$) tetraglyme electrolyte with LiTFSI salt in Ca-S batteries.[47] However, capacity fading was observed within 20 cycles, with the capacity dropping from 800 to 300 mAh g^{-1} . One of the reasons for this degradation could be the presence of polysulfide shuttle effects. Even with changes in the electrolyte, the performance did not significantly improve due to the persisting polysulfide shuttling phenomenon.[42] Positive intercalation and deintercalation of Ca ions were observed for TiS_2 with $\text{Ca}(\text{TFS})_2$ propylene carbonate electrolyte. Although Li was used as the counter electrode, the role of Li^+ in the storage mechanism is still being investigated. In this research, it was found that the addition of a solvent with a low dielectric constant could lower the kinetic hysteresis by reducing the desolvation barrier of ion-solvent interactions.[42] Ren *et al.* studied porous CuS nonocages in $\text{Ca}(\text{TFSI})_2$ with an EC:DMC:PC:EMC (2:3:2:3) electrolyte, achieving a reversible capacity of 200 mAh g^{-1} with a capacity retention of 50% after 30 cycles.[48]

Several trials have been conducted with classical layered oxides as cathode materials in the exploration of Ca metal batteries. One of the earliest pieces of evidence for reversible Ca storage in metal oxides was demonstrated with CaMn_2O_4 using a $\text{Ca}(\text{BF})_4$ propylene carbonate (PC) electrolyte.[49] Subsequently, research focused on CaCo_2O_4 with calcium perchlorate in acetonitrile as the electrolyte, achieving a maximum capacity of 100 mAh g^{-1} within the optimal voltage window.[50] Numerous other layered metal oxides have been investigated in the context of Ca metal batteries.[42] Notably, promising results were obtained with a lithium titanide electrode, delivering a capacity of approximately 170 mAh g^{-1} with 80% retention after 200 cycles.[51] $\text{Ca}_{0.4}\text{MnO}_2$ and $\text{Mg}_{0.15}\text{MnO}_2$ also demonstrated promising Ca ion intercalation/deintercalation.[42, 52, 53]

Other potential cathode materials under investigation include polyanionic phosphates like $\text{Na}_2\text{FePO}_4\text{F}$. However, unlike in other battery systems (Li, Na, K, Mg), no dis-

tinct charge/discharge plateaus were observed in these materials.[42, 54] Promising materials such as Prussian blue analogues, graphitic carbon, and aromatic carbonyl compounds are being explored, but a fundamental understanding of the storage mechanisms is essential for further improving these materials for use in calcium batteries.

Investigations of anode materials, especially focusing on calcium metal electrodes, are still ongoing. Calcium deposition was initially considered difficult in organic electrolytes due to sluggish calcium ion diffusion through passivated surface films or SEIs.[55, 56] Typical calcium salts such as $\text{Ca}(\text{ClO}_4)_2$, $\text{Ca}(\text{PF}_6)_2$, or $\text{Ca}(\text{BF}_4)_2$ resulted in the formation of calcium chloride and fluoride interphases.[49, 55, 56] The presence of CaF_2 and CaCl_2 , which are usually good anionic conductors in monovalent systems, led to continuous anion corrosion and the formation of a thick SEI.[56–59] As mentioned before, this passivation layer caused a high overpotential of more than 1 V, resulting in significant polarization compared to alkali metals.[42] Temperature variation, particularly at higher temperatures, was one approach to address this issue. The initial affirmative account of stripping and plating in a calcium battery involved the use of $\text{Ca}(\text{BF}_4)_2$ in ethylene carbonate (EC) and dimethyl carbonate (DMC) at a working temperature of 100 °C.[55] The electrodeposition and dissolution processes lasted for 92 hours with an overpotential of 0.05 V. However, high-temperature batteries are considered as niche applications.[42] It took two more years until the first reversible stripping and plating at room temperature was reported in 2018.[44] Another calcium borohydride salt ($\text{Ca}(\text{BH}_4)_2$) was used, forming a discrete interphase of CaH_2 . In this case, the stripping and plating processes lasted for at least 100 hours with an overpotential of 0.1 V. However, the anodic stability was compromised due to oxidizability. In 2019, the issue was overcome with the use of $\text{Ca}[\text{B}(\text{hfp})_4]_2$ (Fig. 2.6).[45, 60] In the case of calcium batteries and their current collectors, two scenarios have been observed: using a Pt collector, which provides small capacities but long lifespan, and using an Au collector, which delivers high capacities but with a relatively low lifespan.[42] Future work should focus on developing common current collectors that can balance capacity and lifespan. Many open questions remain, including factors influencing coulombic efficiency, understanding and controlling the formation of the SEI, and elucidating the storage mechanism.[42] Furthermore, the growth be-

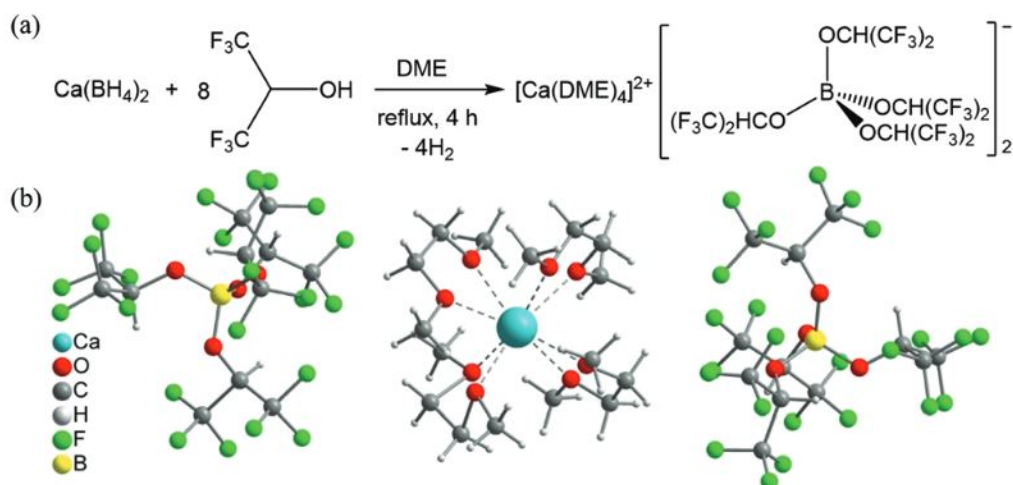


Figure 2.6: Synthesis and single X-ray structure of $\text{Ca}[\text{B}(\text{hfip})_4]_2$. Reproduced with permission[45], Copyright (2019) The Royal Society of Chemistry.

behavior of calcium (excluding the electrolyte) is still under investigation. It has been observed that the growth mechanism differs on Au and Pt surfaces. Au shows smooth deposition, while Pt exhibits more island-like deposition of calcium.[61] The current density also plays a significant role, as excessive current density can lead to dendrite and globule growth, along with non-uniform current distribution due to SEI formation.[62] Non-metallic current collectors, such as graphite paper, have been explored, but their suitability for calcium plating/stripping is limited due to the intercalation of calcium ions.[63] A breakthrough was achieved by the group of Fichtner *et al.*[43] using a Ca-Sn alloy as the anode material in a full cell configuration. They combined the Ca-Sn alloy anode with 1,4-polyanthraquinone as the organic cathode material and $\text{Ca}[\text{B}(\text{hfip})_4]_2$ in dimethoxyethane as the electrolyte. XRD and SEM techniques were employed to investigate the electrochemical processes of calciation and decalciation of the Ca-Sn alloy (Fig. 2.7). The results showed that Sn, formed from the electrochemical dealloying of the Ca-Sn alloy, exhibited unique properties and underwent subsequent reversible calciation/decalciation as CaSn_3 . The newly formed CaSn_3 phase then participated in the reversible calciation/decalciation processes. The complete cell arrangement exhibited outstanding cycling stability, enduring beyond 5000 cycles, and maintaining a capacity of 78 mAh g^{-1} .

The electrolyte utilized in calcium batteries bears more resemblance to that of lithium-ion batteries or sodium-ion batteries (SIBs), in contrast to the electrolytes used in aluminum or magnesium batteries, which tend to be more corrosive.[40] However,

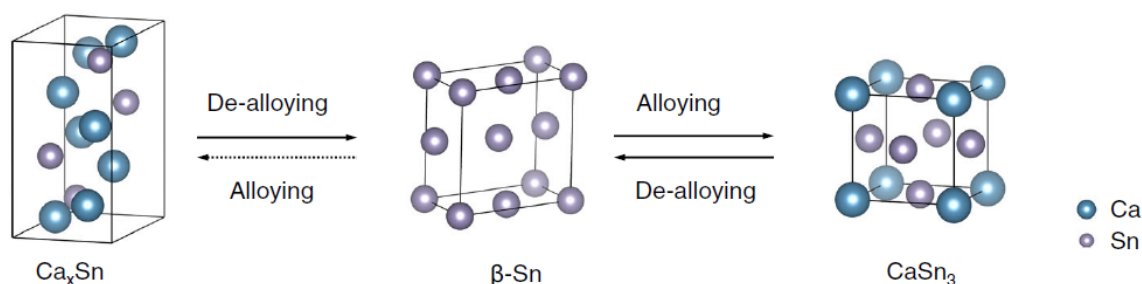


Figure 2.7: Electrochemical transformation of the Ca-Sn alloy. Reproduced with permission[43], Copyright (2022) Springer Nature.

further investigations and improvements are required in this area. There is still a lack of understanding regarding the reaction at the interphases, specifically the formation and behavior of the solid electrolyte interphase. More information on this topic can be found in the relevant literature.[40, 42]

2.2.3 Aluminium Batteries

Aluminum presents numerous advantages within the realm of post-lithium battery technology. As the most abundant metal in the Earth's crust, it stands as a remarkably sustainable and easily accessible resource. Additionally, its cost is relatively low compared to that of Li, Na, K, and Zn. Moreover, aluminum boasts a higher gravimetric capacity than Na, K, and Zn, and its volumetric capacity significantly outperforms others (Fig. 2.8). Additionally, aluminium is non-toxic and recyclable, making it environmentally friendly. In terms of redox chemistry, aluminium can deliver three electrons, providing high energy storage capacity (Energy density: 8.0 Ah cm^{-3} and Li: 3.9 Ah cm^{-3}).[64] Another significant advantage is its safety profile, as aluminium does not exhibit dendrite formation when undergoing plating processes in non-aqueous room temperature ionic liquid electrolytes (RTILs). The history of the aluminium battery dates back to the 1850s when aluminum was utilized as an anode in various cell configurations, including aqueous and non-aqueous primary and secondary batteries. In 1962, the first aluminum-air battery was developed, and in the 1980s, rechargeable aluminum-chlorine (Al-Cl_2) cells were introduced.[65, 66] However, thus far, a suitable cathode material capable of efficiently storing aluminum ions has not been identified.[64]

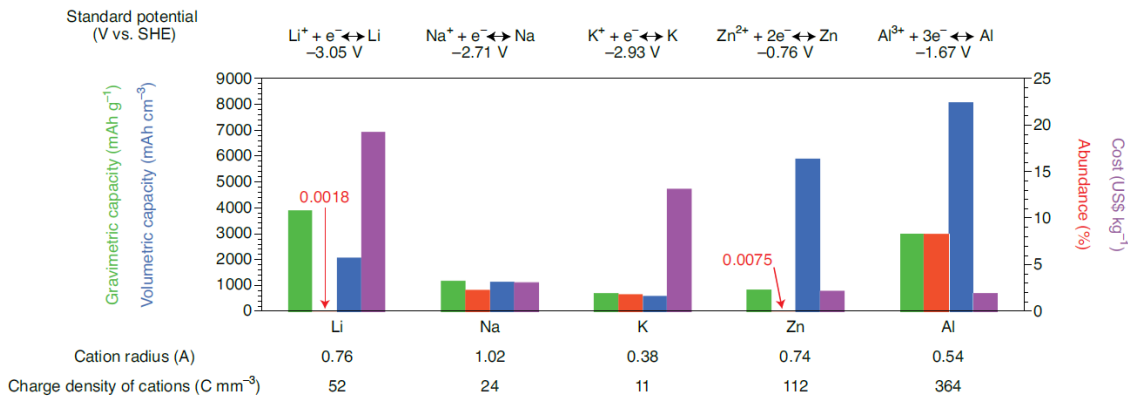


Figure 2.8: A comparative analysis of the gravimetric and volumetric capacities, cost, abundance, standard potentials, cation radius, and charge density of cations including Li, Na, K, Zn, and Al. Reproduced with permission[65], Copyright (2021) Springer Nature.

One common cell configuration (Fig. 2.9) utilizes aluminum foil as the anode and graphite as the cathode, along with an acidic room temperature non-aqueous ionic liquid electrolyte. A widely used electrolyte is $\text{AlCl}_3:\text{[EMIm]Cl} > 1$ with EMIm as 1-Ethyl-3-methylimidazolium chloride. The functioning principle of aluminum batteries

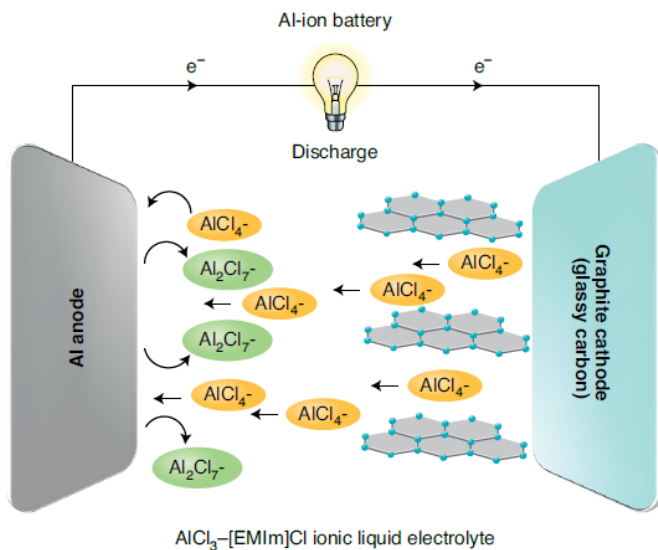


Figure 2.9: Typical configuration of an Aluminium-ion battery using room-temperature ionic liquid (RTIL) as electrolyte. Reproduced with permission[65], Copyright (2021) Springer Nature.

differs from that of LIBs (Fig. 2.9), which operate on a rocking-chair mechanism as described in the previous section. While a rocking-chair mechanism would be ideal for aluminum-ion batteries as it requires smaller quantities of electrolyte, the high cost of ionic liquids poses a challenge. Additionally, the trivalent nature of aluminum makes it quasi-impossible to directly store aluminum ions in the positive electrode. The strong charge interaction between the trivalent aluminum and the host material prevents reversible charge storage. One approach to overcome this limitation is the

storage of monovalent AlCl_4^- and Al_2Cl_7^- anions instead of Al^{3+} . In a partially charged state, both species are stored in the positive electrode, and in a fully charged state, Al_2Cl_7^- anions are depleted, leaving only AlCl_4^- stored (Eq. 2.15). This fundamental difference from lithium-ion batteries becomes evident in that the ions are stored during the charging process, instead of the discharging process.[64]



The mechanism is visualized in Figure 2.10, which shows that during the charging process, both electrodes store charge, while they release it during the discharge process. This highlights the need for an electrolyte that can accommodate all electroactive species involved in the battery in discharge operation. Due to the restricted composition range of the electrolyte, the specific energy and energy density of the battery are contingent on the amount of electrolyte used. This is why the battery is sometimes referred to as an "aluminium chloride battery," which suggests that the electrolyte operates as the effective negative electrode.[64, 67]

Although various electrolytes have been investigated, so far no organic electrolyte have been found to be effective in aluminium batteries. Aqueous electrolytes show more promise, but the formation and passivation of Al_2O_3 on the aluminium anode remains a challenge. One way to mitigate this is by using basic electrolytes, but this leads to corrosion of the aluminium anode and continuous self-discharge. As a result, RTILs are currently the most common electrolyte choice for aluminium batteries.

Research on the positive electrode in aluminium batteries has focused on investigating mechanisms such as the storage of chloroaluminate species in non-aqueous electrolytes or direct aluminium storage.[64] Although the storage of chloroaluminate species has shown higher performance, further exploration is needed for aluminium storage, as it has the potential to significantly reduce the required amount of electrolyte and increase specific energy.[64] Various materials have been investigated for aluminate storage in the positive electrode, including graphite, conducting polymers, and iron chloride. Additionally, sulfur, vanadium-based electrodes, transition metal sulfides, and anthraquinone electrodes have also been explored for aluminium storage. Among these materials, graphite cathodes have shown the highest reported specific energy of

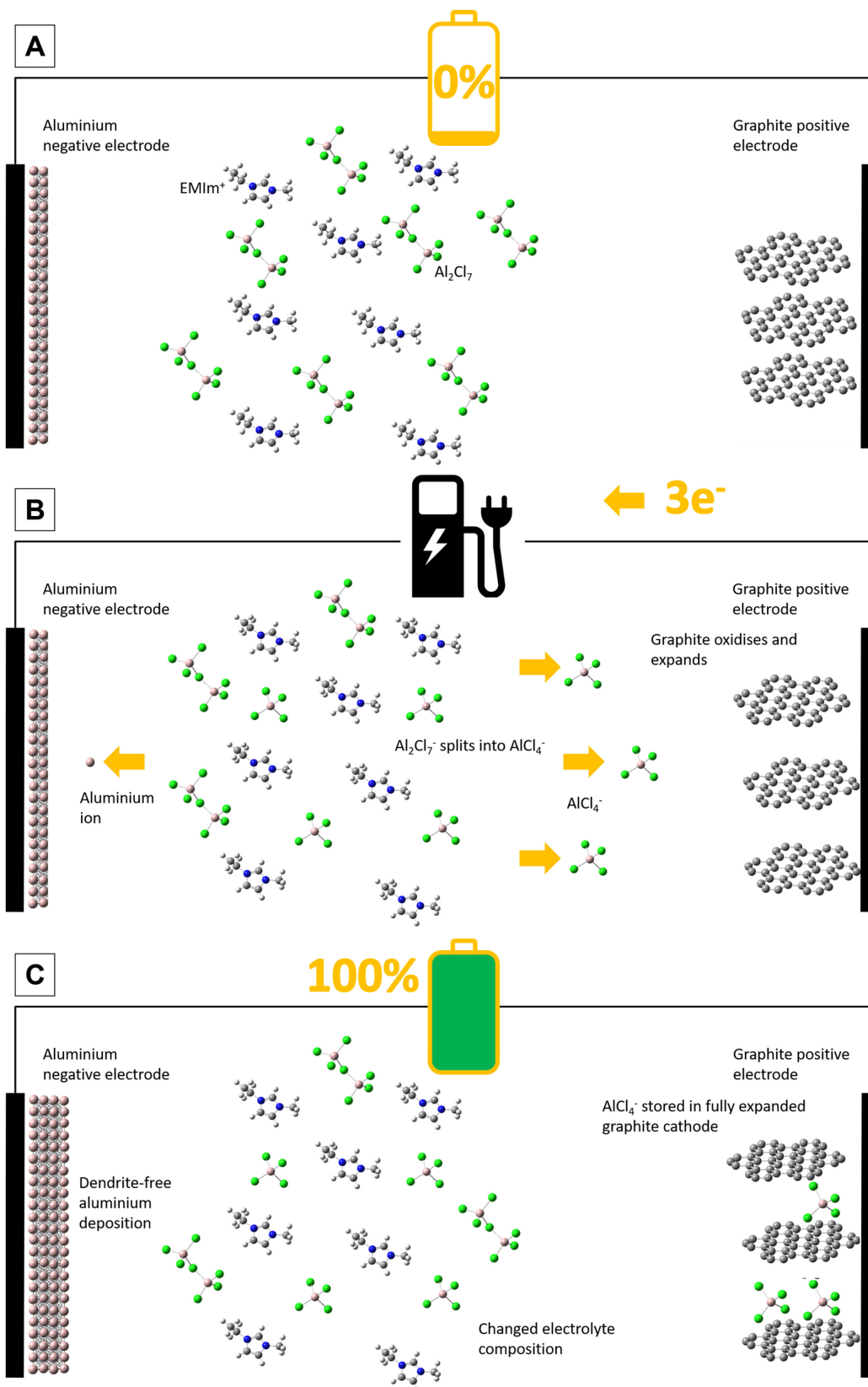


Figure 2.10: Charge Storage mechanism of an AIB with RTIL as electrolyte in A) discharged, B) medium charged and C) fully charged state. Reproduced with permission[64], Copyright (2020) Elsevier.

68 Wh kg⁻¹, taking into account the amount of electrolyte used, with an r value (r value = $c[\text{AlCl}_3]/c[[\text{EMIm}]\text{Cl}]$) of 2 ($r = 2$: 2 mol AlCl₃ to 1 mol [EMIm]Cl). The

choice of the r value is significant as it affects the formation of aluminate species (Fig. 2.11).[64] Until 2017, there was no conclusive evidence of Al^{3+} intercalation into any

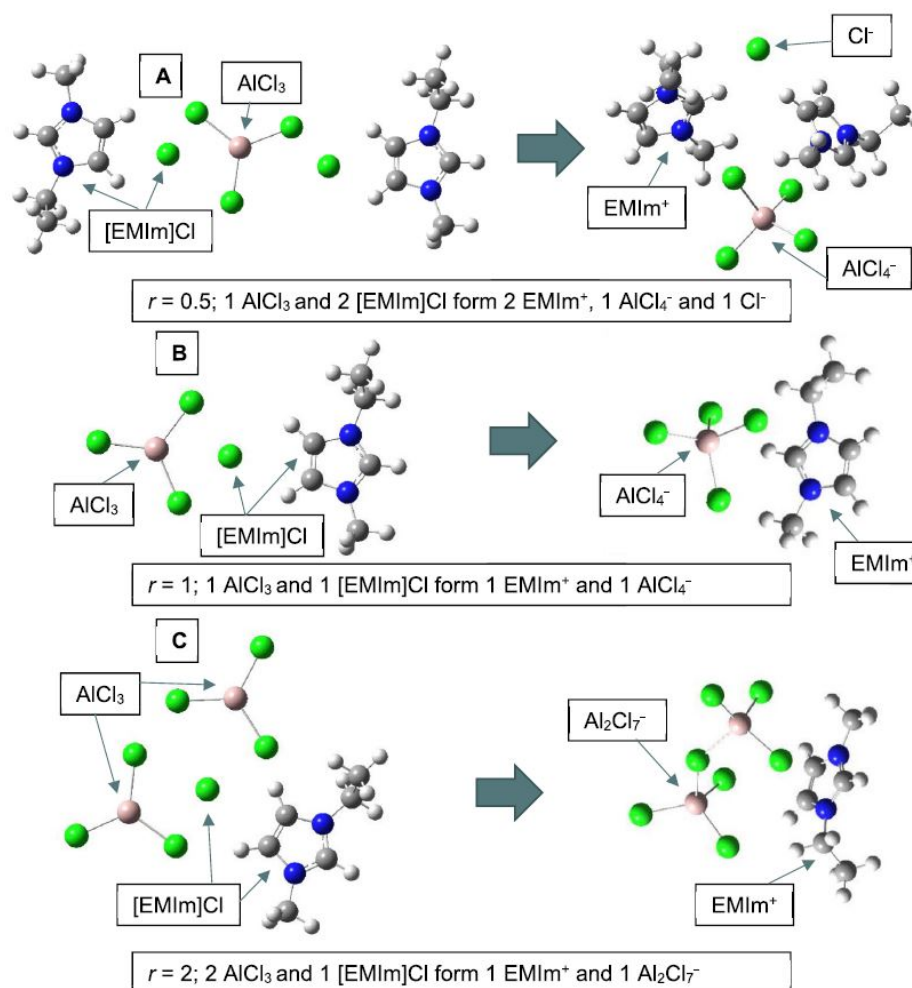


Figure 2.11: Formation of chloroaluminate species at varying ratios of AlCl_3 - $[\text{EMIm}]\text{Cl}$ electrolyte. Reproduced with permission[64], Copyright (2020) Elsevier.

electrode structure in materials storing Al^{3+} [68, 69] However, recent research by Craig *et al.* suggests evidence of intercalation, although it is challenging for multivalent ions like Al^{3+} .[64, 70] In these systems, the electrolyte is not depleted during charge and discharge, and the focus has shifted towards RTILs with an r value of 1.1-1.3, which is close to the minimum Lewis acidity required for aluminium deposition.[64, 70] It should be noted that the intercalation of Al^{3+} has been successfully demonstrated in aqueous electrolytes.[64, 71]

The focus has been on non-aqueous aluminium batteries due to the experiments and research discussed later. More information about aqueous systems can be found elsewhere.[72, 73] Currently, the state of the art shows that no other electrolyte than AlCl_3 - $[\text{EMIm}]\text{Cl}$ offers a wider voltage window. The challenges in finding a suitable

positive electrode have led to the use of known materials like graphite, which exhibits the best stability and highest discharge potential so far. Graphite flakes seem to strike the best balance between price and performance, as they are close to the theoretical specific energy and can remain stable over thousands of cycles. All other materials capable of storing aluminate fall behind graphite in terms of performance. The high costs of ionic liquids (IL) are a major hurdle preventing aluminium batteries from entering the market. Cheaper electrolytes are needed, and if a specific energy of 200 Wh kg^{-1} could be achieved at an affordable cost, aluminium batteries could compete with common LIBs in terms of cycle life and sustainability.[64]

2.3 Organic Electrode Materials

Organic electrode materials are a promising alternative to inorganic intercalation materials for both LIBs and post-lithium systems. They offer various advantages, such as fast electron/ion transfer, lower CO_2 footprint, and the ability for molecular-level structural design, to name a few.[74] The history of organic electrode materials can be traced back to 1969 (Fig. 2.12) when dichloroisocyanuric acid was used for the first time as a cathode against lithium in a battery.[75] In the 1980s and 1990s, conducting polymers and organodisulfides were investigated as potential electrode materials in lithium-ion batteries, although their performance was far from practical use.[14, 76] After 2000, the focus of interest shifted to nitroxyl radical polymers and conjugated carbonyl compounds.[14, 77] Before delving further into the material side, it is essential to clarify the working principle and classification of organic materials. The fundamental requirement for an electrode material in rechargeable batteries, whether cathode or anode, inorganic or organic, is its ability to undergo reversible electrochemical redox reactions. In the case of inorganic materials, the redox reaction involves a change in the valence of the transition metal or elemental substance, while for organic materials, it is based on the change in the charge state of the redox-active organic group or moiety.[14] According to their redox reactions, organic materials can be divided into three groups (Fig. 2.13): n-type, p-type, and bipolar materials (B).[74] For n-type materials, the reaction occurs between the neutral state (N) and the negatively charged state (N^-), requiring a positively charged ion such as Li^+ to

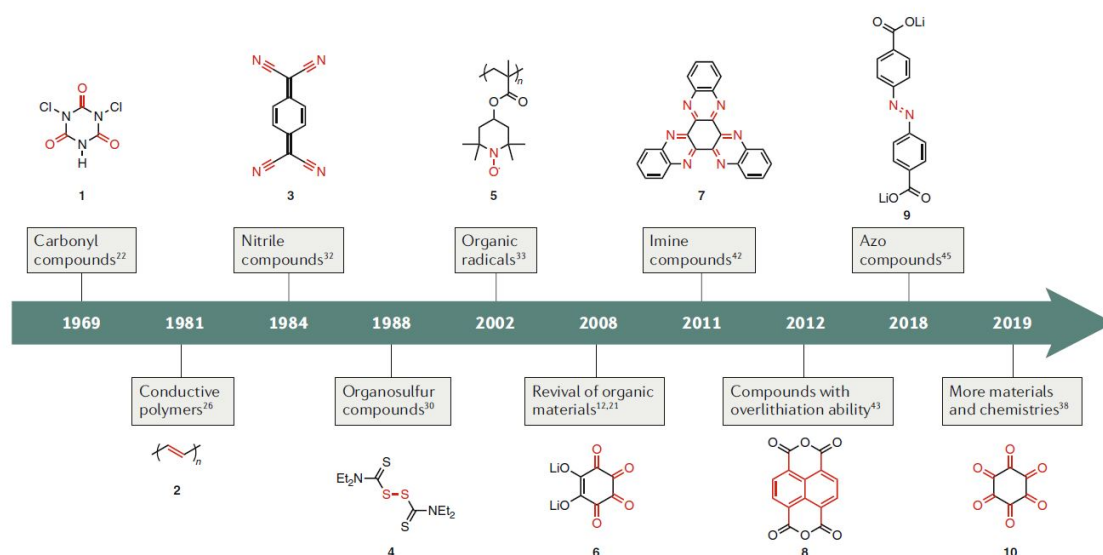


Figure 2.12: The progress in creating organic electrode materials for batteries. Reproduced with permission[78], Copyright (2020) Springer Nature.

neutralize the charge of N^- (Fig. 2.13a). On the other hand, p-type materials start in the neutral state (P) and result in a positively charged state (P^+), where a negatively charged anion (A^-) is needed for neutralization (Fig. 2.13b). The third type, called bipolar materials (B), can be reduced (B^-) or oxidized (B^+) in a reversible manner (Fig. 2.13c). In rechargeable cells, the ions can move back and forth between the electrode and the electrolyte. Many n-type materials are not affected by the exchange of Li^+ with other cations such as Na^+ or K^+ , which is quite different from common inorganic intercalation materials. Similarly, the anions in p-type materials can also be variable, using ClO_4^- , PF_6^- , BF_4^- , or $TFSI^-$ in organic solvents.[14]

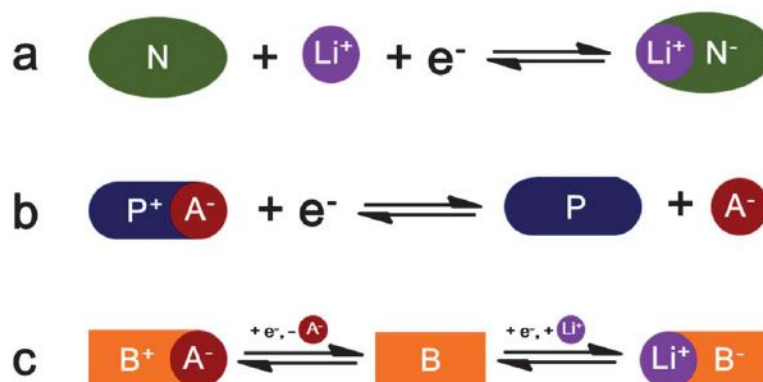


Figure 2.13: Classification of the different organic electrode materials. Reproduced with permission[14], Copyright (2013) The Royal Society of Chemistry.

With this knowledge, different possible cell configurations are depicted in Figure 2.14. When the anode is in the reduced state and the cathode is in the oxidized state, the

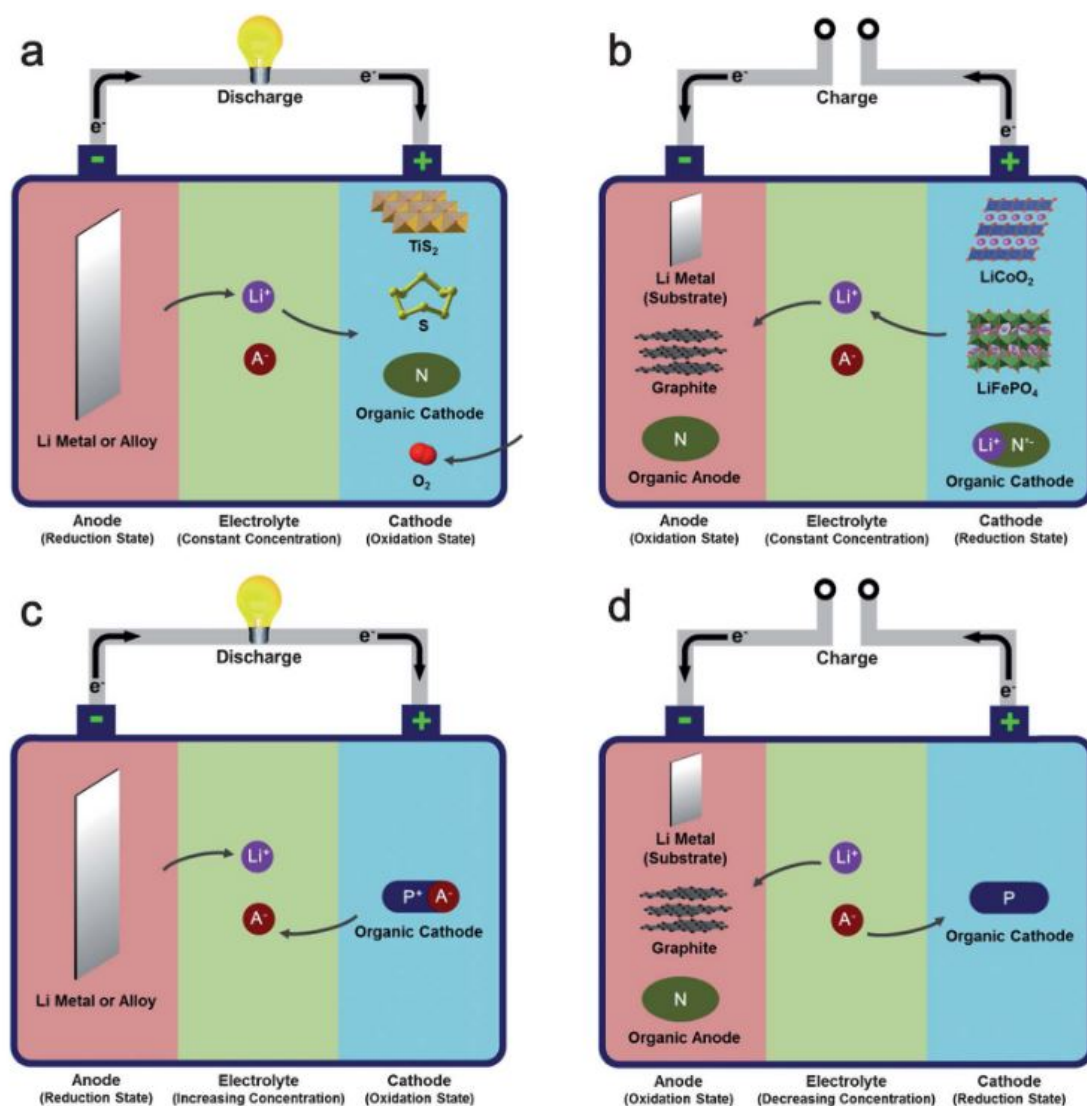


Figure 2.14: Possible cell configurations of organic electrode materials, where bipolar materials (B) can be employed between n-type and p-type materials. Cell configuration a) and b) represent the cases of Li^+ deposition/intercalation in anode and cathode. Configuration c) and d) are common for p-type materials, where the anions are transported from the electrode to the electrolyte or *vice versa*. Reproduced with permission[14], Copyright (2013) The Royal Society of Chemistry.

first step would be discharging of the fresh cell (Fig. 2.14a and 2.14c). Conversely, in the reversed situation, charging would be the first process (Fig. 2.14b and 2.14d).[14] If the material can be used as an anode or cathode is mainly dependent on the redox potential and the stable form of redox-active species, where typically n-type materials can be used in the neutral form or as Li^+N^- , and the p-type materials as P or P^+A^- . The Li^+N^- form of n-type materials is not stable in ambient atmosphere due to hydrolysis or oxidation. This instability becomes especially significant if the redox potential of N/N^+ is below 2.5 V vs. Li/Li^+ . As a result, it is highly unlikely to use this form as an anode material. The P/P^+ redox potential is typically above 2.5 V vs. Li/Li^+ , making it unsuitable for use as an anode material. Therefore, organic materi-

als are typically preferred and used as cathode materials. In this role, they can exist as N, Li^+N^- , P^+A^- , and P. That's why in Fig. 2.14, only N is considered as an anode material, as it is stable in ambient atmosphere and can have a relatively low redox potential. Among all the shown cell configurations in Fig. 2.14, configurations a and b are the most common ones. In these configurations, Li^+ or other metals, such as K^+ or Na^+ , is deposited or inserted on both electrode sides. In configurations shown in Fig. 2.14c and d, the potential use of p-type materials is exemplified. Here, A^- serves as the species responsible for transport between the cathode and electrolyte, while Li^+ is responsible for transport between the anode and electrolyte. In the case of a graphite anode, where the only lithium source is provided through the electrolyte, it is called a dual-ion battery.[79] This leads to a concentration change in the electrolyte, which is different from the other two configurations where the electrolyte only functions as an ion conductor. This concentration change can potentially cause issues since it is desirable to minimize the amount of used electrolyte to achieve improved energy density. Moreover, when using p-type materials, it is important to accurately determine which species is relevant for calculating the correct specific capacity, whether it is P or P^+A^- .

Redox polymers undergo a process in which either a radical cation or a radical anion is formed. In p-type materials, this results in the formation of P^+ , while in n-type materials, it leads to N^- . [80] The equations shown in Fig. 2.13 are abstract representations used to demonstrate the mechanisms, but a closer examination of the individual molecule classes is necessary, especially concerning their redox chemistry. In the literature, there are typically seven groups of organic electrode materials that cover the significant efforts made in the field of organic batteries in recent years. Organodisulfides and conjugated carbonyl structures belong to the n-type materials. Conjugated amine and conjugated thioether belong to p-type materials. Conjugated hydrocarbon and nitroxyl radical belong to bipolar materials, where the nitroxyl radicals are practically used as p-type materials. The mechanism of the thioether (4e) is not represented in any of the groups shown in Fig. 2.13, and it has not been clarified yet. Further research is needed to understand the redox chemistry and mechanism of thioether (4e) materials as organic electrode materials.[14] Table 2.4 shows the seven groups of organic electrode materials and their redox chemistry, along with examples

from the literature.

Table 2.4: Different Types of organic electrode materials and their redox mechanism.[42]

Structure	Redox mechanism	Example	Reference
1. Organodisulfide	$R-S-S-R \leftrightarrow R-S^- + R-S^-$		[81, 82]
2. Conjugated carbonyl			[83, 84]
3. Conjugated amine	$R-\overset{+}{N}(H)-R \leftrightarrow R-\overset{-}{N}(H)-R$		[85–87]
4. Conjugated thioether	$R-\overset{+}{S}-R \leftrightarrow R-S-R$		[88–90]
5. Conjugated hydrocarbon	$(-R)^{x+}_n \leftrightarrow (-R)_n \leftrightarrow (-R)^{y-}_n$		[91–93]
6. Nitroxyl radicals	$R-\overset{+}{N}(O)-R \leftrightarrow R-\overset{\cdot}{N}(O)-R \leftrightarrow R-\overset{-}{N}(O)-R$		[94–96]
7. Thioether (4e)	$R-\overset{+}{S}(O)_2-R \leftrightarrow R-\overset{\cdot}{S}(O)-R \leftrightarrow R-S-R$		[97]

The various named organic electrode materials shown in Table 2.4 exhibit different advantages, making them even more interesting as they can be used for different applications. For instance, conducting polymers like polyacetylene offer high conductivity but have low capacity and a sloping plateau in their voltage profile. On the other hand, organosulfur compounds, encompassing disulfides and thioethers, generally exhibit high capacity; however, they encounter challenges like high solubility, sluggish kinetics, compromised cycle stability due to limited reversibility, and low conductivity. Organic radicals like TEMPO show fast kinetics and a flat plateau in their voltage profile, but they have a low capacity, low conductivity, and high self-discharge. Carbonyl compounds, such as quinones, provide a high capacity and fast kinetics, but they are usually highly soluble and show low conductivity. These differences in properties make each material suitable for specific battery applications based on the desired performance characteristics.[98] The comparison of organic materials highlights three main disadvantages: high solubility, low conductivity, and a low volumetric energy

density.[99] To address these challenges, flexible structures and molecular design become even more crucial in overcoming these bottlenecks. By carefully designing the molecular structures and optimizing the material properties, researchers can enhance the performance of organic electrode materials and unlock their full potential for various battery applications. Herein, it is important to keep an eye on the material level and the practical performance on battery level (Fig. 2.15). Sometimes improve-

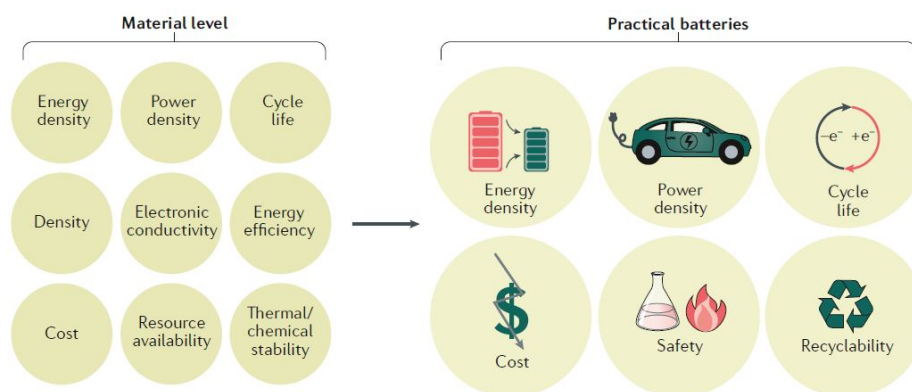


Figure 2.15: Key Parameters at Material and Device Levels for Practical Batteries. Reproduced with permission[78], Copyright (2020) Springer Nature.

ments made at the material level can have unintended consequences at the battery level. For instance, adding conducting carbon to improve material conductivity may increase the theoretical capacity on the material level.[78] However, at the battery level, it can lead to a decrease in practical capacity for the electrode. Such trade-offs between material-level and battery-level performance need to be carefully considered during the development and optimization of battery materials. There are several typical design strategies aimed at improving energy density, power density, and cycle life in organic electrode materials. Energy density depends on both capacity and voltage, and these factors can be tuned through molecular design and other approaches (Fig. 2.16). To enhance capability, techniques such as lowering the molecular weight, raising the specific area[100], or increasing the carbon content[101] could be implemented. Voltage can be adjusted through the use of electron-donating or electron-withdrawing groups[98] and by optimizing the position of active groups.[102] Power density can also be influenced by voltage and current. The current can be increased by designing more conductive structures[103] or increasing carbon content.[104] Cycle life, on the other hand, is mainly dependent on issues such as the solubility of organic materials and volume changes during cycling.[78] The solubility problem can be addressed

through binder optimization[105] or polymerization/salification.[106, 107] Volume-related problems can sometimes be mitigated through microstructure control, such as reducing particle size.[78, 108] In the literature, there are many available reviews

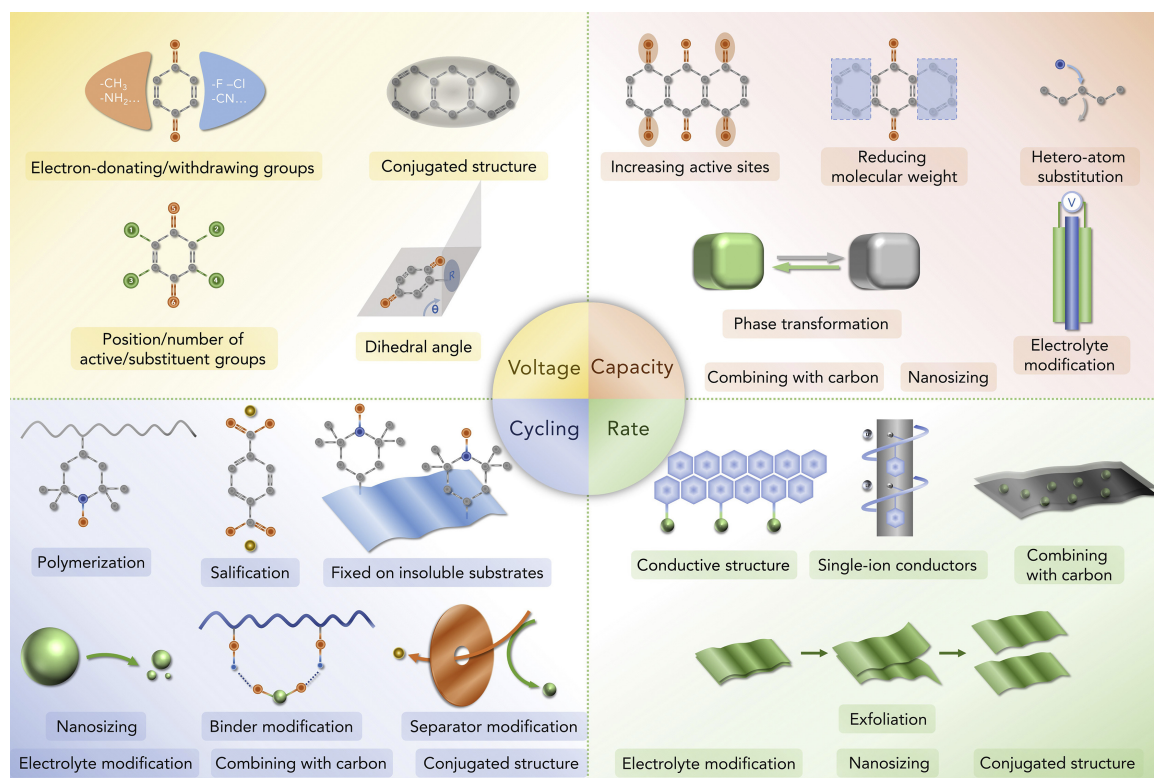


Figure 2.16: Strategies to improve the performance of organic electrode materials. Reproduced with permission[98], Copyright (2018) Elsevier.

about organic electrodes that provide summaries of tested materials, electrode compositions, and their performance.[14, 77, 98, 109, 110]

In the following, one aspect of organic electrode materials based on the research conducted by C. Wang will be discussed.[111] The focus is on the weak intermolecular interactions that are inherent in organic materials, which are in stark contrast to the strong covalent and ionic bonds in inorganic materials. This difference gives rise to significant differences in physicochemical and electrochemical behavior. Three different types of interactions will be described: the interaction between two active organic molecules, between the active molecule and carbon as an additive, and between the active material and the binder. Understanding and addressing these weak intermolecular interactions are crucial for enhancing the performance and stability of organic electrode materials.

Organic materials, whether they are small molecules or macromolecules with polymeric structures, can exhibit a variety of interactions, such as van der Waals forces,

hydrogen bonds, $\pi - \pi$ interactions, and electrostatic Coulomb forces. These interactions play a significant role in determining the physicochemical properties of the materials, including their boiling/melting points, density, solubility, morphology, charge transport, and ionic diffusion. Additionally, these interactions can also influence the electrochemical interactions between the organic molecules and the electrolyte in battery systems. One example of an interaction between neighboring active molecules

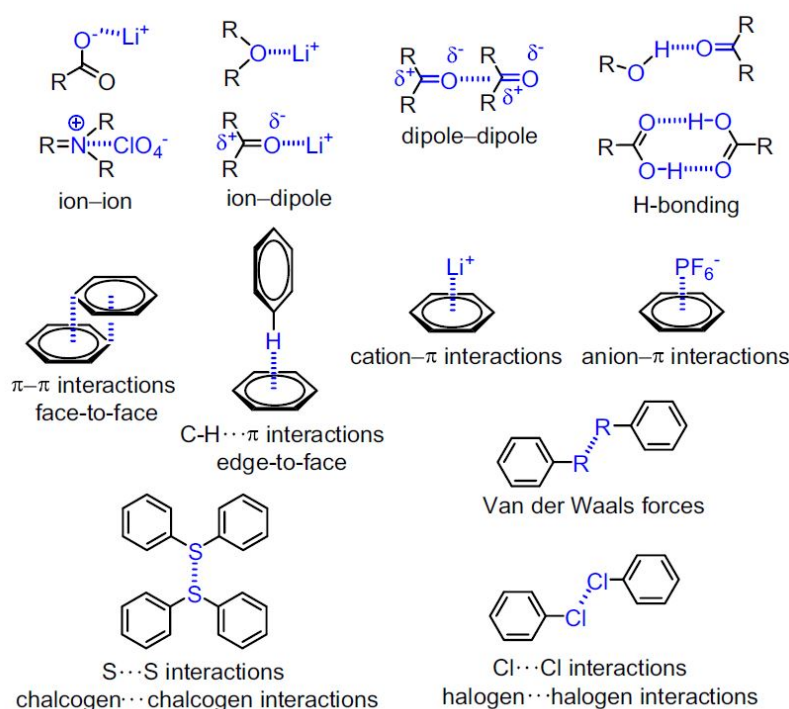


Figure 2.17: Weak intermolecular interactions in organic batteries. Reproduced with permission[111], Copyright (2020) Wiley.

is caused by extending the π -system in organic materials. This extension typically enhances the electrochemical performance, especially in terms of fast-charge and fast-discharge properties. The elongation of the π -system leads to improved charge transport properties and enhances the stability of the charged and discharged states. This is due to the delocalization of charge not only within the π -conjugated system of individual molecules but also between adjacent molecules. Furthermore, it strengthens the intermolecular interactions, such as $\pi - \pi$ or C-H $\cdots\pi$ interactions (Fig. 2.17), which can facilitate a layer-by-layer arrangement,[112] promoting ion diffusion within the material. Ion-ion and ion-dipole interactions can also play a significant role in the behavior of organic electrode materials. These interactions can be useful in forming crosslinked networks[113] within the material, which can effectively lower its solubility in the electrolyte. The interaction between active molecules and conductive

additives, such as 2D graphene or 1D carbon nanotubes (CNTs), plays a crucial role in enhancing the electrochemical performance of organic electrode materials. These carbon materials form a conductive composite within the electrode, facilitating charge transfer and improving overall conductivity. The strong $\pi - \pi$ interactions between carbon and active molecules further contribute to material stability and performance. One notable success in this regard is the combination of graphene with 2D covalent organic framework (COF) structures. The resulting graphene-COF composite exhibits greatly improved electrochemical properties.[114] The interaction between the active material and binder in organic electrode materials can vary significantly depending on the type of binder used. One example is polyvinylidene fluoride (PVDF), where the fluorine atoms in the polymer structure play a crucial role. Dipole-dipole and ion-dipole interactions between the active material and PVDF binder can lead to a nucleophilic substitution, where fluoride ions (F^-) may leave the PVDF structure.[115] This interaction can influence the overall performance and stability of the electrode. In the case of PEDOT:PSS (poly(3,4-ethylenedioxythiophene):poly(styrene sulfonate)) based electrodes, another interaction mechanism comes into play. The sulfur-sulfur ($S \cdots S$) interactions between PEDOT:PSS and the active material can decrease the solubility of dibenzo[b,i]thianthrene-5,7,12,14-tetraone (DTT) in the electrolyte. This interaction helps to retain the active material within the electrode and prevents its dissolution into the electrolyte, contributing to the stability of the battery. The study highlights the significance of weak interactions in organic electrode materials and how these interactions can be effectively utilized to improve the overall performance. These weak interactions, such as van der Waals forces, hydrogen bonds, $\pi - \pi$ interactions, and ion-dipole interactions, may seem relatively subtle compared to the strong covalent and ionic bonds found in inorganic materials. However, their collective impact can be substantial in enhancing physicochemical and electrochemical properties. By understanding and harnessing these weak interactions, researchers can design organic electrode materials with improved charge transport, stability, and capacity. Molecular design strategies can be developed to optimize the arrangement of active molecules, conductive additives, and binders, all working in harmony to enhance the battery's performance.[111]

2.4 Porphyrinoids

Porphyrins are a remarkable class of molecules that occur widely in nature, including in plants as chlorophyll and in our blood as heme. In the following section, the utility of porphyrin-based materials as electrode materials for batteries will be described. However, prior to this, the fundamental aspects of porphyrins will be explained.

The porphyrin macrocycle consists of four pyrrole rings connected *via* methine groups, with porphin (Fig. 2.18a) being the simplest structure. Close structures to porphyrins also exist, such as chlorin, corrin or isophlorin (Fig. 2.18b-d). The porphyrin molecule

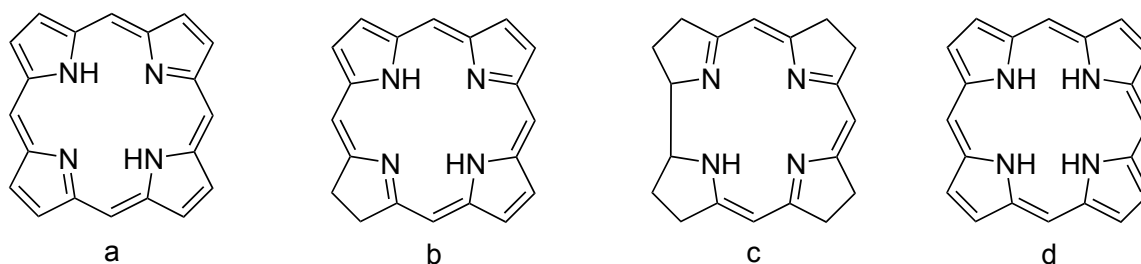


Figure 2.18: Porphyrins and closely related structures: a) porphin b) chlorin c) corrin and d) isophlorin.

can undergo substitution with various functional groups at either the β - or *meso*-position. Porphyrins typically have 22 π -electrons, with 18 π -electrons contributing

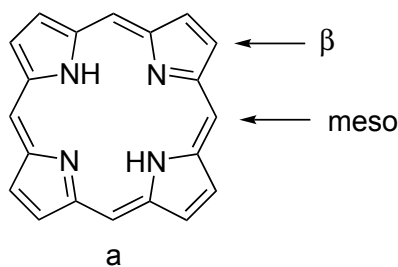


Figure 2.19: Possible positions for substitution.

to the aromaticity and fulfilling Hückel's rule. The aromatic form of porphyrins is the most stable and commonly found in nature.[116] When the porphyrin ring is not coordinated with any metal, it is often referred to as the "free-base" due to the presence of protons on the nitrogen atoms.[117] Porphyrins can form complexes with a wide range of metal ions, and there are more than 80 known metalloporphyrins.[118] Additionally, when porphyrins form complexes with half-metals like boron, they are known as subporphyrins.[119] These metal complexes of porphyrins exhibit diverse properties and have various applications in chemistry and biology, such as bioimaging

[120] or as dyes in photovoltaic applications [121]. Metallation of the porphyrin causes structural changes in the porphyrin core. The planarity of the porphyrin ring can be distorted, resulting in a more saddle-shaped structure. The presence and charge of the metal ion can also influence the coordination geometry and the binding of axial ligands to the metal center. The overall crystalline structure and arrangement can be affected by adding substituents to the porphyrin ring, particularly when bulky groups are introduced. One important electronic structure characterization method of porphyrins is UV-Vis spectroscopy due to their characteristic absorption and the highly conjugated π -system, which allows them to absorb in the visible range. The electronic properties arise from transitions between the ground state (S_0) and two excited states (S_1 and S_2), resulting in distinct spectral bands. The Soret band ($S_0 \rightarrow S_2$) is typically observed around 400 nm, while the Q-bands ($S_0 \rightarrow S_1$) are observed in the visible region; 500-700 nm. The number of Q-bands depends on the symmetry of the porphyrin. Upon metallation, the symmetry of the porphyrin changes from D_{2h} to D_{4h} , resulting in a reduction in the number of Q-bands due to higher symmetry. The position and intensity of the absorption bands can be further influenced by substituents on the porphyrin ring. For example, an electron-donating group at the meso-position can cause a bathochromic effect, resulting in a redshift in the UV-Vis spectrum. This occurs because the electron-donating group facilitates the delocalization of π -electrons, requiring less energy for excitation. The four-orbital model proposed by Gouterman[122] explains the presence of the Soret and Q-bands in porphyrins. According to this model, the absorption bands result from transitions between the highest occupied molecular orbital (HOMO) and the HOMO-1 between the degenerate lowest unoccupied molecular orbitals (LUMOs) e_{gx} and e_{gy} . The formation of aggregates, such as J- and H-aggregates, can also cause shifts in the spectra of porphyrins. These aggregates are quite common for porphyrins and can lead to changes in their electronic properties and spectral characteristics. For a more in-depth theoretical background and detailed information on these phenomena, further literature should be consulted.[123] Overall, UV-Vis spectroscopy provides valuable information about the electronic properties and structural changes of porphyrins, making it an essential tool in their characterization.[122, 124]

2.5 Porphyrinoids: Promising Battery Electrode Materials

Porphyrins are a highly versatile molecule class, exhibiting interesting magnetic, photochemical, electrochemical, photophysical, and electronic properties.[125, 126] They find applications in various fields, such as photodynamic therapy[127], molecular wires[128], light energy conversion[129], and are also relevant in natural processes like photosynthesis and oxygen transport with hemoglobin.

As mentioned before, porphyrins have a rich delocalized π -system with 18 π -electrons. In some cases, they can also appear in forms with 16 or 20 π -electrons, which are then in an antiaromatic or non-aromatic form, respectively. These forms are less stable than the aromatic form with 18 π -electrons, following Hückel's rule. The four pyrrolic nitrogen atoms can serve as dianionic ligands for many metal ions.[130] The introduction of metal ions and substituents in the *meso*- or β -positions can influence the electronic properties of porphyrins.[131] Due to their small HOMO-LUMO gap, porphyrins can easily undergo electron transfer reactions, forming cationic and anionic radicals.[130] The HOMO-LUMO gap is relevant for the reaction kinetics of redox reactions and is often analyzed to understand the electron transfer processes.

In recent years, porphyrinoids have emerged as a new class of electrode materials in various battery systems, including lithium and post-lithium systems, Li-S, Li-O₂, and Li-CO₂ batteries, and dual-ion batteries (DIBs).[132] Porphyrinoids offer flexibility in terms of metal centers, substituents, and can also be used in metal-organic framework (MOF) and covalent organic framework (COF) structures, showcasing their versatility in various structures. Wang *et al.* provide an excellent overview of this in their review.[132]

In 2014, the first report about porphyrin as an electrode material was published, and it was a special because it was used in its antiaromatic form, namely Demisetyl norcorrole nickel(II) - NiNC.[133] Typically, antiaromatic forms are known to be unstable, but in this case, the 16 π -electron compound NiNC is stable in air and water. The compound has a small HOMO-LUMO gap, which provides fast redox kinetics. The 16 π -electron NiNC is bipolar and can be reduced and oxidized in two electron steps to the aromatic forms NiNC²⁻ and NiNC²⁺ (Fig. 2.20). The 14- and 18 π com-

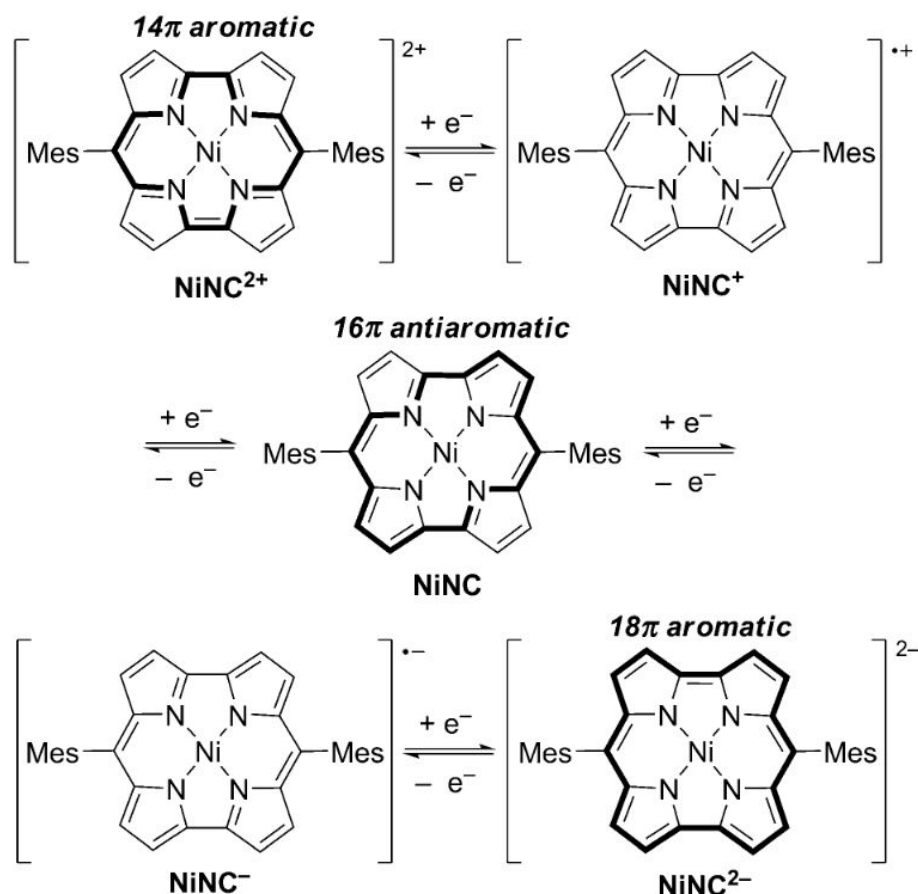


Figure 2.20: Redox chemistry of NiNC with Mes = 2,4,6-trimethylphenyl. Reproduced with permission[133], Copyright (2014) Wiley.

pounds are also stable and insoluble in the electrolyte (LiPF₆ in EC:DEC), allowing them to be used in both asymmetrical and symmetrical cells. In an asymmetrical cell against Li, a specific discharge capacity of 207 mAh g⁻¹ could be obtained after 100 cycles. Solubility is a significant drawback for many organic molecules, including porphyrins. One strategy to overcome this issue is to increase their polarity. Wu *et al.* demonstrated this approach using (4-carboxyphenyl)porphyrin as an anode material in LIBs, achieving impressive results with a specific capacity of 1200 mAh g⁻¹ at 358 mA g⁻¹ and excellent capacity retention of 89% after 2500 cycles at 6 A g⁻¹. [134] Another issue with organic materials is their low conductivity. One solution to address this is the combination of porphyrins with conductive carbon, as demonstrated with [5,10,15,20-tetra(4-carboxylatophenyl)porphinato]cobalt(III) chloride (CoTCPP), where the porphyrin was integrated into the structure of multiwall carbon nanotubes. [135] Another strategy involves the synthesis of covalent organic frameworks (COFs) or metal-organic frameworks (MOFs). For example, a 2D COF, a poly-porphyrin 5,10,15,20-tetra(4-thiophenophenyl)-21*H*,23*H*-porphin (TThPP) linked by

4-thiophenophenyl groups, was used as an anode material in a LIB, achieving a specific capacity of 666 mAh g⁻¹. [136] The COF structure facilitates ion diffusion, while the nanopores can hold the electrolyte, contributing to its improved performance. [132] In general, the performance of porphyrins can be enhanced through metalation, particularly with lithium ions, which have difficulty adsorbing well on demetallated porphyrins. Metalation reduces the energy level gap and increases conductivity, resulting in improved discharge capacity. [137] Further studies of the influence of the metal center will be discussed in upcoming chapters.

One great advantage of porphyrinoids as electrode materials is their ability to accommodate larger ions like Na⁺/K⁺ in post-lithium systems. Unlike inorganic materials, which may face difficulties with the larger ion size, organic materials, including porphyrinoids, exhibit more flexibility and can effectively host these ions. [132] For example, porphyrins have been successfully utilized to increase the interlayer spacing of graphene, facilitating the intercalation of larger ions. [138] It has been successfully demonstrated that porphyrinoids can serve as cathode materials in aluminum ion batteries. Two specific porphyrins, namely 5,10,15,20-tetra(phenyl)-21*H*,23*H*-porphin (H₂TPP) and 5,10,15,20-tetra(4-carboxyphenyl)-21*H*,23*H*-porphin (H₂TCPP), were studied as cathode materials against aluminium. Notably, the specific capacity of H₂TCPP (101 mAh g⁻¹) showed an improvement compared to H₂TPP (24 mAh g⁻¹). This enhancement can be attributed to the removal of the carboxyl functional groups in H₂TCPP, which reduces the basicity of the porphyrin due to electron-withdrawing effects. Furthermore, the investigation delved into the electrochemical reaction mechanism between AlCl₂²⁺ and porphyrin, as well as the ionic diffusion behaviors on the electrode's surface. [139] Li-S batteries are a promising energy storage system, offering high specific capacity and energy density of 1675 mAh g⁻¹ and 2600 Wh kg⁻¹. [140, 141] However, there are challenges that need to be addressed before commercialization can be considered. The sluggish redox kinetics and the shuttle effect of lithium polysulfides currently limit the practical capacity and energy density to 1100 mAh g⁻¹ and 350 Wh kg⁻¹. [132] To overcome these issues, new cathode materials with suitable pore structures are being designed to host sulfur and inhibit the shuttle effect of lithium polysulfides. Additionally, cathode materials that exhibit strong physical and chemical adsorption for rapid trapping of LiPSs and fast ionic transportation paths to accel-

erate LiPSs diffusion are sought after. Porphyrin-based frameworks, especially metal-organic frameworks (MOFs), have shown interesting and promising results in this regard. MOFs with lewis acidic open metal sites effectively absorb sulfur and polysulfides, such as S@MOF-525(Cu) which delivered a specific capacity of 700 mAh g^{-1} after 200 cycles.[142] Porphyrin covalent organic frameworks (COFs) (Fig. 2.21) have also reported positive outcomes, as the $\pi - \pi$ stacking of the π -conjugated porphyrin units between layers creates numerous highly sorted nano pores. These nano pores facilitate charge migration and increase sulfur impregnation, while more importantly, they inhibit sulfur aggregation and prevent the shuttle effect of LiPSs. S@Por-COF cathodes showed a specific capacity of 633 mAh g^{-1} after 200 cycles.[143] Lithium-

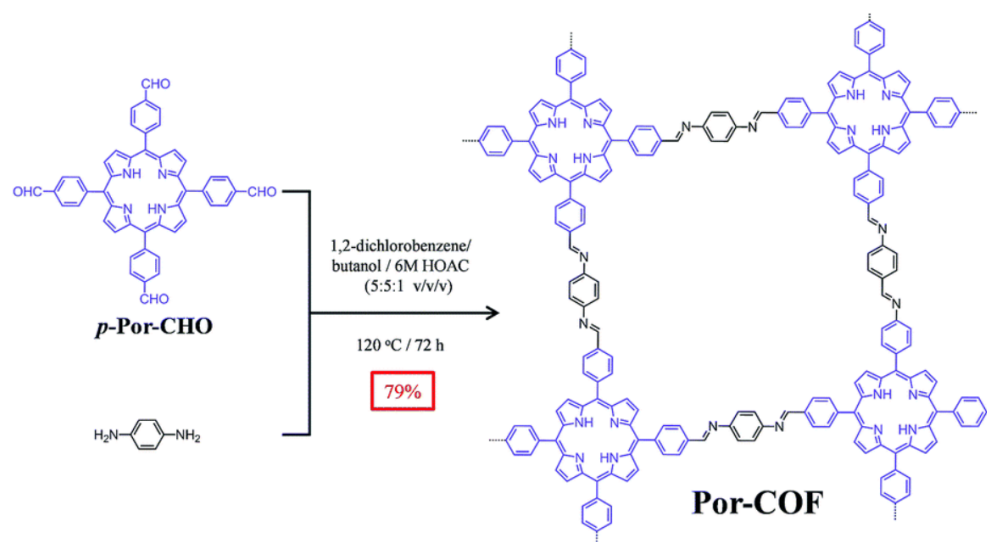


Figure 2.21: Synthesis of Por-COF used as cathode material in Li-S batteries. Reproduced with permission[143], Copyright (2016) The Royal Society of Chemistry.

air batteries have garnered attention as a promising and more sustainable battery system, boasting the highest theoretical energy density ($>3500 \text{ Wh kg}^{-1}$). However, compared to Li-S batteries, there have been fewer reports on the use of porphyrins in this context. In nonaqueous lithium-air batteries, oxygen needs to undergo reversible redox reactions to form Li_2O_2 . [132] The complexity of the three-phase boundary and sluggish dynamics of oxygen reduction and oxygen evolution make this redox reaction challenging. To address these issues, various catalysts have been investigated.[144, 145] Porphyrins have shown good oxygen reduction activity. For example FePor was used as a redox mediator and oxygen shuttle to promote oxygen oxidation and enhance battery performance.[146]

The Li-CO₂ battery, a new energy storage system, has high potential for capturing CO₂ emissions. With a theoretical energy density of 1876 Wh kg⁻¹ and a discharge potential around 2.8 V[132], this technology shows promise. However, its development has been hindered by the sluggish kinetics of CO₂ reduction and evolution, as well as the high stability and insulating nature of the discharge product ($4\text{Li} + 3\text{CO}_2 \rightleftharpoons 2\text{Li}_2\text{CO}_3 + \text{C}$). This results in challenges such as high electrode impedance, charging polarization, low reversibility, and poor cycle performance. Efforts are being made to identify suitable catalysts that can lower the charging overpotential and promote the decomposition of Li₂CO₃. One notable example is the cathode catalyst based on a porphyrin-based covalent organic framework (TTCOF-Mn) with single metal sites. This framework exhibits intrinsic catalytic sites for aprotic CO₂ conversion at the molecular level. The Li-CO₂ battery using TTCOF-Mn as the catalyst demonstrates a low overpotential of 1.07 V at 100 mA g⁻¹ and excellent stability at 300 mA g⁻¹, making it one of the most promising Li-CO₂ battery cathode catalysts to date.[147]

In the review of Wang *et al.*, the immense potential of porphyrinoids in battery applications was clearly demonstrated. These materials are versatile electrodes with a broad range of structural designs. They can also act as excellent redox mediators, O₂/CO₂ shuttles, and electrocatalysts in Li-air and Li-CO₂ batteries. Their remarkable stability and flexibility enable them to perform exceedingly well in various battery systems, thus making them highly promising candidates for future energy storage technologies.[132]

2.6 CuDEPP: An Exceptional Porphyrin-based Electrode Material

This study takes inspiration from the pioneering research carried out by the groups of Ruben and Fichtner in 2017 on CuDEPP [5,15-bis-(ethynyl)-10,20-diphenylporphinato] copper(II) (Fig. 2.22) as an outstanding electrode material for high-performance energy storage.[148] Subsequently, numerous further investigations have been undertaken, exploring the exchange of functional groups[149–151], the variation of metal centers[152], and diversifying the battery system to include Na[153], K[154], Mg[155],

metal-free[156], Al and Ca. Furthermore, the influence of the electrolyte and temperature has been investigated.[157, 158] After the initial testing of CuTPP, which

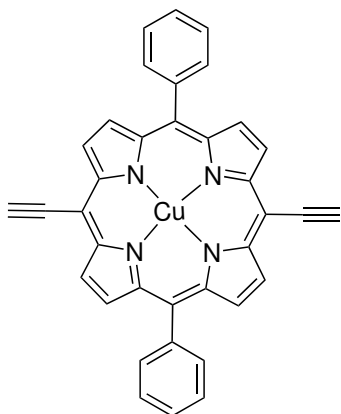


Figure 2.22: Molecular structure of [5,15-bis-(ethynyl)-10,20-diphenylporphinato]copper(II) (CuDEPP).

demonstrated high solubility in the electrolyte and limited its practical use, a modification was made by introducing two terminal acetylene groups to the structure. This modification effectively reduced the solubility and enhanced the material's conductivity and intriguing electrochemistry. CuDEPP demonstrates high stability, even at temperatures as high as 220 °C. This can mostly be attributed to its π -stacked structure and aromatic stabilization.[148] As typical for porphyrins, CuDEPP can undergo both two-electron oxidation and reduction processes (Fig. 2.23), resulting in the formation of the dicationic species (CuDEPP^{2+}) and dianionic species (CuDEPP^{2-}), respectively: The resulting bipolar nature of CuDEPP led to its evaluation as both

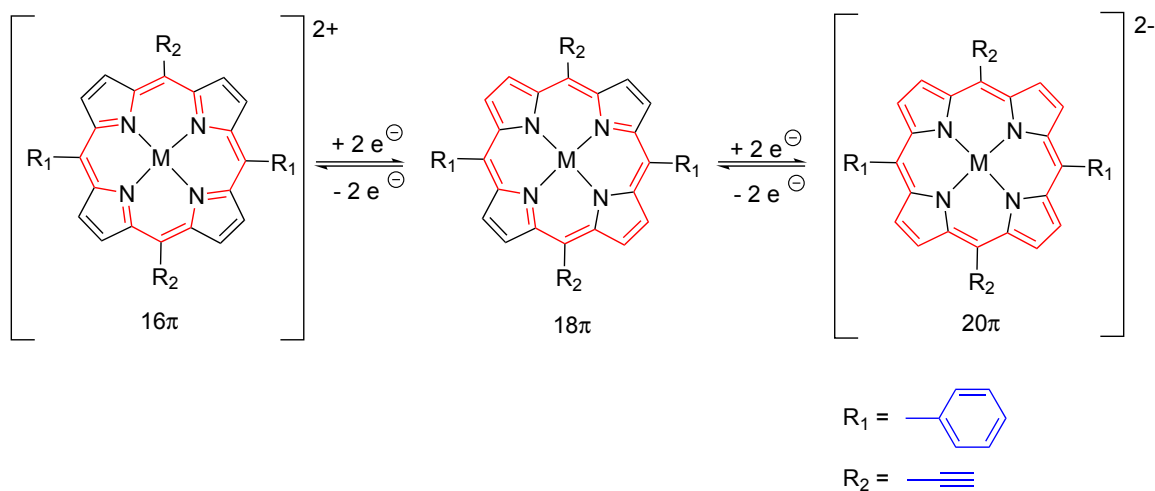


Figure 2.23: Redox reaction of CuDEPP forming dicationic and dianionic species.

a cathode against Li metal (cell 1) and as anode material (cell 2) against a positive graphite electrode. To determine the suitable voltage window for cell 1, the first cyclic

voltammetry (CV) measurement was conducted within a range of 0.05-4.5 V, revealing also some irreversible peaks (Fig. 2.24). Two reversible reduction peaks at approximately 1.27 V and 0.78 V were identified through XPS studies, corresponding to the reduction of Cu(II) to Cu(0). Additionally, an irreversible peak at 4.2 V was observed, which plays a crucial role in the working principle of CuDEPP as an electrode material with high cycle stability. The authors suggest this peak is due to self-conditioning of the material, involving electrochemically induced polymerization that makes the material insoluble, leading to a remarkably stable material. CuDEPP demonstrated excellent cycle stability with more than 8000 cycles at 4 A g⁻¹, retaining 80% of its capacity in the first 2000 cycles and 60% until 8000 cycles, while also maintaining stability at fast charging rates of 53 C (153 mAh g⁻¹). The self-conditioning step at 4.2 V occurs only once in the first cycle and is not observed in the subsequent cycles (Fig. 2.24). Due to its critical role in achieving outstanding performance, the practical voltage window of the cell was limited to 1.8-4.5 V to avoid the reduction of Cu(II), which could lead to structural changes and the formation of elemental Cu(0). However, the irreversible self-conditioning step is intentionally retained at 4.2 V. The two reversible redox pairs at 2.22/2.95 V and 3.55/3.68 V correspond to the redox reactions between [CuDEPP]²⁺ and [CuDEPP]²⁻. The nature of the self-conditioning step will be extensively discussed in detail in chapter 8 of this thesis. It has to be noticed that the discharge capacity of 182 mAh g⁻¹ is close to the theoretical value of 187 mAh g⁻¹. The charge/discharge behavior does not exhibit any voltage plateaus, indicating fast redox reactions, which suggests a pseudo capacitive charge storage mechanism. In cell 2, 1-butyl-1-methylpiperidinium bis(trisfluoromethylsulfonyl)imide (PP14TFSI), an ionic liquid, is used as the electrolyte, instead of LiPF₆ that was used in cell 1. As a result, there may be additional visible reduction peaks in the cyclic voltammetry, which suggests multistage deintercalation of TFSI⁻ anions in the graphite. Cell 2 was tested in a voltage range of 0.0-4.0 V, where an initial discharge capacity of 94 mAh g⁻¹ could be obtained at 1 A g⁻¹, which is close to the theoretical value of the two-electron step (CuDEPP ⇌ CuDEPP²⁻) of 93.5 mAh g⁻¹.

Ren *et al.*'s study investigated improvements on the electrolyte side of cell configuration 1, where CuDEPP acted as the positive electrode in a half-cell against Li. Var-

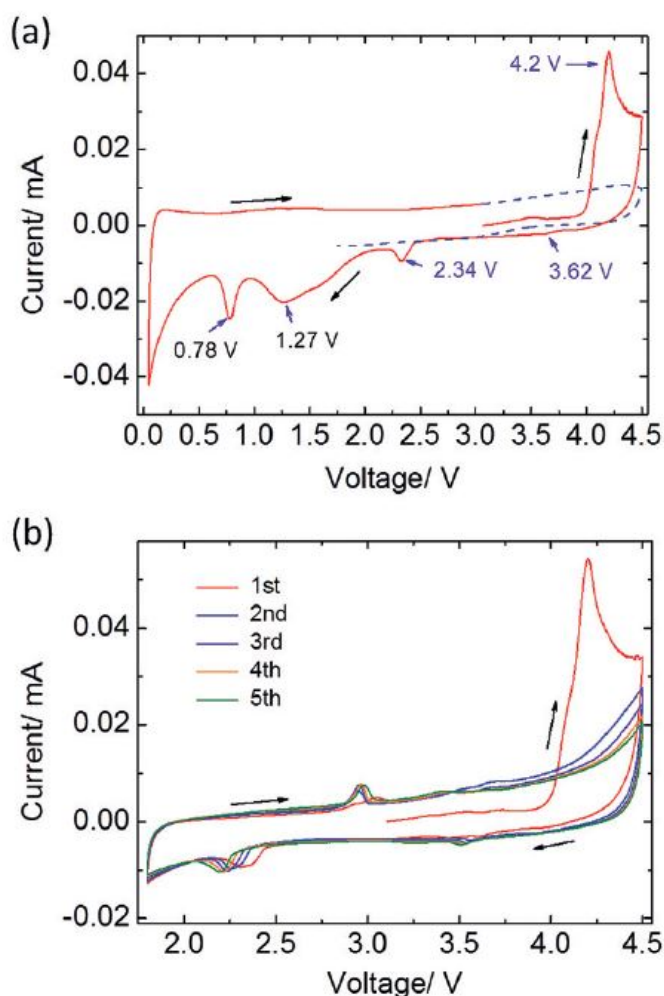


Figure 2.24: Cyclic voltammograms (CVs) of CuDEPP: a) First cycle in a voltage range of 0.05-4.5 V b) 1st to 5th cycle in a voltage range of 1.8-4.5 V. Reproduced with permission[148], Copyright (2017) Wiley.

ious salts, including lithium hexafluorophosphate (LiPF_6), lithium tetrafluoroborate (LiBF_4), lithium bis(oxalate)borate (LiBOB) and lithium bis(trifluoromethylsulfonyl)imide (LiTFSI), were tested.[157] The choice and concentration of the electrolyte can heavily influence the voltage window. Initially, tests were conducted between 1.0-4.5 V. In the case of the boron electrolyte, a significant irreversible reduction peak was noticed between 1.5-1.0 V, indicating a different storage mechanism compared to LiPF_6 . Within this voltage range, LiPF_6 in propylene carbonate (PC) showed the highest performance after 100 cycles compared to all other combinations. For further investigation, a more stable voltage window of 1.8-4.5 V was used. In all electrolyte cases, the self-conditioning peak could be observed above 4.0 V, although the cyclic voltammograms (CVs) show some differences in the anodic peaks.[157] The best performance was achieved using phosphorous (PF_6^-) and nitrogen (TFSI $^-$) based electrolytes compared to boron-based ones. Since TFSI $^-$ showed promising results, the

influence of the electrolyte concentration was studied using 1, 3, and 6 molar solutions (Fig. 2.25). Increasing the concentration to 3M led to an increase in reversible capacity, possibly due to nitrogen acting as an active site for cations and anions. However, further increasing the concentration resulted in poorer performance due to higher viscosity causing slower kinetics. Improved specific capacities of up to 250 mAh g⁻¹

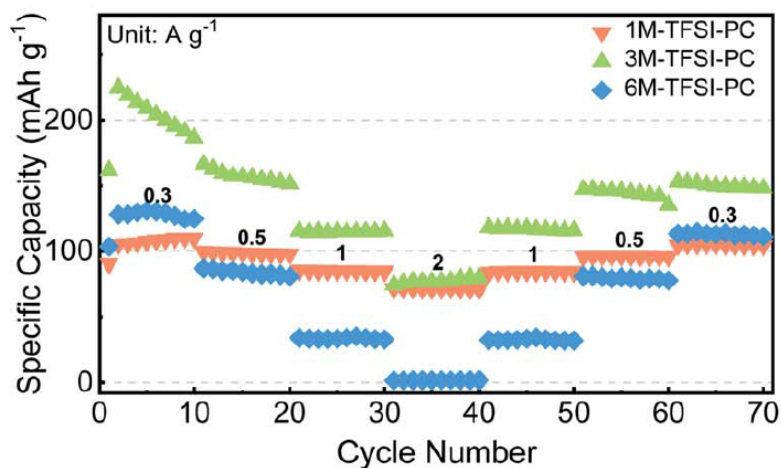


Figure 2.25: Rate performance of CuDEPP in a half-cell with different concentrations of the LiTFSI electrolyte 1, 3 and 6M. Reproduced with permission[157], Copyright (2022) The Royal Society of Chemistry.

could be observed for LiTFSI. This study opens up more possibilities to enhance the performance, especially considering the typically high solubility of organic molecules. The choice and concentration of the electrolyte can play a major role in achieving these improvements and solve common problems.

An alternative approach for the study involved exploring other functional groups as potential replacements for the phenyl group. Zhou *et al.* replaced the phenyl group with furyl groups while retaining the two terminal acetylene groups, resulting in [5,15-bis(ethynyl)-10,20-difurylporphinato]copper(II) (CuDEOP). The idea behind this modification was to introduce heteroatoms with lone pairs of electrons into the π -electron system, aiming to promote multielectron transfer and enhance intrinsic conductivity. CuDEOP was tested in a lithium half-cell.[150] When testing the cell in the previously set voltage range of 1.8-4.5 V, no significant reduction peak could be observed, only an oxidation peak at 3.98 V in the first cycle of the CV. Broadening the voltage range to 1.0-4.5 V revealed an irreversible peak at 4.04 V and a reductive peak at 1.18 V, indicating the decomposition of the electrolyte and formation of a

SEI. However, the oxidation peak shifted to lower voltages with subsequent cycles. Additionally, one reduction peak was observed in the set voltage range, indicating a two-electron redox reaction occurring at low voltage (1.8-1.0 V), likely involving lithium ion storage at the furyl functionality. The cell performance evaluation was conducted between 1.8-4.5 V. At a low current of 200 mA g^{-1} , a specific capacity of 165 mAh g^{-1} could be obtained after 300 cycles with a capacity retention of 85%. At higher currents of 2 A g^{-1} , a specific capacity of 166 mAh g^{-1} was obtained after 25 cycles, remaining stable over more than 200 cycles with a capacity retention of 79%. It was also shown that at temperatures above $50 \text{ }^\circ\text{C}$, a reversible capacity of 199 mAh g^{-1} was achieved after 100 cycles at 200 mA g^{-1} . Kinetic studies revealed a high capacitive contribution leading to a pseudocapacitive charge storage mechanism, known for its fast charge storage kinetics. Overall, six-electron transfer was achieved, with a discharge capacity of 223 mAh g^{-1} at 200 mA g^{-1} , a high energy density of 411 Wh kg^{-1} , and a power density of 16 kW kg^{-1} with a Coulombic efficiency close to 100%. [150]

In a further study the replacement of phenyl functionality with thiophene groups was carried out. [151] [5,15-bis-(ethynyl)10,20-dithienylporphinato]M(II) with M(II) = Cu, Zn, Co, and 2H (MDETP) and [5,10,15,20-tetra(thienyl)porphinato]copper(II) (CuTTP) were investigated (Fig. 2.26), where both nitrogen and thiophene can act as active sites, resulting in an eight-electron transfer during the redox reaction with interactions involving both Li^+ and PF_6^- ions. CuDETP exhibited a high reversible

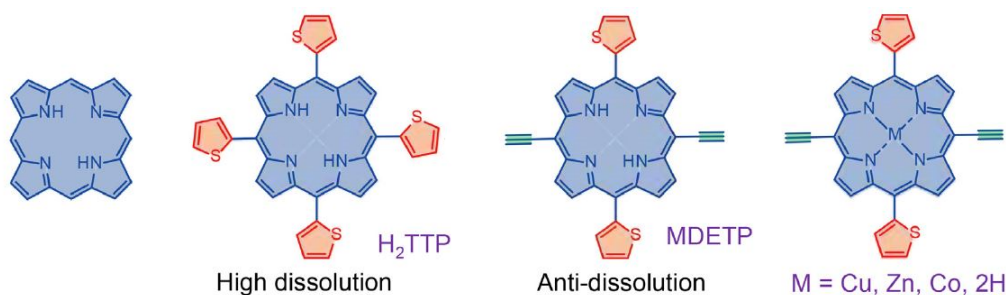


Figure 2.26: Structures of porphyrins functionalized with thiophene and ethynyl groups. Reproduced with permission [151], Copyright (2022) Elsevier.

capacity in a half-cell against Li metal, achieving 350 mAh g^{-1} at 100 mA g^{-1} , and a high specific energy density of 773.6 Wh kg^{-1} , demonstrating excellent stability over more than 9000 cycles. MDETP showed higher discharge capacity and better cycling stability in the voltage range of 1.0-4.5 V, thanks to the contribution of the thio-

phene groups. However, when the terminal acetylene groups were also replaced in [5,10,15,20-tetra(thienyl)porphinato]copper(II) CuTTP, its performance significantly decreased compared to theoretical values due to its high solubility. The variation of the metal center revealed the following trend: $\text{Cu} > \text{Zn} > 2\text{H}$, with Co demonstrating a very high capacity of 760 mAh g^{-1} but experiencing a fast capacity decay within the first 12 cycles, resulting in a capacity of 200 mAh g^{-1} compared to Cu's stable capacity of 350 mAh g^{-1} . The self-conditioning peak was also observed at 4.3 V. Kinetic studies of CuDETP revealed a high capacitive contribution of more than 70% at low sweep rates, indicating fast redox kinetics.[151]

Previously, all attempts were focused on preserving the terminal acetylene group, which appeared crucial for self-conditioning.[148–150, 156] However, recent findings demonstrated that electrochemically induced polymerization can also be achieved with 5,10,15,20-tetra(4-Aminophenyl)-21*H*,23*H*-porphin (TAPP) (Fig. 2.27).[159] Investigations were carried out on both the free-base and its metal complexes with Cu and Zn. Among these, CuTAPP exhibited a specific capacity of 120 mAh g^{-1} , with a high active material contribution of 70% at 1 A g^{-1} . Commonly, the electrode slurry contained 50% active material in all investigations. Comparing different metal centers and the free-base, Cu outperformed Zn, and metallated porphyrins showed better performance than the free-base porphyrin. Kinetic studies indicated that the introduction of metal centers increased the capacitive contribution, likely explaining the improved rate capability. Cyclic voltammetry investigations further revealed an irreversible oxidative peak at 3.9 V for CuTAPP, accompanied by high overpotential in charge-discharge profiles, possibly indicating the occurrence of self-conditioning. The amine group is known to undergo electrochemically induced polymerization, forming dihydrophenanthrazine.

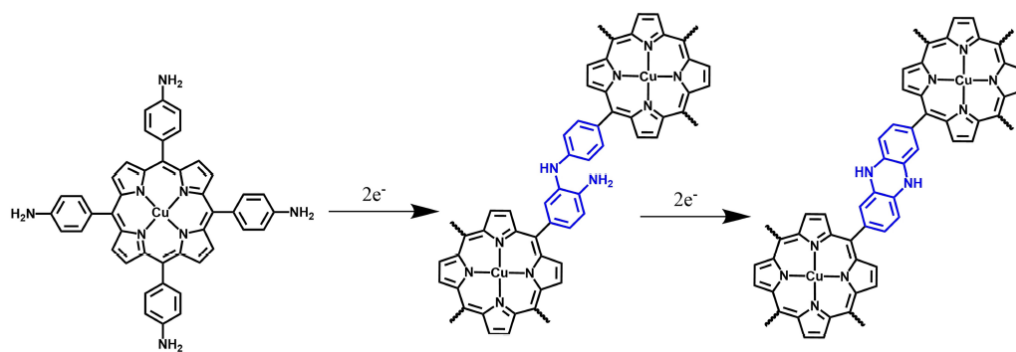


Figure 2.27: Mechanism[160] of electrochemically induced polymerization of CuTAPP. Reproduced with permission[159], Copyright (2023) Wiley.

Through the concept of electrochemically induced polymerization, it has been demonstrated that porphyrins, exemplified by CuDEPP and CuTAPP, function effectively as electrode materials, showing great potential for further improvement. To enhance their performance, a better understanding of the underlying processes is crucial. Apart from molecular and cell design, porphyrins have proven to be excellent candidates for post-lithium systems such as SIBs. CuDEPP exhibited a specific energy of 384 Wh kg^{-1} and a specific power density of 28 kW kg^{-1} , along with outstanding cycling stability of 93% after 600 cycles at 5 A g^{-1} . [153] In the case of KIBs, CuDEPP as the cathode material also showed promising results, with a reversible capacity of 181 mAh g^{-1} and a capacity retention of 87% after 300 cycles. Furthermore, in the half-cell against K metal, high energy densities of 408 Wh kg^{-1} and power densities of 859 W kg^{-1} were observed. [154] CuDEPP was investigated as a cathode material for magnesium batteries in multivalent systems. This investigation led to a specific capacity of 155 mAh g^{-1} at a current density of 1 A g^{-1} . Even at higher currents of 4 A g^{-1} , a capacity of 70 mAh g^{-1} was achieved after 500 cycles, boasting energy density of 92 Wh kg^{-1} and power density of 5100 W kg^{-1} . [155]

Chapter 3

Experimental methods

3.1 UV-Visible Spectroscopy

UV-Vis spectroscopy is an absorption spectroscopy technique that operates in the ultraviolet (200-400 nm) and visible (400-800 nm) regions of the electromagnetic spectrum, typically between 200-800 nm. In a common double beam UV-Vis spectrometer, light is split into two parallel beams, one of which passes through a cell containing the solvent and the other through a cell containing the dissolved sample in the same solvent. The detector measures the intensity of transmitted light through both cells. The absorbance (A) is then calculated using the equation:

$$A = \log_{10} \frac{I_0}{I} \quad (3.1)$$

where I_0 is the intensity of the light transmitted through the reference cell with pure solvent, and I is the intensity of the light transmitted through the cell with the dissolved sample. The absorption process involves exciting an electron from its lowest electronic energy level (ground state) E_1 to a higher energy level E_2 . The energy required for this transition, denoted as ΔE , is given through the equation:

$$\Delta E = h \cdot f = \frac{h \cdot c}{\lambda} \quad (3.2)$$

with h as the Planck constant ($6.626 \times 10^{-34} \text{ J}\cdot\text{Hz}^{-1}$), c is the speed of light ($299792458 \text{ m s}^{-1}$), f is the frequency, and λ is the wavelength of the electromagnetic wave. The extinction, E_λ , which represents the absorbance of a specific material at a given wavelength,

can be described by the Beer-Lambert law:

$$E_{\lambda} = \log_{10} \frac{I_0}{I} = \epsilon \cdot c \cdot l \quad (3.3)$$

Here, l represents the length of the cell (in cm), and c is the concentration of the solution (in mol L⁻¹). The extinction coefficient, ϵ , is expressed in units of cm² mol⁻¹ or dm³ mol⁻¹ cm⁻¹. Generally, $\pi \rightarrow \pi^*$ transitions (Fig. 3.1) exhibit higher ϵ values compared to $n \rightarrow \pi^*$ transitions. UV-vis spectroscopy can be used to analyze various chromophores and determine the concentration of different solutions.[161]

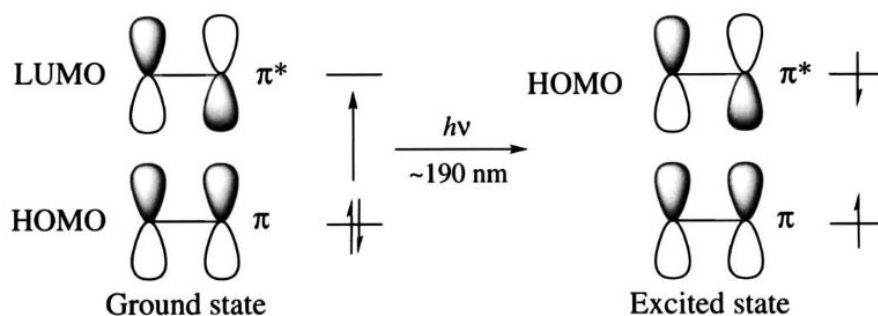


Figure 3.1: $\pi \rightarrow \pi^*$ transition of ethane. Reproduced with permission[161], Copyright (2004) American Chemical Society.

3.2 Scanning Electron Microscopy

Scanning electron microscopy (SEM) is a method used to analyze the microstructure and morphology of samples by scanning a surface with a focused beam of electrons. The resulting image is generated by acquiring signals, which can be of two different types: elastic and inelastic interactions. Backscattered electrons (BSE) are incident electrons that are elastically scattered back at an angle of more than 90°. Inelastic scattering occurs through interactions between incident electrons and the electrons and atoms of the sample, transferring energy to the atom via the beam. Secondary electrons (SE) are generated when species' electrons are excited during the ionization of the specimen atom, and these SE are typically utilized for imaging or sample analysis. In addition to these two signals, other signals like x-rays, Auger electrons, and cathodoluminescence can also be obtained in SEM analysis (Fig. 3.2).[162] Secondary electrons in SEM have energies below 50 eV, which means they originate from just a few nanometers below the sample surface. Due to their highly localized nature close to

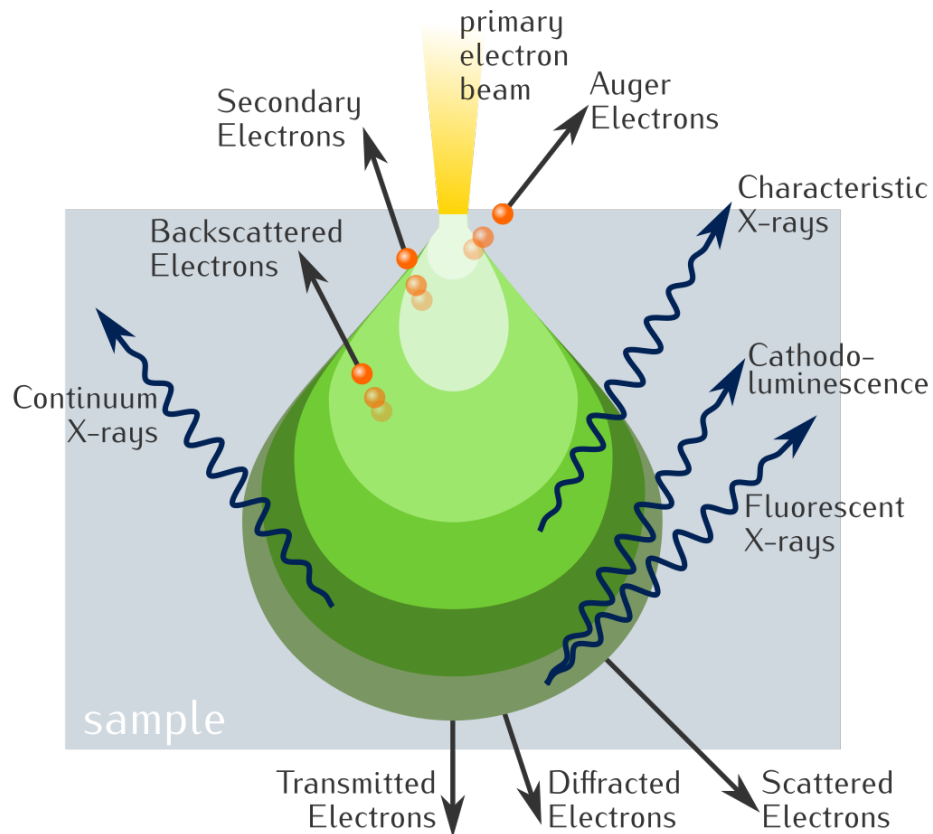


Figure 3.2: Signals generated by the electron beam. [By Ponor - Own work, CC BY-SA 4.0, <https://commons.wikimedia.org/w/index.php?curid=93635964>][07.26.23].

the electron beam, high-resolution images can be obtained with a resolution of up to 1 nm. On the other hand, backscattered electrons (BSE) have much higher energies, leading to limited resolution. BSE detection can provide information about sample composition and topography. Heavier elements tend to have more positive charge on their nuclei, resulting in more electrons scattering back. Analyzing characteristic x-rays is a widely used method to obtain chemical information. When a primary electron collides with an inner electron, an outer-shell electron can fill the vacancy created. This process leads to the emission of an x-ray photon, causing the ionized atom to return to its ground state.[162] This technique, known as energy-dispersive x-ray spectroscopy (EDS/EDX), can be employed to identify elements and determine the chemical composition of a sample composition.

3.3 FIB-SEM Tomography

FIB-SEM Tomography is a technique that combines focused ion beam (FIB) with scanning electron microscopy (SEM) to generate images at micro- to nanometer scales. This method enables immediate imaging after employing the FIB for tasks like etching

or depositing materials onto solid specimens. For the purpose of 3D reconstruction using tomography, thin 2D slices are obtained. Typically, the specimen of interest is embedded in resin to prevent charge buildup at the edges of the pores, eliminate shine-through artifacts, and ideally, enhance the contrast. Furthermore, the specimen is coated with a metal layer to protect it from undesired sputtering during FIB milling, and having smooth edges can assist in minimizing curtaining effects and improving conductivity. The process starts by creating a U-shaped trench cut around the VOI. This trench reduces shadow effects and prevents the re-deposition of materials onto the cross-section surface. Subsequently, multiple cross-sections of the internal structure are revealed through the gradual removal of thin layers with the FIB, and these sections are then sequentially imaged using the SEM. The outcome is a stack of SEM micrographs capturing the cross-section. These images can be processed and aligned to reconstruct the selected volume in three dimensions (Fig. 3.3). The typical volume

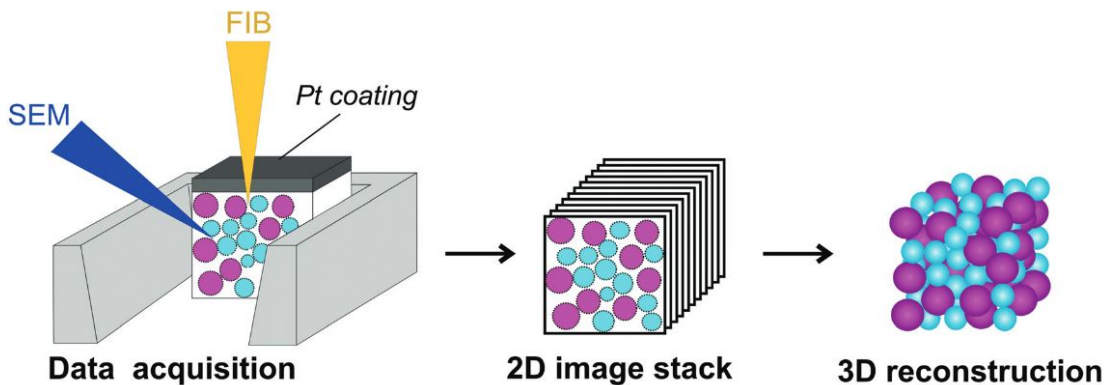


Figure 3.3: Working principle of FIB-SEM-Tomography. Reproduced with permission[163], Copyright 2019, Royal Society of chemistry.

that can be examined ranges from 1 to 50 μm^3 , with achievable resolutions as fine as 10 to 30 nm. This level of resolution renders it suitable for investigating parameters such as pore size and tortuosity.[164]

3.4 Nano-Computed X-ray Tomography

Nano-computed X-ray tomography (nanoCT) is a non-destructive method used to explore the three-dimensional structures of samples across multiple length scales, providing a resolution at the nanometer level. Through the use of X-ray penetration, even thick and opaque materials can be investigated, enabling the creation of magnified images. In CT techniques, a series of projection images are captured over a

range of angles, typically covering either 180 or 360 degrees. In industrial nanoCT, the sample rotates while the X-ray source remains stationary, which is in contrast to medical X-ray CT where both the X-ray source and the detector rotate. The nanoCT method employed here uses a semi-monochromated X-ray beam generated from a chromium anode (5.4 keV) and a sequence of optics to achieve a pixel size as small as 16 nm (Fig. 3.4). To initiate the reconstruction of the 3D structure, hundreds

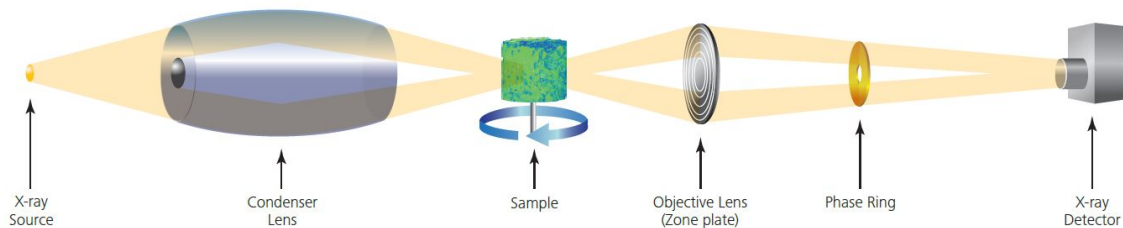


Figure 3.4: Optical schematic of nanoCT. Reproduced with permission[165], Copyright (2022) Taylor& Francis group.

to thousands of projections are essential. This reconstruction is carried out using computer software, primarily relying on the filtered back projection algorithm. The resulting reconstructed volume can be examined on a per-slice basis or visualized in three dimensions. Generally, the reconstructed volume is subjected to segmentation, often based on grayscale or other distinguishing characteristics linked to the sample's density or phase contrast fringes. For low-density materials, where the X-ray absorption through the sample is weak, the phase contrast mode is employed. In the current setup, a gold phase ring generates Zernike phase contrast in the imaging process, enhancing the edges of the features in the samples. These segmented volumes can subsequently facilitate quantitative analyses, such as assessing pore size or tortuosity.[165, 166]

3.5 Galvanostatic Cycling

Galvanostatic cycling is a valuable method used to analyze the voltage behavior during the discharge and charge processes, while keeping the current defined and constant. The selection of an appropriate voltage window is crucial to avoid irreversible side reactions while ensuring that all significant redox reactions occur within the window, leading to the highest possible capacity. During galvanostatic cycling, various important values are obtained from the measurements. Analyzing the discharge/charge

curves (Fig. 3.5) provides insights into the processes occurring within the cell. A single, well-defined plateau in the curve indicates a stable discharge/charge process with a single conversion of the redox material. On the other hand, the presence of multiple plateaus usually indicates multiple redox reactions taking place. If the

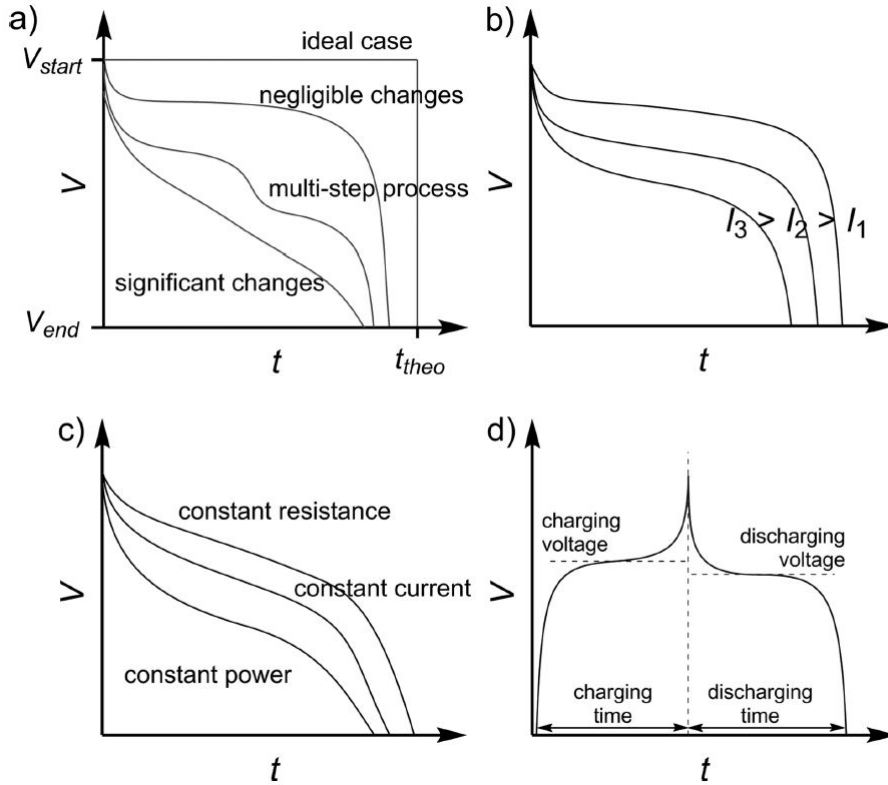


Figure 3.5: Typical discharge curves: (a) for different redox-system behavior; (b) at different discharge currents, and (c) for different discharge modes. (d) Typical charge/discharge curve. Reproduced with permission[22], Copyright (2016) American Chemical Society.

voltage deviates from the expected theoretical behavior during galvanostatic cycling, this discrepancy can be attributed to internal resistance or polarization effects. The current rate, especially at higher rates, can significantly influence these phenomena. Another crucial value obtained from galvanostatic cycling is the capacity, which is determined from the charging time and the applied current.

$$Q_1(mAh) = \int_0^t i(t)dt \quad (3.4)$$

Comparing the capacity obtained with the theoretical capacity is a relevant step to evaluate the battery's performance. The ratio of the discharge and charge capacity gives the Coulombic efficiency. By considering the operating voltage, the energy and energy efficiency of the battery can also be determined. To assess the battery's long-

term performance, it is essential to conduct cycling tests over several thousand cycles, which provide valuable information about cycle life and rate capability.[22, 25]

3.6 Cyclic Voltammetry

Cyclic voltammetry is a valuable technique for investigating electrochemical processes involving redox reactions occurring at different voltages. This method helps determine if the process is reversible or irreversible and allows the identification of the potential at which oxidation or reduction occurs (Fig. 3.6b). By varying the sweep rate, valuable insights into the kinetic behavior can be obtained, shedding light on the capacitive contribution to the charge storage mechanism. During cyclic voltammetry, the current is measured while the potential is linearly swept as a function of time. The rate at which the voltage changes over time is known as the sweep rate (mV s^{-1}). When the voltage range from E_1 to E_2 is measured, the curve cycles back to E_1 (Fig. 3.6a).[167] Cycling the system over multiple cycles provides valuable insights into the

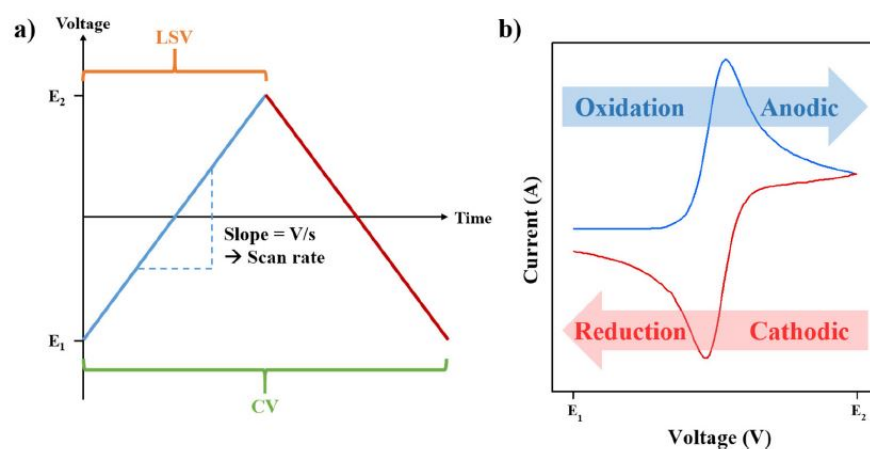


Figure 3.6: a) Voltage vs. time for linear sweep and CV b) typical CV. Reproduced with permission[167], Copyright (2020) The Korean Electrochemical Society.

reversibility and cycleability of the redox reactions. A fully reversible process can be assumed if the ratio between the oxidation and reduction peak currents ($i_{p,a}$ and $i_{p,c}$) is 1:1 and if the peak split ΔE_p ($E_{p,a} - E_{p,c}$) is $57/n$ mV (Fig. 3.7).[22]

3.7 Electrochemical Impedance Spectroscopy

Electrochemical impedance spectroscopy (EIS) is a valuable AC-based technique used to study *in situ* processes occurring in electrochemical systems (Fig. 3.8). This

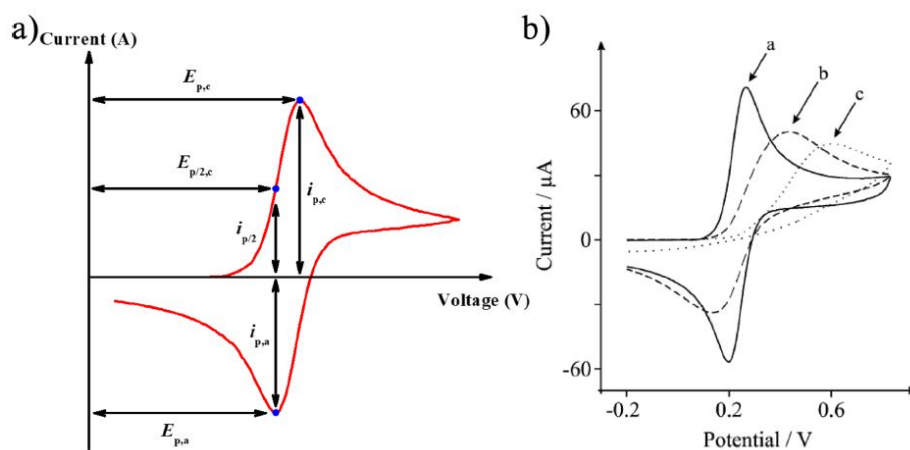


Figure 3.7: a) A typical CV and parameters that can be derived from it and b) CV of reversible (a), quasi-reversible (b) and irreversible case (c). Reproduced with permission[167], Copyright (2020) The Korean Electrochemical Society.

method allows complex processes to be simplified based on their relaxation time. EIS is a valuable tool for analysing the electron-transfer characteristics of electrode materials. When analyzing the interaction of dissolved redox-active compounds at an electrode surface, it is common to represent these interactions using an equivalent circuit (Fig. 3.9a). The equivalent circuit (Fig. 3.9a) comprises different elements to

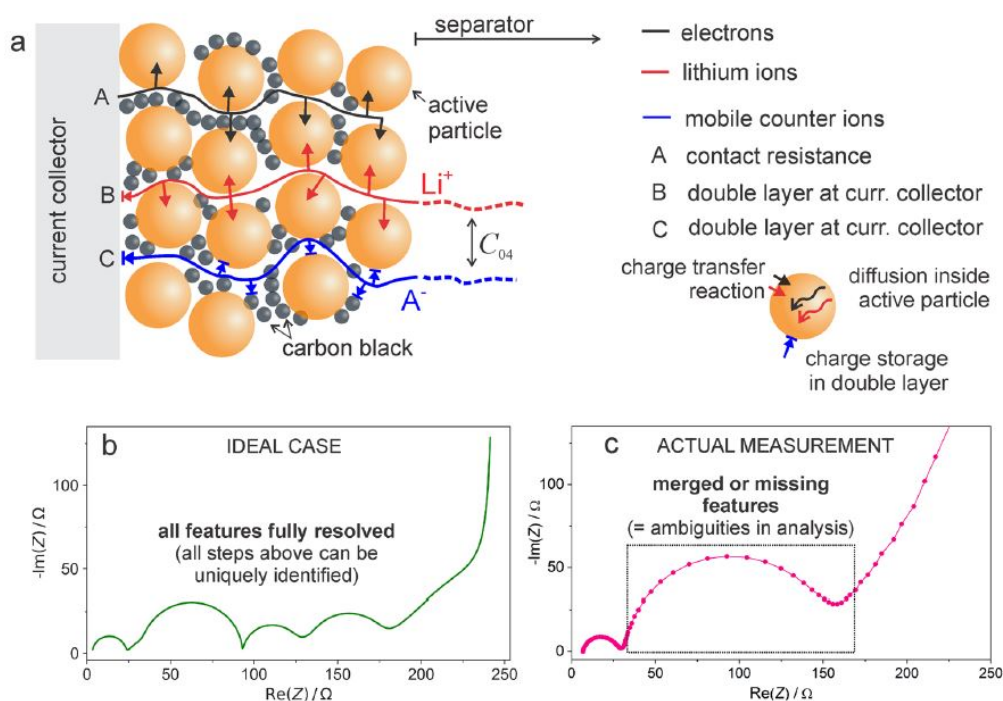


Figure 3.8: a) Processes occurring at electrode surface b) theoretical impedance spectrum showing all processes separately c) practical example of EIS spectrum. Reproduced with permission[168], Copyright (2021) Springer Nature.

represent specific aspects of the electrochemical system. R_E represents the electrolyte resistance, R_{CT} is the charge-transfer resistance, and Z_W is known as the Warburg

element, describing the diffusion behavior of the redox-active molecule. C_D accounts for the capacitance characteristics of the surface electrochemical double layer. By plotting the obtained Nyquist plot (Fig. 3.9b), one can analyze the electron transfer and diffusion characteristics. Typically, a semicircle appears in the high-frequency area, while a straight line is observed for small AC frequencies, with the offset representing R_E . The diameter of the semicircle on the abscissa corresponds to R_{CT} and

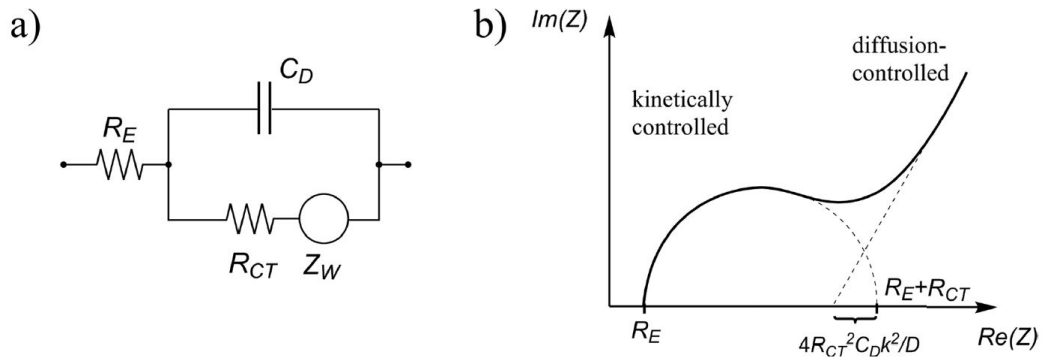


Figure 3.9: a) Randles circuit as an electrical equivalent circuit and b) Nyquist plot with semi circle representing kinetic control and diffusion controlled linear part. Reproduced with permission[22], Copyright (2016) American Chemical Society.

can be related to the exchange current, i_0 :

$$R_{CT} = \frac{RT}{nF i_0} \quad (3.5)$$

making it possible to calculate the standard heterogeneous transfer rate k^0 , the straight line in the Nyquist plot at lower frequencies represents the Warburg impedance and can be expressed using the following equation:

$$Im(Z) = Re(Z) - R_E - R_{CT} + R_{CT}^2 C_D \left(\frac{k_{ox}}{\sqrt{D_{ox}}} + \frac{k_{red}}{\sqrt{D_{red}}} \right)^2 \quad (3.6)$$

The abscissa intersects at:

$$R_E - R_{CT} + R_{CT}^2 C_D \left(\frac{k_{ox}}{\sqrt{D_{ox}}} + \frac{k_{red}}{\sqrt{D_{red}}} \right)^2 \quad (3.7)$$

The equivalent circuit can be simplified to the following expression if equal rate constants and diffusion coefficients for oxidation and reduction are assumed:

$$R_E + R_{CT} - 4R_{CT}^2 C_D \frac{k^2}{D} \quad (3.8)$$

This enables us to calculate the diffusion coefficient D .

Chapter 4

Aim of the thesis

This thesis aims to improve understanding of the relationship between the structure and performance of organic electrode materials used in rechargeable battery systems. The thesis also aims to advance the development of new materials that are cost-effective, environmentally friendly, and widely available for future battery technologies.

Chapter 5 examines a widely recognized porphyrin (xDEPPs) that could serve as a cathode material for lithium-ion batteries. The research looks into the impact of different metal centers that include first-row transition metals from Co to Zn. Moreover, it covers the free-base porphyrin variant of the A2B2 porphyrin DEPP; specifically, 5,15-bis(ethynyl)-10,20-diphenyl-21*H*,23*H*-porphin. In addition, the chapter sheds light on the synthetic methodology employed, the electrochemical evaluation and the DFT calculations conducted to explain the behavior of the material.

Chapter 6 focuses on the interplay between structure and performance of the cobalt complex CoDEPP [5,15-bis(ethynyl)-10,20-diphenylporphinato]cobalt(II), with its morphology and microstructure examined in four distinct configurations, including amorphous and crystalline forms. The evaluation of material performance was undertaken using a lithium half-cell. The chapter additionally discusses the application of 3D reconstruction techniques, which aim to provide a deeper understanding of the porosity of the materials.

Chapter 7 presents the utilization of a pyridine-functionalized porphyrin metal organic framework as a potential electrode material. After thorough analytical examinations, the material's performance was evaluated initially in a lithium half cell configuration and subsequently in multivalent post-lithium systems, including aluminium and calcium batteries.

In Chapter 8, the focus was directed towards gaining a profound understanding of the phenomenon known as "self-conditioning". In order to validate the hypothesis regarding the occurrence of polymerization, new functional groups were incorporated into the porphyrin core at the *meso*-position, and their electrochemical behavior was extensively examined. The investigation revealed intriguing distinctions, and the kinetics and charge storage mechanism of these modified structures were thoroughly assessed.

The utilization of organic materials as potential electrode material could be a significant stride towards sustainable materials. Consequently, a comprehensive understanding of the working principle and probable design methods is indispensable.

Chapter 5

Central Metal Matters

5.1 Introduction

This chapter is based on the publication ChemSusChem, **2023**, 16, e202202090, titled "Molecular Engineering of Metalloporphyrins for High-Performance Energy Storage: Central Metal Matters". Shirin Shakouri synthesized and characterised the materials and mainly contributed to the writing of the manuscript, while Dr. Ebrahim Abouzari-Lotf supervised the electrochemical test, Jie Chen worked on electrode optimisation, DFT calculations were provided by Dr. Frank Pammer, XPS was performed by Dr. Thomas Diemant and Asato Mizuno assisted with single crystal XRD.

One way of tuning the properties of porphyrin-based electrode materials is, through the metal center. Several studies have shown that the storage performance will be influenced by implementing a metal center into the free-base porphyrin.[153, 160] However, for certain applications there is a preference for different metals. The fact that mainly Cu(II)-complexes of porphyrins[148, 151], phthalocyanines[160], and Ni(II)-norcorrole[133] complexes are applied as cathode materials in energy storage systems illustrates this. Apart from that, on the anode side Co(II)-complexes were investigated.[135] Why these specific ions are preferred over others is a question that needs to be addressed to design useful electrode materials for battery application without formation of species that limit rechargeability and cycling stability. Indeed, the role of the metal ion in the whole process is still poorly understood. For instance, metal tetraaminephthalocyanine (TAPc) seems to favour copper due to the robust

interaction between $[CuTAPc]^{+/2+}$ and PF_6^- , as well as the electropolymerization of CuTAPc monomers[160]. Nonetheless, it is uncertain if the copper complex functions singularly in this capacity.[131] Furthermore, changes in properties such as redox stability window[169], conductivity[170], solubility[171], crystallinity and porosity have been neglected in the design of porphyrin-based electrode materials. In this chapter the electrochemical behaviour of 5,15-bis(ethynyl)-10,20-diphenyl-21*H*,23*H*-porphin (DEPP) and its complexes, using divalent first-row transition metals from Co to Zn in LIBs has been studied experimentally and theoretically.

5.2 Electrochemical Experiments

5.2.1 Electrode Preparation

The xDEPP electrodes were identically prepared using a water-based method, containing 32 wt% solid content. In this process, a mixture of sodium carboxymethyl cellulose (CMC) and styrene-butadiene rubber (SBR) was used, with a mass ratio of 1:1.1. To obtain the desired concentration, CMC was dissolved in distilled water under heat and stirring overnight. The electrode slurries were prepared by combining xDEPP (46.4 wt%), Super P (46.4 wt%), and binder (7.2 wt%) in distilled water using a Thinky mixer. After stirring at 2000 rpm for 10 minutes, a homogeneous slurry was obtained. This slurry was then applied to a carbon-coated aluminum foil using a doctor blade. Finally, the coated material was dried and punched into 11.8 mm discs, which underwent further drying at 70 °C under vacuum conditions (1×10^{-3} mbar) for 15 hours. The loading of active materials ranged between 1 and 1.3 mg cm⁻².

5.2.2 Cell Assembly

The electrochemical tests were carried out using a coin cell from type CR2032 (Hohsen Corp., Japan). After the electrodes were prepared and dried, they were transferred into a argon-filled glove box ($O_2/H_2O < 0.1$ ppm) for cell assembly. Two layers of glass fiber filter Whatmann GF/C (diameter 16 mm) were used as separator. In case of *post-mortem* analysis a polypropylene film (PP, Celgard 2400) was used as a separator. The electrolyte used was a 1M solution of $LiPF_6$ in a mixture of ethylene carbonate (EC), dimethyl carbonate (DMC) and propylene carbonate (PC) in a volume ratio of

1:3:1. Typically, 80 μL of electrolyte was used in the cell, while in the case of a PP separator, the amount was reduced to 35 μL due to its lower absorbency.

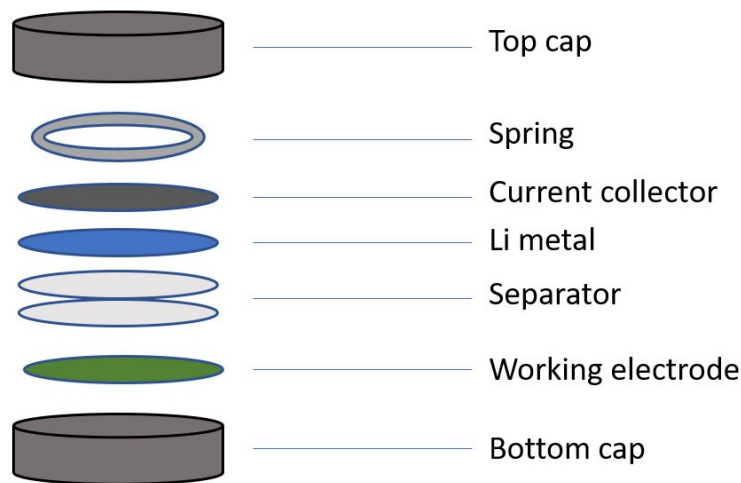


Figure 5.1: Coin cell assembly for half-cell measurements.

5.2.3 Electrochemical Measurement

The galvanostatic cycling with potential limitation (GCPL) tests were performed at 298 K using a BCS-800 system from Biologic. For cyclic voltammetry (CV) measurements, the VMP-3 multichannel potentiostat from Biologic was used with a sweep rate set at 0.1 mV s^{-1} . Testing always began with a three hour record of open circuit voltage (OCV). To analyze the charge transfer resistance and ionic diffusion characteristics of the recently developed xDEPP cathodes, EIS was employed as an alternative to cyclic voltammetry, owing to the possibility of partial dissolution of xDEPPs during long-term measurements. EIS measurements were conducted using the VMP-3 multichannel potentiostat from Biologic, over a frequency range of 1 MHz to 50 mHz. The spectra were fitted using EC-Lab software to calculate the ion diffusion coefficient using the given equation 5.1[172]:

$$D = \frac{R^2 T^2}{2A^2 n^4 F^4 C^2 \sigma^2} \quad (5.1)$$

with D as diffusion coefficient ($\text{cm}^2 \text{ s}^{-1}$), R as gas constant ($8.134 \text{ J mol}^{-1} \text{ K}^{-1}$), T as absolute temperature (294.3 K), A as surface area of the cathode (1 cm^2), n as number of transferred electrons, F as faraday constant (96485 C mol^{-1}), C as concentration of the electrolyte ($3 \times 10 \text{ mol cm}^{-3}$) and the Warburg factor ($\Omega \text{ s}^{-1/2}$), represented by

σ , is calculated by fitting it to an equivalent circuit model that includes a Warburg impedance.

5.3 Results and Discussion

The TMS protected DEPP ligand-frame (2) was synthesized by a one-pot process involving the condensation of 3-(trimethylsilyl)-propionaldehyde with *meso*-aryl dipyrromethane (1). This reaction took place in the presence of boron trifluoride diethyletherate, followed by oxidation using 2,3-dichloro-5,6-dicyano-1,4-benzoquinone (DDQ) as the oxidizing agent.

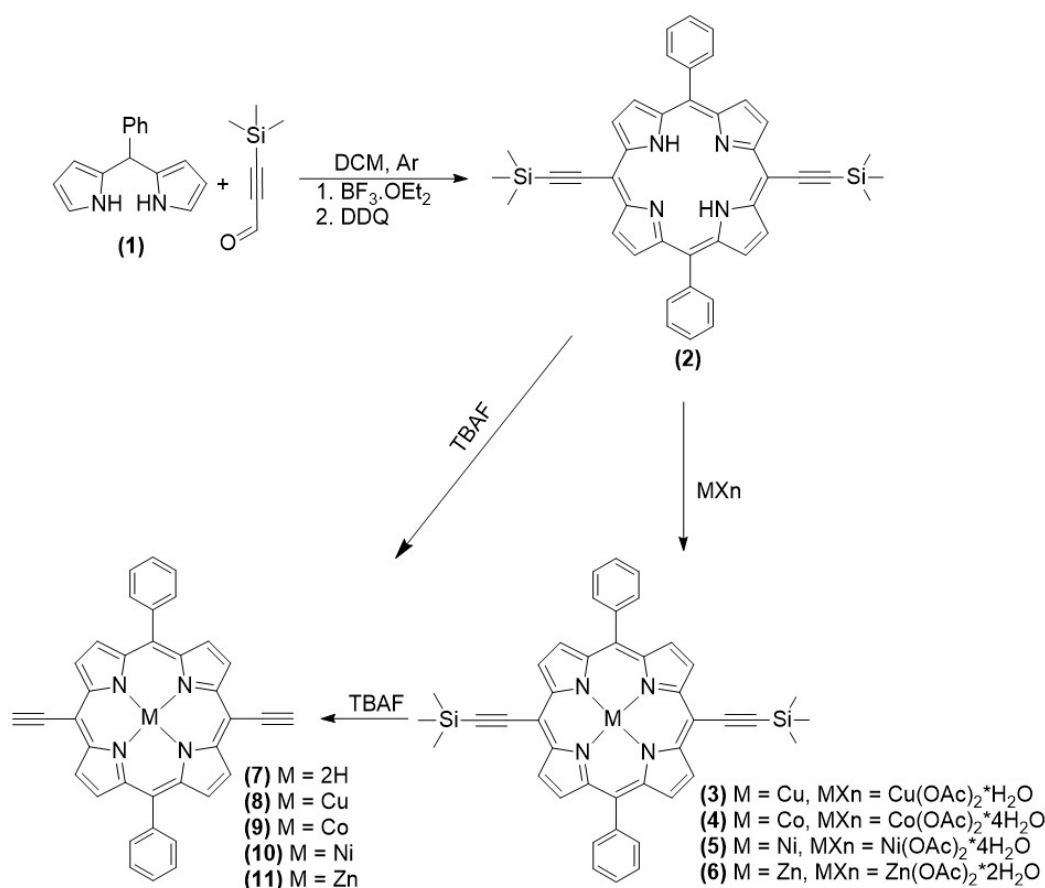


Figure 5.2: Synthesis of free-base DEPP and its metal complexes with M: Co²⁺, Cu²⁺, Ni²⁺ and Zn²⁺.

The free-base DEPP (7) was obtained after deprotection of TMS-groups with tetra-*n*-butylammonium fluoride (TBAF). For metalloporphyrins, DEPP-TMS (2) was transformed into the xDEPP-TMS metal complexes (x = Co, Ni, Cu, Zn) (3-6) and then underwent deprotection by means of TBAF (8-11). Nuclear Magnetic Resonance (NMR), Fourier Transform Infrared (FTIR), Matrix-Assisted Laser Desorp-

tion/Ionization Time-of-Flight Mass Spectrometry (MALDI-ToF), Ultraviolet-Visible (UV-Vis) spectroscopy, elemental analysis, and powder X-ray diffraction (XRD) were employed to characterize all the compounds. The TMS-protected Co-complex (CoDEPP-TMS) can be obtained, enabling the structure determination employing single crystal X-ray diffraction analysis.

Changing the metal atoms in DEPPs leads to modifications in their solubility. The solubility of xDEPPs in the electrolyte was assessed quantitatively using UV-Vis measurements. The concentrations were determined using Beer's law (Eq. 5.2) and the extinction coefficient specific to the solvent (electrolyte) employed:[173]

$$A = \epsilon \cdot b \cdot c \quad (5.2)$$

with A as absorbance, b as path length, c as concentration and ϵ as extinction coefficient.

Table 5.1: Concentration and ϵ of saturated solutions of xDEPPs and DEPP in the electrolyte after 1 day confirm that CuDEPP has limited solubility, while NiDEPP is the more-soluble xDEPP in the series.

	ϵ [$L/mol \times cm$]	Concentration [mol/L]	Concentration [g/L]
DEPP	3787.27	0.11259	57.59
CoDEPP	5107.10	0.01055	5.99
NiDEPP	1393.33	0.02638	14.96
CuDEPP	35.20	0.00345	1.97
ZnDEPP	10595.64	0.00492	2.82

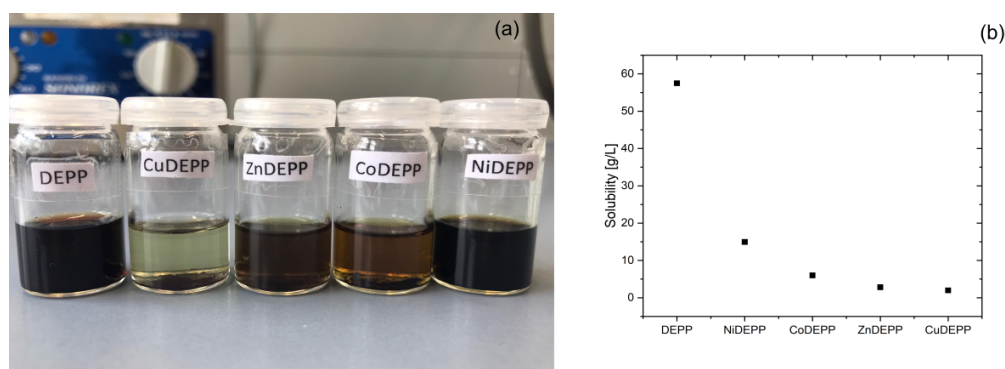
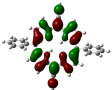
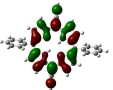
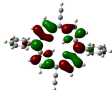
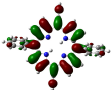
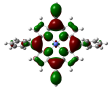
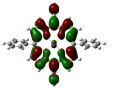
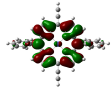
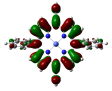
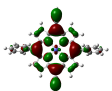
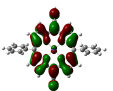
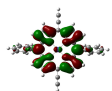
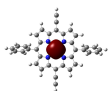
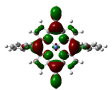
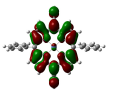
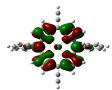
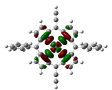
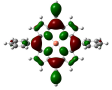
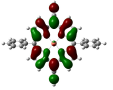
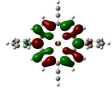
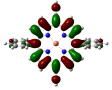
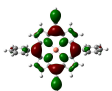
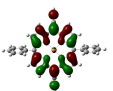
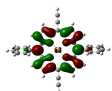
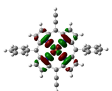
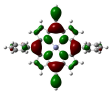
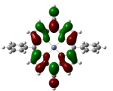
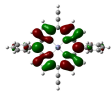
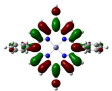


Figure 5.3: Visual comparison of the solubility of xDEPPs and DEPP in dichloromethane after one day, confirming the limited solubility of CuDEPP and the more soluble NiDEPP (a). Comparison between the saturation concentrations of DEPP and xDEPPs in electrolyte (b).

Density functional theory (DFT) calculations were conducted to investigate how the electronic properties and molecular geometries of xDEPPs are influenced by the central metal. In summary, the DFT calculations indicate that the frontier molecular orbitals (FMOs) of xDEPPs are predominantly localized on the porphyrin skeleton, as depicted in Table 5.2. Significant contributions from the ethynyl groups can also be observed. Notably, variations in electron density distribution along the coordinate bonds (x-N4) are evident, providing evidence of charge transfer between the metal and ligand.

Table 5.2: Frontier molecular orbitals HOMO and LUMO and LUMO+n ($n = 1$ and 2) orbitals of DEPP and xDEPP. LUMO+n denotes the orbitals lying energetically higher above the LUMO. For complexes containing unpaired electrons with a multiplicity $\neq 1$ the corresponding α and β orbitals are provided.

	HOMO	LUMO	LUMO+1	LUMO+2
DEPP				
CoDEPP α				
CoDEPP β				
NiDEPP				
CuDEPP α				
CuDEPP β				
ZnDEPP				

In terms of energy, the highest occupied molecular orbital (HOMO) of ZnDEPP shows minimal changes compared to the DEPP reference, as shown in Fig. 5.9. However, this charge transfer phenomenon is more pronounced in the Ni and Co complexes, which possess vacant d orbitals. This charge transfer contributes to the stabilization of the HOMO orbitals in these complexes. This observation is consistent with the significantly shorter x-N bond length (approximately 1.96 Å) in NiDEPP and CoDEPP compared to ZnDEPP and CuDEPP (around 2.0 Å), as shown in both calculated and experimental (single crystal XRD of TMS-protected species) data presented in Table 5.3.

Table 5.3: Calculated and experimental bond lengths (Å) in xDEPPs.

		CoDEPP	NiDEPP	CuDEPP	ZnDEPP
x-N	Calc.	1.964, 1.961	1.934, 1.937	2.044, 2.037	2.043
	Exp.	1.959, 1.957, 1.962, 1.964	-	1.996, 2.002	-
N-C	Calc.	1.393, 1.388, 1.397, 1.389	1.371, 1.379, 1.380	1.381, 1.374	1.379, 1.371
	Exp.	1.385, 1.377, 1.384, 1.376	-	1.363, 1.368, 1.381, 1.364	-

In contrast, there is a partial shift of the lowest unoccupied molecular orbital (LUMO) towards the central metal atom as we move from Zn to Cu, Ni and Co. Consequently, the relative energy difference between the HOMO and LUMO follows the order of CoDEPP > NiDEPP > CuDEPP > ZnDEPP. As a result, we anticipate an increased electron transfer for CuDEPP and ZnDEPP. Conversely, Co and Ni may utilize their readily accessible higher HOMO-1 orbitals for additional redox reactions. The electrochemical performance of the xDEPP complexes were assessed in half-cells, utilizing a lithium metal anode. To mitigate the potential loss of xDEPP from the cathodes through dissolution into the electrolyte, a limited volume of approximately 25 $\mu\text{L mg}^{-1}$ was employed in all cells. Figures 5.4b-e illustrate the cyclic voltammograms of the xDEPP complexes, focusing on the voltage range of 1.0-4.5 V, revealing how the central metal influences the reversibility of the redox reactions.

Additionally, Fig. 5.5 presents the discharge capacities and Coulombic efficiencies of all the complexes during the initial 10 cycles. During the initial anodic sweep, noticeable irreversible oxidative peaks emerged above 3.8 V, which are unique to this particular group of compounds. These peaks are believed to be related to the self-conditioning characteristic of the xDEPPs, as supported by spectroscopic investi-

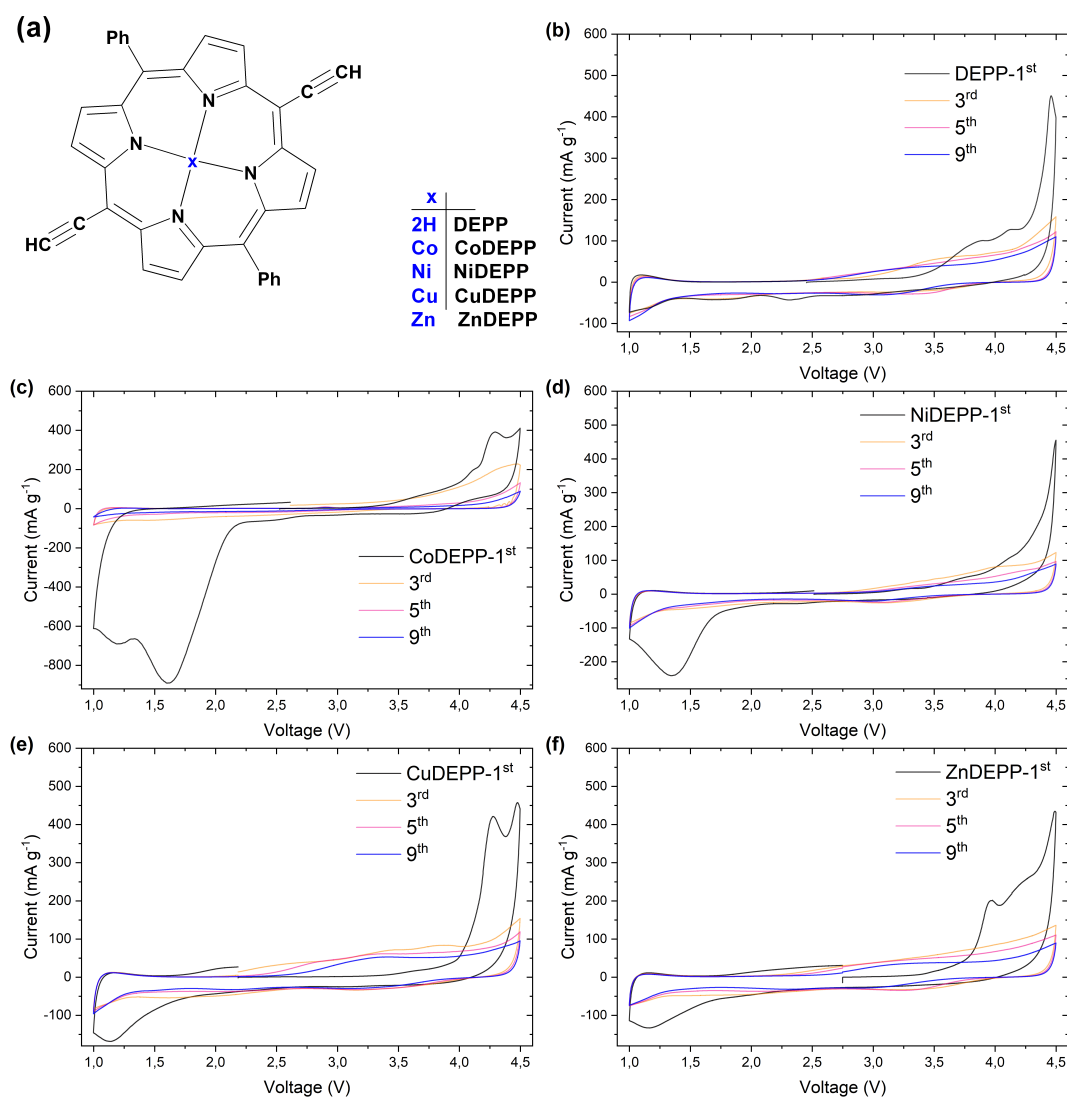


Figure 5.4: Structures of porphyrin molecules xDEPPS used in this chapter (a) and CVs of DEPP (b), CoDEPP (c), NiDEPP (d), CuDEPP (e), and ZnDEPP (f) complexes in Li half-cell with LiPF_6 electrolyte at the voltage range of 1-4.5 V.

gations.[148] Similar phenomena have been observed in systems based on sodium[153], potassium[154], and magnesium[155], but further discussion on this topic will be omitted in this context.

All four metal complexes display distinct irreversible reductive peaks with initial onsets below 2.2 V, which are observed exclusively in the first cycle (Fig. 5.4 and Fig. 5.5a). Significantly, the peaks exhibit a sequential shift in potential according to the elemental order: ZnDEPP and CuDEPP at 1.12 V, NiDEPP at 1.35 V, and CoDEPP at 1.61 and 1.20 V. If the addition of electrons were limited to the π -ring system, minimal variations in the potential would be anticipated. Therefore, these irreversible peaks likely originate from subsequent reductions taking place in the central metal rather than the π -ring system. Certainly, the involvement of metal

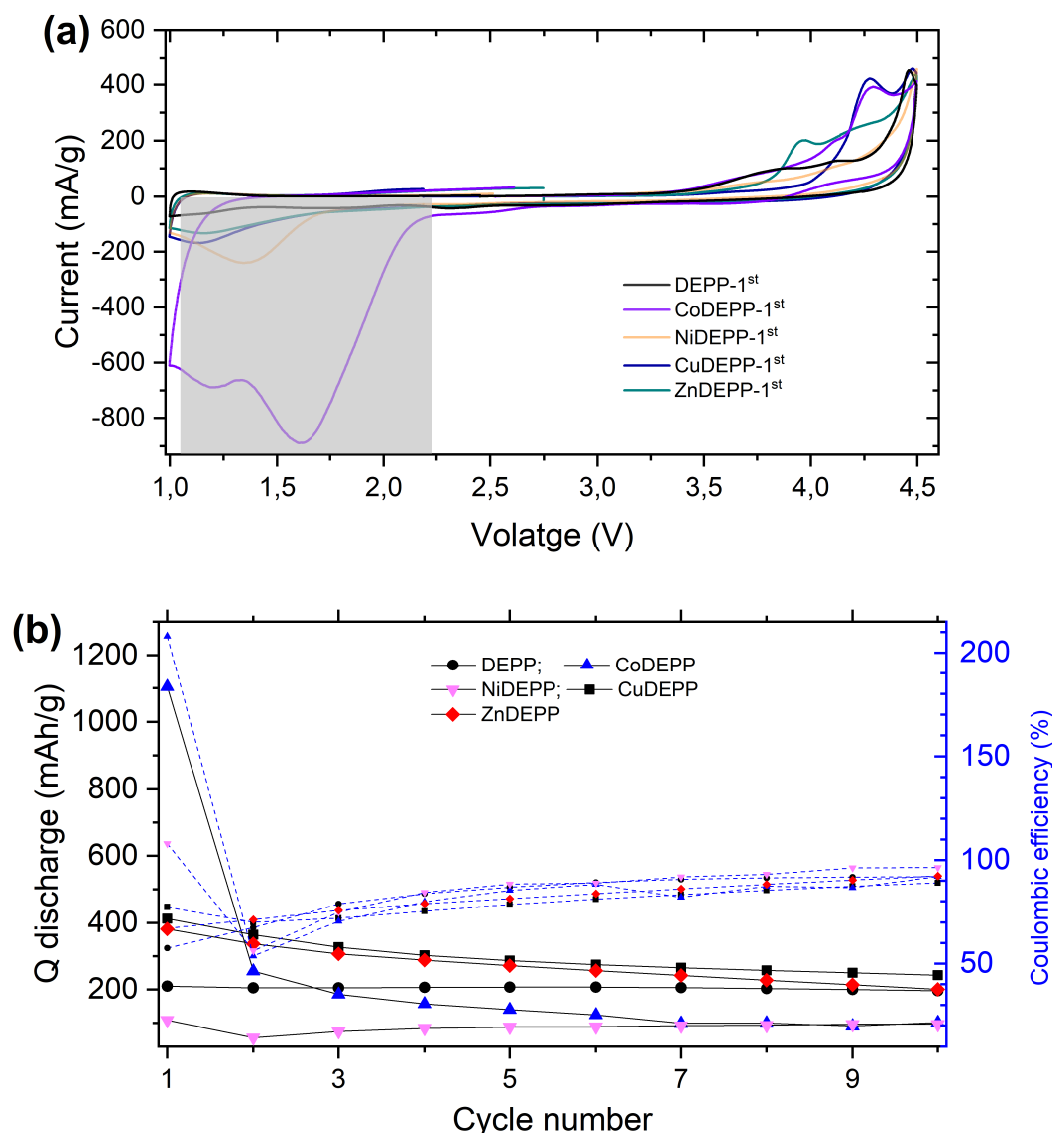


Figure 5.5: Comparison of the electrochemical properties of the xDEPPs electrodes: (a) the first CV curves obtained at 0.1 mV s^{-1} and (b) discharge capacity and CE of xDEPPs in the initial 10 cycles based on the CV measurement in the potential range of 1-4.5 V (Fig. 5.4b-e).

centers in electron uptake has been experimentally verified in Co(II)-porphyrin[174], Ni(II) complexes[175], and Cu(II)-porphyrin.[148] The location and intensity of the peaks observed in CoDEPP significantly differ from those observed in other metal porphyrins (Fig. 5.5a). Furthermore, the Co complex exhibits noticeable capacity degradation during the initial 10 cycles (see Fig. 5.5b). The DFT calculations indicate that the unoccupied orbitals of CoDEPP have a higher metal character compared to the other metal porphyrins (Table 5.2). Additionally, the presence of two distinct peaks in the cyclic voltammogram of CoDEPP indicates a difference in the nature of the reduction process compared to other metal porphyrins. This observation suggests that the successive electron is also being added to the central metal in CoDEPP. This

preference for electron uptake by a Co(II) metal center has been reported in other Co(II)-porphyrin complexes as well.[174, 176] To gain deeper insights into the inherent characteristics of the materials, a detailed investigation was conducted by cycling the cells at a constant current of 100 mA g^{-1} between the voltage limits of 4.5 and 2.2 V. This cycling protocol allowed for a comprehensive evaluation of the electrochemical performance, providing valuable information about the intrinsic properties of the materials (Fig. 5.6).

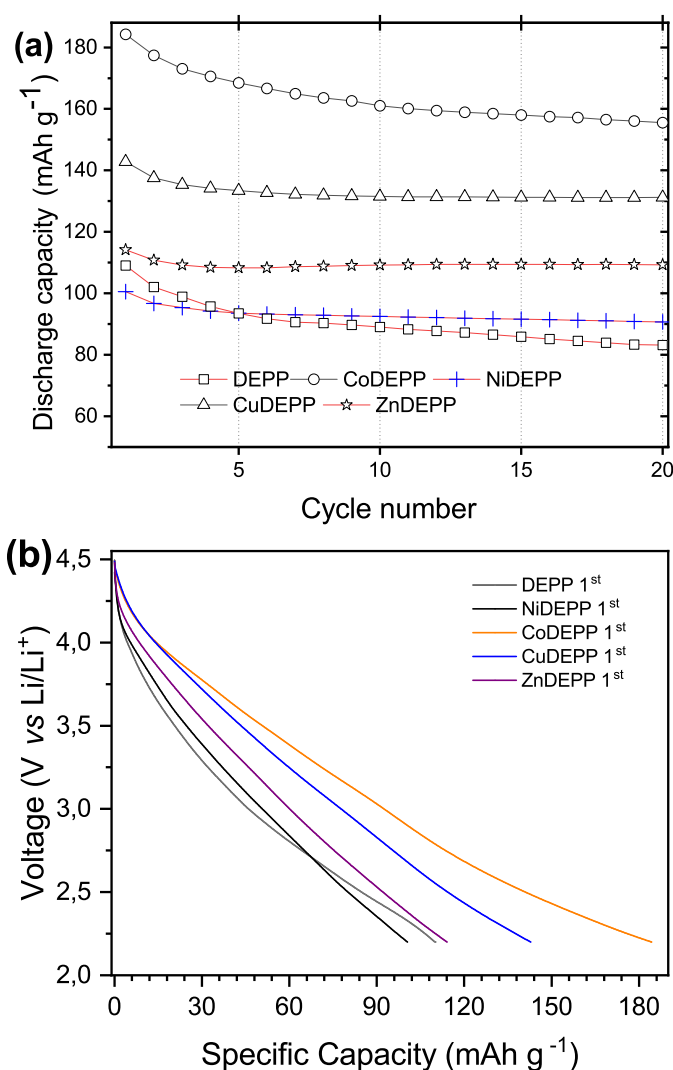


Figure 5.6: Cycling performance (a) and first discharge curves (b) of xDEPPs at 100 mA g^{-1} in the potential range of 2.2-4.5 V.

Following the initial charging process, a noticeable improvement in the reversibility of the discharge-charge behaviors was observed. The coulombic efficiency also exhibited a gradual increase during the initial cycles and remained consistently around 90% for the subsequent 10 cycles across all xDEPPs. The discharge capacity of the xDEPP

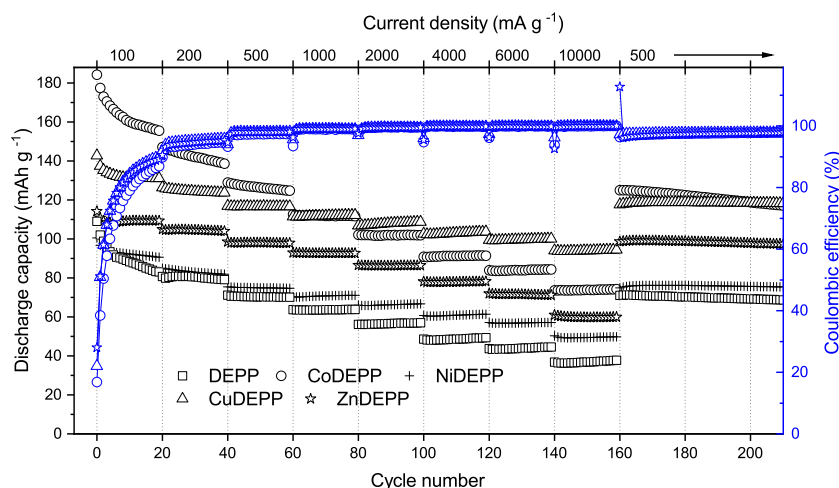


Figure 5.7: The rate capability of xDEPP electrodes with an increase in the charge-discharge rate from 100 mA g⁻¹ to 10 A g⁻¹ and then a decrease to 500 mA g⁻¹.

electrodes follows a specific order, with CoDEPP exhibiting the highest capacity, followed by CuDEPP, ZnDEPP, DEPP, and NiDEPP. The first discharge capacities for these electrodes are 184, 143, 114, 109, and 101 mAh g⁻¹. These capacities correspond to specific energy densities of 565, 446, 356, 327, and 307 Wh kg⁻¹ for the electrodes containing Co, Cu, Zn, metal-free, and Ni complexes, respectively. The absence of distinct voltage plateaus in the discharge profiles (Fig. 5.6b) indicates the occurrence of fast pseudocapacitive redox reactions. The gradual discharge profiles can be attributed to a combination of double-layer capacitance and multiple redox reactions,[177] which is commonly observed in other organic electrodes.[133, 177–179] The comparatively lower capacity of NiDEPP may be attributed to the fact that the Ni²⁺ ion is relatively smaller and does not fit perfectly into the square planar cavity formed by the four pyrrole nitrogen atoms. In contrast, Co²⁺, Cu²⁺, and Zn²⁺ ions have similar ionic radii (ionic radii Co²⁺ (88.5 pm) \cong Cu²⁺ (87 pm) \cong Zn²⁺ (88 pm) $>$ Ni²⁺ (83 pm))[180], which allows for more efficient intermolecular interactions. The imperfect fit of Ni²⁺ in the cavity can lead to weaker interactions and higher solubility of NiDEPP in the electrolyte solution (Tab. 5.3). It is worth noting that Ni²⁺ ions fit precisely into the smaller cavity of certain tetrapyrrolic macrocycles, such as norcorrole.[181] This favorable fit prevents undesired solubility issues and leads to a significantly improved reversible capacity for the Ni complex.[133] In the second cycle, the discharge capacity of CuDEPP reaches 138 mAh g⁻¹, which is close to the theoretical value of 140 mAh g⁻¹ expected for the three-electron reaction [CuDEPP]

$\rightleftharpoons [\text{CuDEPP}]^{2+}$. This suggests that the majority of the added capacity in CuDEPP can be attributed to this specific redox process. On the other hand, in CoDEPP, an additional one-electron redox process is observed, contributing to an extra capacity of approximately 45 mAh g^{-1} . X-ray photoelectron spectroscopy was employed to investigate the redox activity of the central atoms. In the case of CuDEPP, the XPS measurements revealed that there was no change in the Cu oxidation state (+II) when transitioning from the pristine to the charged state. However, during discharge, a reduction from Cu^{2+} to Cu^+ was observed in a portion of the Cu center atoms (Fig. 5.8d-f). Earlier studies have reported the formation of mixed-valence metal-porphyrins[182, 183] and the presence of $\text{Cu}^{2+}/\text{Cu}^+$ species in Cu-porphyrins during the redox process[148, 184]. X-ray photoelectron spectroscopy (XPS) measurements revealed that in the case of CoDEPP, there was no evidence of a change in the oxidation state of Co (which remained at +II) during the cycling process (Fig. 5.8a-c). Despite the theoretical potential for the oxidation of Co^{2+} to Co^{3+} to contribute an additional capacity of 47 mAh g^{-1} , the XPS results indicated that metal redox activity was not involved.

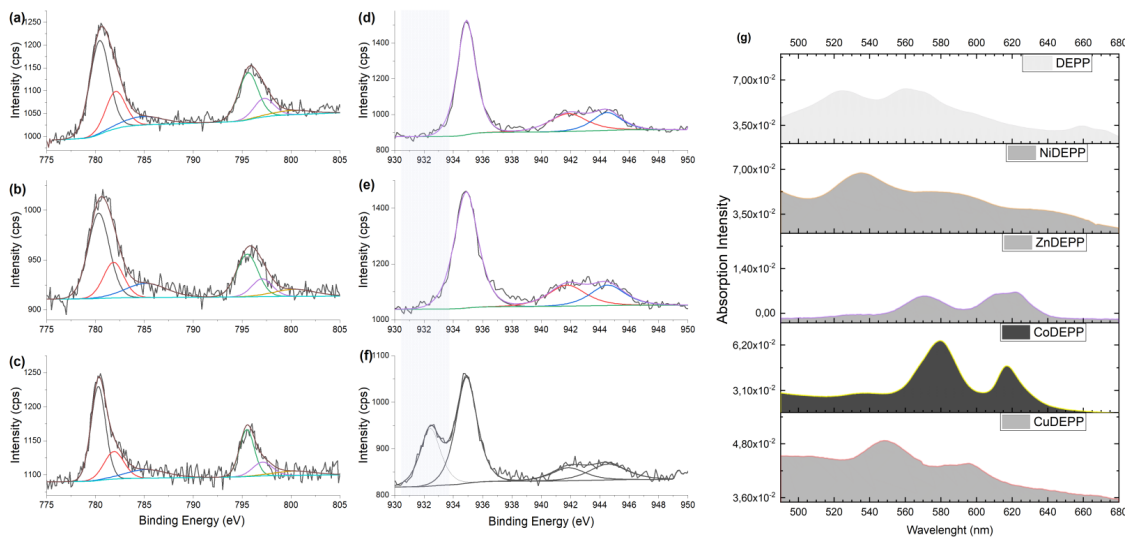


Figure 5.8: XPS measurements in the Co 2p region for CoDEPP (a, b, c) and the Cu 2p region for CuDEPP (d, e, f) electrodes at OCV (a, d), charged (b, e), and discharge (c, f) states. UV-Vis absorption spectra of xDEPPs in the Q-band region between 480-680 nm (g).

The observations suggest that in the Co-complex, the third electron is also extracted from the aromatic ligand, leading to the formation of $[\text{Co}(+\text{II})\text{DEPP}]^{3+}$. This viewpoint is further supported by our theoretical investigation of the frontier orbitals, which reveals the smallest energy difference between the HOMO and the HOMO+1

orbital for CoDEPP compared to other xDEPPs (Fig. 5.9c).

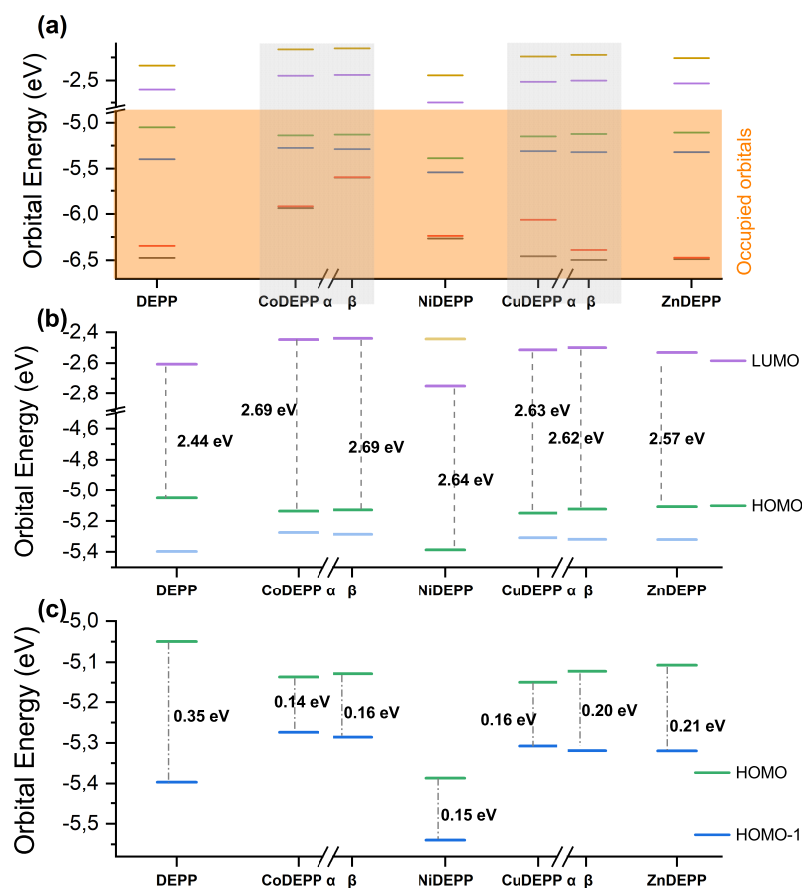


Figure 5.9: Calculated frontier molecular energies in DEPP and its metal complexes (xDEPPs) (a) and (b) HOMO-LUMO and (c) HOMO-HOMO-1 energy gap of xDEPPs.

The results of rate performance tests for electrodes containing different xDEPPs, as shown in Fig. 5.10, highlight several interesting findings. Firstly, the presence of metal ions noticeably improves both the discharge capacity and rate capability of DEPP compared to the metal-free counterpart, across a range of rates from 0.1 to 10 A g⁻¹. Typically, specific metal centers can actively participate in the redox processes, while the unpaired electrons in certain metals or oxidation states can also act as catalysts for ion insertion and extraction.[185, 186] This phenomenon contributes to additional capacity, enhances redox stability, and facilitates the overall redox reactions. At lower current rates (up to 1000 mA g⁻¹, region I), the discharge capacities of the xDEPP electrodes exhibit a clear trend, with CoDEPP > CuDEPP > ZnDEPP > NiDEPP > DEPP. However, at higher current rates (from 22 to 10 A g⁻¹, region II), CuDEPP demon-

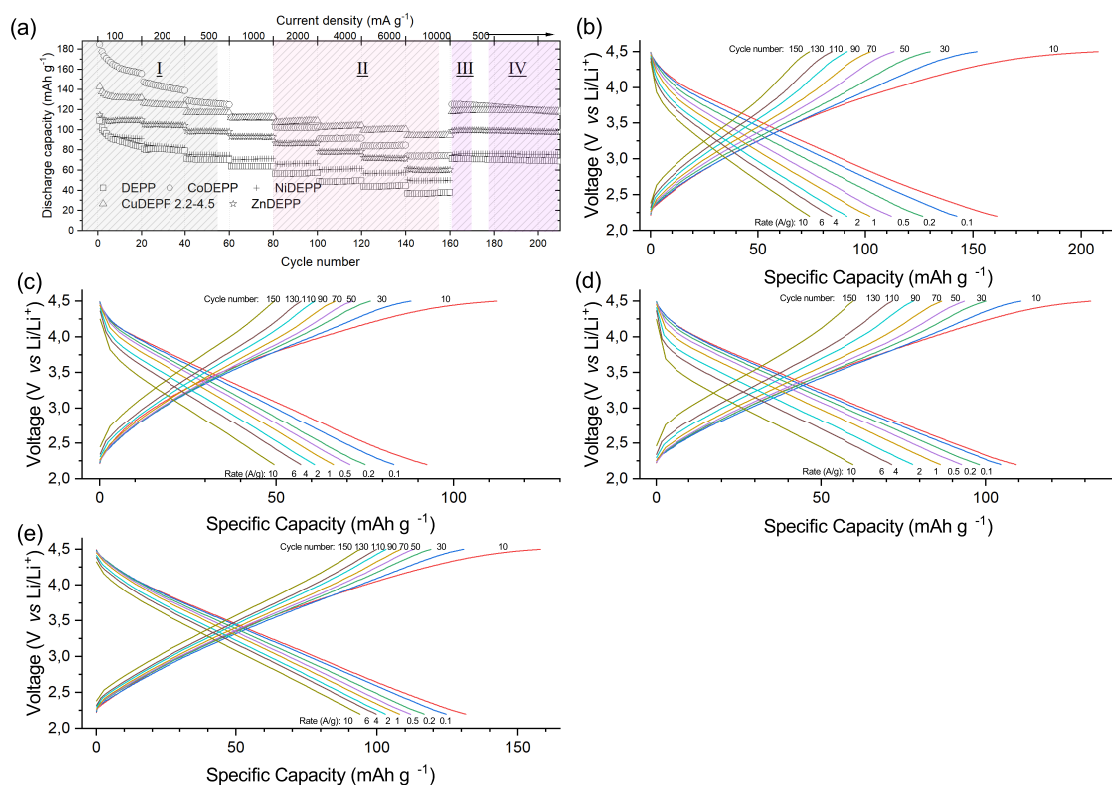


Figure 5.10: Rate performance of the xDEPPs (a) and selected voltage profile of CoDEPP (b), NiDEPP (c), ZnDEPP (d), and CuDEPP (e) at various current densities from 0.1 to 10 A g⁻¹ in the potential range of 2.2-4.5 V.

strates the highest discharge capacity. The rate capability factor, calculated as the discharge capacity at 10 A g⁻¹ divided by the value at 1 A g⁻¹, is 71.9, 54.9, 54.0, 46.3, and 41.6% for CuDEPP, ZnDEPP, NiDEPP, CoDEPP, and DEPP, respectively. Importantly, the original capacities at a rate of 500 mA h g⁻¹ were fully restored after operation at higher rates (region III). The rate capabilities of the electrodes differ significantly based on the central metal in the xDEPP complexes. Typically, the rate capability is improved by promoting ion diffusion and enhancing electronic conductivity in composite electrodes. While the type of central metal and the nature of π -bond conjugation and stacking can potentially affect the electrical conductivity of porphyrins[187], the presence of a large amount of conductive carbon in the electrode mitigates the influence of the central metal on the overall electrical conductivity of the electrode. The variation in rate capability among the different xDEPP complexes is likely to be attributed to differences in their bulk structures. This is supported by the SEM and powder XRD results, which indicate that the Cu and Zn porphyrins, exhibiting higher rate capability, possess a more crystalline structure (Fig. 5.11 and Fig. 5.16e). In contrast, NiDEPP and CoDEPP were found to be predominantly

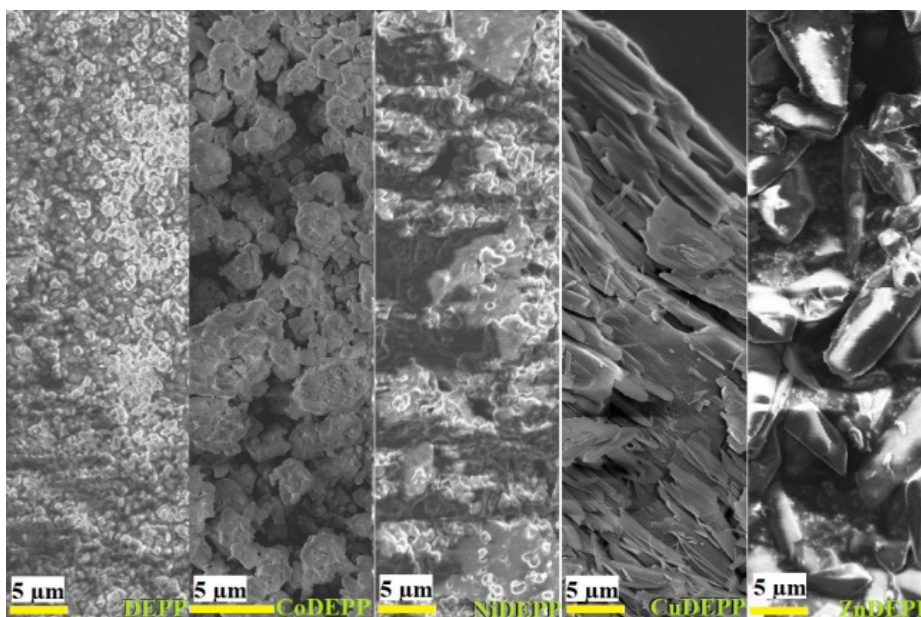


Figure 5.11: SEM images of the different xDEPP electrode materials that have been used in this chapter.

amorphous. Comparing the powder XRD patterns of the investigated xDEPP materials, it becomes evident that only ZnDEPP and CuDEPP exhibit a highly crystalline nature (Fig. 5.16), further supporting the correlation between crystallinity and rate capability. The morphological features of the xDEPP electrodes were observed to remain consistent even after extended cycling, as depicted in Fig. 5.12. CuDEPP exhibited a uniform needle-like morphology, with needle lengths reaching a few tens of micrometers. On the other hand, ZnDEPP displayed a distinct morphology characterized by crystallites of 5-10 μm in size, which aggregated with a random orientation. This random orientation of the crystallites in ZnDEPP electrodes may contribute to a less preferred orientation overall.

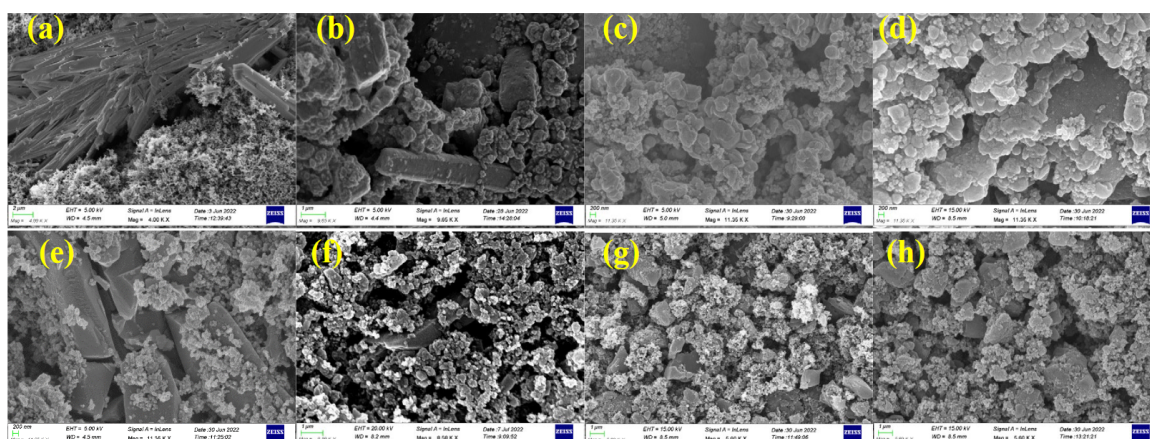


Figure 5.12: Morphology of the as prepared metal DEPP electrodes (a, c, e, g), and after 100 cycles (b, d, f, h) for CuDEPP (a, b), CoDEPP (c, d), ZnDEPP (e, f), and NiDEPP (g, h).

The level of molecular ordering and packing in tetrapyrrolic macrocycles (TPMs) can have a significant influence on their solid-state properties, including charge transport characteristics.[188, 189] DFT calculations showed that the molecular geometry of the xDEPPs is notably influenced by the nature of the metal. While the majority of xDEPPs exhibit a nearly planar structure in their optimized geometries, NiDEPP and CoDEPP exhibit saddling distortions (Fig. 5.13). These diverse geometries lead

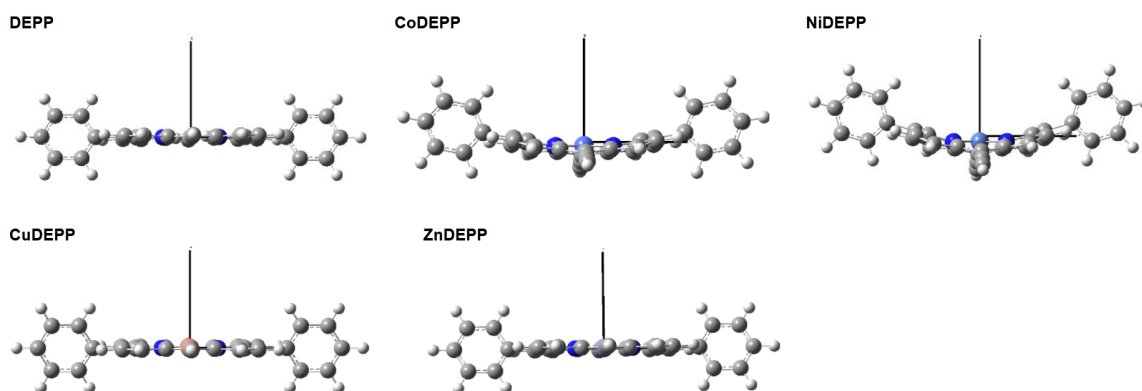


Figure 5.13: The DFT-optimized structures of xDEPPs showing saddled distortion for NiDEPP and CoDEPP.

to changes in the conjugation pathway, thereby impacting the UV-Vis absorption spectrum of the xDEPPs.[190–192] The UV-Vis spectrum of DEPP (Fig. 5.14) exhibits a prominent Soret band ($S_0 \rightarrow S_2$ transition) and four weaker Q-band transitions ($S_0 \rightarrow S_1$). With the introduction of the central metal, the Soret band is minimally affected, while the wavelengths and intensities of the Q-bands are significantly influenced. In general, the coordination of metals to porphyrins leads to a reduction in the number of Q-bands due to the increased symmetry of the resulting metalloporphyrin complex. Additionally, the distortion in the structure of metalloporphyrins is expected to cause a redshift in their spectra.[193–197] By examining Fig. 5.8g, it can be observed that the incorporation of Ni into DEPP induces nonplanar distortions, resulting in slight redshifts in the electronic spectra of NiDEPP. Specifically, the redshift is more pronounced in the Q-bands, with a shift of over 10 nm. The introduction of Co into the porphyrin framework resulted in a notable redshift of the main Q-bands. In DEPP, these bands were initially observed around 525 and 560 nm, while in CoDEPP, they shifted to approximately 580 and 620 nm. Additionally, there was an increase in the relative absorption intensity of these bands in CoDEPP. The obtained results are highly consistent with the predictions from DFT calculations.

It is well-established that non-planarity tends to enhance the solubility of condensed aromatic systems.[198, 199] This observation provides a possible explanation for the noticeable decrease in discharge capacity observed in the Co and Ni complexes during the initial cycles, as it is likely attributed to the progressively increased solubility (as indicated in Fig. 5.3, Table 5.1) of these complexes.

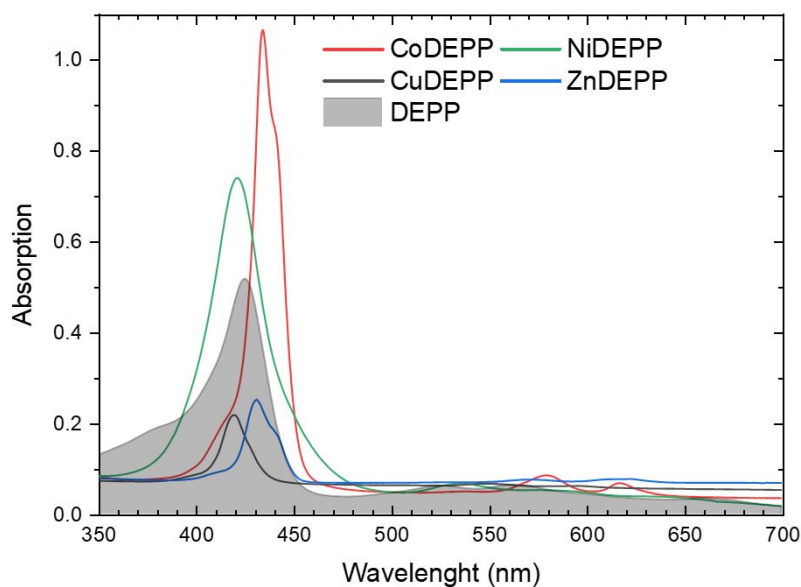


Figure 5.14: UV-Vis absorption spectra of DEPP and xDEPPs in DCM.

The molecular structure of CoDEPP-TMS was determined through single crystal X-ray diffraction, as shown in Fig. 5.15. This structure was then compared to the previously reported structure of the TMS-protected Cu complex (CuDEPP-TMS).[148] Molecular structure of the protected complexes obtained from single crystal XRD show that the core porphyrin structure and packing remain largely unchanged. These structures are consistent with the DFT-optimized structures of CoDEPP and CuDEPP, as depicted in Fig. 5.13. CuDEPP exhibits crystallization in the triclinic space group $P\bar{1}$, with a single molecule present in the unit cell ($Z = 1$). The cell dimensions are $a = 6.068$, $b = 11.958$, $c = 12.765$, and the angles are $\alpha = 79.1^\circ$, $\beta = 81.1^\circ$, and $\gamma = 84.9^\circ$. [148] In the crystal structure, the CuDEPP molecules within a layer exhibit partial tilting, resulting in non-overlapping molecular planes. Within the same layer, a Cu atom from one molecule is positioned adjacent to two ethynyl groups on neighboring molecules. Furthermore, the stacking of layers in the crystal structure is arranged in a manner where the aromatic porphyrin cores do not directly align with each other. Additionally, the phenyl rings maintain a twisted conformation relative

to the porphyrin core plane.

The crystal structure of CoDEPP was determined to be in the triclinic space group $P\bar{1}$, with a unit cell containing two molecules ($Z = 2$). The cell dimensions were measured as follows: $a = 9.368$, $b = 14.055$, $c = 15.002$, with angles $\alpha = 66.8^\circ$, $\beta = 82.4^\circ$, and $\gamma = 79.8^\circ$. Unlike the Cu-complex, the porphyrin core in CoDEPP-TMS exhibits a saddled geometry instead of being planar. It has N-Co-N angles of 173.3° and -173.3° , deviating from the angle of 180° observed in CuDEPP-TMS. The Co-complex exhibits torsion angles between the N atoms and pyrrole Cs exceeding 3° , whereas the Cu-complex has torsion angles of less than 1.5° . Furthermore, noticeable variations in torsion angles are observed between the plane formed by the pyrrole rings and the plane of the *meso*-substituted phenyl groups (Fig. 5.15).

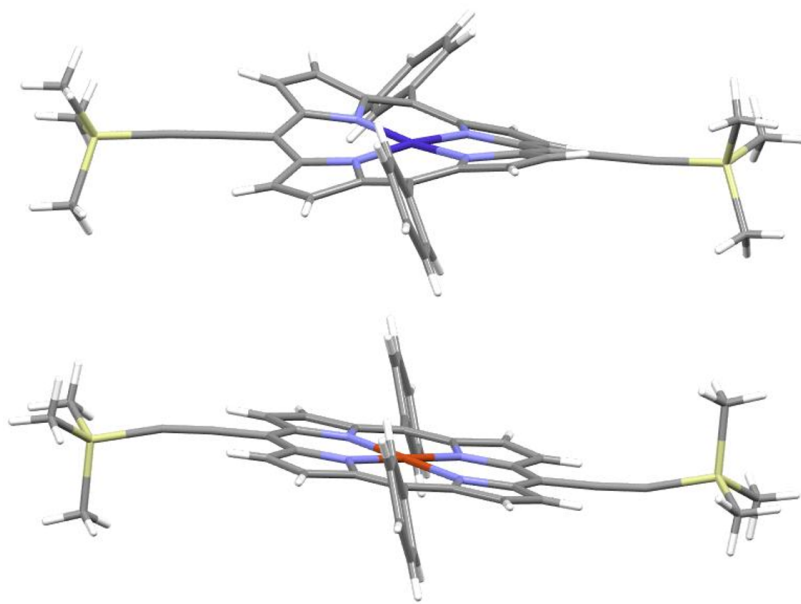


Figure 5.15: Comparison between the molecular structures of CoDEPP-TMS (top) and CuDEPP-TMS[148] (bottom). The structures were from single crystal XRD studies discussed in the text.

In CuDEPP, the dihedral angle between the aryl group and the porphyrin plane is approximately 69° , allowing for effective packing due to the coplanarity of the aryl groups. However, in CoDEPP, the π -system is significantly saddled, resulting in non-coplanar phenyl rings with dihedral angles of 75° and 57° , unlike the coplanar arrangement observed in CuDEPP. The arrangement of metal porphyrin layers in CuDEPP promotes a substantial increase in π -electron overlap, resulting in a reduction of the HOMO-LUMO gap. Specifically, the bandgap of a single CuDEPP molecule is measured at 2.51 eV, but this value decreases to 2.3 eV when three molecules are stacked together. This suggests that the stacking of CuDEPP molecules enhances electronic

delocalization and leads to a narrower bandgap.

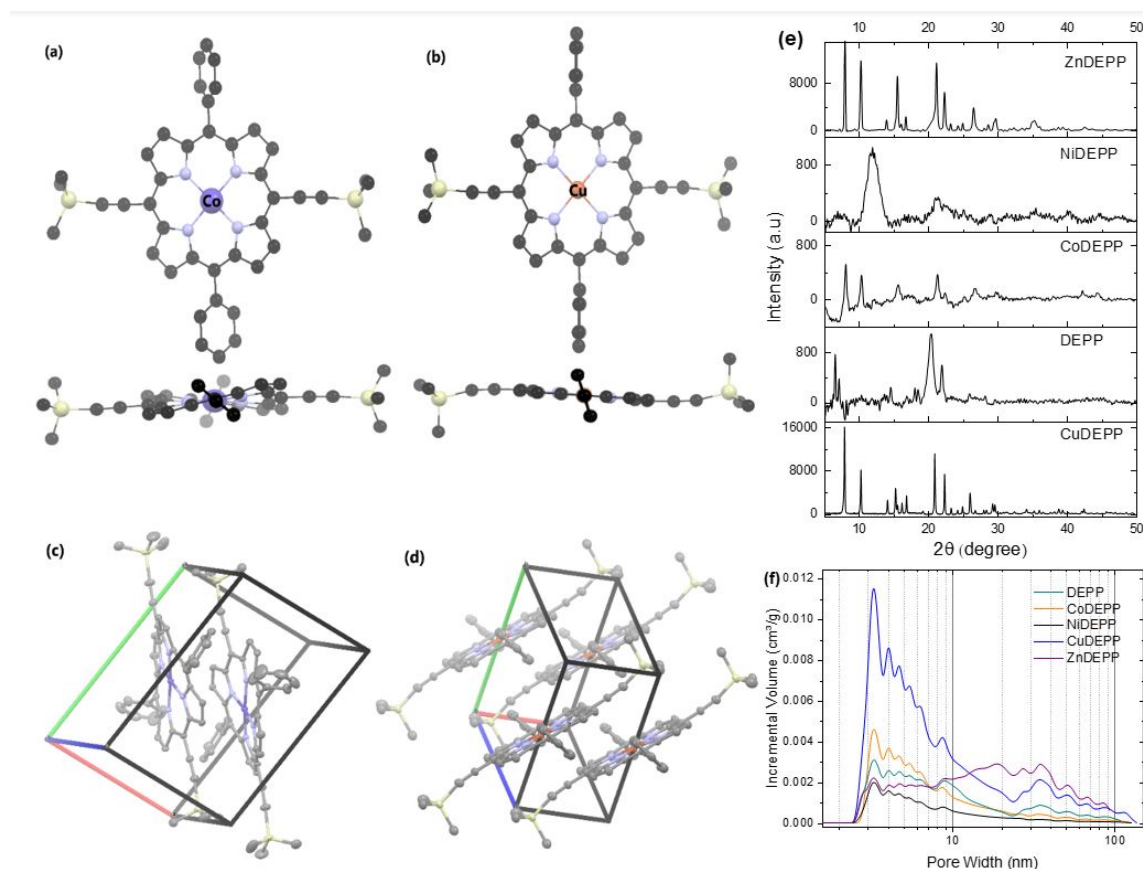


Figure 5.16: Crystal structures of CoDEPP-TMS and CuDEPP-TMS showing the top and side views of (a) ruffled Co-porphyrin and (b) planar Cu-porphyrin, and the packing of (c) Co-complex and (d) Cu-complex. Images were generated from CCDC Nos. 1506859[148] and 2143452. Powder XRD patterns (e) and pore size distribution curves (f) of the xDEPP active materials used in this study.

Electrochemical impedance spectroscopy (EIS) was employed to delve deeper into the electrochemical characteristics of the xDEPPs (Fig. 5.18a, see also Fig. 5.17). The obtained data were analyzed using an equivalent circuit (Fig. 5.17 and Table 5.4), where different elements were assigned to specific electrical parameters. In this circuit, R_s corresponds to the internal resistance of the cell, R_{ct} represents the charge transfer resistance associated with electron and ion movement, CPE is attributed to the constant phase element, and W_o represents the Warburg impedance, which signifies the ion diffusion within the electrode. Fig. 5.18a provides an enlarged view of the high-frequency region of Fig. 5.17. The fitted results indicate that the charge transfer resistance (R_{ct}) values for CuDEPP, NiDEPP, DEPP, CoDEPP, and ZnDEPP are determined to be 90.6 Ω , 167.4 Ω , 361.9 Ω , 452.4 Ω , and 608.1 Ω , respectively. The obtained data provide an explanation for the enhanced rate performance observed in the CuDEPP electrode. Interestingly, after 10 cycles, there is a significant reduction

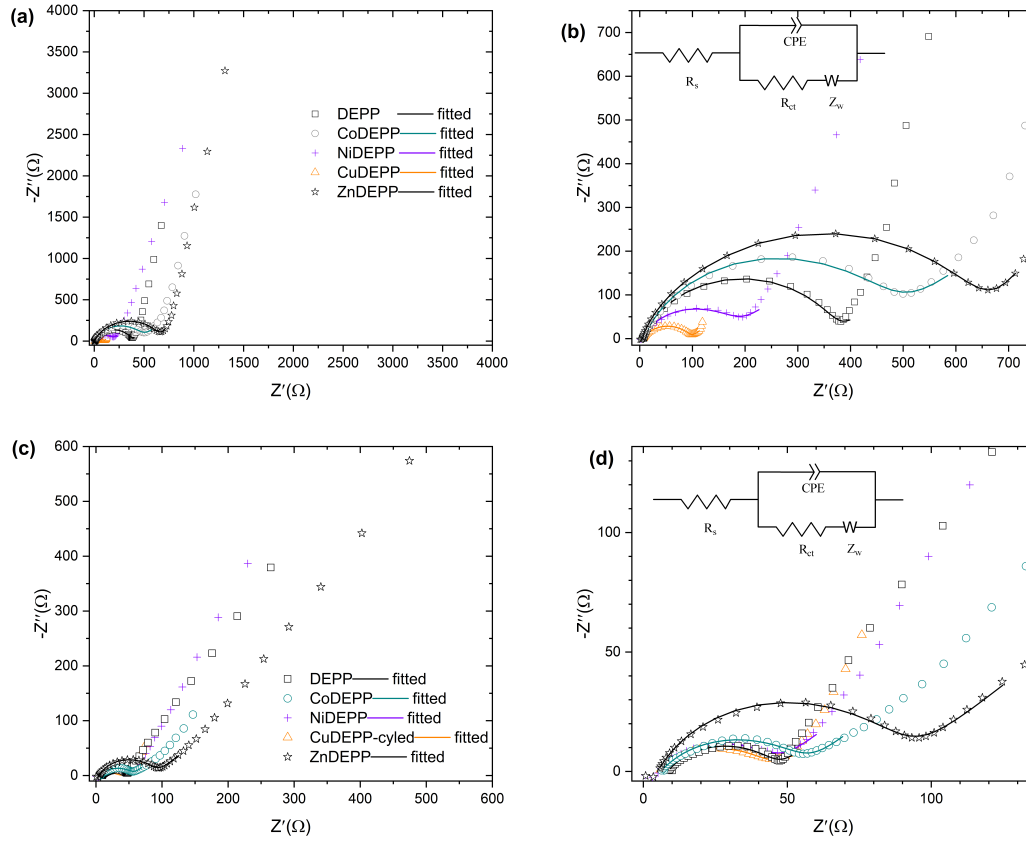


Figure 5.17: EIS of the xDEPP electrodes before (a) and after cycling at 100 mAh g^{-1} (c) with enlarged part of the high frequency region (b, d) and the equivalent circuit model (inset).

in the charge transfer resistance (R_{ct}) values for the xDEPPs, resulting in R_{ct} values of $38.6 \text{ } \Omega$, $42.0 \text{ } \Omega$, $38.6 \text{ } \Omega$, $51.3 \text{ } \Omega$, and $86.3 \text{ } \Omega$ for CuDEPP, NiDEPP, DEPP, CoDEPP, and ZnDEPP, respectively.

Table 5.4: EIS analyses results of the cell based on the xDEPP cathodes (fresh cell and after 10 cycles).

	R_s (Ω)		R_{ct} (Ω)		σ ($\Omega \text{ s}^{1/2}$)	
	Fresh cell	Cycled cell	Fresh cell	Cycled cell	Fresh Cell	cycled Cell
DEPP	7.0	8.5	361.9	38.5	235.9	58.3
CoDEPP	6.3	6.1	452.4	51.3	626.9	65.5
NiDEPP	4.3	5.1	167.4	42.0	501.2	85.4
CuDEPP	6.2	5.8	90.6	38.6	24.9	21.4
ZnDEPP	5.4	5.2	608.1	86.3	694.0	201.8

These results indicate that the charge transfer process and kinetics of all xDEPPs are improved after the initial conditioning cycles, facilitating charge transfer.[153] Subsequent analyses have demonstrated that the ion diffusion coefficient of CuDEPP is significantly higher, by 2-3 orders of magnitude, compared to other xDEPPs (Fig.

5.18c). Typically, the kinetics of lithium-ion diffusion are associated with the porosity and specific surface area, as greater contact areas between the active material and electrolyte create more pathways for ion diffusion.[200]

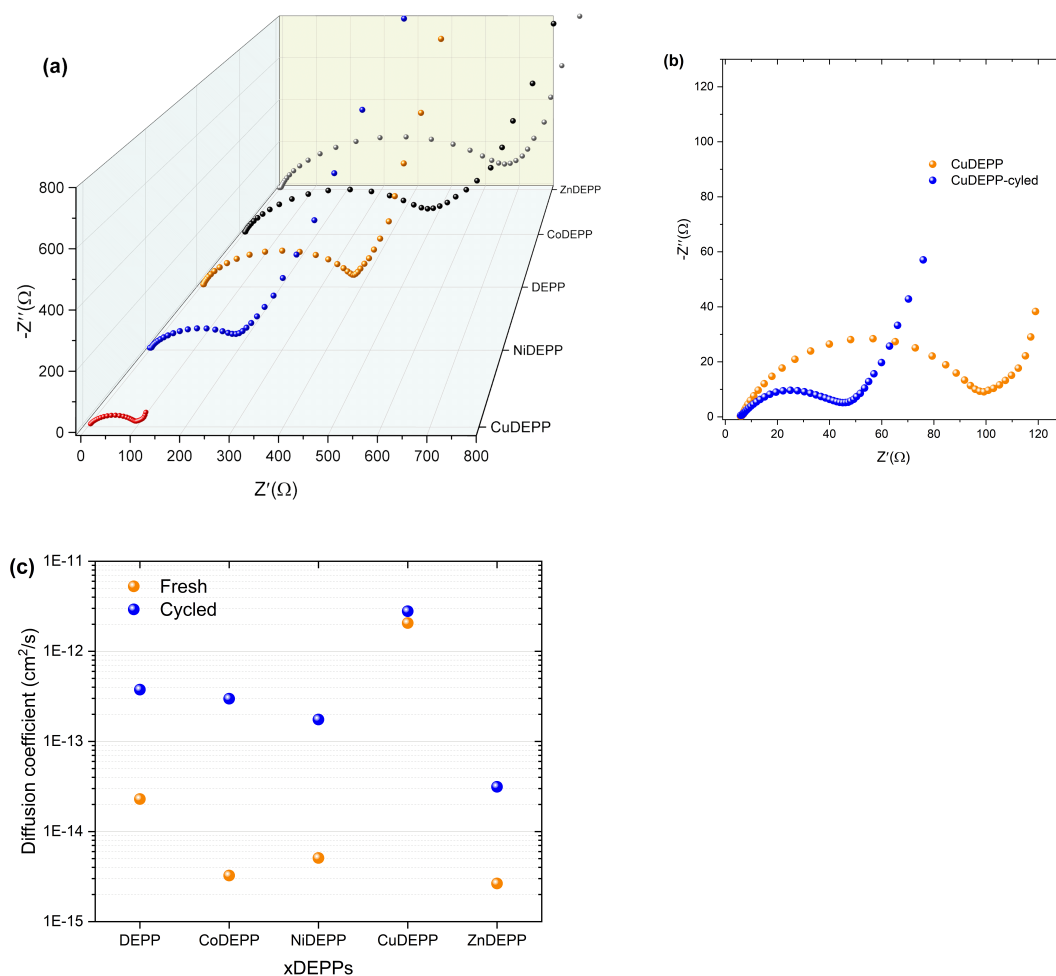


Figure 5.18: Comparison of Nyquist plots of xDEPP electrodes before cycling (a) and CuDEPP electrodes in fresh cells before cycling and after the 10th cycle (b). Estimated diffusion coefficient in fresh and cycled xDEPPs determined by EIS (c). (The equivalent circuit model and fitting results are shown in Fig. 5.17 and Table 5.4).

The surface area of the xDEPPs was assessed using N₂ adsorption-desorption isotherm experiments (Fig. 5.19). Notably, CuDEPP demonstrated a significantly larger overall surface area compared to the other xDEPPs. Furthermore, the pore size distribution curves (Fig. 5.16f) indicated that CuDEPP exhibited a greater pore volume for pores larger than a few nanometers in size. The presence of these large pores is advantageous for facilitating rapid redox reactions and promoting efficient mass transport of the electrolyte.[201] CuDEPP exhibited a significant proportion of pores within the range of 1.5 ~ 3 nm, which is well-suited for the insertion of anions and matches the size of solvated PF₆⁻ ions.[202] This favorable pore size distribution is believed to

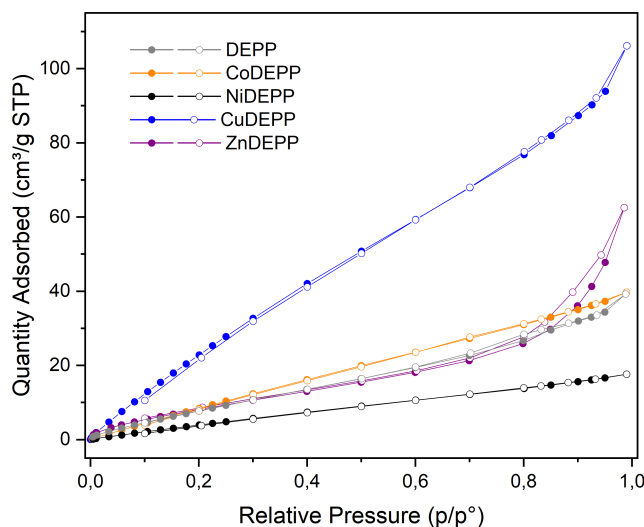


Figure 5.19: Nitrogen adsorption-desorption isotherms of the xDEPP active materials.

contribute to the exceptional rate capability of CuDEPP, allowing it to retain 72% of its capacity even at a high current density of 10 A g^{-1} . CuDEPP and CoDEPP both exhibit triclinic crystal structures and form layered arrangements, creating two-dimensional diffusion pathways that are perpendicular to the planes of the coplanar π -stacked porphyrin cores. In contrast, the ring system of CuDEPP maintains a nearly perfect planar conformation, whereas CoDEPP exhibits a saddled geometry. Additionally, CuDEPP molecules display reduced π -overlap, as indicated by larger distances between Cu atoms within the same stack ($d(\text{Cu}\dots\text{Cu}) = 6.069(1) \text{ \AA}$), compared to the distances between Co atoms ($d(\text{Co}\dots\text{Co}) = 5.436 \text{ \AA}$ and $5.272(1) \text{ \AA}$). The flatter π -stacking arrangement in CuDEPP results in reduced steric hindrance between the *meso*-phenyl rings of neighboring molecules. This creates more vacant spaces between the stacked π -systems and contributes to the formation of a distinct pore structure in CuDEPP (Fig. 5.20). These empty spaces potentially facilitate the insertion and extraction of ions within the material.

Thermogravimetric analysis and differential scanning calorimetry (TGA-DSC) were employed to investigate the thermal characteristics of xDEPPs. The findings revealed that the decomposition of DEPP begins at temperatures above $200 \text{ }^\circ\text{C}$, with a 5% weight loss occurring at approximately $270 \text{ }^\circ\text{C}$ ($T_{(5)}$) (Table 5.5). Additionally, no preceding phase transition was observed (Fig. 5.21). With the exception of the Ni complex, the insertion of the central metal significantly enhances the thermal stability

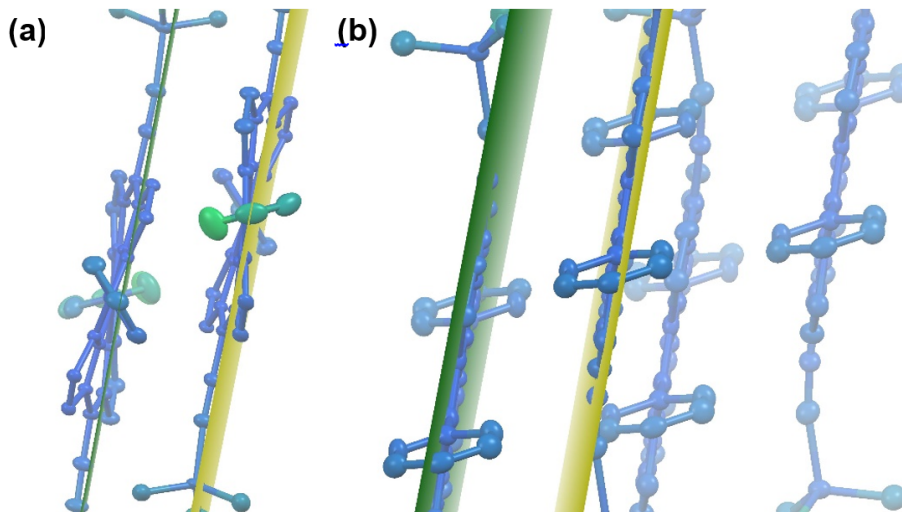


Figure 5.20: Molecular level stacking of CoDEPP (a) and CuDEPP (b).

of the xDEPPs, as evidenced by an increase in the $T_{(5)}$ value to above 400 °C (Table 5.5). Notably, both the Co and Cu complexes exhibited a weight retention of approximately 85% even at a high temperature of 800 °C. The exceptional thermal stability

Table 5.5: Thermal characterizations of xDEPPs with $T_{(5)}$ Temperature of 5% weight loss, $T_{(10)}$ temperature of 10% weight loss, and $W\%_{@800^{\circ}\text{C}}$ the percentage of solid residue after heating from room temperature to 800 °C under argon.

	$T_{(5)}$	$T_{(10)}$	$W\%_{@800^{\circ}\text{C}}$
DEPP	268	320	56
CoDEPP	398	706	85
NiDEPP	244	277	64
CuDEPP	425	502	85
ZnDEPP	408	490	78

exhibited by the xDEPPs is an important characteristic that ensures the safe operation of the storage system, even under elevated temperature conditions. This property enables the potential utilization of the system at higher operating temperatures without compromising its safety.[203] The thermal stabilities demonstrated by the xDEPPs are comparable to, or even surpass, those of various other organic electrode materials, including anthraquinone[204, 205], terephthalate[206], phosphazene[207], and polyimide-based[208] materials. Moreover, TPMs serve as oxygen-free cathodes, eliminating the risk of oxygen gas evolution resulting from the decomposition of the active material. This sets them apart from commercial lithium-ion batteries that utilize cathode materials based on layered transition metal oxides, which are prone to oxygen gas evolution. In this context, the main safety concern lies in the exother-

mic decomposition of the cathode at high temperatures, which can lead to the rapid release of oxygen, subsequent temperature and pressure escalation, and potentially result in fire or explosion.[209] However, the oxygen-free structures of TPMs offer inherent thermal safety, as they eliminate the common pathway of battery thermal runaway associated with oxygen liberation.[210] Based on the TGA profiles shown in Fig. 5.21, both the Cu and Co complexes exhibit excellent stability up to 260 °C. In the case of the Cu complex, no gas release was observed before the initial degradation region, indicating a high level of stability (any minor gas release in the Co complex could be attributed to trace impurities). Mass spectrometry analysis of the evolved gases detected various general C_xH_y species (m/z : 15, 16, 24, 26, 28) during thermal decomposition. Additionally, hydrogen cyanide (HCN, m/z 27) was identified at temperatures of 275 °C (after a 2% weight loss in TGA) and 470 °C. The presence of hydrogen cyanide, a highly toxic gas, during the thermal decomposition of the material presents an additional risk. However, it is important to note that the nitrogen content, and consequently the concentration of HCN, is relatively small compared to the overall organic content of the battery. Furthermore, the decomposition temperature of the material (2% weight-loss at 275 °C for CuDEPP) is higher than the boiling point of electrolyte solvents such as propylene carbonate (242 °C). As a result, the risk associated with the decomposition of the active material is significantly lower compared to the risk posed by the decomposition of the general LIB electrolyte.

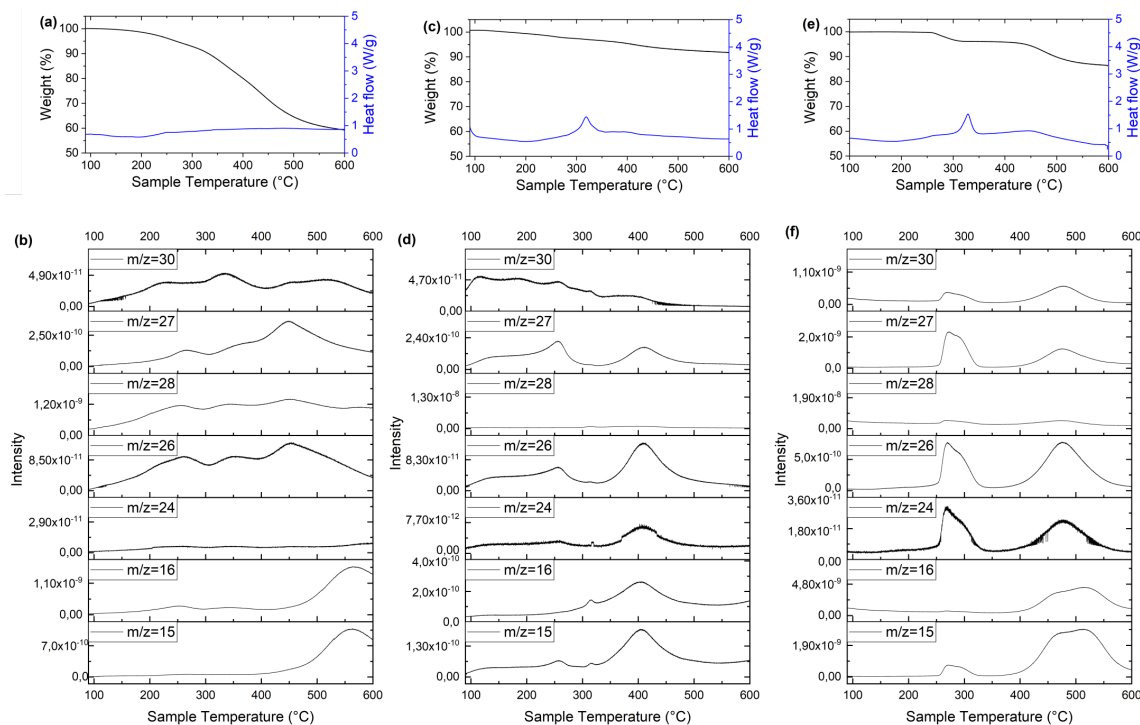


Figure 5.21: Thermogravimetric analysis TGA (black signals), differential scanning calorimetry DSC (blue signals) and mass spectrometry MS of selected DEPP, CoDEPP and CuDEPP. The TGA and DSC profiles (a, c, e) and analysis of the evolved gases (b, d, f) of DEPP, CoDEPP and CuDEPP, respectively.

5.4 Conclusion

In this research, porphyrins of the A2B2-type (DEPP) were synthesized and its corresponding metal complexes with first-row transition metals ranging from Co to Zn were obtained. A comparative analysis of the bulk structures and electrochemical properties of xDEPP revealed that the selection of the central metal atom has a dual effect: 1) It promotes noncovalent π - π interactions, ensuring stable battery operation, while also impacting the capacity and rate capability of the energy storage systems. This study presents a novel discovery where the choice of the central metal atom leads to additional redox reactions within the π -ring system. This finding paves the way for the development of high-capacity cathodes in advanced lithium- and post-lithium-ion storage systems, offering new possibilities for future designs. 2) It appears that the ion diffusion coefficient observed in xDEPPs can be attributed to a combination of porosity and specific surface area, while the rate capability is influenced by the crystallinity of the material. Consequently, effective control of these factors holds significant potential for enhancing the performance of TPM electrodes in targeted applications. We anticipate significant advancements in the optimization of metal-TPMs

by exploring various central metal atoms and modifying their size and morphology. These modifications are expected to enhance structural stability, rate capability, and cycling stability of the materials.

Chapter 6

Morphological Aspects in Designing Organic Electrode Materials

6.1 Introduction

The investigation of the morphological design of active materials is a well-established approach to tailor the properties of electrode materials, as demonstrated before.[156, 211, 212] Morphological features profoundly impact in various aspects the performance of LIBs, including phenomena as lithium ion diffusion pathways, diffusion resistance, the active material's surface area, electrochemical performance, and energy density.[213] Key factors in evaluating encompass particle shape[214], particle size[215], and particle distribution.[216] Smaller particles generally contribute to enhanced rate performance due to shorter ion diffusion paths.[108] However, the higher surface area can promote increased side reactions.[217] Conversely, higher crystallinity is often associated with greater material density and improved cycling performance, though it can introduce more complex synthesis procedures. Particle size distribution, on the other hand, can lead to improved energy density and cycle performance, but it comes with challenges related to production consistency and electrode homogeneity.[218]

Exploration of morphological properties of organic materials has been relatively limited. In a recent study by Chen *et al.*[156], revealing how the morphology of [5,10,15,20-tetra(ethynyl)porphinato]copper(II) (CuTEP) can effectively modulate battery performance. This study underscores the potential of adjusting simple material properties

to achieve enhanced performance.

In this study, various synthetic routes are presented to control the morphology of [5,15-bis(ethynyl)-10,20-diphenylporphinato]cobalt(II) (CoDEPP). Diverse characterization techniques were employed to elucidate their influence on battery performance. Moreover, 3D reconstruction using Nano-Computed X-ray Tomography (nanoCT) was introduced to gain deeper insights into the porosity and pore volume of the CoDEPP-base architectures.

6.2 Electrochemical Experiments

6.2.1 Electrode Preparation

The CoDEPP electrodes were fabricated using a water-based slurry with a 34 wt% solid content. This process involved combining sodium carboxymethyl cellulose (CMC) and styrene-butadiene rubber (SBR) in a mass ratio of 3:2. To achieve the desired concentration, SBR was dispersed in distilled water and mixed for five minutes. The electrode slurries were prepared by blending CoDEPP (50 wt%), Super P (40 wt%), and binder (10%) in distilled water using a Thinky mixer. After stirring at 2000 rpm for 17 minutes, a uniform slurry was obtained. This slurry was then paint-casted with a fine brush onto a carbon-based gas diffusion layer (GDL) (GDL 29 AA Diffusionsmedien DIN A4 21x29cm from the company ion power). The GDL was coated from both sides, dried for 3 hours under atmospheric conditions, and the process was repeated 3-4 times until the target loading of ~ 1 mg active material was achieved. Subsequently, the coated material was dried overnight, punched into 11.8 mm discs, and further dried at 70 °C under vacuum conditions (1×10^{-3} mbar) for 15 hours. The active material loading ranged between 1 and 1.3 mg cm⁻².

The preparation of the electrodes for FIB-SEM Tomography and nanoCT is as follows: To prepare the electrode slurries, CoDEPP (50 wt%), Super P (40 wt%) and PVDF (10 wt%) binder were mixed in a mortar for 25 minutes using NMP as the solvent. The slurry was drop-cast onto the SS electrodes (11.8 mm diameter). The electrodes were subsequently dried on a heat plate for two hours, and then for an additional 15 hours under high vacuum (1×10^{-3} mbar) at 80 °C. The electrodes had a loading of 1-1.2 mg cm⁻² of active material.

6.2.2 Cell Assembly

Electrochemical tests were conducted using a CR2032-type coin cell (MTI, SS316). Once the electrodes and all other cell components were dried to eliminate water, they were moved to a glove box ($O_2/H_2O < 0.1$ ppm) for assembling the cell. To serve as the separator, two layers of glass fiber filter Whatmann GF/D were employed. The electrolyte utilized was a 1M solution of $LiPF_6$ in a mixture of ethylene carbonate (EC) and dimethyl carbonate (DMC) in a 1:1 volume ratio. Generally, 80 μ L of electrolyte was added to the cell. As the cathode electrode (GDL) was thinner, an additional SS disk was employed. In case of *post-mortem* analysis a polypropylene film (PP, Celgard 2400) was used as a separator, the electrolyte amount was reduced to 35 μ L. No additional SS disk was used when conducting FIB-SEM Tomography and nanoCT with the SS electrodes.

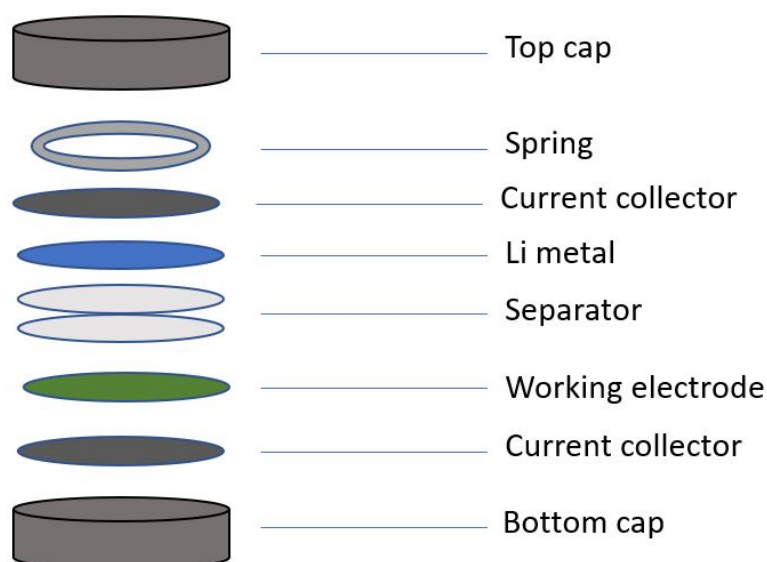


Figure 6.1: Coin cell assembly for half-cell measurements with GDL current collector.

6.2.3 Electrochemical Measurement

The galvanostatic cycling with potential limitation (GCPL) experiments were conducted at 298 K using the BCS-800 system from Biologic. For cyclic voltammetry (CV) measurements, the VMP-3 multichannel potentiostat from Biologic was utilized with a sweep rate set at 0.1 mV s^{-1} . The testing procedure always commenced with a three-hour recording of open circuit voltage (OCV). To analyze the charge transfer resistance and ionic diffusion characteristics of the CoDEPP cathodes, electrochemi-

cal impedance spectroscopy (EIS) was employed. EIS measurements were performed using the VMP-3 multichannel potentiostat from Biologic, over a frequency range of 1 MHz to 50 mHz. The spectra were fitted using RelaxIS software, and the ion diffusion coefficient was calculated using equation 5.1.

6.3 Results and Discussion

Porphyrinoids are an emerging category of electrode materials, as discussed in the previous chapters. Notably, CuDEPP[148] exhibited remarkable performance with self-conditioning during the initial charge process. This material possesses bipolar characteristics, allowing it to function as both anode and cathode, demonstrating high energy and power densities. While the influence of the central metal was studied (see chapter 5), it was observed that CoDEPP, in the first 60 cycles, exhibited higher specific capacity than CuDEPP at particularly low current densities of 0.1, 0.2, and 0.5 mA g⁻¹. At loading rates greater than 0.5 mA h g⁻¹, CuDEPP shows a higher specific capacity and exhibits a superior rate capability factor (discharge capacity at 10 A g⁻¹ divided by the value at 0.1 A g⁻¹). The initial capacities were 184 mA h g⁻¹ for CoDEPP and 143 mA h g⁻¹ for CuDEPP at a current density of 0.1 mA g⁻¹. [152] The objective of this study is to investigate whether the performance of CoDEPP can be tuned through morphological changes to achieve higher stability at higher current densities while retaining its superior initial performance. The primary focus here is to assess if the performance can be enhanced through morphological changes in the microstructure.

In this study, various synthetic approaches were explored to synthesize [5,15-bis(ethynyl)-10,20-diphenylporphyrinato]cobalt(II) (CoDEPP) with different morphologies (Fig. 6.2). Among them, four distinct morphologies were selected for further investigation as cathode materials in a half-cell against lithium metal. The materials underwent thorough characterization using cyclic voltammetry and galvanostatic cycling. EIS measurements were conducted to determine the diffusion coefficient, a relevant parameter of interest due to its impact on rate capability. [156] The four obtained microstructures exhibit different crystalline features, with one sample having a needle-shaped morphology, another resembling a flower, another appearing like coral-

shape, and the fourth sample exhibiting an amorphous popcorn-like shape.

The precursor for all reactions is [5,15-bis(trimethylsilanylethynyl)-10,20-diphenylporphinato]cobalt(II) (CoDEPP-TMS), and the microstructure tuning was achieved through the deprotection reaction by varying the temperature and the amount of water used in the reaction solution. Another significant factor affecting crystallization was the relationship between crystallization time and the removal of tetrahydrofuran. To deprotect CoDEPP-TMS, the precursor was dissolved in THF, and tetra-*n*-butylammonium fluoride (TBAF) was employed as the deprotection agent. In the case of the amor-

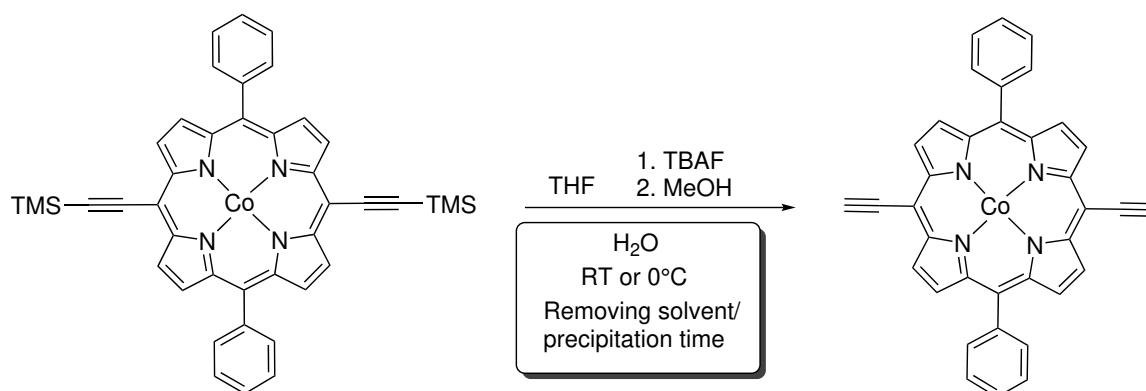


Figure 6.2: Deprotection reaction of CoDEPP-TMS, leading to the formation of CoDEPP. Different reaction conditions have been utilized to prepare CoDEPP with different morphologies.

phous sample, after a 3-hour reaction time, methanol was added in a ratio of 4:1 (THF:MeOH), and the THF was removed under reduced pressure, resulting in the fast precipitation of CoDEPP **12**. The most crystalline CoDEPP **14**, according to the intensity of the powder XRD pattern, was obtained after adding 1 mL of distilled water to the reaction. After a 30-minute reaction time, methanol was added in a ratio of 2:1 (THF:MeOH). The resulting mixture was left overnight, and the obtained precipitate was collected after filtration. The flower-shaped CoDEPP **13** was obtained through a more advanced procedure. First, as for **14**, 1 mL of distilled water was added, and after a 30-minute reaction time, half of the THF was removed under reduced pressure. Then, methanol was added dropwise as an antisolvent to cause a slow precipitation of CoDEPP, but no precipitate or turbidity could be seen. Subsequently, methanol was added in a higher ratio (1:3 - THF:MeOH), and the reaction was left for full two weeks to form the precipitate. The last CoDEPP **15**, which was investigated, appears amorphous in the SEM, though showing stronger peaks in the powder XRD as observed for **13**. **15** was obtained after cooling the reaction mixture to 0 °C and

adding 1 mL of distilled water. After 30 minutes, methanol was added in a ratio of 2:1 (THF:MeOH), and due to the absence of precipitate, half of the THF was then removed under reduced pressure. Some methanol was unavoidably removed due to the close boiling points of THF and methanol. The formed precipitate was collected after two days of precipitation time. Further attempts were made to obtain more variations in the morphology (Table 6.1), but due to the low yield in some attempts, full electrochemical characterization would be impossible. Therefore, we will provide only SEM images (Appendix) for comparison. The reaction conditions are shown in Table 6.1, see experimental section for the details..

Table 6.1: Different reaction attempts to tune the morphology of CoDEPP with * samples employed in this study.

Code	THF:MeOH	Temperature	H ₂ O	Shape
12*	4:1	RT	/	popcorn-shape; amorphous
13*	1:3	RT	1 mL	flower-shape; 2.5 μm
14*	2:1	RT	1 mL	needles; 2.5-6 μm
15*	2:1	0 $^{\circ}\text{C}$	1 mL	coral-shape
16	2:1	RT	/	amorph
17	2:1	RT	5 mL	needles; 1 μm
18	2:1	RT	/	a) flower-shape; 16 μm b) disks; 2-6 μm
19	2:1	0 $^{\circ}\text{C}$	/	a) flower-shape 20-30 μm b) amorphous

CoDEPP **12** was obtained in an amorphous form, displaying a popcorn-like shape, which suggests a high surface area. In contrast, CoDEPP **13** appeared as flower-shaped crystals, formed from smaller brick-shaped crystals with an approximate size of 2.5 μm . Sample **14** exhibited needle-shaped crystals with lengths ranging from 2.5 to 6 μm , and some smaller broken needles were also visible in the SEM image (Fig. 6.3). The CoDEPP **15** appears amorphous in the SEM images, but its shape differs from **12** and resembles a coral-like structure, suggesting a potentially distinct surface area.

Upon comparing all reactions from **12-19**, it becomes clear that the most crystalline samples were obtained when the solvent was not removed under reduced pressure. Longer periods of crystallization generally lead to higher levels of crystallinity. The two reactions that resulted in needle-shaped crystals (**14** and **17**) were conducted without removing the solvent under reduced pressure, and small quantities of water were used in the case **14** with 1 mL of distilled water. In the case of **17** 5 mL of water was used, resulting in smaller needles in the range of 1 μm . Here, water can

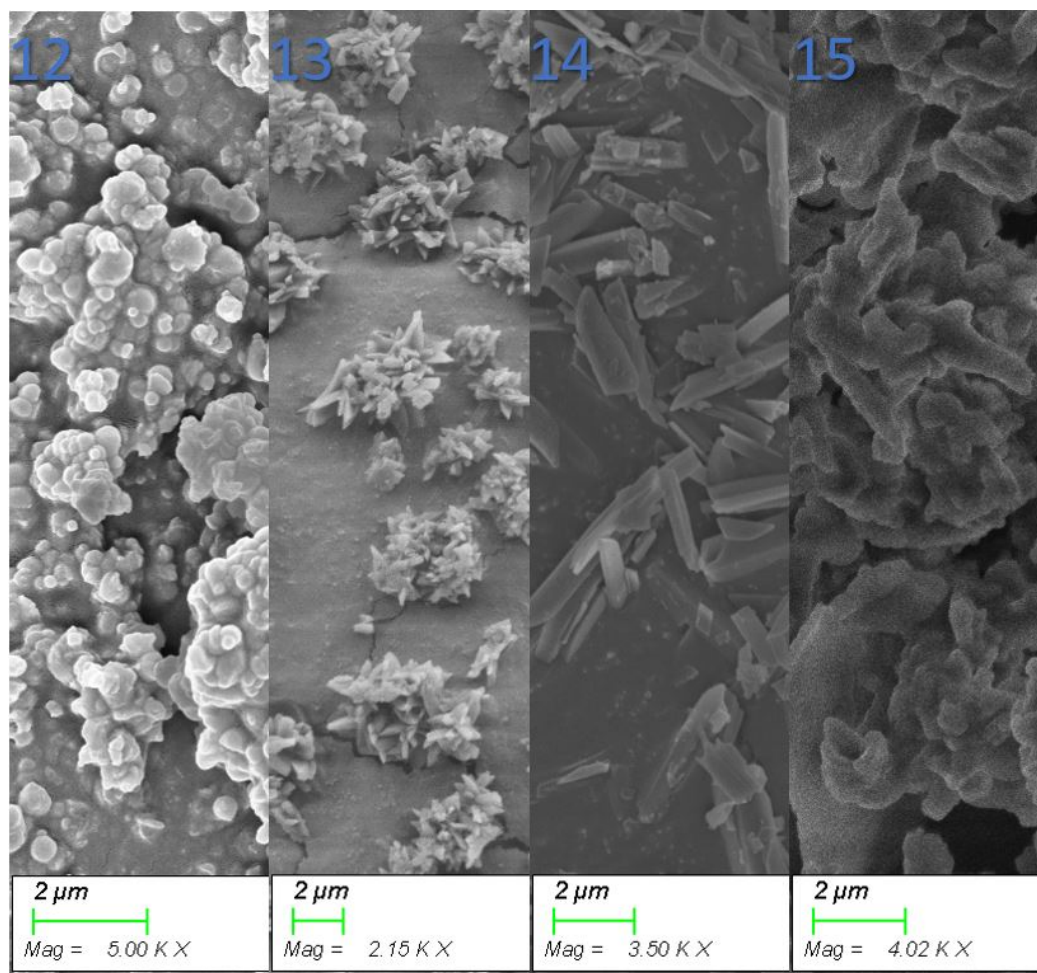


Figure 6.3: SEM Images of CoDEPP **12-15**.

act as a proton source during the deprotection reaction, leading to improved crystallization processes.[156] The two other reactions (**13** and **15**) that involved distilled water resulted in less crystalline structures. In the case of **13**, removing half of the solvent resulted in the formation of crystalline flower shapes. Low temperatures can alter reaction kinetics and affect crystal formation by reducing the reaction rate.[219, 220] The reaction **19a** predominantly resulted in large flower-shaped crystals with a size of 20-30 μm , though in small yields. It is possible that for CoDEPP **15**, lower crystallinity was obtained since the solvent was removed under reduced pressure, and no precipitate was formed after two days storing at low temperatures (8 $^{\circ}\text{C}$), possibly indicating a need for a longer crystallization time.

The morphology of CoDEPP **12-15** was analysed using SEM imaging and powder XRD (Fig. 6.4). Regrettably, attempts to obtain TEM images were not successful. When exposed to high-energy electrons in a TEM, crystalline materials can undergo electron beam-induced amorphization due to electron-phonon interactions, atomic

displacement, radiation damage, and localized heating, which results in the loss of their crystalline structure and the formation of an amorphous phase. The extent of amorphization depends on various factors, including the electron beam properties such as current, kinetic energy, and exposure time, as well as the specific properties of the material. Minimizing the amorphization effects may be possible by using lower electron beam energies and optimizing imaging conditions.[221] Nonetheless, electron beam-induced damage remains an inherent limitation of TEM imaging, especially for organic materials.

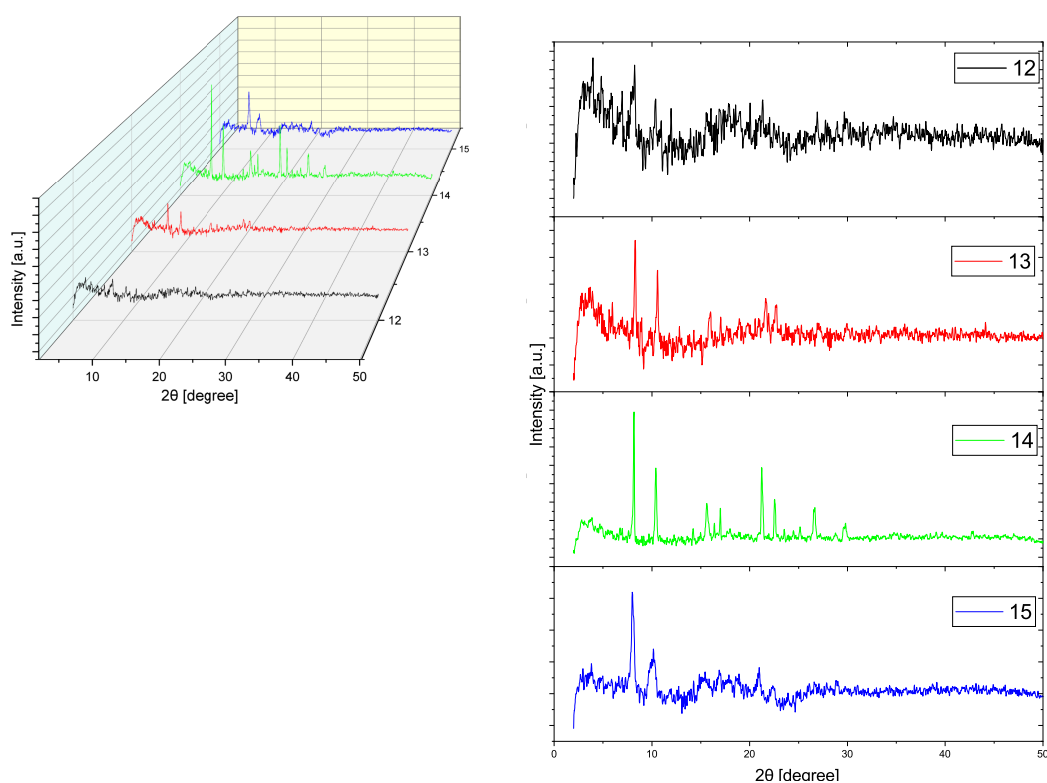


Figure 6.4: Powder XRD patterns of CoDEPP **12-15**.

The powder XRD analysis (Fig. 6.4) indicates a trend in crystallinity as follows: **12** < **13** < **15** < **14**. Notably, the peaks for sample **13** appear sharper, and the SEM image of this sample shows a more pronounced crystalline structure.

The electrochemical tests were performed in a lithium half-cell (Fig. 6.5): CoDEPP/LiPF₆/Li. The voltage window, previously established in other studies, was set to 2.2-4.5 V.[152] In order to investigate reversibility and compare the mechanisms, CV measurements were performed with a sweep rate of 0.1 mV s⁻¹ (Fig. 6.6). During the first cycle, oxidative self-conditioning peaks were observed for compounds **12-15**,

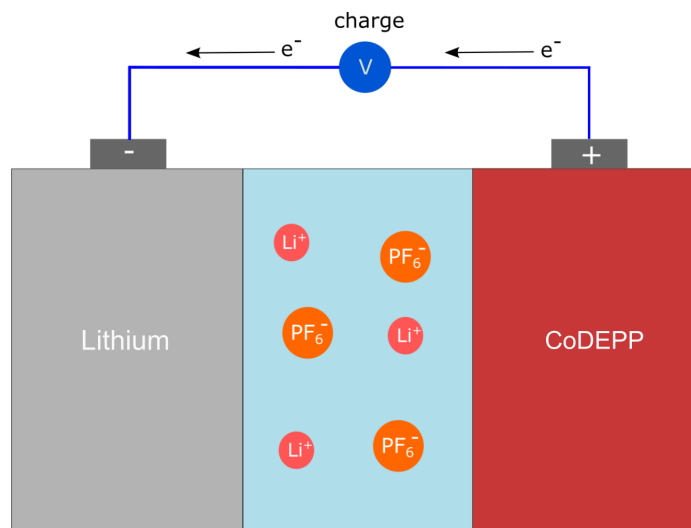


Figure 6.5: Cell configuration with CoDEPP in a lithium half-cell (in the charging state).

with slight shifts in voltage and variations in intensity. Due to the pseudocapacitive behavior,[148] no other significant redox steps were observed. The self-conditioning peaks were observed at 4.01 V **12**, 4.13 V **13**, 4.21 V **14**, and 4.09 V **15**, with the intensity following the pattern **14** > **13** > **12** > **15**. Notably, the two compounds appearing in a more crystalline morphology, **13** and **14**, showed the highest intensity in the CV, especially **14**. This observation suggests that the electrochemically

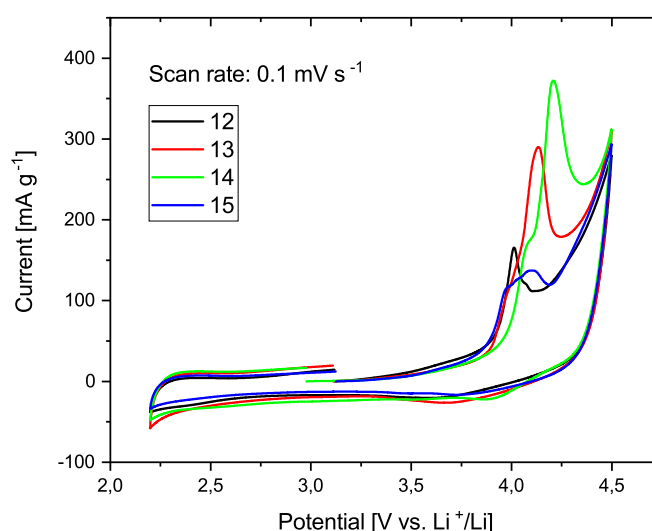


Figure 6.6: CV of CoDEPP **12-15** at 0.1 mV s⁻¹ in a potential range of 2.2-4.5 V.

induced polymerization behind the self-conditioning may be more facile in the case of a crystalline morphology. In crystalline materials, the molecules exhibit a higher degree of order, which could facilitate a polymerization reaction, especially in the case of large molecules where polymerization groups have to overcome steric hindrance. In

the subsequent cycles, the self-conditioning peak disappears, indicating that the electrochemical polymerization process is fully completed after the initial charge (Fig. 6.7). Subsequently, the cycles stabilize and exhibit the typical rectangular shape characteristic of pseudocapacitive materials. After conducting further investigations,

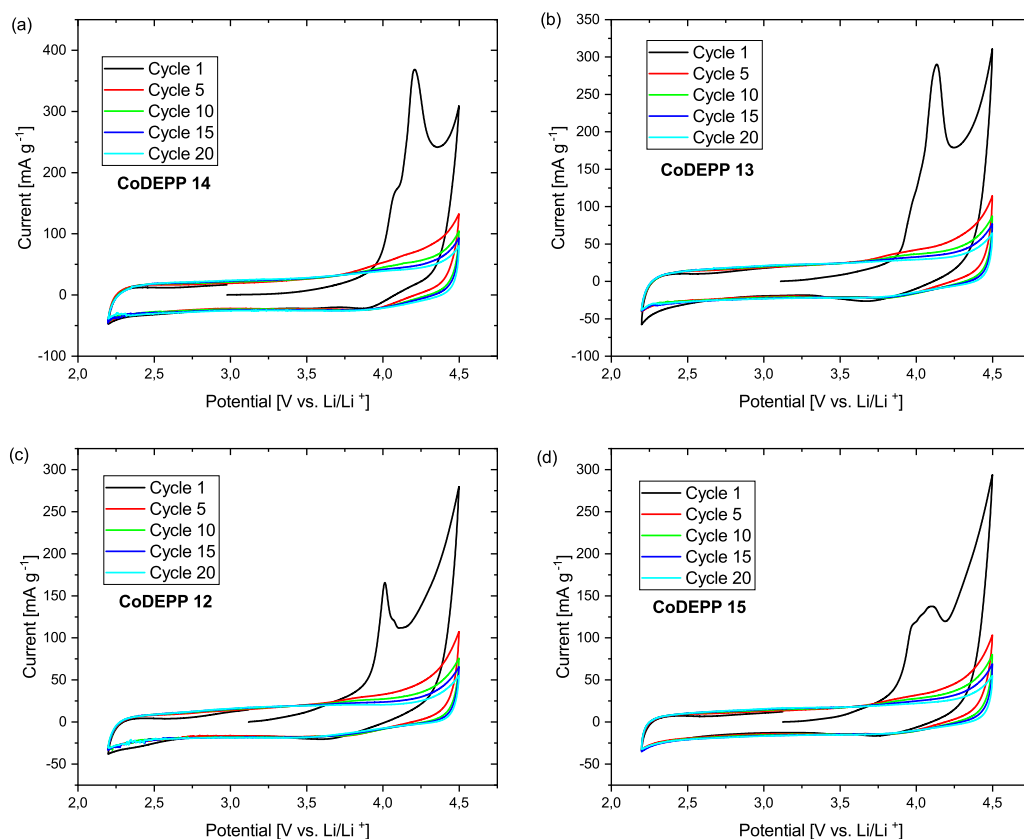


Figure 6.7: CVs of CoDEPP **12-15** (a-d) at 0.1 mV s^{-1} in a potential range 2.2-4.5 V - Cycles 1, 5, 10, 15 and 20.

the electrochemical performance was evaluated through galvanostatic cycling (GCPL) tests in the same half-cell configuration (Fig. 6.8). The voltage range was set between 2.2 V and 4.5 V, while varying the current densities from 0.1 to 0.2, 0.5, 1, 2, 4, and finally back to 1 A g^{-1} . The initial specific discharge capacity achieved at a current density of 0.1 mA g^{-1} was found to be 172 **14**, 145 **13**, 131 **12**, and 112 **15** mAh g^{-1} . These values are slightly lower than the theoretical capacity of 188.9 mAh g^{-1} for a four-electron process $[\text{CoDEPP}]^{2-} \rightleftharpoons [\text{CoDEPP}]^{2+}$. Correspondingly, the specific energy densities for these values are 540, 486, 408, and 349 Wh kg^{-1} for **14**, **13**, **12**, and **15**, respectively. The lack of a voltage plateau in the discharge profile (Fig. 6.8b) points to the occurrence of swift pseudocapacitive redox reactions. The promi-

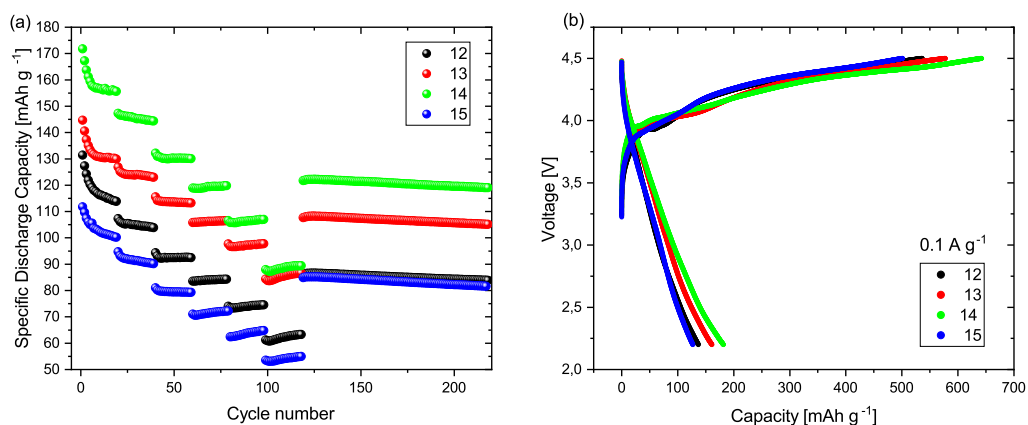


Figure 6.8: a) Rate performance of CoDEPP **12-15** at different current densities between 0.1-4 A g⁻¹ in a potential range of 2.2-4.5 V and b) 1st charge-discharge profiles.

gent slope in the discharge profile indicates the presence of double-layer capacitance and multiple redox reactions.[152, 177] Additionally, the initial rapid capacity fading within the first 5-10 cycles may be ascribed to some dissolution in the electrolyte, but it stabilizes thereafter. At 0.1 mA g⁻¹, the stable capacities are 156, 130, 114, and 100 mAh g⁻¹ for samples **14**, **13**, **12**, and **15**, respectively. All samples show a loss of capacity around 15 mAh g⁻¹, which suggests that the loss due to dissolution of the active material in the electrolyte is the similar for all morphologies. The SEM analysis of **14** and **13** revealed highly ordered crystalline materials (Fig. 6.3), resulting in the highest specific discharge capacities. In contrast, **15** did not show any ordered structures in the SEM, which is reflected in its lower specific discharge capacity. However, the intensities observed in the powder XRD for **15** were higher than those for **13**. Surprisingly, even though **12** exhibited complete amorphous characteristics in both SEM and powder XRD analyses, it displayed a greater specific discharge capacity compared to **15**.

Moreover, the rate capability factor reveals interesting information about the impact of the morphology (Table 6.2). To obtain the rate capability factor, the specific discharge capacity at 4 A g⁻¹ (cycle 118) was divided by the specific discharge capacity at 0.1 A g⁻¹ (cycle 19). Remarkably, the rate capability factor is the highest for the flower-shaped CoDEPP **13**. Previous research has indicated that the rate capability is higher for crystalline materials.[152] This characteristic is particularly dominant in the specific flower shape. This could also explain why CoDEPP **13** outperforms CoDEPP **15**, as it exhibits higher peak intensities in the powder XRD

Table 6.2: Rate capability factor CoDEPP **12-15**.

Code	Dis. Capacity at 0.1 A g ⁻¹	Dis. Capacity at 4 A g ⁻¹	Rate capability factor
12 (popcorn)	114	63	0.56
13 (flower)	130	87	0.67
14 (needle)	156	89	0.57
15 (coral)	100	55	0.57

analysis. Numerous studies have shown that flower-shaped structures generally facilitate fast pathways for lithium ions, resulting in a high rate capability.[222] The 3D flower-shaped structure provides a high surface area which contributes to improved chemical and physical properties, especially in terms of electrochemical properties in lithium-ion batteries.[222] Several studies have reported enhanced performance in high-rate energy storage. The large surface area increases the contact between the electrolyte and active material, improves the transmission distance for lithium ions and electrons, and facilitates the insertion and extraction of lithium ions.[222–228] The performance of the battery is impacted not only by the electrode materials shape, but also by the size of particles, which influences the diffusion path of lithium ions, the diffusion resistance, and the contact area between the active material and electrolyte.[213, 215, 229] Smaller particles typically have a shorter path from inside to outside of the surface, and the flower shape offers a larger contact area. This increases the active material content.[213] These improvements generally result in enhanced electrochemical performance and particularly in better rate capability.[213, 230, 231] As the path for lithium-ion diffusion (L) decreases due to smaller particles, the time constant for ionic diffusion (t) is reduced according to the equation:

$$t = \frac{L^2}{D} \quad (6.1)$$

where L represents the diffusion length and D is the solid-state chemical diffusion constant.[213] Enhanced rate capability may be achieved through faster cathode diffusion resulting from a reduced time constant. Faster ion transport in smaller particles leads to a smaller concentration gradient (referred to as dC/dR), with C representing the Li^+ concentration as a function of the radial distance from the center of the particle. The concentration gradient can trigger mechanical stress, which can be circumvented by using smaller particles, leading to improved cycle performance.[213, 232]

In addition to rate capability, evaluating the long-term stability is also important for materials. A stability factor (Table 6.3) was calculated based on the rate capability measurement shown in Figure 6.8a. The specific discharge capacity at 1 A g^{-1} (cycle 175) was divided by the discharge capacity at 0.1 mAh g^{-1} (cycle 19) for this purpose: The stability factor indicates higher stability for CoDEPP **13** and **15** (Table 6.3).

Table 6.3: Stability factor CoDEPP **12-15**.

Code	Dis. Capacity at 0.1 A g^{-1}	Dis. Capacity at 1 A g^{-1}	Stability factor
12 (popcorn)	114	85	0.75
13 (flower)	130	107	0.82
14 (needle)	156	123	0.77
15 (coral)	100	83	0.83

CoDEPP **15** shows the highest stability, despite having the lowest specific capacity. The amorphous CoDEPP **12** obtained the lowest stability, although its factor is close to that of CoDEPP **14**, the most crystalline compound. To further confirm these values, as no trend could be seen, the samples were subjected to long-term cycling for over 2000 cycles (Fig. 6.9). The first 20 cycles were performed at a current density of 0.1 A g^{-1} to initiate self-conditioning, after which the current density was increased to 1 A g^{-1} . At first glance, it is evident that all morphologies remain stable

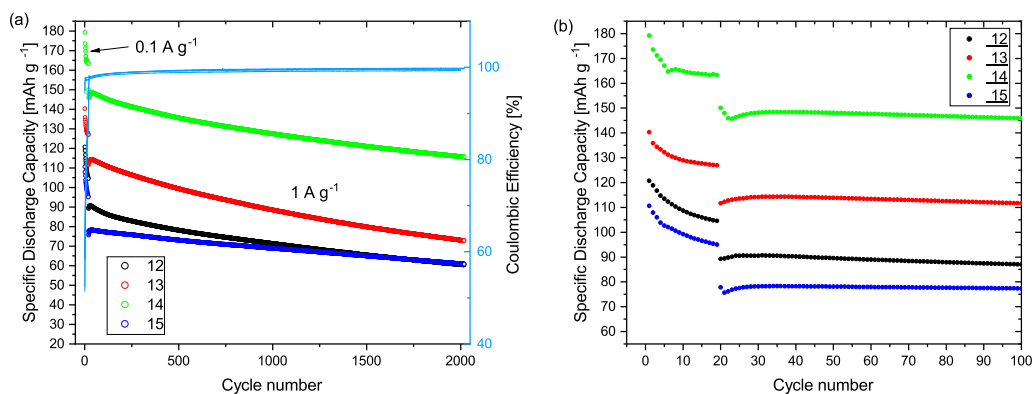


Figure 6.9: a) Long-term cycling of CoDEPP **12-15** at 0.1 A g^{-1} for the first 20 cycles and 1 A g^{-1} at the further cycles in a voltage range of 2.2-4.5 V and b) zoom in to the first 100 cycles.

over 2000 cycles without significant capacity loss. To evaluate the capacity retention accurately, the calculation was done at 1 A g^{-1} both for the first 1000 cycles and the subsequent 2000 cycles: Regarding **15**, the highest capacity retention (Table 6.4) was obtained with 89% after 1000 cycles and 78% after the following 2000 cycles. CoDEPP **14** showed a highly crystalline needle morphology with similar capacity re-

Table 6.4: Capacity retention of CoDEPP **12-15** at 1 A g^{-1} for the first 1000 cycles and further 2000 cycles.

Code	Capacity retention after 1000 Cycles	Capacity retention after 2000 Cycles
12	80%	68%
13	79%	65%
14	85%	77%
15	89%	78%

tention. Particularly over the long term, exceeding 2000 cycles, the values almost reach those of **15**. Comparable literature has demonstrated that the enhanced performance is observed in the needle or nanoribbon structure, as opposed to nanosheets and nanobricks, although the high crystallinity of **14** may also contribute.[156] Possibly, the needles in **14** can interconnect better, allowing for faster electron transfer, resulting in higher cycle stability.[156, 233, 234] CoDEPP **12** and **13** show no significant difference in capacity retention, which contradicts the previously calculated stability factor. This difference may arise because the initial 20 cycles at 0.1 A g^{-1} were not taken into account when calculating the capacity retentions. This demonstrates the benefits of the flower-shaped structure in cycle performance and rate capacity. However, for long-term stability, other properties become more important and side reactions need to be considered. According to the literature, a common drawback associated with small particle sizes is that the increased surface area and decreased coordination with surface atoms could potentially result in elevated side reactions, promoting electrolyte dissolution, and ultimately diminishing the cycle life.[213, 217] Specifically, the heightened surface area might contribute to amplified side reactions with the electrolyte, leading to the formation of thicker solid-electrolyte interphases (SEIs).[213, 235]

The coulombic efficiency in all CoDEPP morphologies is approximately 100%, as shown in Figure 6.9a. The charge-discharge profiles do not show any plateaus which could indicate a two-step intercalation process (Fig. 6.10). In all cases, the reduction in capacity may also be correlated with an increase in polarization effects following extended cycling.[156]

Electrochemical impedance spectroscopy (EIS) was performed to assess further electrochemical aspects. The freshly assembled cells and the cells after ten cycles were

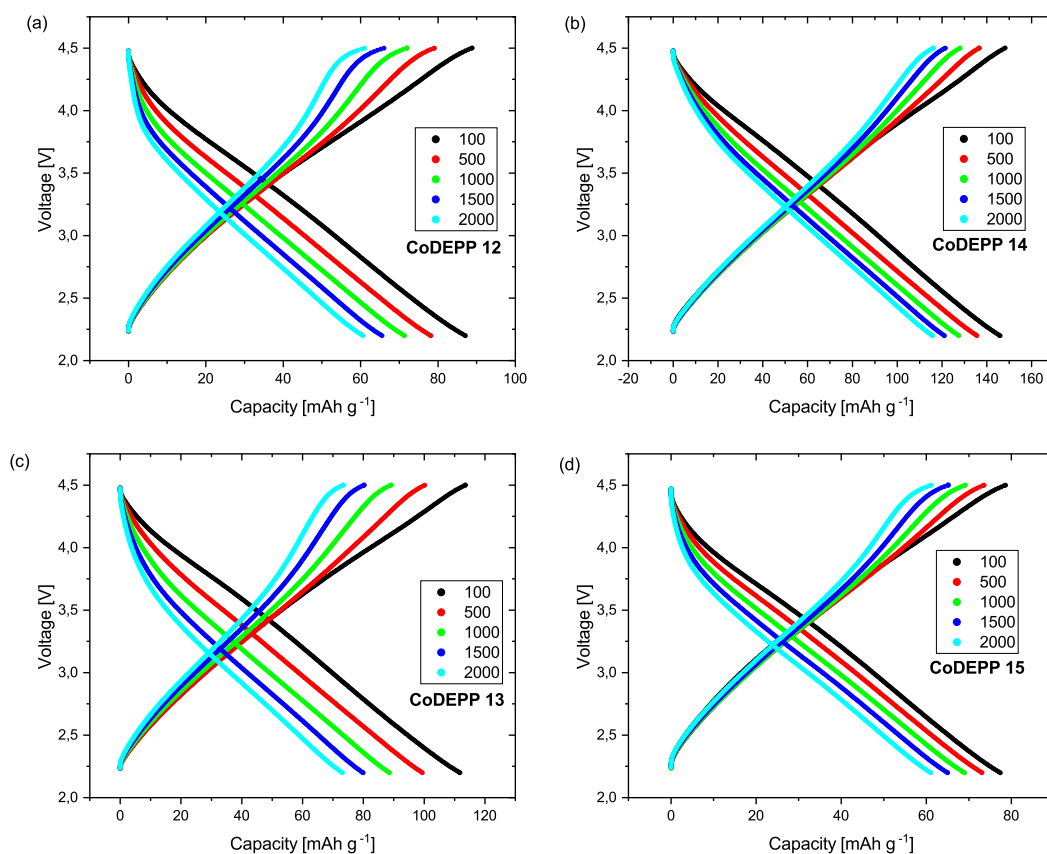


Figure 6.10: Charge-Discharge Profiles of morphological different CoDEPP 12-15 (a-d) after 100, 500, 1000, 1500 and 2000 cycles.

examined and compared. The data obtained were fitted to an equivalent circuit, as shown in Fig. 6.11. Here, R_s represents the internal resistance of the cell, R_{CT} represents the charge transfer resistance related to the resistance of the electrons and ions, CPE is the constant phase element, W is the Warburg impedance, representing the diffusion of the ions within the cell, and C_d represents the double-layer capacitance. The non-cycled cells exhibit a double-layer capacitance that becomes irrelevant in the cycled cells. This change could be attributed to the altered electrode surface resulting from the polymerization of CoDEPP within the first cycle. Additionally, the presence of double-layer capacitance often indicates polarization.[236, 237]

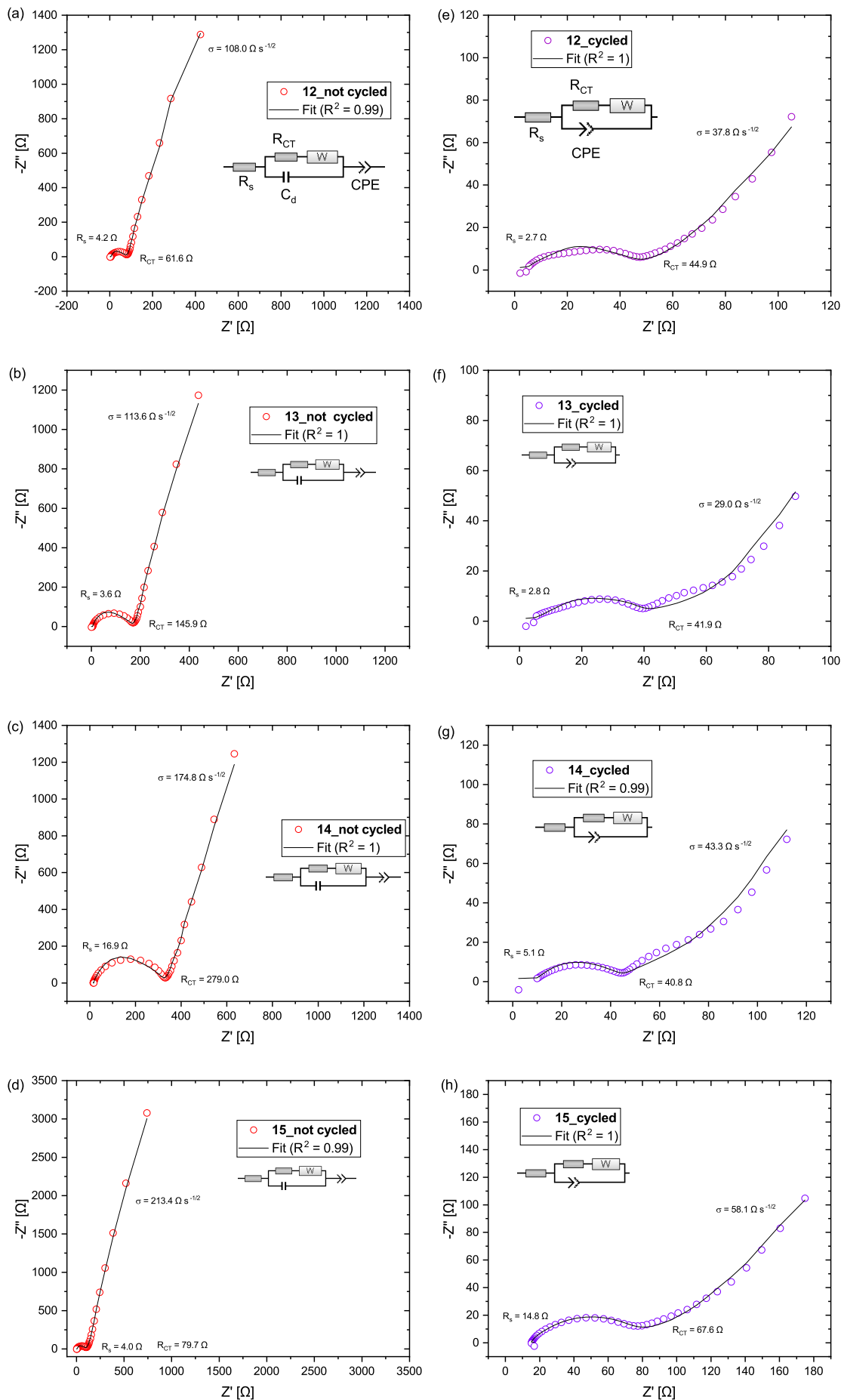


Figure 6.11: Nyquist plots of CoDEPP 12-15 of non-cycled (a-d) and cycled (e-h) cells with their fit and the used equivalent circuit.

Differences were evident when comparing the high frequency region of the fresh cells (Fig. 6.12).

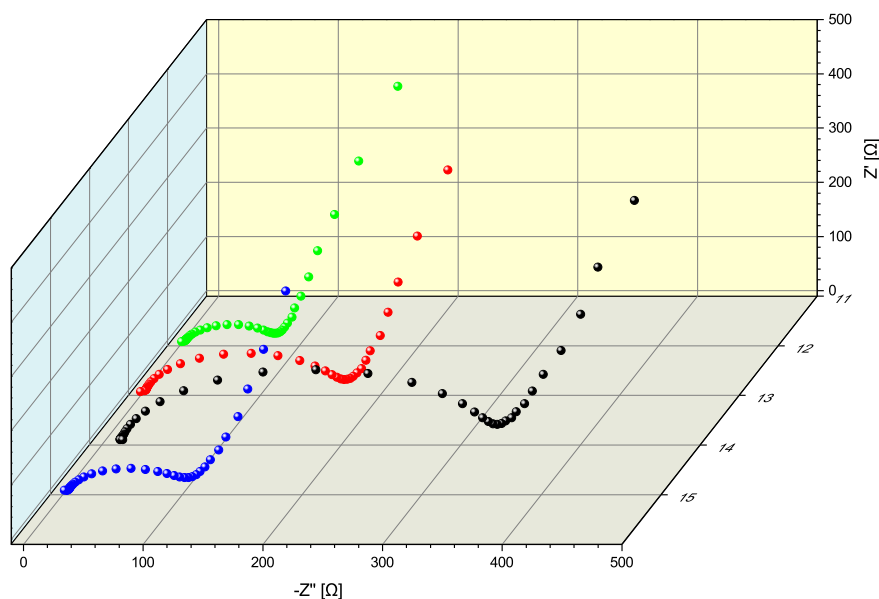


Figure 6.12: Nyquist plots of CoDEPP **12-15** non-cycled cells in the high frequency regions.

The determined charge transfer resistances (Table 6.5) resulting from the fitted plots are as follows: 61.6Ω **12**, 79.7Ω **15**, 145.91Ω **13**, and 279.0Ω **14**. Notably, a clear correlation between the charge transfer resistance and crystallinity, as observed in the SEM images, is evident. Higher R_{CT} values are observed for **13** and **14** in the non-cycled cells. This could be attributed to the larger surface area that may lead to side reactions, subsequently increasing charge-transfer resistance.[238] However, after undergoing 10 cycles within a voltage range of 2.2-4.5 V, the charge transfer resistance experiences a substantial reduction to 44.9Ω **12**, 67.6Ω **15**, 41.9Ω **13**, and 40.8Ω **14**.

These values acquired after cycling also exhibit a notable correlation with the obtained rate performance tests as depicted in Fig. 6.8. Particularly noteworthy is the highest specific discharge capacity achieved for CoDEPP **14** and **13**, which also demonstrate the lowest charge transfer resistance after ten cycles. Moreover, these findings help elucidate the relatively diminished performance of CoDEPP **15**, attributed to its higher charge transfer resistance following cycling. The substantial decrease in the charge transfer resistance of CoDEPP **13** and **14** holds significant importance, as

highlighted in Fig. 6.13.

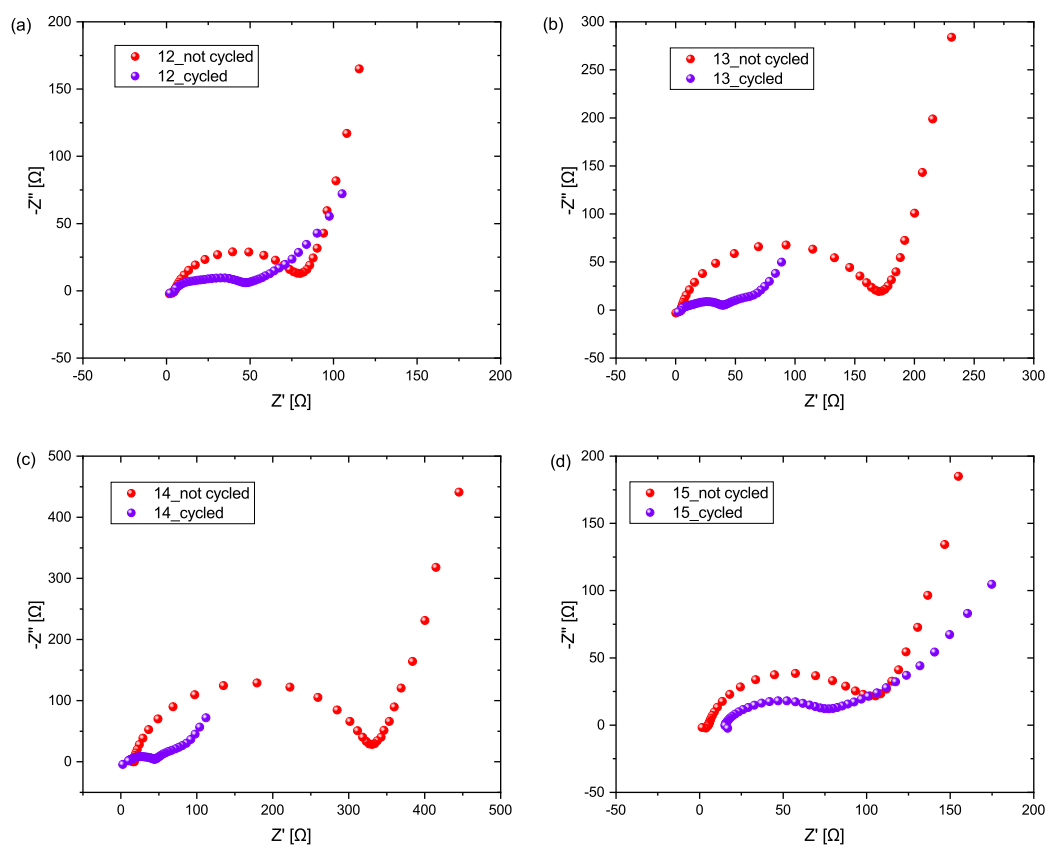


Figure 6.13: Nyquist plots of CoDEPP **12-15** (a-d) comparison of non-cycled and cycled cells.

In general, the decrease in R_{CT} after cycling provides further evidence of enhanced charge transfer and improved kinetics following the initial cycle, during which self-conditioning occurs. This can be attributed to the increasing π -conjugated system and conductivity caused by polymerization. Additionally, the change in the slope of the linear line in the low-frequency range can be related to low diffusive resistivity and fast reaction kinetics.[149, 158]

The diffusion coefficient can be calculated using the Warburg coefficient (σ , see Table 6.5).

Table 6.5: EIS analyses results of the cell based on CoDEPP **12-15** cathodes (non-cycled and after 10 cycles).

	R_s (Ω)		R_{CT} (Ω)		σ (Ω s ^{-1/2})	
	Fresh cell	Cycled cell	Fresh cell	Cycled cell	Fresh Cell	Cycled Cell
12	16.9	5.1	279.0	40.8	174.8	43.3
13	4.2	2.7	61.6	44.9	108.0	37.8
14	4.0	14.8	79.7	67.6	213.4	58.1
15	3.6	2.8	145.9	41.9	113.6	29.0

Following cycling, the diffusion coefficient increases across all morphologies due to self-conditioning (Fig. 6.14). In lithium-ion batteries, diffusion kinetics are typically influenced by porosity, tortuosity and surface area. Elevated surface areas foster heightened contact between the active material and electrolyte, offering additional diffusion channels for ions.[152, 200].

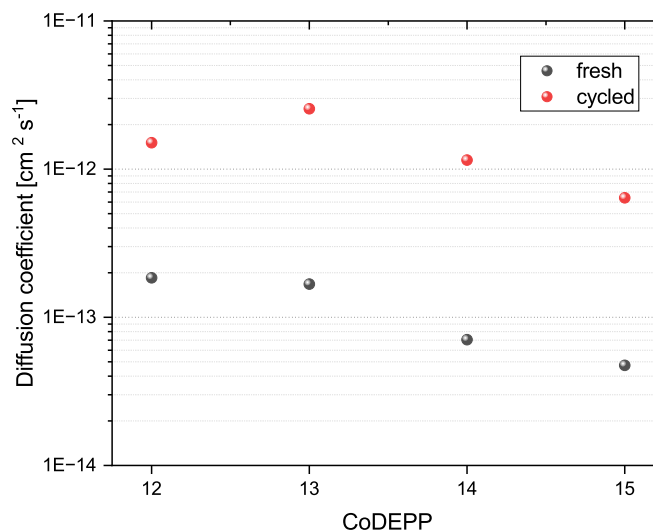


Figure 6.14: Diffusion coefficient estimated by EIS of non-cycled and cycled CoDEPP cells.

Among the non-cycled cells, the highest diffusion coefficient is observed for **12** and **13**. While **12** is amorphous and likely possesses high porosity, **13** is anticipated to exhibit a notably large surface area due to its small flower-shaped crystals. After cycling, the diffusion coefficient remains the highest for **13**, reinforcing its overall high performance. Conversely, the poor performance of **15** is again underscored by its lowest diffusion coefficient, both in cycled and uncycled cells.

Due to the high diffusion coefficient of **12** and **13**, both samples were selected for in-depth investigation. Furthermore, the study aimed to examine one amorphous and one crystalline material. The objective was to explore the porosity, pore size, and tortuosity of the two materials using nanoCT and FIB-SEM Tomography, as demonstrated for other inorganic materials.[239–242]

6.3.1 NanoCT and FIB-SEM Tomography

Dr. Rafaela Debastiani carried out the nanoCT measurements and reconstruction, whereas Dr. Torsten Scherer performed the FIB-SEM tomography measurements.

The electrode preparation for the 3D reconstruction of the materials has been outlined in the preceding section. For non-cycled electrodes, the process involved drying, while cycled electrodes were washed in DME after disassembly and then dried overnight under high vacuum at room temperature. Achieving a good contrast among various components of interest, such as pores, carbon, and active material, is crucial for 3D reconstruction through both nanoCT and FIB-SEM Tomography. To enhance contrast, a procedure was employed, building upon a previous approach.[241] Some modifications were introduced due to differences in equipment. In the case of cycled samples, the electrode material was entirely exfoliated from the SS disk after washing. Fragments of the exfoliated material were attached to copper tape. Conversely, the coated SS disks of non-cycled samples were suitable for subsequent steps. All samples, both CoDEPP **13** and **12** in cycled and non-cycled forms, were placed in a glass desiccator overnight with **12** drops of 2% aqueous OsO₄ solution. OsO₄ enriches the gaseous phase and reacts with non-aromatic double bonds,[241, 243, 244] which might form during self-conditioning and could serve as evidence for the electrochemically induced polymerization of terminal acetylene groups. To enhance the contrast between pores and carbon and to prevent any potential artifacts due to electron beam damage, the samples were subjected to embedding. However, before embedding the samples, a small amount (less than 1 mm²) was removed for nanoCT. These small particles, with sizes smaller than 100 μm, were manually attached to the tip of a needle. After removing the sample particles from the electrode surface, the remaining sample was embedded. Sylgard 185, a silicon resin, was employed for this purpose in a ratio of

10:1. The freshly prepared resin was carefully applied to the electrode/copper tape containing the material using a syringe. In the initial step, the samples were placed under vacuum for 5 minutes, achieving a vacuum level of 5.0×10^{-1} to 2.7×10^{-5} mbar. After this 5-minute interval, the samples were removed, and any excess silicon resin was meticulously wiped away using a tissue. To further facilitate resin infiltration, the samples were subjected to a second vacuum step for 30 minutes, this time at a vacuum level of 1.7×10^{-1} to 2.1×10^{-5} mbar. Subsequently, the resin was allowed to cure at 60 °C for a duration of two days. Ion beam polishing was then employed to refine the surface, eliminating excess resin. This step was crucial to mitigate charging effects in the SEM and to facilitate the precision of cuts during FIB processing.

Three samples underwent nanoCT analysis to investigate their porosity, pore size, and tortuosity. The non-cycled CoDEPP **12** and **13** samples were chosen for examination, both in their non-embedded forms. Additionally, the CoDEPP **13** sample was embedded due to difficulties in achieving suitable contrast without embedding. The 3D imaging was conducted using the X-ray microscope Xradia 810 Ultra (nanoCT). This system employs a semi-monochromated X-ray beam from a Cr anode with an energy of 5.4 keV, along with a sequence of optics to achieve a pixel size of 16 nm within a high-resolution field of view setup of 16 μ m. The experiments in this thesis utilized a field of view of 16 μ m and a pixel size of 32 nm for the embedded CoDEPP **13** sample, and a field of view of 65 μ m and a pixel size of 64 nm for the non-embedded CoDEPP **12** and CoDEPP **13** samples. Zernike phase contrast mode was employed. In the case of the non-embedded samples, a portion of the material was carefully extracted from the SS disk and affixed to a needle's tip. For the embedded sample, a cylindrical section was meticulously extracted using FIB techniques, yielding a cylinder with a height and diameter of **13** μ m. The non-embedded samples underwent scanning over a larger field of view (65 μ m) with a pixel size of 64 nm, resulting in a resolution of 150 nm. This process encompassed a 180° scan, capturing 901 projections for CoDEPP **13** and 1001 projections for CoDEPP **12**. Each projection was exposed for 110 seconds for CoDEPP **13** and 90 seconds for CoDEPP **12**. Conversely, the embedded sample was scanned over a smaller field of view (16 μ m) with a pixel size of 32 nm, achieving a resolution of 100 nm. This scan covered 180°, capturing 901

projections, with each projection exposed for 100 seconds. Subsequently, the datasets were reconstructed using Zeiss Scout and Scan Reconstructor, proprietary software based on the filtered back projection algorithm.

For visualization, segmentation, and statistical calculations, the software Dragonfly ORS was employed, with all samples segmented using the UNet deep learning model. Grayscale thresholding (lower Otsu) was applied to segment CoDEPP **13** (non-embedded) after employing an Unsharp filter on the data. Statistical analyses were conducted through Multi-ROI analysis of the segmented pores.

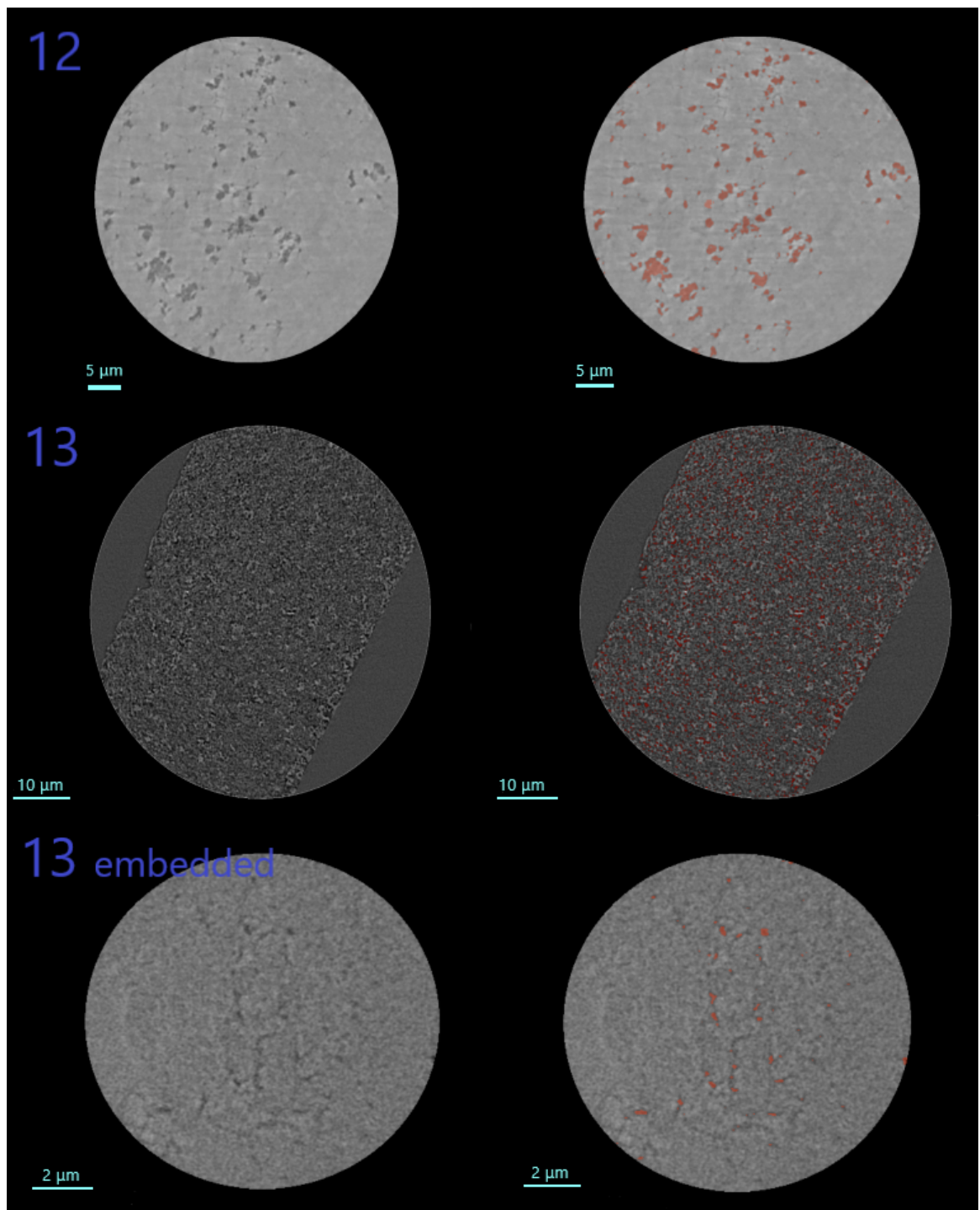


Figure 6.15: 2D slices of of the 3D reconstructed datasets, where the red dots represent the set pores within in the material.

Looking at Figure 6.15, it is clear that the contrast in the embedded sample **13** is of poor quality. It is difficult to differentiate between pores, material, and air. At first glance, the CoDEPP **12** sample appears to have larger pores compared to the CoDEPP **13** sample. After 3D reconstruction, it becomes clear that **12** has a significantly higher porosity than **13**. In addition, the pore size is much larger for **12**. The values obtained for pore volume vary significantly. As a result, the minimum, median, and maximum values are presented in Table 6.6 for the three samples.

Table 6.6: Pore volume of CoDEPP **12**, **13** and **13** (embedded).

Code	min. volume [nm ³]	median [nm ³]	max. volume [nm ³]
13 (embedded)	771807	6946267	8.77x10 ⁹
13	102216	1124379	2.86x10 ⁷
12	791510	2.05793x10 ⁷	8.45x10 ¹⁰

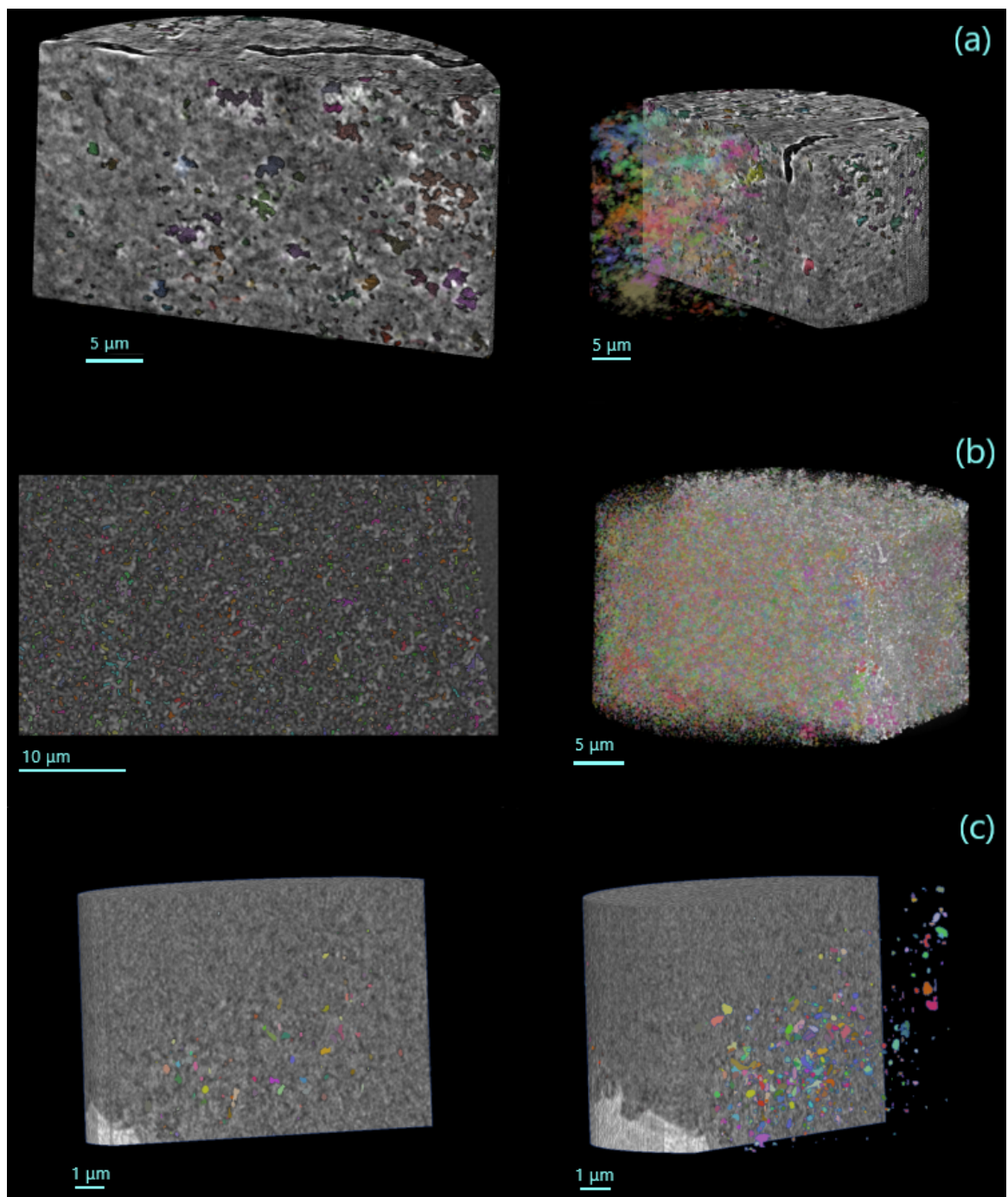


Figure 6.16: 3D visualization of the datasets with the pores highlighted in colors (similar color correspond to similar volume in the respective sample) of CoDEPP **12** (a), **13** (b) and **13** (embedded) (c). Right side: the reconstructed image was cropped in half for a better visualization of the pores distribution in the segmented volume. The distribution is better seen in the sample c) due to the higher density of pores in samples a) and b).

The visual representation of these findings is depicted in Figure 6.16. When evaluating the information obtained from the nanoCT analysis, it is essential to emphasize that these results provide no more than a general trend. This limitation stems from certain challenges encountered during sample preparation. Primarily, the use of the drop-casting method in electrode preparation leads to a non-uniform surface. Given that only a tiny portion is reconstructed, this non-homogeneity can significantly influence the outcomes. Additionally, the contrast was too low to utilize automated segmentation, thus AI software was required for full segmentation, necessitating manual training and further corrections on the segmentation, which is time consuming and can lead to errors. Moreover, previous work[152] involved BET investigations on CoDEPP, revealing pore sizes below 10 nm. As nanoCT resolution has its limits (50 nm), pores of this size cannot be explored. Consequently, only larger pores were considered in this study. Nevertheless, the observed trend supports our results, indicating that the amorphous CoDEPP **12** compound likely possesses higher porosity compared to the smaller flower-shaped CoDEPP **13** material. An analysis of both embedded and non-embedded CoDEPP **13** materials highlighted notable differences. This discrepancy primarily results from the non-uniform electrode preparation. The embedding process should ideally not alter the size or number of pores within the material. Unfortunately, obtaining tortuosity values was unattainable due to the complexity of the reconstruction process.

For the purpose of comparison and to surmount the resolution limitations, we turned to FIB-SEM Tomography as an alternative method to explore pore size, porosity, and tortuosity. The FIB-SEM cross-sectioning and Tomography procedures were executed using the FEI Strata 400S instrument. The cutting thickness is 50 nm, the cutting current is 0.92 nA (30 kV). The images were taken using the TLD (through-the-lens) detector at an image resolution of 2048x1768.

Regrettably, our endeavor to commence reconstruction was met with an early setback, stemming from the inadequately distinct contrast between the pores and the material in the images. Moreover, the size of the pores (<10 nm) might be below the resolution limit for SEM analysis. Furthermore, an observation was made indicating incomplete infiltration of the material by the silicon resin. Lastly, another

hindrance emerged in the form of material instability during the relatively slow scan rate employed. The material seemed to react and form bubbles (Fig. 6.17) under the influence of the electron beam, rendering reconstruction unfeasible. The process

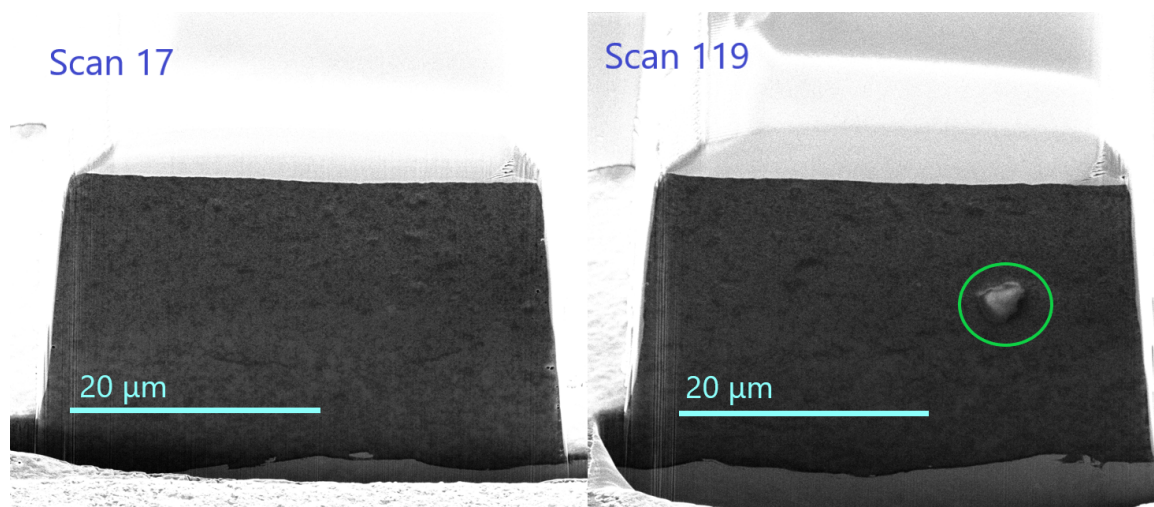


Figure 6.17: Instability of CoDEPP **12** in the electron beam, appearance of bubble in the scan 119 compared to scan 17.

of 3D reconstructing battery materials, particularly those containing organic active components, proved to be quite challenging. Achieving optimal conditions, including the right resin and possibly refining electrode preparation techniques, is necessary. Regrettably, all these experiments are quite time-intensive; for instance, the sample preparation alone spanned three weeks, while the measurement process took roughly two weeks per sample. Subsequent reconstruction requires an additional 2 to 4 weeks of work. Consequently, we were unable to initiate measurements for the cycled samples. Nevertheless, the outcomes derived from the nanoCT results did provide a reliable trend in terms of pore volume.

Furthermore, we successfully confirmed the presence of Os staining in the cycled samples through EDX (Fig. 6.18). This analysis distinctly revealed that Os was only detected in the cycled electrodes (in the circles), whereas the non-cycled samples showed no such indication (Fig. 6.19). The very weak red dots are negligible. This validation is in line with the findings of Philipp *et al.*[241] and provides evidence for the occurrence of aliphatic double bonds within the CoDEPP material. The investigation of Os staining is specifically shown on CoDEPP **12**. The Os staining was clearly observable, with successful removal of the silicon resin achieved using the ion beam

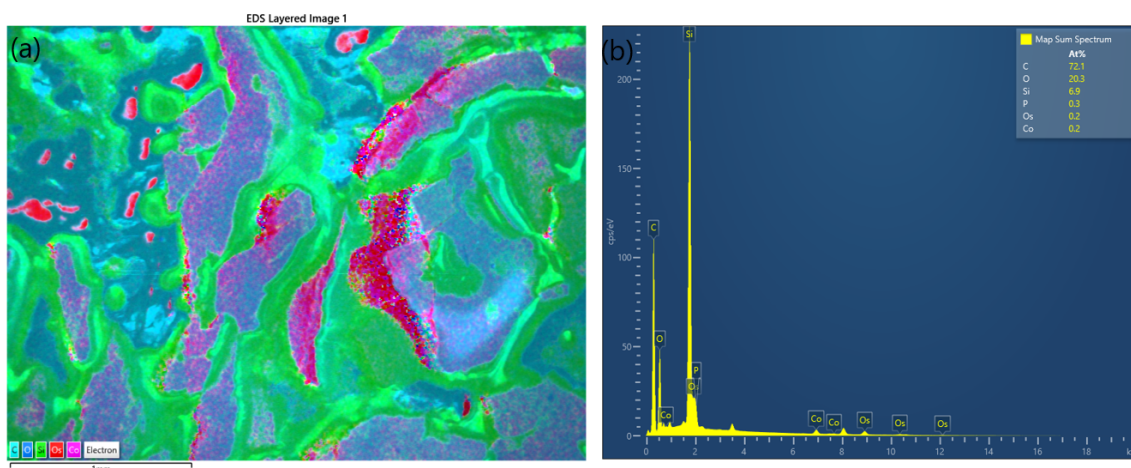


Figure 6.18: (a) EDX layered image with element mapping (Os-red, C-turquoise, O-blue, Si-green, Co-purple) and (b) showing element distribution of cycled sample CoDEPP **12**.

(Fig. 6.18a). The presence of Co in the same areas confirms that Os staining occurred precisely where the active material is visible.

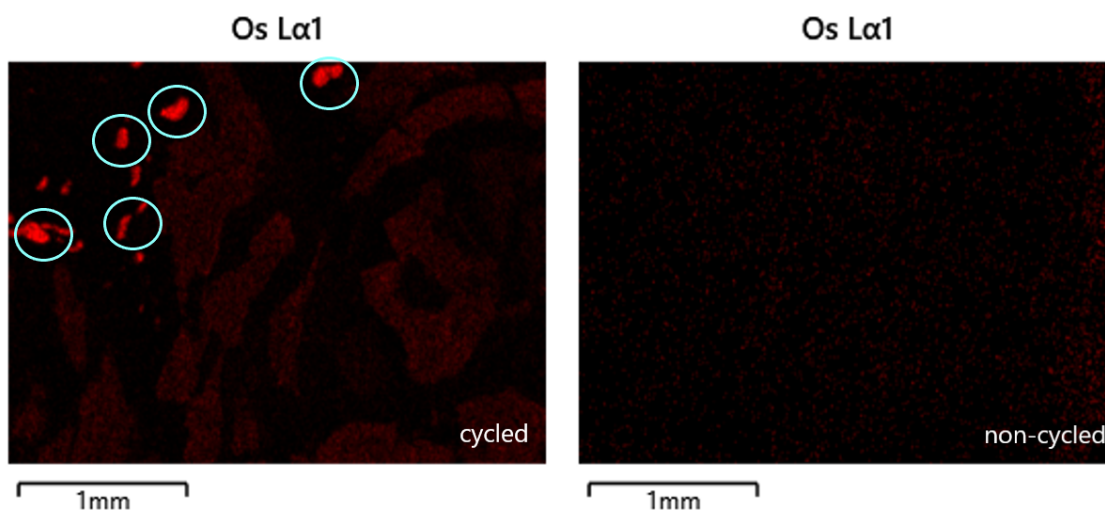


Figure 6.19: Comparison Os mapping of cycled and non-cycled CoDEPP **12** electrode.

6.4 Conclusion

It was effectively demonstrated that the morphology of CoDEPP can be readily adjusted during the deprotection reaction, achieved by varying factors such as temperature, water content, solvent removal, and precipitation time. This variation led to the formation of four distinct morphologies: needle-shaped, flower-shaped, coral-shaped, and amorphous popcorn-shaped structures. A comprehensive comparative study was conducted through material characterization and electrochemical assessments. This investigation conclusively established that the morphology, encompassing both shape

and size within the microstructure, profoundly influences the properties of the electrode material. Among the evaluated morphologies, CoDEPP **15** exhibited the lowest specific discharge capacity, reaching 100 mAh g^{-1} , while the highest capacity was observed for CoDEPP **14**, recording 156 mAh g^{-1} at a current density of 1 A g^{-1} . Notably, the flower-shaped crystals of CoDEPP **13** displayed numerous advantages, particularly in terms of surface area, which facilitated efficient lithium ion pathways and bestowed the material with exceptional rate capability. Regarding long-term stability, CoDEPP **14** and **15** demonstrated the most robust capacity retention, retaining 77% and 78% of their initial capacity after 2000 cycles, respectively. Impedance measurements provided insights into diffusion coefficients, indicating that both CoDEPP **12** and **13** possessed notably higher values. To delve deeper into the distinctions between amorphous and crystalline materials, both morphologies underwent investigation using 3D reconstruction methods. Through nanoCT analysis, it was revealed that CoDEPP **12** exhibited substantial porosity, which correlated with its enhanced diffusion coefficient. In contrast, CoDEPP **13** showcased a prevalence of smaller pores. While these findings offer valuable insights, the complexity of sample preparation and the limitations of the employed techniques prevented a more comprehensive understanding. In addition, convincing evidence based on Os staining was presented for CoDEPP, confirming the formation of aliphatic double bonds during the self-conditioning process. This result strongly suggests that the stabilization mechanism involves polymerization induced by electrochemistry (see chapter 8).

Chapter 7

Pyridine-Functionalized Porphyrin MOF as Cathode Material in Lithium-, Calcium- and Aluminium- Rechargeable Batteries

7.1 Introduction

Metal-organic frameworks (MOFs) constitute a relatively novel category of porous materials that have found applications across diverse fields such as gas sorption, catalysis, medicine, optics, and sensing.[245] This makes MOFs intriguing candidates for electrode materials, as their adjustable pores can interact with ions during charging and discharging processes. Additionally, MOFs typically exhibit high surface areas due to their porous nature.[246] A wealth of literature has reported various MOFs as electrode materials,[247, 248] and porphyrin-based MOFs are also well-documented, including examples like [5,10,15,20-tetra(4-carboxylatophenyl)porphinato]copper(II) (Cu-TCPP) in Li-CO₂ batteries[249] and [5,10,15,20-tetra(4-carboxyphenyl)porphinato]cobalt(II) (CoTCPP-MOF) in lithium-ion batteries.[250] The inherent flexibility of MOF structures allows their use as both anodes and cathodes across diverse systems, including sodium-ion batteries (SIBs)[251], potassium-ion batteries (KIBs)[252], and zinc batteries.[253]

Recently, pyridine-functionalized porphyrins have garnered attention as promising

electrode materials in lithium and sodium dual-ion batteries. Remarkable cycle life exceeding 5000 cycles (103 mAh g^{-1} at 1 A g^{-1}) and high-power density of 18.7 kW kg^{-1} have been reported for these materials.[254] In this study, a pyridine-functionalized copper(II) porphyrin, linked via tetraacetate paddlewheel clusters, was employed as a cathode material in its initial state for a lithium half-cell. Subsequently, its potential was further explored in aluminum and calcium batteries. Various synthetic approaches were detailed, each influencing the crystallinity of the resulting material. A range of analytical tools was employed for comprehensive characterization, complemented by in-depth investigations into the electrochemical properties.

7.2 Synthesis and Characterization

The synthesis of CuTPyrP-MOF is straightforward and does not require any heating or intricate purification steps (Fig. 7.1). The starting point involves metallating the free-base 5,10,15,20-tetra(4-pyridyl)-21*H*,23*H*-porphin (TPyrP) with Cu(II)-acetate monohydrate. The conditions under which this reaction takes place significantly influence the resulting crystallinity of the metal-organic framework (MOF) formed. The synthesis route employed for the batch used in all subsequent sections as a cathode material yielded a more amorphous product. In this procedure, the reaction was conducted as a one-pot reaction under continuous stirring for the duration of one day. The product was subsequently obtained through filtration and subjected to washing with water and methanol to eliminate any unreacted Cu(II) acetate salt. The resulting reddish powder was then dried under high vacuum overnight, leading to a significant impact on its crystallinity. The product, denoted as CuTPyrP-MOF $[\text{CuTPyrP}(\text{Cu}_2(\text{OAc})_4)_2]_n$, consists of CuTPyrP wherein the nitrogen from the pyridine functionality coordinates with a dicopper(II) tetraacetate (paddle wheel cluster) as linking molecule. The provided molecular formula represents the smallest unit used to build a 2D coordination network.

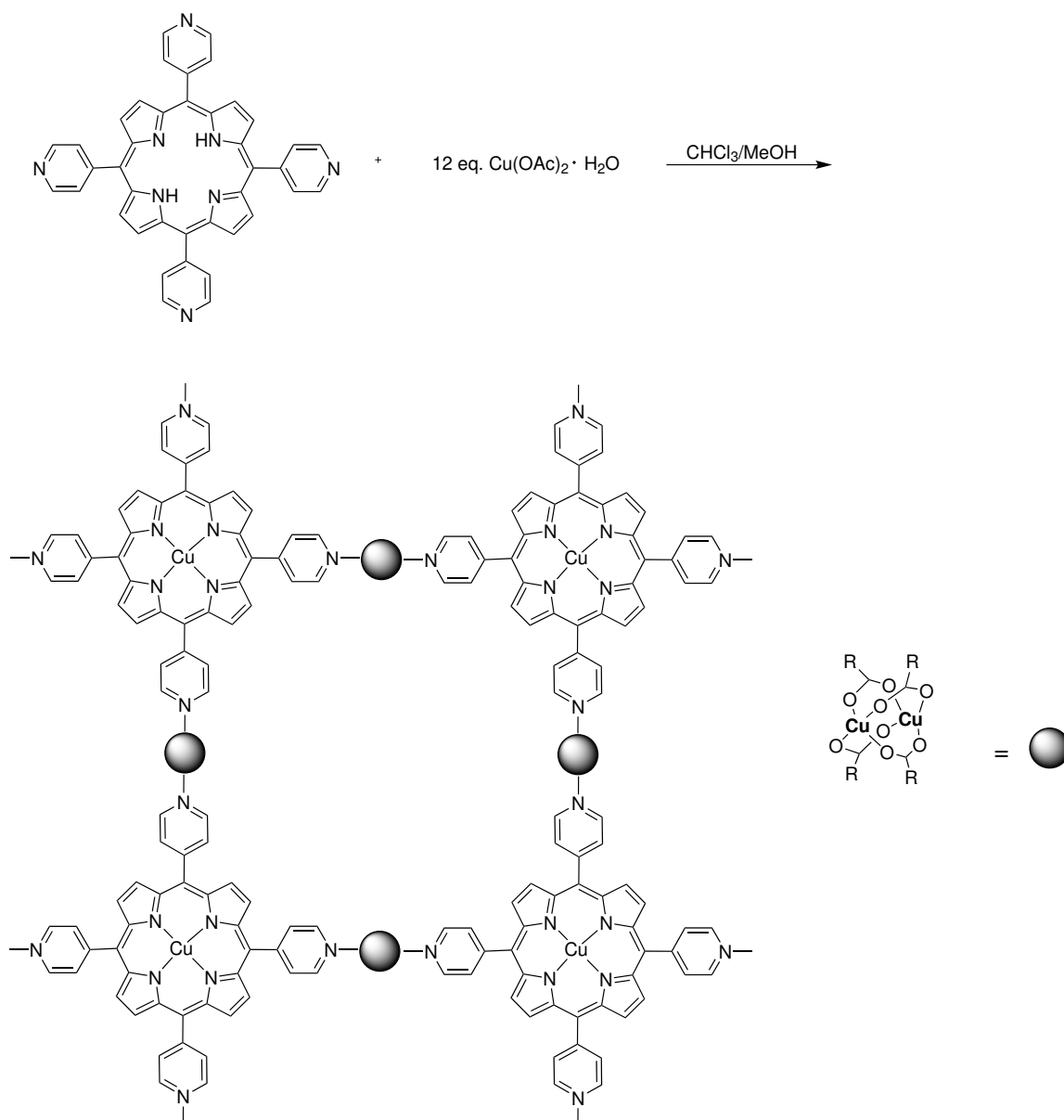


Figure 7.1: Synthetic route to obtain CuTPyrP-MOF.

In order to confirm that a single porphyrin molecule had not been synthesized, as previously described in the literature with similar reaction conditions [254–256], several analyses were conducted. These include UV-Vis spectroscopy, IR-spectroscopy, MALDI mass analysis, elemental analysis, XPS and powder XRD. Elemental analysis provided a clear indication of the MOF formation, especially as the carbon content was significantly lower than expected for a single porphyrin molecule. Table 7.1 shows the values for the single molecule and MOF calculated and the experimental result and the values taken from literature.

Table 7.1: Elemental Analysis results CuTPyrP-MOF.

	C%	H%	N%
CuTPyrP	70.63	3.56	16.47
CuTPyrP·(Cu ₂ (OAc) ₄) ₂	47.81	3.44	7.97
Experiment	49.89	3.88	10.24
Literature[257]	49.12	4.32	/

The presence of the Cu(II) tetraacetate paddlewheel cluster was confirmed using infrared spectroscopy (Fig. 7.2b), where prominent peaks at 1619, 1603, and 1422 cm⁻¹ correspond to the symmetric and asymmetric stretching vibrations of carboxylate (CO₂⁻) groups.[258]

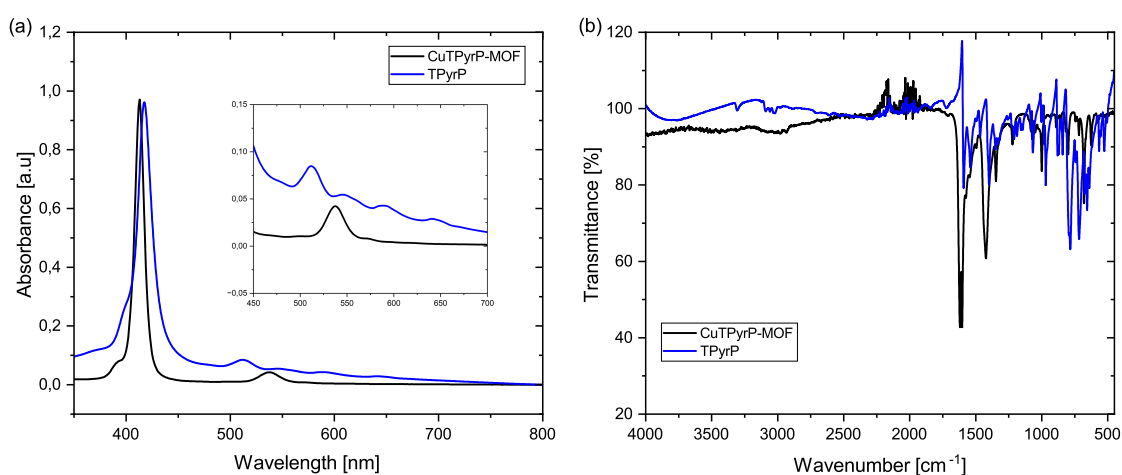


Figure 7.2: (a) UV-Vis spectra of CuTPyrP and TPyrP and (b) IR spectrum of CuTPyrP-MOF and TPyrP.

Upon comparing the UV-Vis absorption spectra (Fig. 7.2a) of the free-base porphyrin TPyrP and the CuTPyrP-MOF, it becomes evident that the metallated porphyrin exhibits a reduced number of Q-bands, which can be attributed to the increased symmetry of metallated porphyrins ($D_{2h} \rightarrow D_{4h}$).

Further characterization of the material was performed in collaboration with T. Smok and Dr. Thomas Diemant using XPS. It is noteworthy that the pristine sample contained an unexpected presence of Cu(I) (Fig. 7.3). The use of Cu(I) as the metal center in a porphyrin context is atypical and not reported in the current literature. The discovery of Cu(I) supports the formation of the MOF structure, as the presence of Cu(I) at the nodes of MOF structures is well-established in the literature.[259] One possible explanation for this is the presence of unsaturated metal sites (UMS) within the MOF.[259] Additionally, it is important to consider the presence of defects

in the MOF structure and impurities of Cu_2O .^[260] These structural defects,^[261] could also account for the higher nitrogen content observed in the elemental analysis. Morphological investigation was conducted using powder X-ray diffraction, with a

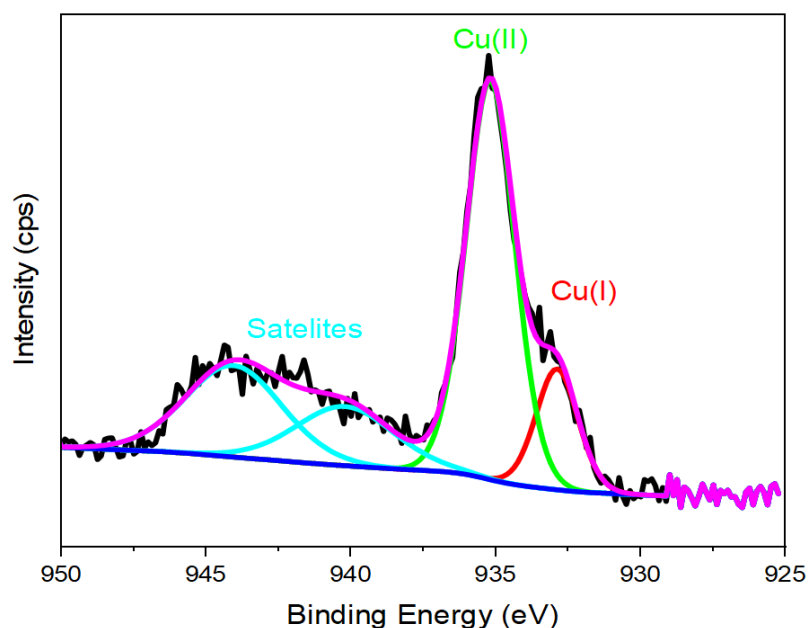


Figure 7.3: Detailed XPS $\text{Cu}2\text{p}_{3/2}$ spectrum of CuTPyP-MOF. Reprduced with permission^[260], Copyright 2023, Wiley.

comparison being made to patterns found in literature.^[262] The cathode material batch obtained exhibits lower crystallinity than published structure (Fig. 7.4), making comparison difficult. Two factors can explain the loss of crystallinity. The first is the rapid crystallization step performed in the synthetic route described thus far, where the product was achieved after one day of stirring. Another cause could be the drying process during the sample preparation, which involved overnight drying in high vacuum. Solvent molecules that may have been encapsulated in the MOF structure could be lost during this process, leading to a loss of crystallinity. The contrast between dried and fresh samples was demonstrated previously^[262] and has been replicated in the current study.

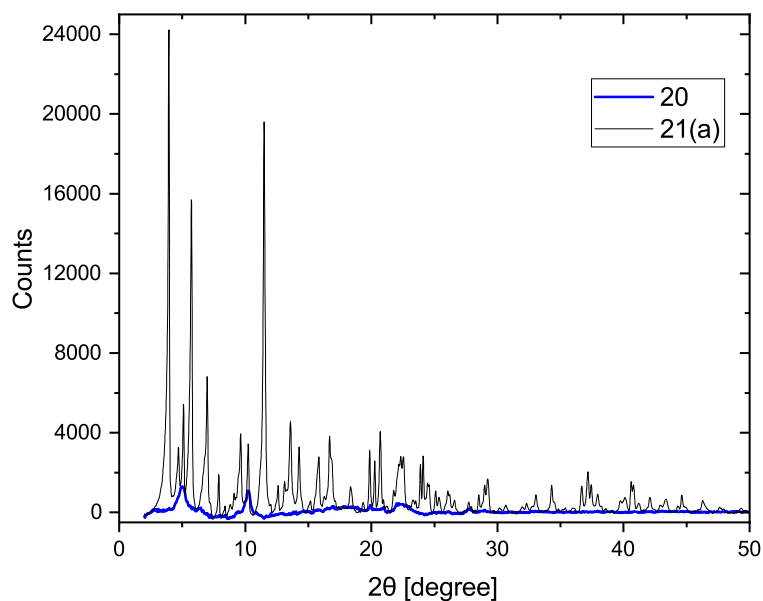


Figure 7.4: Comparison of powder XRD diffraction pattern of batch 20 used in battery cells (blue), batch 21(a) freshly prepared sample from solution.

In order to replicate the previously described experiment, the synthetic route was also modified to utilize a layered reaction without stirring.[257] The free-base porphyrin was dissolved in chloroform, and a layer of Cu(II) acetate monohydrate in methanol was gently added on top. The reaction was allowed to proceed for a duration of two weeks without any agitation. Unfortunately, no crystals suitable for single-crystal X-ray analysis could be obtained under these conditions. A portion of the precipitate was extracted directly from the solution and immediately subjected to powder X-ray diffraction (XRD) (21(a)), revealing a higher degree of crystallinity than the MOFs obtained from stirring process. Additionally, drops of the solution containing the precipitate were placed on a glass surface and allowed to air dry, without applying further vacuum (21(b)). However, this drying method led to a decrease in the crystallinity of the material. In light of these challenges, and considering the success of Ohmura *et al.* in obtaining single crystals, an attempt was made to compare the obtained diffraction patterns with the simulated diffraction pattern of CuTPyrP-MOF as reported by Ohmura *et al.*[257] Interestingly, the observed diffraction patterns neither align with one another, nor did they correspond to the diffraction pattern provided in an earlier publication by the same research group.[262] This discrepancy might be attributed to potential polymorphs.[263–265] Particularly when crystallisation or precipitation

occurs rapidly, which is the case here, it is more likely to result in polymorph formation.[266] Notably, the earlier study utilized a synthetic approach more similar to the one performed here, with the primary difference being a longer stirring period of three days compared to the one-day stirring in this work. In Figure 7.6, MOF 20 and 21 do not match. However, it should be noted that MOF 20 is amorphous, which is more apparent in Figure 7.4, so the position of the peaks appearing in the pattern cannot be discussed. Additionally, for the overall comparison, the graph was heavily zoomed in (Fig. 7.6).

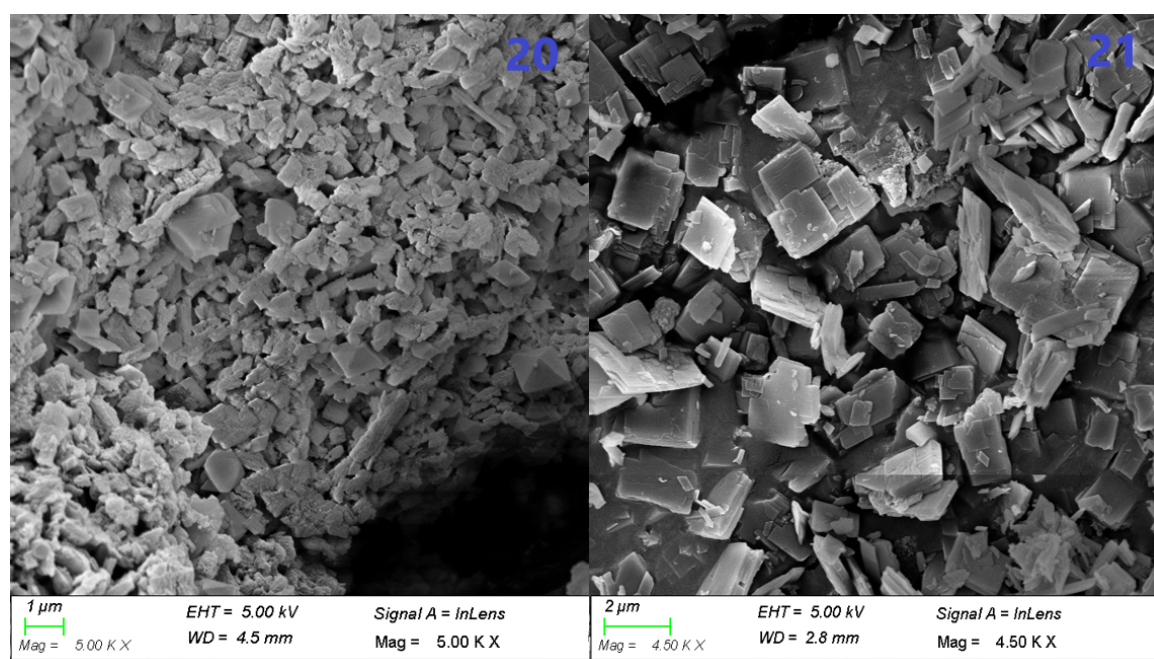


Figure 7.5: Comparison of SEM images of MOF 20 and 21.

The morphology of the two MOF batches was evaluated using SEM imaging. The obtained SEM images (Fig. 7.5) clearly reveal the difference in morphology between the two MOF batches. In the case of MOF 20, agglomerates consisting of single octahedron-like crystals with a size of 1 μm were formed, while MOF 21 showed higher crystallinity and rectangular sheets with a size of 1-2 μm were observed.

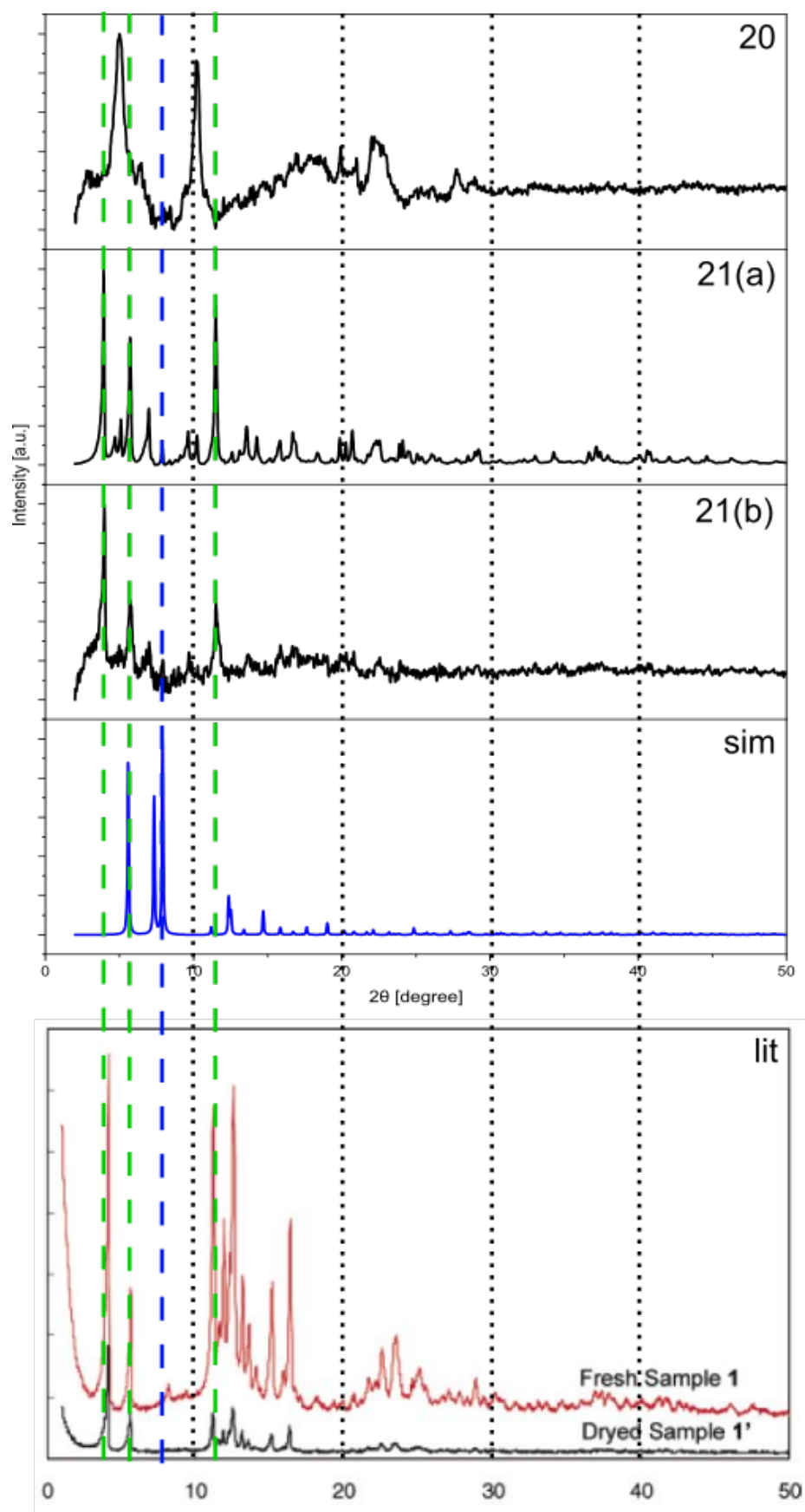


Figure 7.6: Comparison of powder XRD diffraction pattern of batch 20 used in battery cells, batch 21(a) freshly measured, 21(b) dried before measured, simulated pattern (blue) and pattern from literature[262], reproduced with permission, Copyright (2016), American Chemical Society.

Before delving into the electrochemical characterizations of CuTPyrP-MOF, it's important to clarify that the presence of Cu(II) tetraacetate linker does not influence the electrochemistry within the applied voltage window. To verify this, calculations (carried out by Dr. Frank Pammer) for a model of the CuTPyrP-MOF were performed on a singlet tetramer with a charge of -4 using (m06-2x/6-31G(d,p)), pseudo-potential mdf10 for Cu, no solvent). The results revealed that the acetate-centered frontier orbitals (LUMO, LUMO+1) remain unoccupied, while the highest occupied orbitals (HOMO, HOMO-1, and HOMO-2) are mainly localized on the porphyrin rings (Fig. 7.7). The calculations indicate that the Cu-acetate-clusters do not participate directly in redox processes that involve oxidation or reduction by ± 1 .

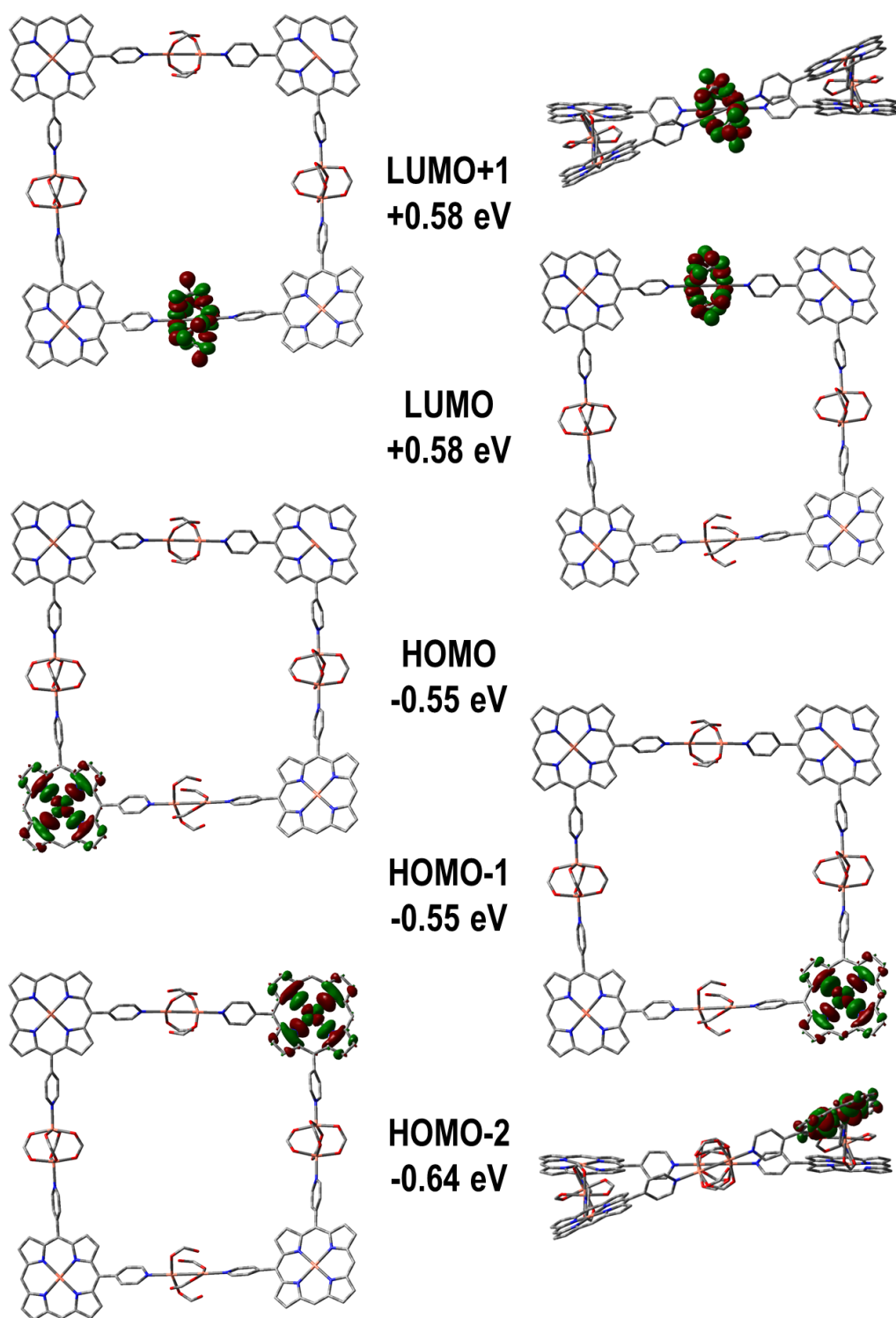


Figure 7.7: Visualization of Frontier Molecular Orbitals (FMO) for the Tetraanion Model of CuTPyP-MOF.

7.3 Lithium-ion Battery

7.3.1 Electrode Preparation and Cell Assembly

To formulate the electrode slurries, a mixture of CuTPyrP-MOF (20) (50 wt%), GNP (graphene nanoplatelet):CNF (carbon nanofibers) (0.93:0.07) (40 wt%), and CMC binder (10 wt%) was combined in a mortar for 25 minutes, using water as the solvent. Subsequently, the slurry was drop-casted onto stainless steel (SS) electrodes with a diameter of 11.8 mm. Following this, the electrodes underwent a two-hour drying period on a heated plate at 60 °C, followed by an extra 15-hour drying under high vacuum conditions (1×10^{-3} mbar) at 100 °C. Notably, the electrodes exhibited a loading of 1 mg cm^{-2} active material.

Electrochemical assessments were carried out within CR2032-type coin cells (MTI, SS316). After the electrode preparation and drying stages, they were transferred to a glove box for the assembly of the cells. Glass fiber filter Whatmann GF/D, comprising two layers, was employed as the separator. The electrolyte utilized was a 1M solution of LiPF_6 dissolved in a mixture of ethylene carbonate (EC) and dimethyl carbonate (DMC) in a 1:1 volume ratio. Approximately 80 μL of electrolyte was used in each cell. The instruments of experimental procedures used to characterize the cells described in chapters 5 and 6.

7.3.2 Results and Discussion

CuTPyrP-MOF compound lacks terminal acetylene groups as opposed to the well-investigated CuDEPP. Therefore, the first step is to investigate the redox chemistry by analyzing the cyclic voltammogram obtained in lithium half-cells. The measurements were conducted within a voltage range of 1.0-4.5 V with a sweep rate of 0.1 mV s^{-1} (Fig. 7.8). During the initial cycle's anodic sweep, an oxidation process emerges at around 4.18 V. This finding is comparable to the behavior observed for TPyrP, as investigated by He *et al.* under the same voltage range in their study against lithium.[254] Notably, the oxidative peak at 4.18 V in their research was found to be irreversible. In contrast, the MOF being studied exhibits the reversibility of the oxidative peak, at least in the initial cycles. He *et al.* speculate that this peak might be

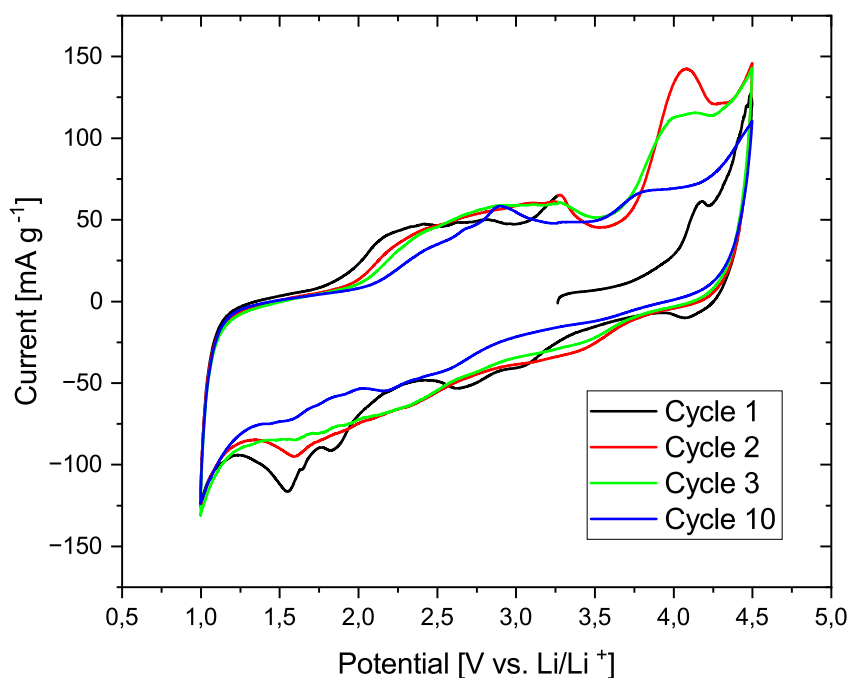


Figure 7.8: Cyclic Voltammogram of 20 in a lithium half-cell with a sweep rate of 0.1 mV s^{-1} .

attributed to interactions with PF_6^- ions.[254] However, this peak's behavior shifts as subsequent cycles unfold: in cycles 2 and 3, it moves to 4.08 V, broadens significantly, and exhibits a shift towards higher currents, while also losing its initial reversibility. Interestingly, after approximately 15 cycles, this peak vanishes and not already after the first as described for CuTPyP in literature.[254] This could be attributed to the porousness of the MOF structure, allowing for deeper penetration of PF_6^- , resulting in a more prolonged interaction over multiple cycles. Furthermore, during the cathodic sweep, reductive peaks become apparent at 1.55, 1.84, 2.64, and 3.04 V. As subsequent cycles progress, the intensity of these peaks diminishes substantially while also slightly shifting, making it challenging to ascertain their reversibility. After an initial series of cycles, the system appears to stabilize, with the intense redox peaks decreasing in intensity. This observation potentially indicates a transition towards pseudocapacitive behavior, suggesting that while the material initially exhibits battery-like characteristics where redox reactions transpire throughout the bulk material, its charge storage mechanism eventually evolves.[267, 268] To prevent potential reduction of Cu(II) to Cu(0) in future investigations, avoiding leaching, the voltage window was set to a range of 1.8-4.5 V, consistent with previous work and rate tests,

and charge-discharge curves were conducted. During the initial 20 cycles, the current

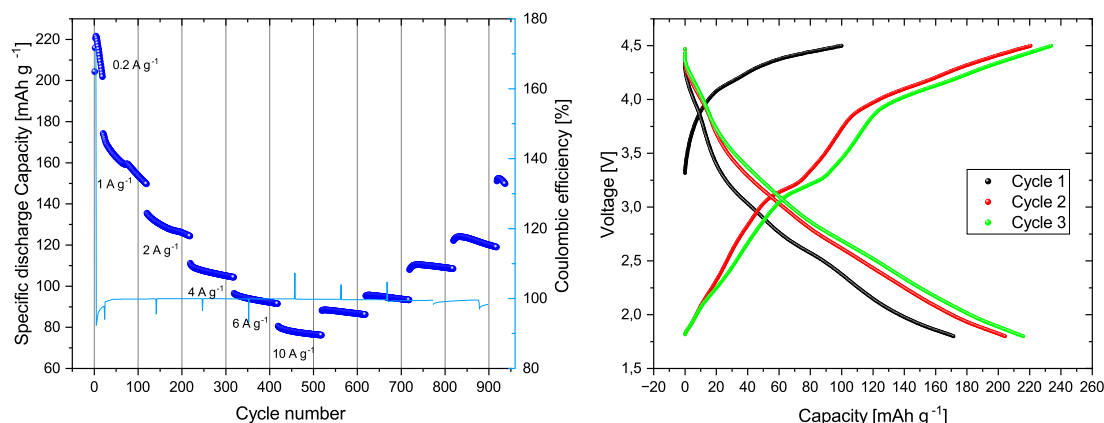


Figure 7.9: (a) Rate test of 20 in lithium half-cell (b) initial charge-discharge curves in a voltage range of 1.8-4.5 V.

densities were maintained at 0.2 A g⁻¹, after which they were progressively increased to 1, 2, 4, 6, and 10 A g⁻¹, with each level sustained for 100 cycles before being reversed. In the first approximately 100 cycles, a rapid decline in capacity was observed, attributed to dissolution in the electrolyte (Fig. 7.9). However, in the subsequent cycles, the system appeared to stabilize, yielding notable specific discharge capacities. Despite this, a certain degree of capacity retention loss became apparent. At current densities of 0.2, 1, 2, 4, 6, and 10 A g⁻¹, the specific discharge capacity is 220, 174, 135, 111, 96, and 80 mAh g⁻¹, respectively. At 1 A g⁻¹, the discharge capacity decreases to 123 mAh g⁻¹ and could be not fully recovered. The specific energy density decreases from 608 Wh kg⁻¹ at 0.1 A g⁻¹ during initial cycles to 211 Wh kg⁻¹ at 10 A g⁻¹. The Coulombic efficiency is close to 100%, although it is greater than 100% during the first cycle. This is also evident in the charge-discharge profile of the first cycle (Fig. 7.9b). This could be attributed to some side reactions or interaction with the PF₆⁻ anion. In this case, current is consumed without affecting the voltage. During the charge, the charge-discharge profile of the second and third cycles reveal two plateaus. The plateaus, appearing at approximately 3.14 and 3.89 V, probably demonstrate a two-phase intercalation of PF₆⁻ anions. The first plateau disappears within the first eight cycles and the second plateau shifts to higher voltages, gradually decreasing in dominance after 80 cycles and eventually not appearing as a plateau anymore (Fig. 7.10).

CuTPyrP-MOF shows potential as a cathode material due to its simple synthesis

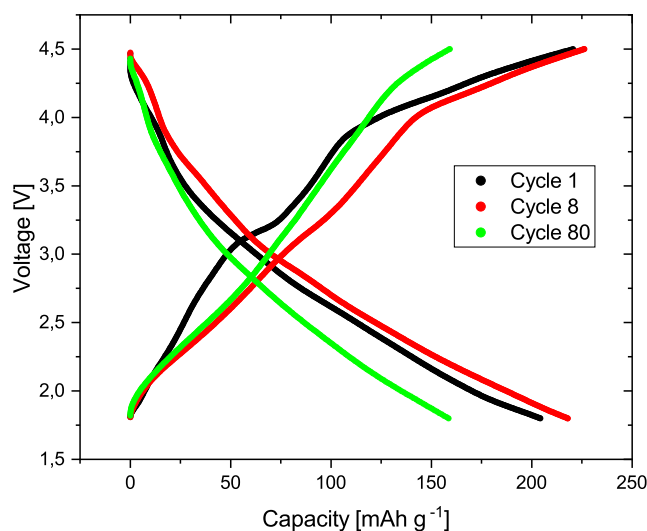


Figure 7.10: Charge-discharge curves of CuTPyrP-MOF visualizing disappearance of plateaus in cycle 8 and 80 compared to cycle 1 with a voltage range of 1.8-4.5 V.

and higher symmetry compared to CuDEPP and similar A2B2-porphyrins. Moreover, the free-base porphyrin TPyrP also presents potential for cathode application. Previous investigations have shown that even the empty free-base TPyrP is working in dual-ion batteries and can function in SIBs.[254] CuTPyrP-MOF indicates exceptional battery-like behaviour and offers high energy density, in contrast to the usual pseudocapacitive properties of porphyrins in batteries. Following the initial results in a lithium half-cell, the material was investigated in aluminum and calcium batteries without any further cell optimization in the lithium half-cell.

7.4 Aluminium Battery

The electrochemical experiments described were carried out by Dr. Rafael Córdoba Rojano under the supervision of Dr. Sonia Dsoke in the research group led by Prof. Dr. Ehrenberg.

7.4.1 Electrode Preparation and Cell Assembly

The electrode slurries were prepared by blending CuTPyrP-MOF (and TPyrP) (50 wt%), C65 carbon (40 wt%), and PAN (polyacrylonitrile) as a binder (10 wt%) in DMSO using a Thinky mixer. Following stirring at 2000 rpm for 10 minutes, a uniform slurry was achieved. This slurry was then applied onto a carbon paper using a doctor blade.

Subsequently, the coated material was dried and formed into 11.8 mm diameter discs, which underwent additional drying at 110 °C under vacuum conditions (1×10^{-3} mbar) for 12 hours. The loading of active materials ranged from 0.8 to 1 mg cm⁻².

Electrochemical tests were performed using a Swagelok cell with tungsten bars. After completing the electrode preparation and drying steps, they electrodes were transferred to a glove box for cell assembly. Two Whatmann GF/D glass fiber filter were used as separators. The electrolyte used was an ionic liquid consisting of AlCl₃ and EMImCl (1-ethyl-3-methylimidazolium chloride) with varying ratios of 1.5:1, 1.3:1, and 1:1. Typically, approximately 250 μL of electrolyte was added to each cell.

The galvanostatic cycling with potential limitation (GCPL) experiments were carried out at 298 K using a BCS-800 system from Biologic. Cyclic voltammetry (CV) measurements were conducted using the VMP-3 multichannel potentiostat from Biologic, with a sweep rate of 0.1 mV s⁻¹. Each test commenced with an initial open circuit voltage (OCV) measurement that lasted for 30 min.

7.4.2 Results and Discussion

CuTPyrP-MOF and the free-base TPyrP were investigated for the first time in a rechargeable aluminum battery. In the initial experiments, the voltage range was set to 0.3-2.3 V (vs. Al/Al³⁺) and the current density was set at 50 mA g⁻¹ (Fig. 7.11). An ionic liquid electrolyte, AlCl₃:EMImCl, was utilized with a ratio of 1.5:1. When considering the free-base porphyrin, the specific discharge capacity exhibited extremely low values, starting at 23 mAh g⁻¹ and decreasing further to 11 mAh g⁻¹. The CuTPyrP-MOF, on the other hand, demonstrated higher stability with less notable capacity loss than TPyrP. In comparison, the initial specific discharge capacity was 129 mAh g⁻¹. It declined to 10 mAh g⁻¹ over 350 cycles for CuTPyrP-MOF, while for TPyrP, it happened within 10 cycles. It is worth noting that typically the first 1-2 cycles are attributed to activation processes in battery materials.[139]

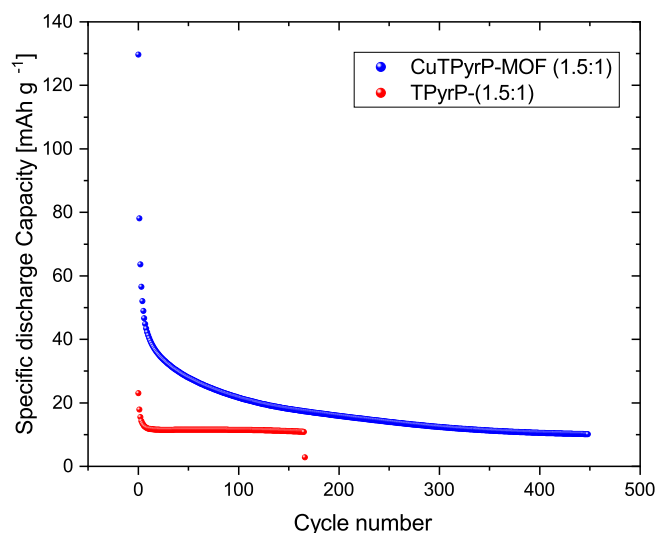


Figure 7.11: Galvanostatic cycling of TPyrP and CuTPyrP-MOF in a voltage range of 0.3-2.3 V (vs. Al/Al³⁺) at 50 mA g⁻¹ using an electrolyte of 1.5:1 AlCl₃:EMImCl.

Unfortunately, the results were unsatisfactory and indicated that the porphyrins are not stable under the influence of a strong acidic electrolyte, indicating corrosion. To address this issue, electrolytes with a less acidic composition were investigated, with ratios of 1.3:1 and 1.1:1 AlCl₃:EMImCl (Fig. 7.12). For the free-base TPyrP, a slight

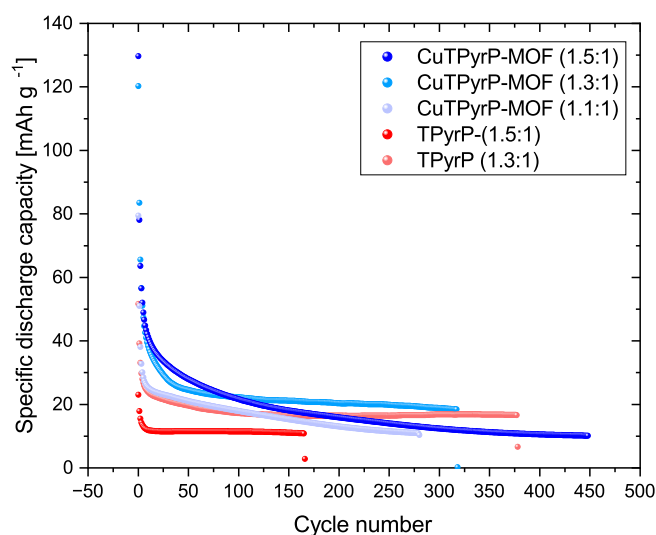


Figure 7.12: GCPL of TPyrP and CuTPyrP-MOF in a voltage range of 0.3-2.3 V (vs. Al/Al³⁺) at 50 mA g⁻¹ comparing electrolyte ratios of 1.5:1, 1.3:1 and 1.1:1 AlCl₃:EMImCl.

improvement was observed for an electrolyte mixture of 1.3:1, where the specific discharge capacity was increased from 11 mAh g⁻¹ to 17 mAh g⁻¹. For the CuTPyrP-MOF, two lower electrolytes were tested, revealing that the 1.3:1 composition is showing a

small improvement from 10 to 20 mAh g⁻¹, whereas the composition of 1.1:1 leads to even lower discharge capacities. This could be due to the lower concentration of the redox active species required in the electrolyte. Since the cause of the issue with the electrolyte could not be proven, the charge-discharge profile was studied (Fig. 7.13a). A surprising plateau was observed below 1 V. This plateau could potentially explain the significant capacity loss, the voltage range was subsequently adjusted to 1-2.3 V (Fig. 7.13b). Even in the above electrolyte compositions of 1.3:1 and 1.5:1, extreme capacity loss was observed cycle after cycle. A slight improvement of approximately

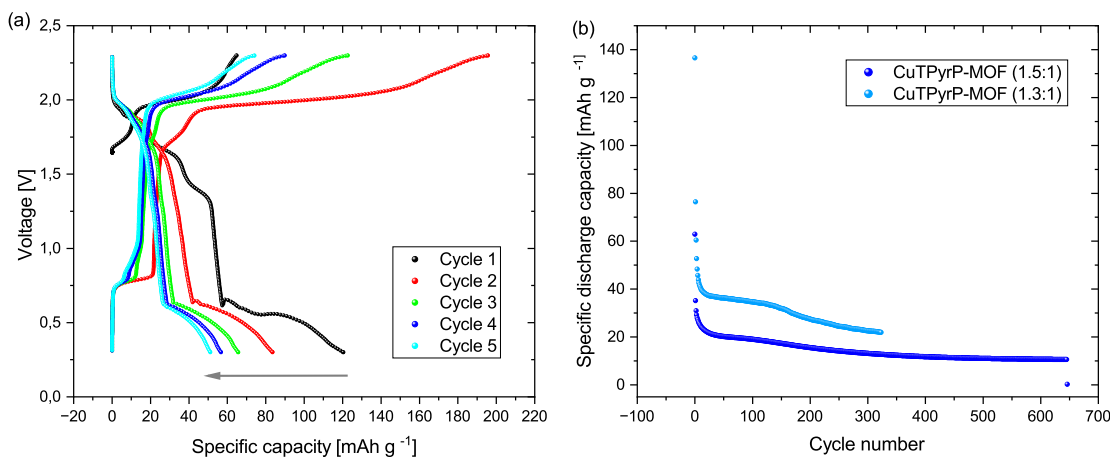


Figure 7.13: (a) Charge-discharge profile CuTPyrP-MOF with 1.3:1 AlCl₃:EMImCl and (b) GCPL in voltage range of 1-2.3 V (vs. Al/Al³⁺) of CuTPyrP-MOF with 1.3:1 and 1.5:1 AlCl₃:EMImCl.

10 mAh g⁻¹ was observed, but the value remained significantly low, below 40 mAh g⁻¹. Two further attempts were made to increase the material's capacity. One attempt was made to change the binder to PVDF and NMP was used as solvent during electrode preparation to make the electrode slurry (Fig. 7.14b). Additionally, one cell was observed via CV until stabilization, which was achieved after 10 cycles (Fig. 7.14a), and then the GCPL measurement was started. Unfortunately, both experiments did not result in the desired improvement of the CuTPyrP-MOF.

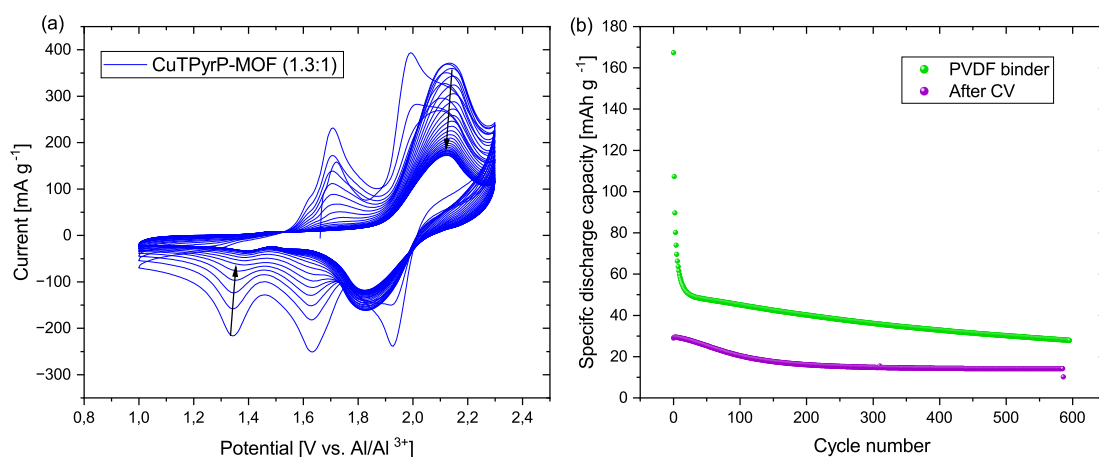


Figure 7.14: (a) CV of CuTPyrP-MOF between 1-2.3 V of cell with 1.3:1 electrolyte composition and (b) GCP of CuTPyrP-MOF after observing in CV and using PVDF as binder.

Although there was a slight increase in the cell's discharge capacity with PVDF binder, it was not stable and showed capacity fading within 600 cycles. Regrettably, both the CuTPyrP-MOF and the free-base TPyrP exhibit instability within a rechargeable aluminum battery, potentially attributed to corrosive interactions with the highly acidic electrolyte or dissolution effects. However, due to the disappointing results, no further attempts have been conducted to optimize the cell.

7.5 Calcium Battery

This section presents the findings reported in the publication titled "A π -conjugated Porphyrin Complex as Cathode Material Allows Fast and Stable Energy Storage in Calcium Batteries", which was accepted in *Batteries and Supercaps* on 4th September 2023. The synthesis and characterization of CuTPyrP were conducted by Shirin Shakouri, while the electrochemical characterization was performed by Thomas Smok, who is also the first author of the manuscript.

7.5.1 Electrode Preparation and Cell Assembly

The electrode slurries were prepared by blending the active materials, CuTPyrP-MOF/TPyrP (60 wt%), along with Ketjen black (30 wt%) and PVDF (10 wt%) in NMP, using a Thinky mixer. A uniform slurry was achieved after 20 minutes of mixing at 2000 rpm. This slurry was then coated onto a graphite-based gas diffusion layer (GDL 29AA, Ion Power) and left to dry overnight under ambient atmospheric

conditions. Subsequently, the coated electrodes were cut into disks measuring 11.8 mm in diameter and subjected to a 12-hour drying process under a vacuum of 1×10^{-3} mbar at 80 °C. The electrode loading was approximately ~ 2 mg cm^2 . Finally, the dried electrodes were transferred to a glove box filled with argon for cell assembly.

Electrochemical cycling tests were conducted using a BCS-805 system from Biologic. CR2032 coin cells were cycled in a voltage range of 0.5-3.3 V using CaSn_3 alloy[43] as the anode material and 0.3M $\text{Ca}[\text{b}(\text{hfp})_4] \cdot 4\text{DME}_2$ solution in DME[45] as the electrolyte. Cyclic voltammetry measurements were conducted with a sweep rate of 0.1-10 mV s^{-1} . Galvanostatic cycling was conducted with a current density of 0.1 and 1 A g^{-1} , except for the rate capability test where the current density was set to 0.2-2 A g^{-1} .

7.5.2 Results and Discussion

DFT calculations were conducted to understand the electronic properties of the investigated materials TPyrP and CuTPyrP (single molecule). The 4-pyridiyl functional groups are estimated to be at a dihedral angle of 70° to the porphyrin plane, which could be the reason for hindered conjugation between the macrocyclic porphyrin ring and the substituents. However, no influence on HOMO-1 and LUMO+1 was detected in the frontier orbital plots for TPyrP. The introduction of copper(II) d^8 changes the electronic structure to a doublet spin state. Although the introduction of copper(II) (TPyrP: HOMO = -5.61 eV, CuTPyrP; SOMOs- α = -5.61, β = 5.64 eV) did not result in any changes in the HOMO. copper(II) is only slightly contributing to the SOMO-1 through the LUMO, where the π -orbitals are very similar to those of the free ligand.

To evaluate redox processes occurring in the cell, cyclic voltammetry measurements were conducted with a sweep rate of 1 mV s^{-1} within a 0.5-3.3 V voltage range (Fig. 7.15). Calcium ion insertion is evident in the cathodic scan at 0.7 V (TPyrP) and 0.8 V (CuTPyrP-MOF), whereas deinsertion occurs in the anodic scan at 1.1 V (TPyrP) and 0.9 V (CuTPyrP-MOF). For free-base TPyrP, the reductive peak representing the insertion gradually decreases in intensity over the consecutive cycles, indicating the entrapment of some calcium ions within the electrode. This is substantiated by

a comparison with the charge-discharge profiles of the galvanostatic cycling, where a large plateau is observed in the discharge curve at around 0.7 V. It is possible for

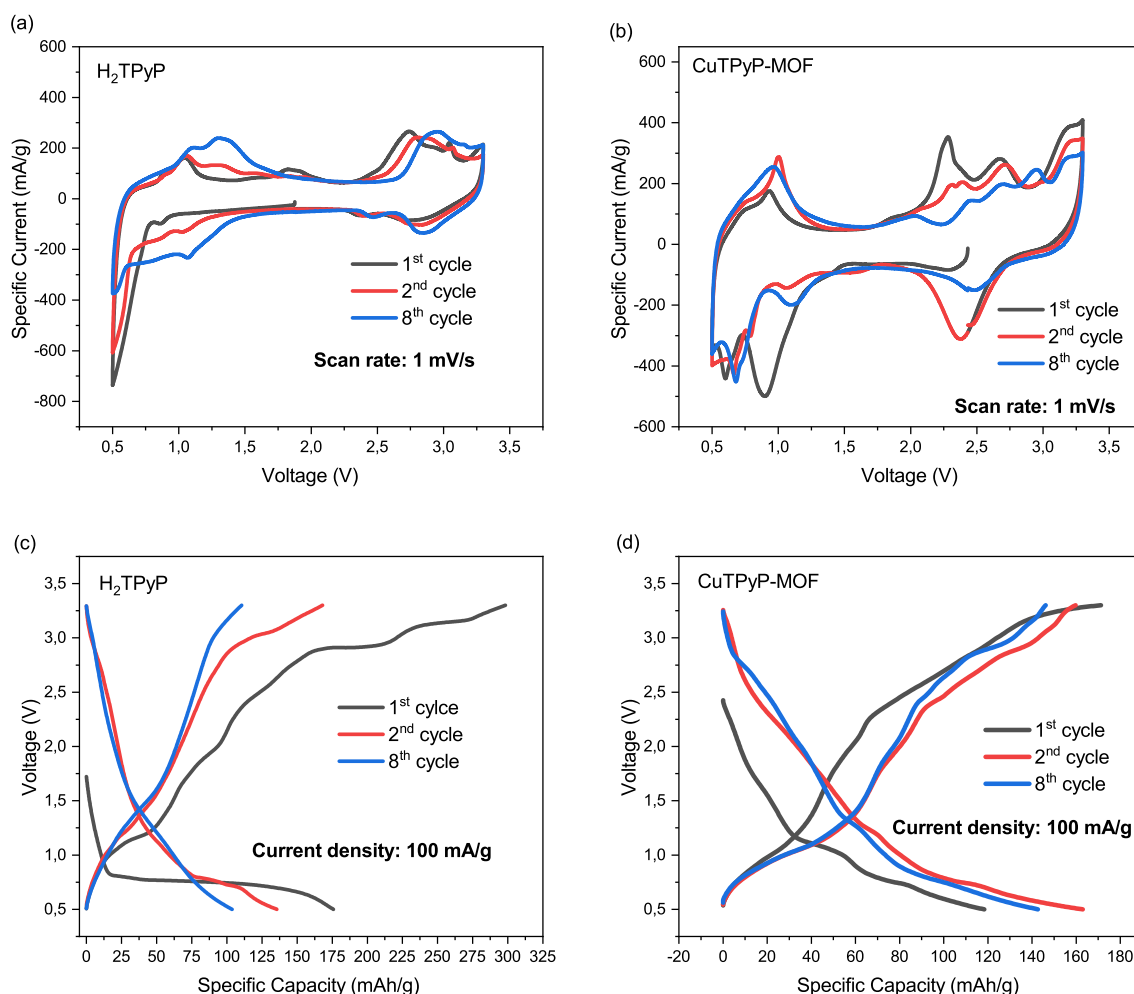


Figure 7.15: CVs of (a) TPyrP and (b) CuTPyrP-MOF in the voltage range of 0.5–3.3 V with sweep rate of 1 mV s^{-1} and the charge-discharge profiles (a) TPyrP and (b) CuTPyrP-MOF performed at a current density of 0.1 A g^{-1} . Reproduced with permission[260], Copyright (2023) Wiley.

calcium ions to become trapped in the central cavity of the free-base TPyrP during the discharging process. Computational methods have demonstrated that structural reorientation occur in both TPyrP and CuTPyrP during calcium ion insertion and deinsertion. Strong interactions between the calcium and the central coordination sites of the free-base TPyrP lead to a deinsertion energy of 3.95 eV mol^{-1} . Nonetheless, because of the robust interactions, the reversibility is notably reduced, and there is a low likelihood of additional irreversible reactions taking place, especially considering the positive reaction energy (0.66 eV mol^{-1}). On the other hand, the direct incorporation of Ca ions is not facilitated by CuTPyrP because of the presence of a central copper ion. In order to enable Ca ion insertion, the copper ion must be displaced from the central cavity. This displacement reduces the deinsertion energy

of CuTPyrP by 1.27 eV mol^{-1} (in comparison with the deinsertion energy of a single CuTPyrP molecule, which is 2.68 eV mol^{-1}). As a result, it increases the likelihood and efficacy of deinsertion in the charging procedure. However, the probability of completely extracting copper from the central cavity and introducing Ca ions or partially reducing the central copper is extremely low because of their positive reaction energies, which are measured at 2.03 eV mol^{-1} and 2.94 eV mol^{-1} , respectively.

Galvanostatic cycling reveal significant differences in performance due to varying levels of calcium insertion and deinsertion. During the initial cycle, TPyrP exhibits a specific discharge capacity of 176 mAh g^{-1} , which decreases to 135 mAh g^{-1} in subsequent cycles. CuTPyrP-MOF exhibits greater stability due to its more reversible calcium ion insertion and deinsertion, resulting in specific discharge capacities of 162 mAh g^{-1} (Fig. 7.15d).

Ex-situ XPS measurements of the Ca 2p region were conducted to obtain deeper insights into the process of calcium ion insertion (Fig. 7.16). As anticipated, calcium was detected in the cycled electrodes, and the concentration of calcium ions was found to be higher in the discharged electrodes. Additionally, calcium trapping was confirmed by SEM/EDX measurements, in which the Ca/Cu ratio was compared between the charged and discharged states (0.3 vs. 2.33 V).

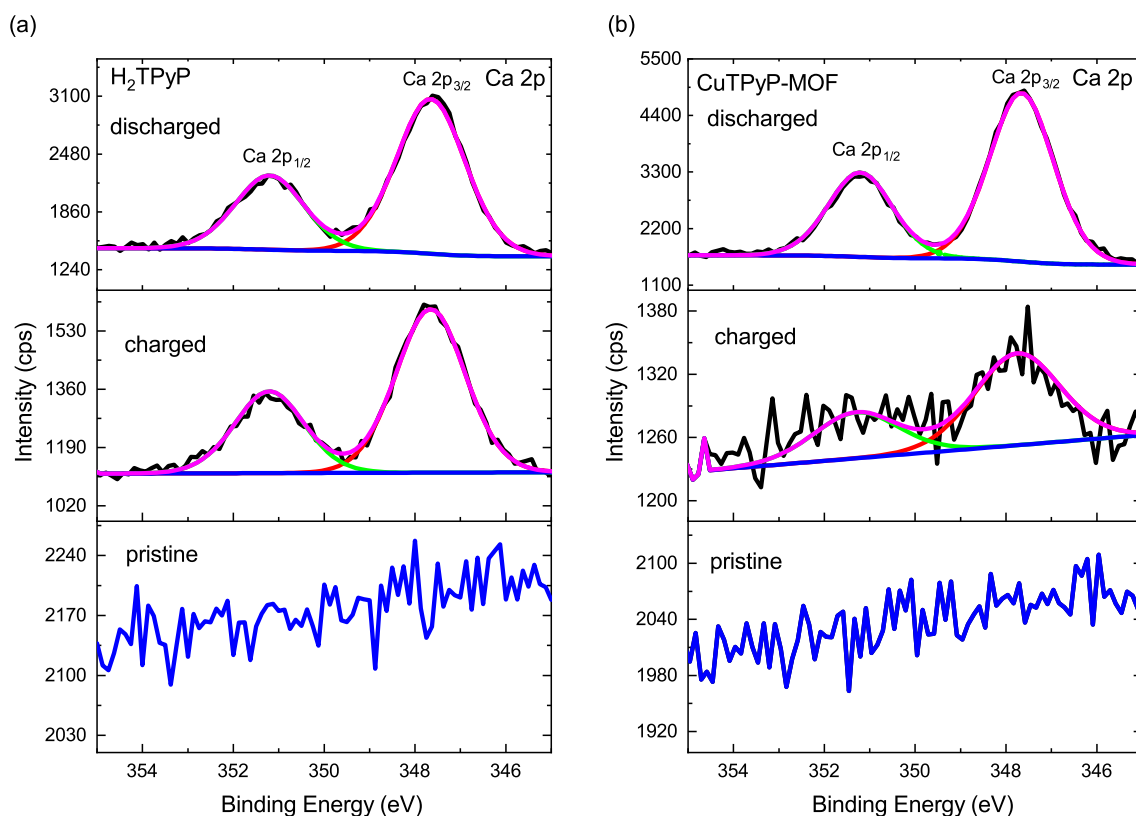


Figure 7.16: Ex-situ XPS in Ca 2p region of discharged (0.5 V), charged (3.3 V) and pristine TPyRP (a) and CuTPyRP-MOF (b). Reproduced with permission[260], Copyright (2023) Wiley.

In relation to CuTPyRP-MOF, cyclic voltammetry (CV) revealed a reversible redox reaction involving the Cu(II) center. The oxidation event occurred at 2.7 V, while the reduction took place at 2.5 V (Fig. 7.15). Previous literature has also indicated the possible reduction of Cu(II) to Cu(I).[150, 152, 155, 159] In this case, the redox reactions seem to exhibit to be more complete. Ex-situ X-ray photoelectron spectroscopy (XPS) analysis of the Cu 2p region indicated a notable appearance of Cu(I) species in the discharged state (Fig. 7.17). In the charged state, a roughly equal ratio of both copper oxidation states was detected. The presence of Cu(I) could likely stem from the nodes of the CuTPyRP-MOF structure.[259] Additionally, there might be an irreversible redox reaction involving copper during charging and discharging, possibly due to interactions with calcium ions.

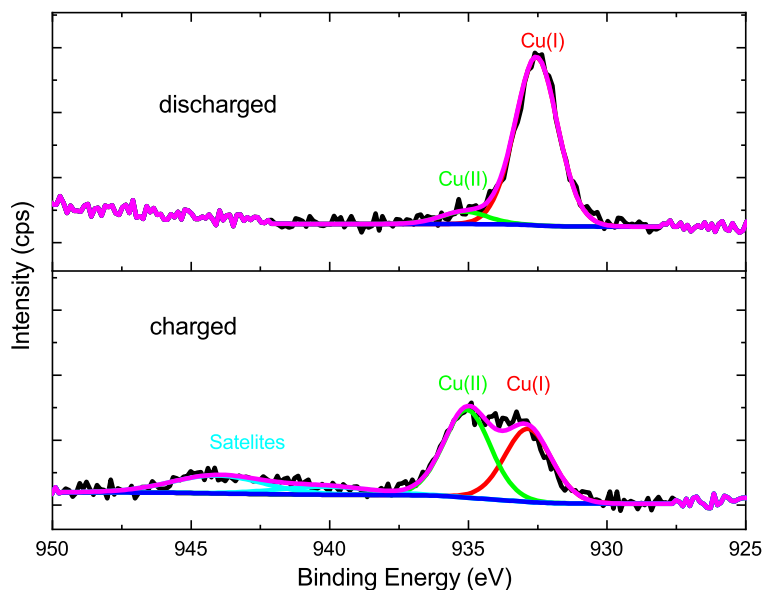


Figure 7.17: Cu $2p_{3/2}$ -XPS spectra of CuTPyP-MOF in charged (at 3.3 V) and discharged (at 0.5 V) state. Reproduced with permission[260], Copyright (2023) Wiley.

In comparison to TPyrP, CuTPyrP-MOF exhibits enhanced performance and rate capability, with both materials displaying excellent stability over more than 3000 cycles. Specifically, CuTPyrP-MOF demonstrates a specific capacity of 115 mAh g^{-1} at a current density of 1 A g^{-1} and maintains a high capacity retention of 78% after 3000 cycles. On the other hand, TPyrP shows a capacity retention of 72% (excluding the first cycle due to calcium trapping). Both TPyrP and CuTPyrP-MOF exhibit impressive rate capability, as evidenced in Figure 7.18, showcasing their performance across current densities ranging from 0.2 to 2 A g^{-1} . The remarkable capacity retention of 90 mAh g^{-1} even at a high rate of 2 A g^{-1} underscores the significant promise of CuTPyrP-MOF as a high-power cathode material in calcium batteries. Additionally, both materials are capable of recovering their initial capacities when returning to lower current densities.

Finally, the successful use of porphyrinoid materials in calcium batteries was demonstrated for the first time.

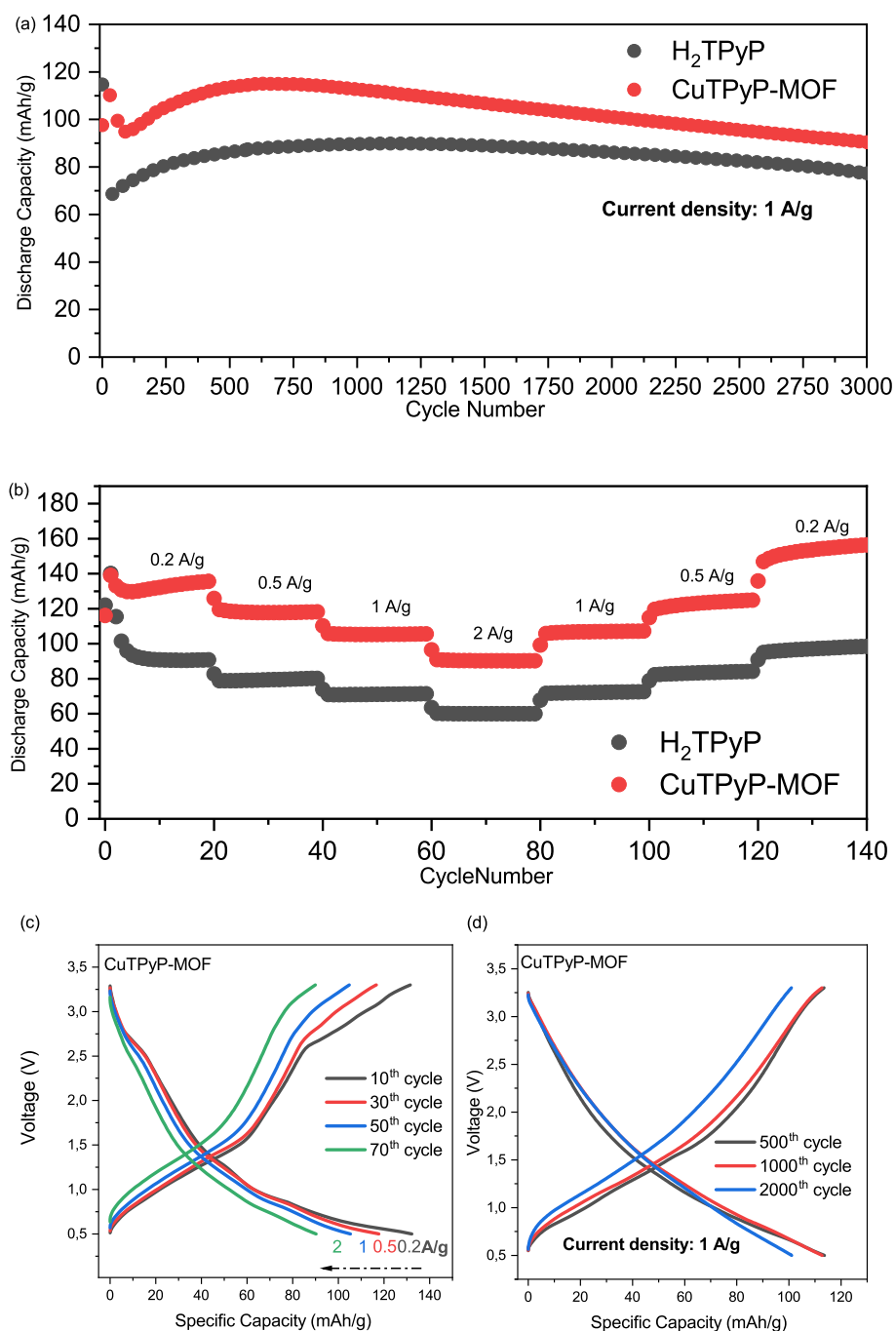


Figure 7.18: (a) long-term cycling at 1 A g⁻¹, (b) Rate capability test with current densities between 0.2-2 A g⁻¹ and charge discharge profiles of CuTPyP-MOF at various current densities (c) and in long-term cycling at 1 A g⁻¹ (d). Reproduced with permission[260], Copyright (2023) Wiley.

7.6 Conclusion

In this section, we present a straightforward method for synthesizing a CuTPyrP-MOF, which offers a simpler and potentially more cost-effective approach compared to the previously used A2B2-porphyrins. Initial tests in a lithium half-cell revealed the promising potential of the MOF structure as an electrode material. The synthesis procedure, cost considerations, yield, and the anticipated porous structure make this material highly appealing for electrode applications. Comprehensive characterization was conducted, indicating that the material is a polymorph. Additionally, further exploration of CuTPyrP-MOF and its free-base counterpart TPyrP was extended to aluminum batteries. Unfortunately, these yielded poor performance, possibly due to the corrosive nature of the electrolyte used. Several attempts were made to improve the performance, such as adjusting the voltage window, modifying the electrolyte composition, and changing the binder.

Surprisingly, despite the lackluster performance in the aforementioned system, both materials exhibited significantly improved stability and performance in calcium batteries, enduring over 3000 cycles. They displayed high discharge capacities even at elevated current densities, positioning them as potential candidates for high-power applications. The outcomes observed in lithium half-cells and calcium batteries offer optimism that these materials could be relevant for other emerging energy storage systems as well.

Chapter 8

The self-conditioning of porphyrinoids in EES

8.1 Introduction

The exceptional performance of porphyrinoids, especially those containing terminal acetylene functionalities in the *meso*-positions of the porphyrin core, can be attributed to a phenomenon known as self-conditioning. This concept is based on the idea of electrochemically induced polymerization occurring on the acetylene groups. The concept of self-conditioning was for the first time reported for [5,15-bis(ethynyl)-10,20-diphenylporphinato]copper(II) CuDEPP in lithium half-cells, where several pieces of evidence supported the hypothesis.[148] It was observed that self-conditioning seemed to be performed in the first charge to 4.5 V, indicating with an irreversible oxidation peak appearing around 4.2 V in the cyclic voltammogram resulting in reduced solubility of the active cathode material. In-depth investigations were carried out to validate this process. Ex-situ IR spectroscopy was employed to detect chemical changes in the triple bonds. Notably, the vibrational peak of C≡C-H at 3264 cm⁻¹ and the C≡C peak at 1596 cm⁻¹ disappeared after the first charge. *Post-mortem* analysis confirmed the decreased material solubility in electrolyte solvents, indicative of more insoluble structure formation and highly important for the long-cycle stability of the LIBs. Furthermore, reduced crystallinity upon cycling was noted, possibly due to polymerization and the incorporation of PF₆⁻ and Li⁺ ions into the material. The pivotal role of the first cycle in self-conditioning was substantiated by impedance measure-

ments, demonstrating a significant reduction in charge-transfer resistance after the initial cycle. This decrease in resistance led to enhanced electrical conductivity of the material. The decline in charge transfer resistance was also observed in other xDEPP molecules[152] as well as CoDEPP in various morphologies.

Subsequent research employed Operando Raman experiments to investigate CuDEPP paired with a graphite counter electrode in an organic full cell.[269] These experiments unveiled electronic structural changes occurring on the acetylene group during the operation of the cell. However, these experiments did not provide further information about the potential electrochemical polymerization process. In similar studies, when CuDEPP was replaced with [5,10,15,20-tetra(ethynyl)porphinato]-copper(II) (CuTEP) as the active material in a lithium-free cell with a graphite counter electrode and PP₁₄TFSI as the electrolyte, no information was provided regarding any structural changes on the terminal acetylene functionalities.[156] A significant stride in comprehending the self-conditioning process was facilitated by the research conducted by Philipp *et al.* [241], which performed by FIB-SEM tomography investigations. This study successfully demonstrated that staining the sample with osmium tetroxide (OsO₄) revealed the formation of aliphatic double bonds. The validation of this staining method was confirmed through wavelength-dispersive X-ray spectroscopy (WDX), EDX, and its distinctive brightness in SEM images. Notably, the appearance of osmium staining was observed exclusively in the cycled samples, leading to the deduction that aliphatic double bonds are formed after the initial charging process. This provides further evidence supporting the notion of electrochemically induced polymerization, implying that double bond formation occurs during the polymerization mechanism. Additionally, Raman spectroscopy demonstrated that the vibrational band corresponding to C≡C at 2087 cm⁻¹ becomes imperceptible following the initial charging process.

Based on the foundation laid by CuDEPP, numerous new porphyrinoids have been investigated as cathode materials, indicating signs of self-conditioning. These includes various molecules retained the ethynyl functionality while substituting the phenyl group with a furyl-group[150], a thiophene[151, 270], or protons in the case of [5,15-bis(ethynyl)-porphinato]copper(II) (CuDEP).[149] In all instances, irreversible oxidative peaks in CV were observed, along with the characteristic disappearance

of prominent bands of the terminal acetylene groups in both IR and Raman spectroscopic measurements. Additionally, there was typically a decrease in solubility and an amorphization of the material during cycling. However, the concept of self-conditioning, attributed to electrochemically induced polymerization, was not exclusive to the terminal ethynyl group; it was also observed for other functional groups such as thiophene[271] and amino groups.[159] In these cases, authors also referred to the irreversible oxidation at voltages between 3.4-4.5 V. Thiophene[272] and amino groups[273] are well-known for their propensity to undergo electrochemically induced polymerization.

To enhance our understanding of self-conditioning and its potential equivalence to electrochemically induced polymerization, we conducted electrochemical studies on porphyrinoids containing functional groups that are not known to undergo electrochemically induced polymerization, as well as on new variations and those previously studied. In addition, computational calculations were employed to explore the polymerization mechanism.

8.2 Electrochemical Experiments

8.2.1 Electrode Preparation

An aqueous slurry was used for the fabrication of the electrodes, utilizing a solid content of 34 wt% in the slurry. As a binder the combination of sodium carboxymethyl cellulose (CMC) and styrene-butadiene rubber (SBR) in a mass ratio of 3:2 was used. To achieve the desired concentration, SBR and CMC was diluted in distilled water and mixed for a duration of five minutes. The electrode slurries were formulated by blending active material (50 wt%), Super P (40 wt%), and binder (10%) in distilled water using a Thinky mixer. After stirring at 2000 rpm for 17 minutes, a uniform slurry was obtained. This slurry was then brush-coated onto a carbon-based gas diffusion layer (GDL) (GDL 29 AA Diffusionsmedien; ion power). The GDL was coated on both sides, left to dry for 3 hours under ambient conditions, and the process was repeated 3-4 times until reaching the desired loading of approximately 1 mg cm² active material. Subsequently, the coated material was dried overnight, punched into 11.8 mm discs, and further dried at 70 °C under vacuum conditions (1x10⁻³ mbar) for

15 hours. The active material loading ranged between 1 and 1.3 mg cm⁻².

8.2.2 Cell Assembly

The electrochemical assessments were carried out using a CR2032-type coin cell (MTI, SS316). After the preparation and drying of the electrodes, they were transferred to a glove box for the assembly of the cell. Two layers of Whatmann GF/D glass fiber filter were utilized as a separator. The electrolyte contained of a 1M solution of LiPF₆ dissolved in a mixture of ethylene carbonate (EC) and dimethyl carbonate (DMC) in a 1:1 volume ratio. Typically, around 80 μ L of the electrolyte was introduced into the cell.

8.2.3 Electrochemical Measurement

The galvanostatic cycling with potential limitation (GCPL) experiments were conducted at a temperature of 298 K using the BCS-800 system by Biologic. When it came to cyclic voltammetry (CV) assessments, the VMP-3 multichannel potentiostat from Biologic was used, employing a sweep rate of 0.1 mV s⁻¹. The testing procedure consistently started with a three-hour recording of the open circuit voltage (OCV).

8.3 Results and Discussion

Electrochemically induced polymerization with ethynyl, thiophene, and 4-aminophenyl groups in the *meso*-position of the porphyrin core have been reported earlier. Figure 8.1 shows the structure of selected porphyrinoids for investigation. We used substrates with ethynyl groups and replaced them with phenyl and pyridyl group. Pyridyl may have electrochemical polymerization potential.[274] However, there are no reports of electropolymerization during cycling for CuTPyrP.[254] CuTPP, CuDPP, and CuD-PyrPP were purchased commercially, while CuDEPP and CuTEP were synthesized following literature procedures.[156] The synthesis of CuTPyrP-MOF was described in the previous chapter. Attempts to synthesize CuTPyrP as a single-molecule always resulted in the formation of the MOF structure. All compounds were characterized using UV-Vis absorption spectroscopy, Fourier-Transform Infrared spectroscopy (FTIR), Matrix-assisted laser desorption/ionization-time of flight mass spectrometry (MALDI-ToF), and powder X-Ray diffraction (XRD). Density functional theory

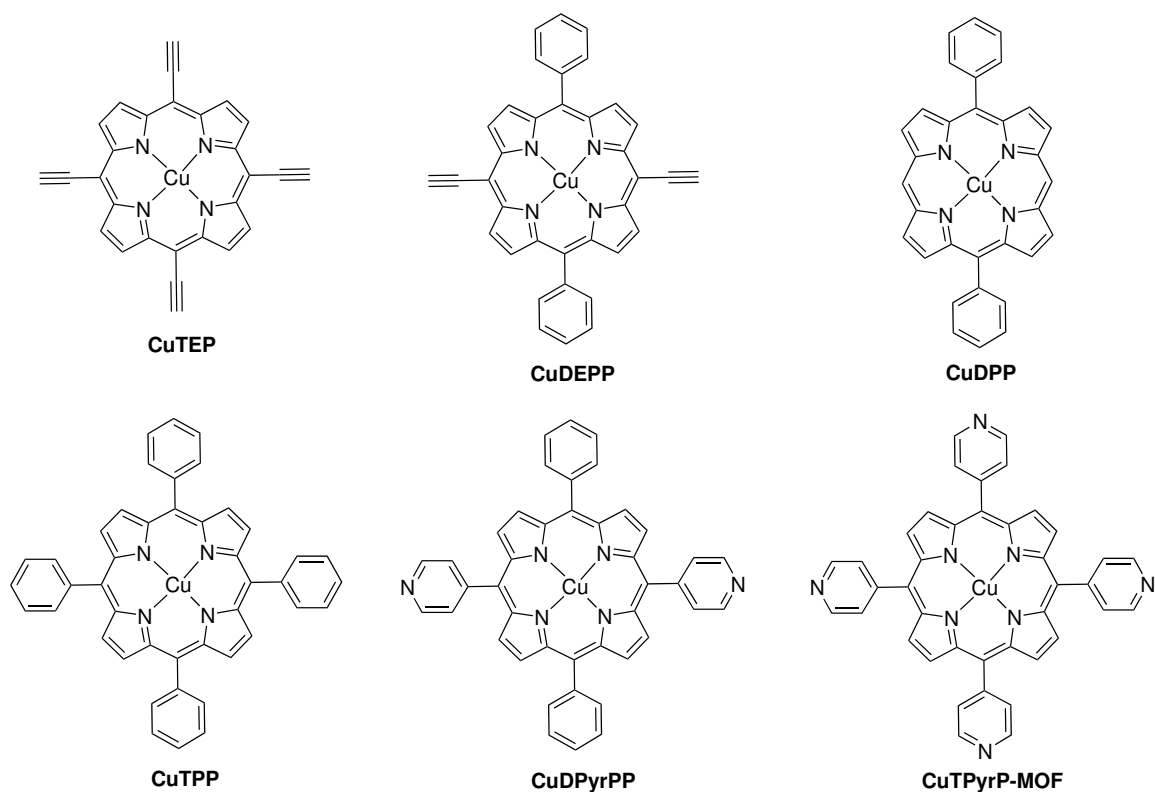


Figure 8.1: Selected porphyrinoids for this study.

(DFT) calculations were performed to evaluate the electronic properties of the materials.

To gain a deeper understanding of the electrochemistry of the newly-introduced porphyrinoids, cyclic voltammetry was performed in a voltage range between 1.8-4.5 V (vs. Li/Li⁺) using a sweep rate of 0.1 mV s⁻¹. The porphyrinoids were used as the working electrode while lithium served as the counter and reference electrode.

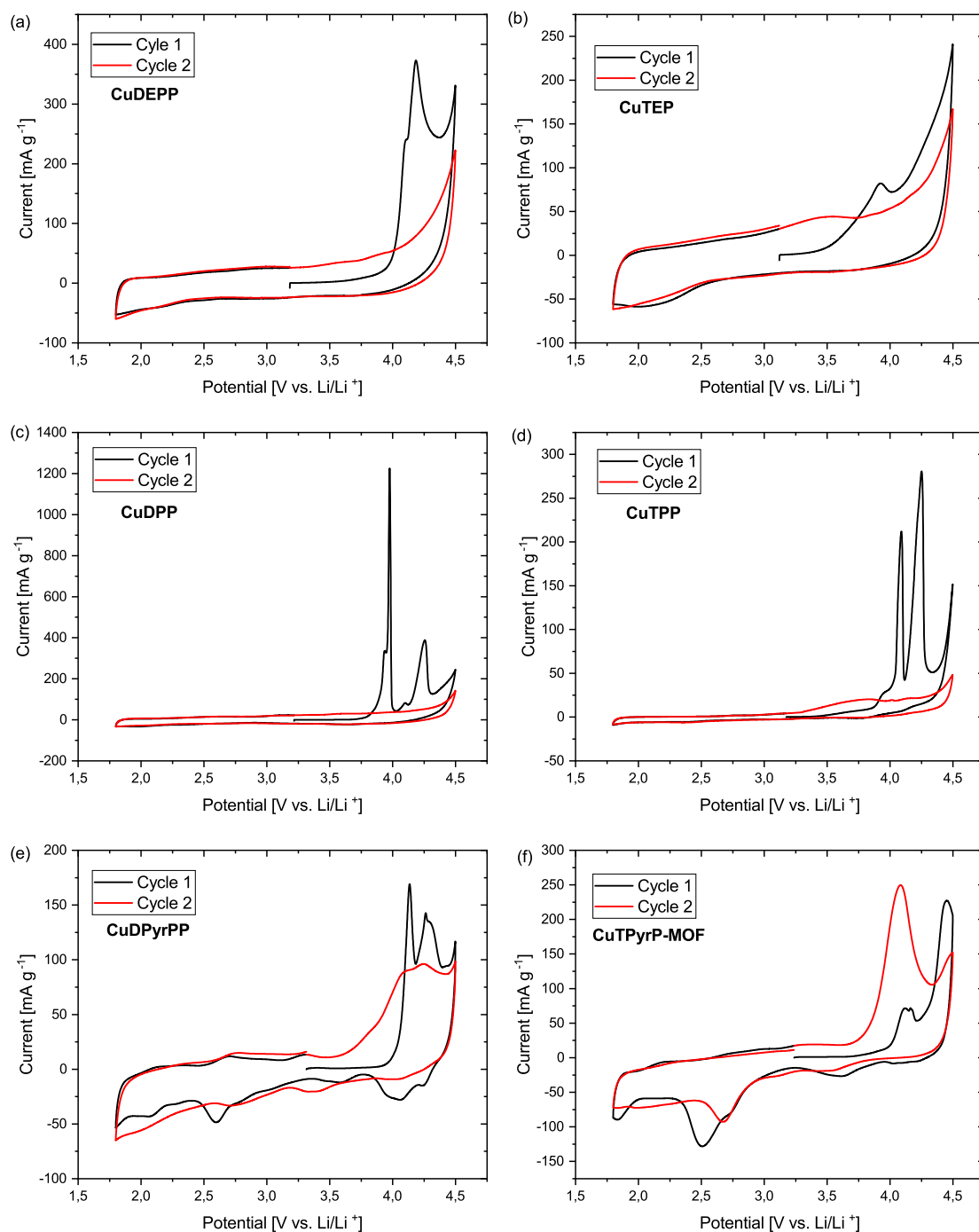


Figure 8.2: Comparison of the first two cycles in CV in a voltage range of 1.8-4.5 V at a sweep rate of 0.1 mV s^{-1} (a) CuDEPP, (b) CuTEP (c) CuDPP (d) CuTPP (e) CuDPyrPP and (f) CuTPyrP-MOF.

All of the first cycles shown in Fig. 8.2 display an irreversible oxidation peak with the exception of CuDPyrPP (Fig. 8.2e), which displays reversibility. CuDPP, CuTPP, CuTPyrP-MOF and CuDPyrPP also exhibit two irreversible peaks. Table 8.1 lists

Table 8.1: Irreversible oxidation peaks observed during the initial charge cycle, potentially correlated with the self-conditioning process.

	Oxidation 1 [V]	Oxidation 2 [V]
CuDPyrPP	4.13	4.26
CuTPyrP-MOF	4.13	4.45
CuDPP	3.98	4.26
CuTPP	4.09	4.25
CuDEPP	4.18	/
CuTEP	3.92	/

the voltages at which the oxidations occurs. The peaks appear within a voltage range of 3.92 to 4.45 V, with strong variations in their intensity and sharpness. In particular, the irreversible oxidation at 3.98 V in CuDPP exhibits very high intensity. The first cycles of the pyridine-functionalized porphyrinoids (Fig. 8.2b) also reveal some additional oxidative and reductive peaks. To determine if the irreversible peaks disappear after the first cycles, successive cycles must be evaluated (Fig. 8.3).

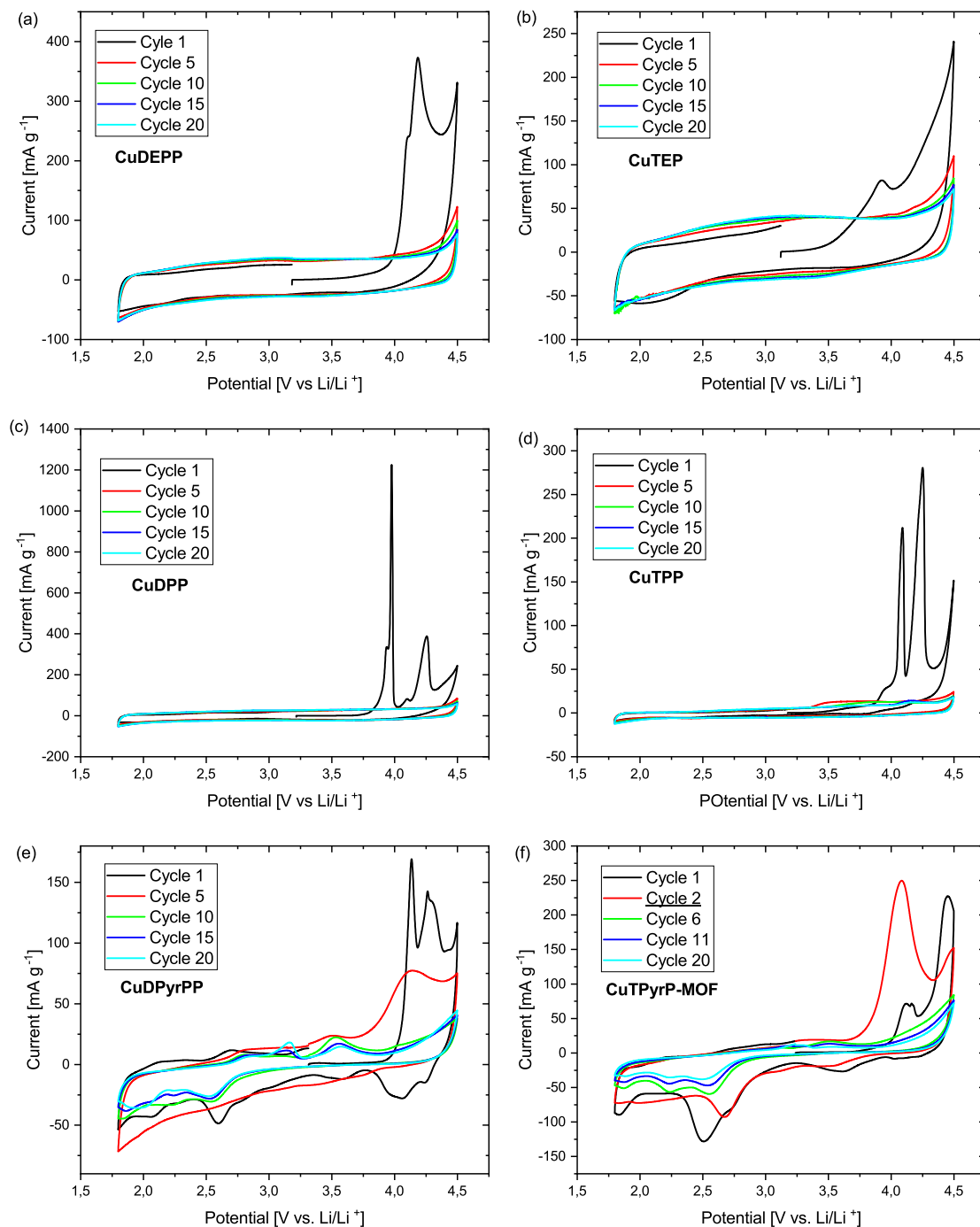


Figure 8.3: Consecutive cycles in CV of CuDEPP, CuTEP, CuDPP, CuTPP, CuTPyrP-MOF and CuDPyrP in a voltage range of 1.8-4.5 V with sweep rate of 0.1 mV s⁻¹.

In CuDEPP, CuTEP, CuDPP, and CuTPP, the irreversible oxidation peaks disappear after the initial cycle. In the case of porphyrinoids containing ethynyl functionalities, this irreversible peak is associated with electrochemically induced polymerization. During the oxidation process, the removal of one electron can lead to the formation of a cationic radical at the ethynyl functionality, which in turn can initiate polymerization. This reaction results in the creation of aliphatic double bonds. A more detailed discussion of the mechanistic aspects will be provided at a later point in this chapter. CuTPP and CuDPP are solely functionalized with phenyl groups, which are not known to undergo electrochemically induced polymerization. Thus, the appearance and disappearance of the irreversible peak in their cases must be attributed to a different process. Furthermore, pyridine functionalities were introduced in the case of CuDPyrPP and CuTPyrP-MOF. In the former, the polymerization at the pyridine functionality might be a possibility[274], although no additional literature could be found reporting on the electropolymerization of pyridine groups. In the investigation by He *et al.*, where single-molecule CuTPyrP was employed as an electrode material, no indications were found of occurring polymerization.[254] Additionally, the self-conditioning peak appears to be reversible in the case of CuDPyrPP, a scenario that would be unlikely in the formation of a polymeric structure. This observation suggests that the irreversible oxidation peak (except for CuDPyrPP, where it is reversible), could be interpreted as a stabilization process. This stabilization process appears to lead to the formation of a polymeric structure in the case of ethynyl-functionalized porphyrinoids. For porphyrinoids lacking functionalities known to undergo electrochemical polymerization, this stabilization could be attributed to interactions with electrolyte anions, such as PF_6^- used in this study. This interaction would also play a role in the case of ethynyl-functionalized porphyrinoids. This hypothesis gains substantial support from the fact that the choice of electrolyte, as demonstrated in the studies by Ren *et al.*, has an impact on the activation process of CuDEPP.[157] It was shown that different electrolytes lead to varying capacity improvements after activation. The interaction between the active material and the PF_6^- anions can be described as an anion- π interaction, as reported in the literature[111] and depicted in Fig. 2.17. This non-covalent force might lead to the formation of sandwich-like anion- π aggregates, where a PF_6^- anion is placed between every porphyrin ring. This

interaction would be more relevant if the active material shows solubility in the electrolyte, as this interaction is mainly reported in organic redox flow batteries.[275] It was qualitatively shown that CuTPP, CuTPyrP-MOF, CuDPyrPP, and CuDPP have the highest solubility (Fig. 8.7), probably causing more interaction, whereas CuDEPP and CuTEP are almost insoluble. In theory, it could also be considered that the irreversible oxidation peak is showing, in the case of CuTEP and CuDEPP, the reported electrochemically induced polymerization, but in the case of the other systems, it is showing the interaction with the PF_6^- anion instead.

Detailed examination of the charge-discharge curves, particularly during the initial cycles, were performed to gain more understanding. The cycling tests were conducted within a voltage range of 1.8 to 4.5 V, varying the current density across 0.1, 0.2, 0.5, 1, 2, 4, and then back to 1 A g^{-1} .

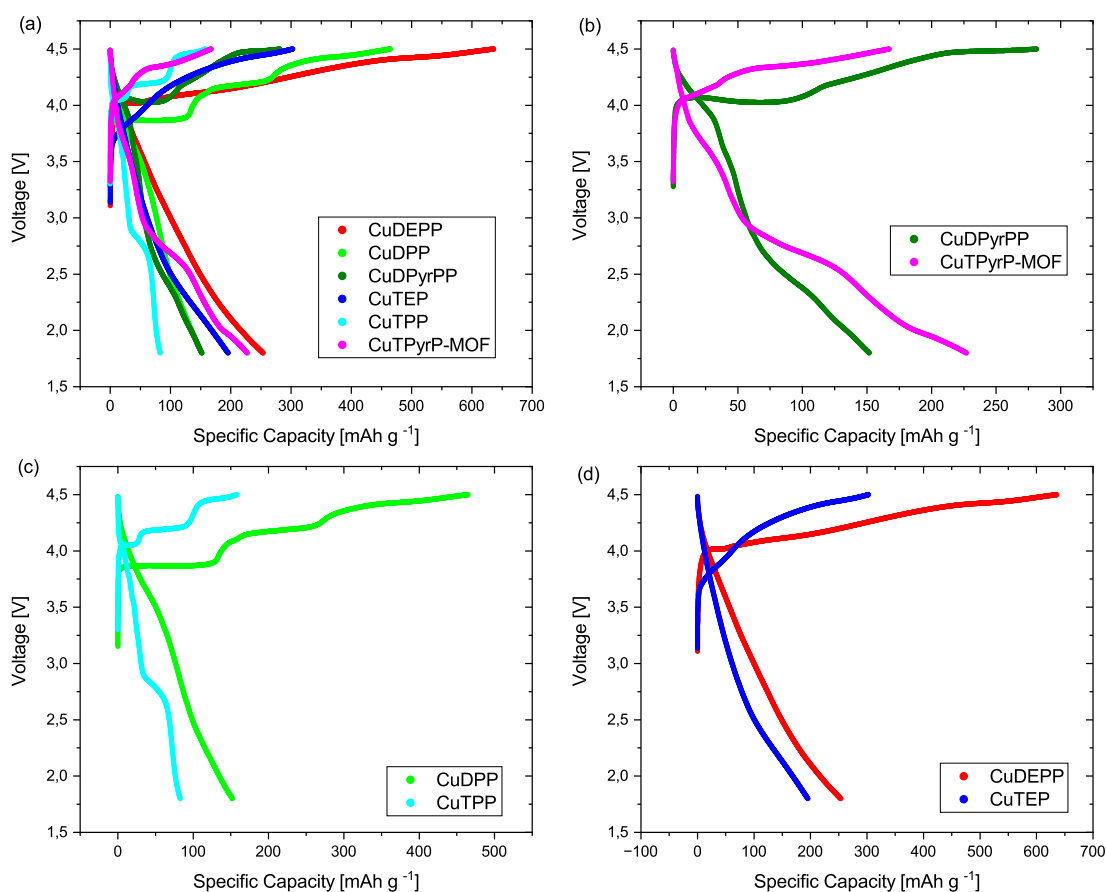


Figure 8.4: Comparison of the charge-discharge profile in a voltage range of 1.8-4.5 V at a current rate of 0.1 mV s^{-1} (a) all, (b) pyridine functionalized porphyrinoids (c) phenyl functionalized porphyrinoids and (d) porphyrinoids with ethynyl functionality.

All charge-discharge profiles, except for CuTPyrP-MOF, display overpotentials (Fig. 8.4), which are commonly associated with the self-conditioning process. However, due to the unique molecular structure of the MOF framework in CuTPyrP-MOF and the possible influence of its internal cavity on charge storage, its direct comparison with those of individual molecule-based porphyrinoids might not be straightforward. Two plateaus are observed during the initial charge of CuDPyrPP at around 4.06 V and 4.48 V, which correspond to the two peaks observed in the CV. Phenyl-functionalized porphyrins display three distinct plateaus that are shown in Figure 8.4(c). In the case of CuDPP, plateaus are observed at 3.86, 4.18, and 4.42 V, while for CuTPP, they are observed at 4.05, 4.19, and 4.46 V. The voltages are relatively similar to each other, except for the initial plateau. CuDPP shows a first plateau appearing at lower voltages. The peaks observed in the CV measurements correspond to the well-defined steps in the charge curve. These plateaus could result from multiphase insertion of PF_6^- ions or indicate a phase transformation process.[276] Notably, the presence of three distinct plateaus suggests that the self-conditioning mechanism of phenyl-functionalized porphyrins may involve a conditioning process other than polymerization. This alternative process could potentially encompass a unique interaction with PF_6^- ions. Another possibility to consider is the interaction between different porphyrin molecules. Both CuDEPP and CuTEP (Fig. 8.4d) demonstrate the typical charge-discharge profile with CuTEP having a significantly smaller overpotential than CuDEPP. This difference suggests that the polymerization process of CuTEP may be more facile compared to that of CuDEPP. This observation is supported by peak appearing at a lower voltage in the CV and GCPL of CuTEP compared to CuDEPP. During the initial 20 cycles at 0.1 A g^{-1} in the rate tests, a noticeable rise in specific discharge capacity is observed (Fig. 8.5): CuDEPP's capacity increases from 245 to 252 mAh g^{-1} , CuTEP's from 180 to 193 mAh g^{-1} , CuDPyrPP's from 140 to 148 mAh g^{-1} , and CuDPP's from 136 to 149 mAh g^{-1} . This capacity augmentation, except for CuDPyrPP and CuDEPP, which increases by 8 mAh g^{-1} and 7 mAh g^{-1} , amounts to 13 mAh g^{-1} . Such an enhancement could potentially stem from a comparable stabilization process taking place in these cases. Notably, the highest specific capacities are achieved by CuDEPP and CuTEP, both of which feature terminal acetylene groups. This outcome strongly suggests that self-conditioning, potentially

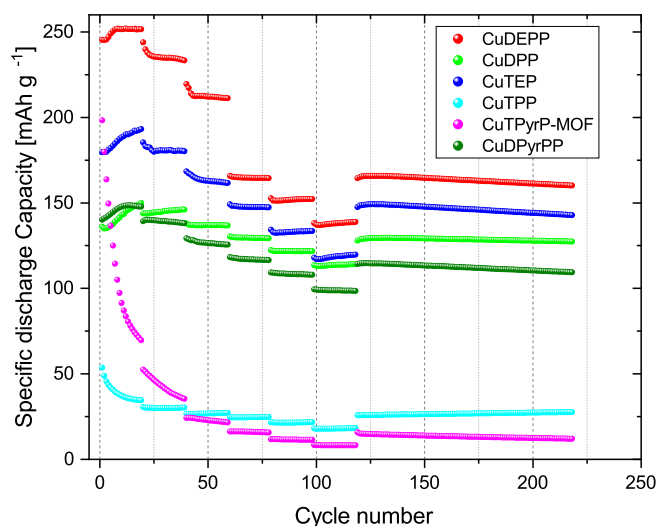


Figure 8.5: Rate tests in a voltage range of 1.8-4.5 V at a current rates of 0.1, 0.2, 0.5, 1, 2, 4 and back to 1 A g⁻¹.

leading to polymerization in the case of CuDEPP and CuTEP, results in the most robust performance. It's worth noting that through further optimization of cell components, better performance might be achievable for all other compounds employed as electrode materials. For instance, the performance of CuTPyrP-MOF improved with the use of different binders and carbon.

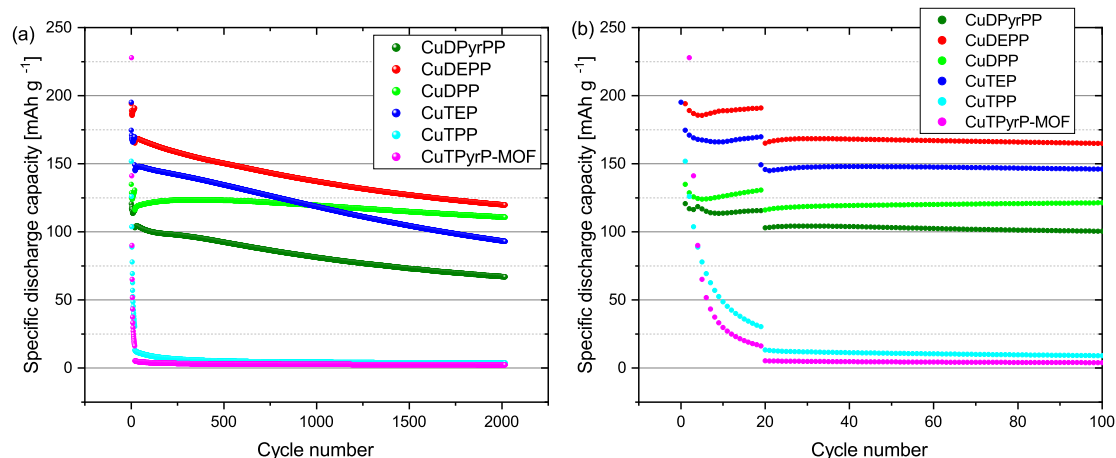


Figure 8.6: Long-term cycling in a voltage range of 1.8-4.5 V with initial 20 cycles at a current rate of 0.2 A g⁻¹, increasing to 1 A g⁻¹ (b) zoom to the first 100 cycles.

To assess long-term stability, the cells underwent an initial 20 cycles activation at a current density of 0.2 A g⁻¹ followed by additional 2000 cycles at 1 A g⁻¹ (Fig. 8.6). The results exhibited remarkable stability and capacity retention for especially CuDPP, with an impressive 95% retention after 2000 cycles at a current density of 1 A g⁻¹.

CuDEPP demonstrated a capacity retention of 72%, while CuDPyrPP and CuTEP exhibited 66% and 62% retention, respectively. In contrast, CuTPP and CuTPyrP-MOF reached a state with very low capacities. Upon zooming in on Figure 8.6b, a closer inspection reveals the dissolution of CuTPP and CuTPyrP-MOF. Solubility tests in DCM revealed that CuTPP has the highest solubility, consistent with the results obtained in the performance test, whereas CuTEP and CuDEPP exhibit the lowest solubility levels. In particular, CuTEP appears to be completely insoluble since no colouring of the solvent was observed (Fig. 8.7). The dissolution of CuTPyrP-MOF may be inherent to the slurry composition rather than the material's solubility. The kinetics of the storage with various materials was further investigated to gain

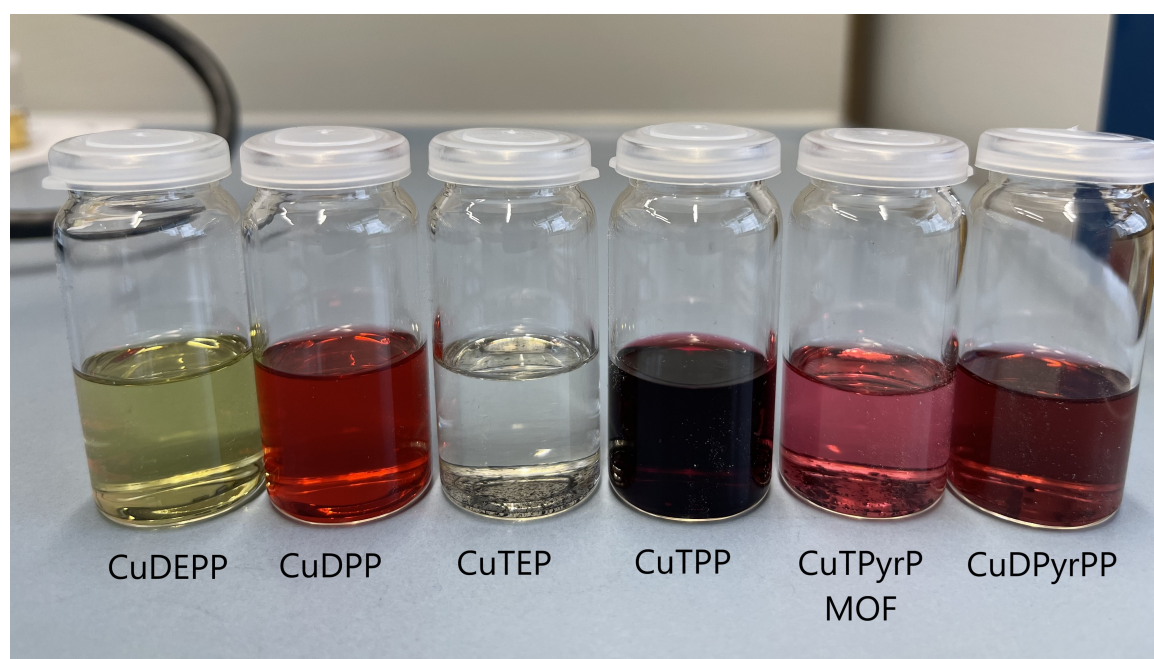


Figure 8.7: Dissolution of CuDEPP, CuDPP, CuTEP, CuTPP, CuTPyrP-MOF and CuDPyrPP in DCM after one hour.

a deeper understanding of the charge storage mechanism. CV curves were recorded with increasing the sweep rate from 0.1 to 10 mV s^{-1} . The current (i_ν) is related to the sweep rate[277] according to the equation:

$$i_\nu = a\nu^b \quad (8.1)$$

where a and b represent adjustable constants and ν the sweep rate. The b -value of 0.5 indicates domination by the diffusion process, while a value of 1.0 indicates a surface-controlled response. To obtain a quantitative understanding of the capacitive

contribution, the following relationship was employed[278]:

$$i_{\nu} = k_1\nu + k_2\nu^{1/2} \quad (8.2)$$

which can be rearranged as:

$$\frac{i_{\nu}}{\nu^{1/2}} = k_1\nu^{1/2} + k_2 \quad (8.3)$$

Here, $k_1\nu$ and $k_2\nu^{1/2}$ correspond to the pseudocapacitive effects and diffusion-controlled effects, respectively. Tests and calculations were conducted on all six listed compounds, and the results can be found in the appendix. This section illustrates the calculation process using CuDPP (Fig. 8.8) and CuTPyrP-MOF (Fig. 8.9) as examples.

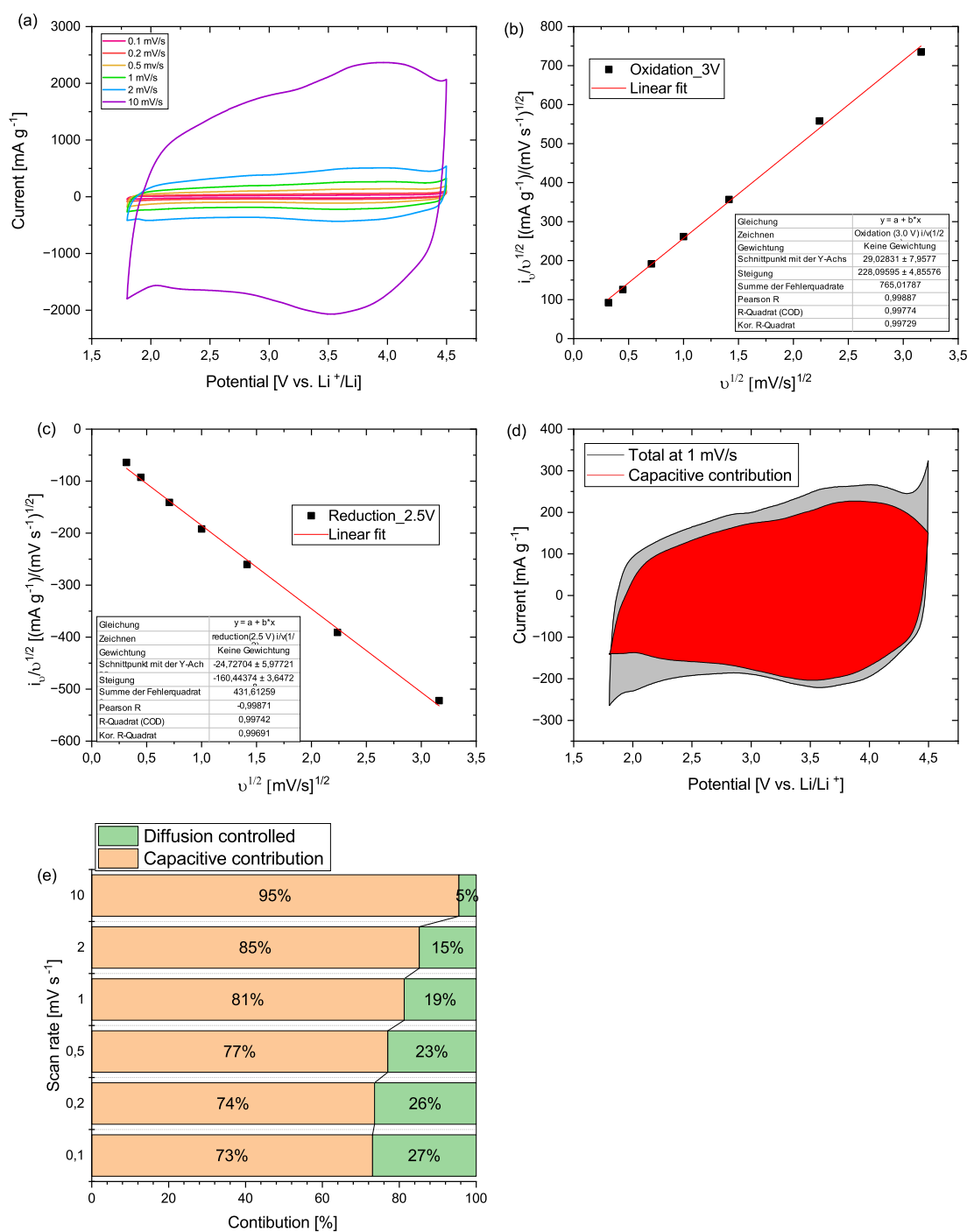


Figure 8.8: (a) CV curves of CuDPP obtained after various sweep rates in voltage range of 1.8-4.5 V (b) and (c) plot of $i_p/\nu^{1/2}$ vs. $\nu^{1/2}$ (d) visualized capacitive contribution at 1 mV s⁻¹ and (e) contribution ratio of all sweep rates.

For CuDPP, the capacitive contribution at 1 mV s^{-1} is approximately 81% (Fig. 8.8). As the sweep rate increases from 0.1 mV s^{-1} to 10 mV s^{-1} , the capacitive contribution rises from 73% to 95%. This indicates that the pseudocapacitive contribution significantly influences the charge storage mechanism, likely related to the surface properties. CuTPyrP-MOF does not exhibit the typical rectangular CV curves of pseudocapacitive materials, which was further confirmed by studying its kinetics.

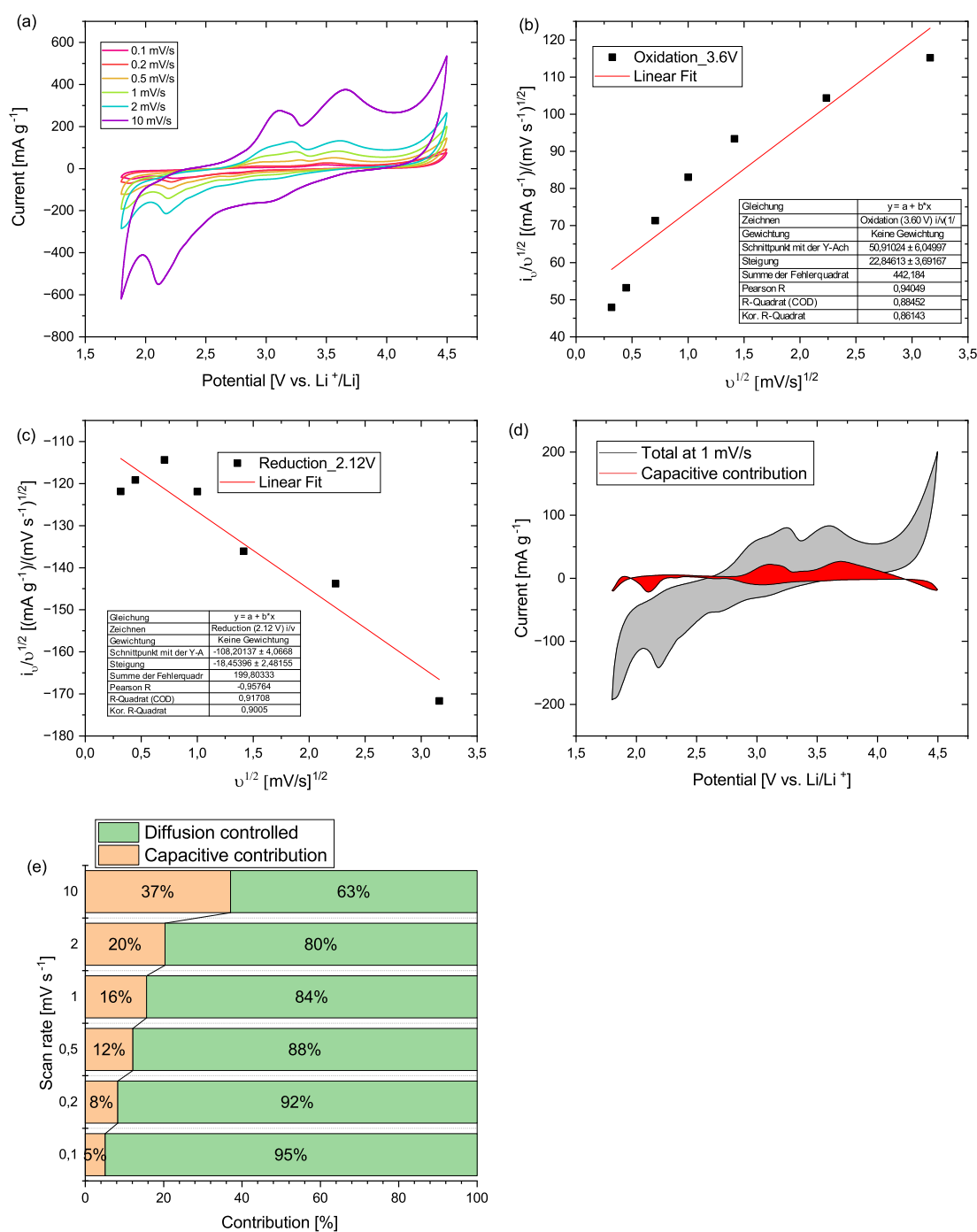


Figure 8.9: (a) CV curves of CuTPyrP-MOF obtained after various sweep rates in voltage range of 1.8-4.5 V (b) and (c) plot of $i_p/\nu^{1/2}$ vs. $\nu^{1/2}$ (d) visualized capacitive contribution at 1 mV s⁻¹ and (e) contribution ratio of all sweep rates.

Interestingly, clear evidence points towards CuTPyrP-MOF being more diffusion-controlled (Fig. 8.9). This marks the first reported instance of a porphyrin structure with such behavior being validated, indicating a battery-like charge storage mechanism. The capacitive contribution is relatively modest, standing at 16% at a sweep rate of 1 mV s^{-1} . As the sweep rate is increased from 0.1 to 10 mV s^{-1} , the pseudocapacitive component rises from 5% to 37%, which is a commonly observed trend.[279] Out of all the six compounds investigated, CuTPyrP-MOF stands out with its more diffusion-controlled contribution in the charge storage mechanism (Fig. 8.10). Here, the faradaic reaction may occur more within the bulk of the electrode material.[280] The battery-type behaviour is likely attributable to its MOF structure, which is highly porous. Although at 0.2 mV s^{-1} it can be observed that CuDPP is slightly more pseudocapacitive-controlled than the other porphyrins (except MOF). This effect disappears at higher sweep rates. The higher capacitive contribution could explain the previously mentioned surprisingly high performance and stability, especially given the absence of terminal acetylene functionality for stabilization.

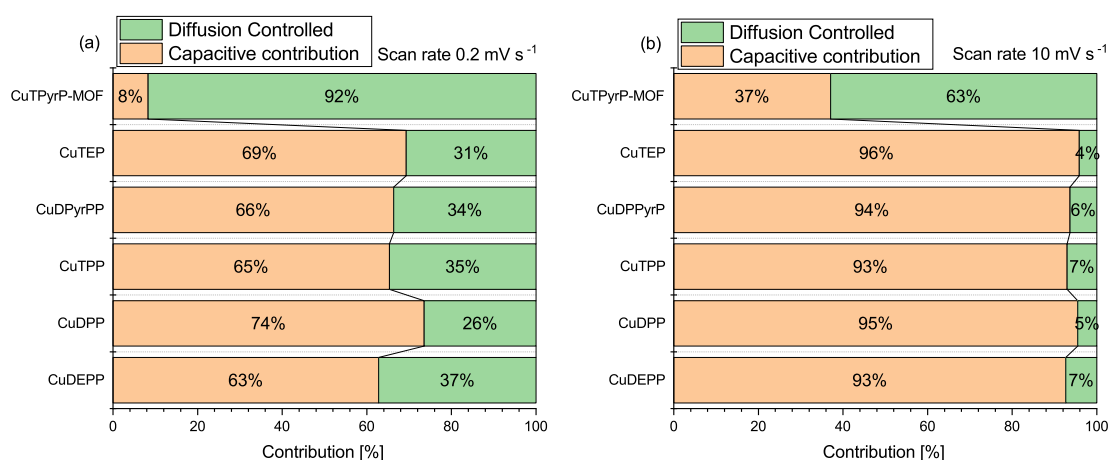


Figure 8.10: Contribution ratio of all compounds at sweep rates of (a) 0.2 mV s^{-1} and (b) 10 mV s^{-1} .

The conducted electrochemical tests show a stabilization reaction appearing in the first cycle, which, in the case of CuDEPP and CuTEP, results in the formation of a polymerized structure. Since the irreversible peak also appears in the case of porphyrinoids with groups not known to undergo electrochemically induced polymerization, the hypothesis is raised that this peak could be related to some interaction with PF_6^- anions. For further evaluation, some computations were performed to gain deeper insights into the mechanism, particularly in the case of CuDEPP.

One initial hint for the polymerization mechanism was provided by earlier investigations using Os staining, which revealed the formation of aliphatic double bonds. This suggests the straightforward idea that polyacetylenic CuDEPP is formed as a result (Fig. 8.11). In the case of CuDEPP, the removal of one electron during oxidation can lead to the formation of a radical cation, which then initiates the polymerization reaction.

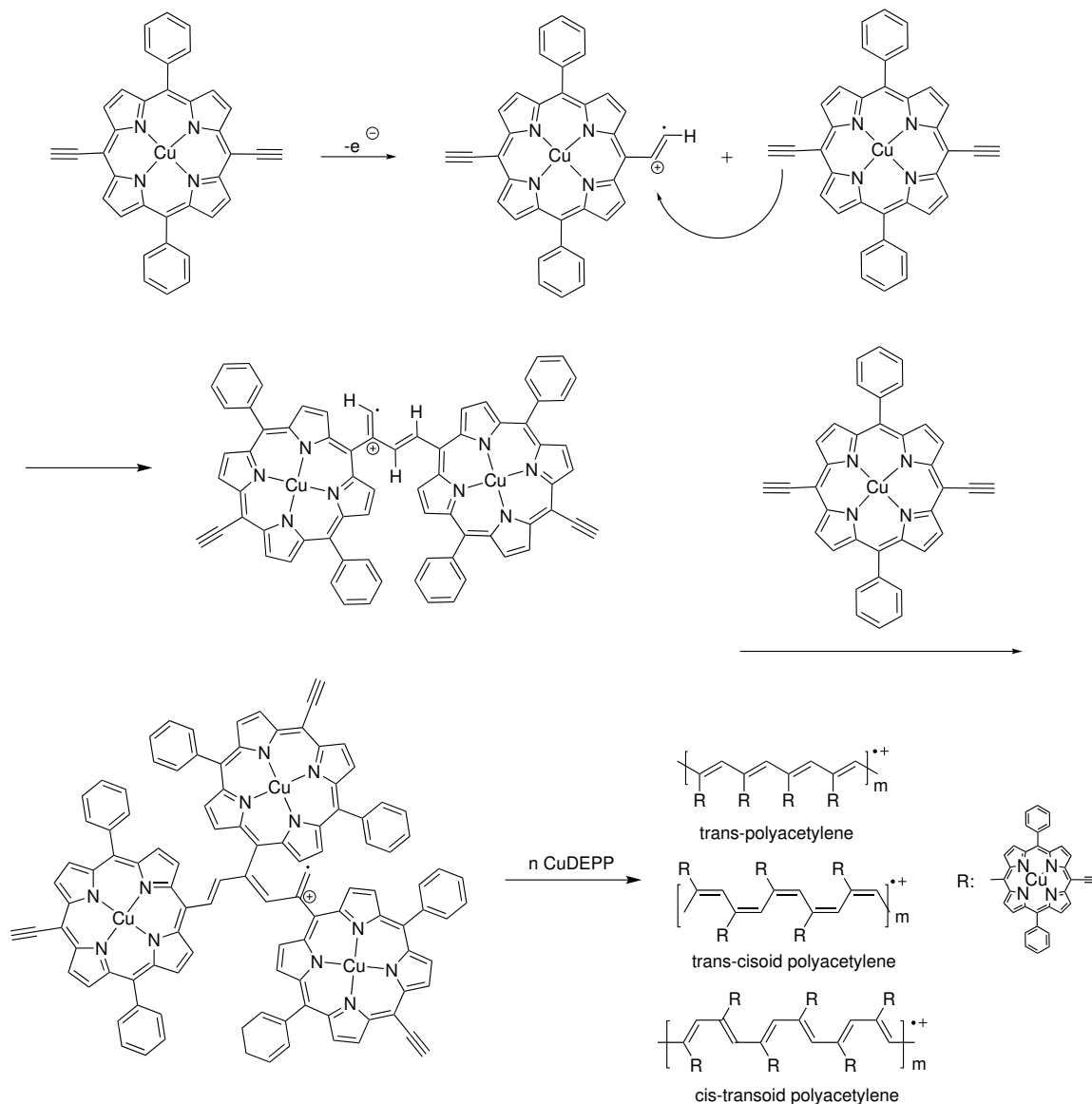


Figure 8.11: Possible Mechanism of the polyacetylene formation of CuDEPP and the arrangements in polyacetylene.

The conjugated structure of polyacetylenic structures can be formed in either the trans-, trans-cisoid, or cis-transoid form (Fig. 8.11).

The structure shown in Fig. 8.11 already demonstrates the potential difficulty of polymerization due to the very bulky porphyrin rings. Previous computational work indicated the formation of a sheet-like polymer structure, suggesting one-plane poly-

merization.[281]

To further assess whether this mechanism is favored, Dr. Saibal Jana provided computational work. The study found that one-plane polymerization is not preferred due to the large size of the porphyrin core, which causes tension in the structure, making it more labile. However, polymerization through different planes is favored (Fig. 8.12). Therefore, the formation of the radical cation initiates the polymerization, but in a different direction.

Furthermore, it has been demonstrated that this mechanism is facilitated by the insertion of PF_6^- anions, which bend the porphyrin. This bending makes polymerization more facile due to reduced steric hindrance (Fig. 8.13). This interaction with the PF_6^- anion could be relevant for all porphyrinoids, stabilizing the structure or facilitating interactions between the porphyrin cores, such as π - π interactions. It has been reported that π - π interactions between active materials can facilitate the formation of ionic channels, resulting in fast charge and discharge properties.[111] This mech-

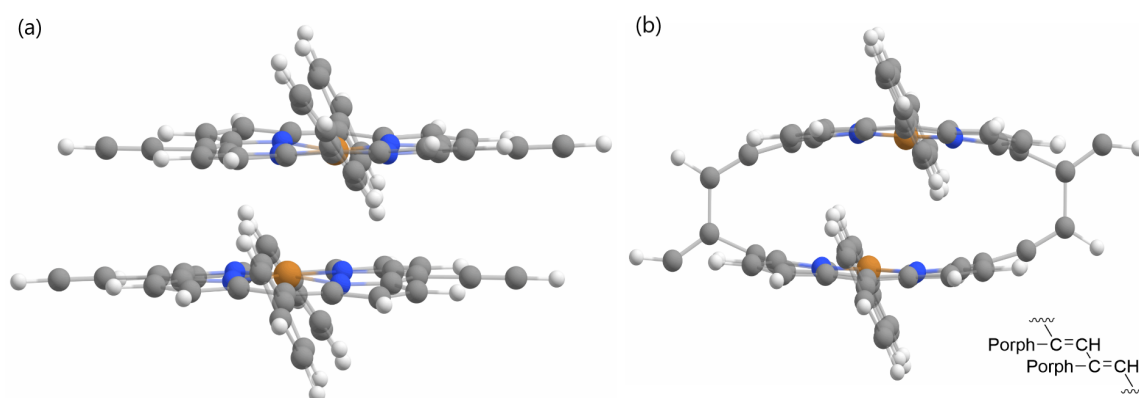


Figure 8.12: Polymerization through plane: (a) arrangement of CuDEPP and (b) polymerization product on example of dimer.

anism possibly reveals that the excellent performance of CuDEPP can be facilitated by improved charge transfer by the additional through-plane conductivity.

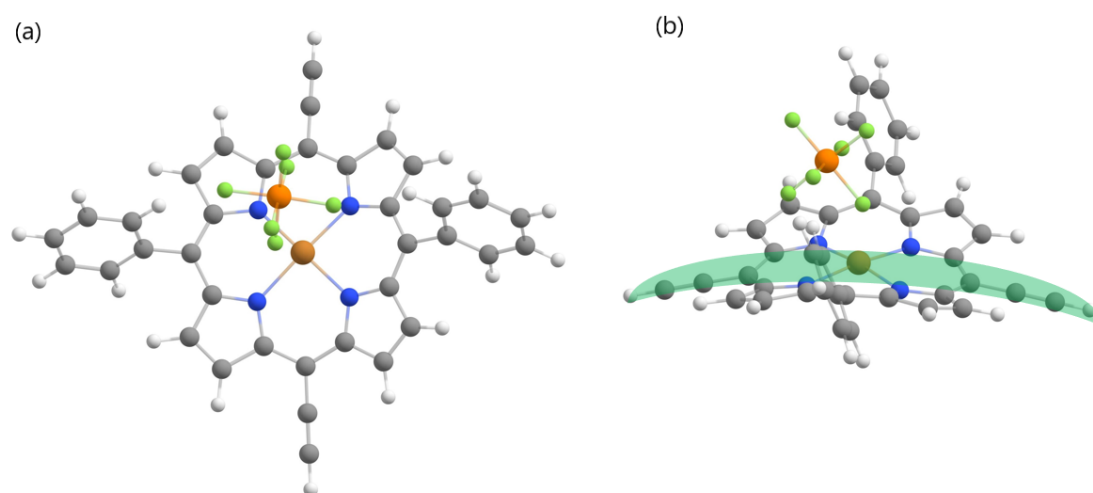


Figure 8.13: Bending of CuDEPP caused by PF_6^- anion (a) top view and (b) side view.

Besides this proposed mechanism, other forms of polymerization should be considered. Just recently, the cyclization and coupling of CuDEP were reported on an Au(III) surface, resulting in a completely different product.[282] The formation of five-membered rings is reported at the periphery of the porphyrin core, where both cis- and trans-formations are possible (Fig. 8.14). Here, double bonds are also formed during the cyclization. If staining with OsO_4 will be possible, further investigation of aromaticity is required. Theoretically it might be possible, but it has to be considered that the double bond is in a conjugated ring system which is partially aromatic.

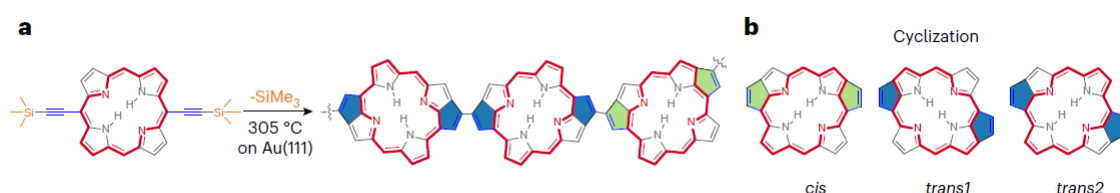


Figure 8.14: Reported Cyclization reaction on Au(III) surface (a) formation of polymeric structure and (b) variation of the cis and trans formation. Reproduced with permission[282], Copyright (2023) Springer Nature.

The dark red lines represent the aromatic π -system, while the green-colored rings represent the cis formations during cyclization, and the blue rings represent the trans formations. This mechanism would represent in-plane polymerization, where the mechanism could be initiated in the same way as already described, with an oxidation where the removal of one electron leads to the formation of a radical cation at the acetylene group. This radical cation then reacts with the pyrrolic ring in a first step, followed by the polymerization or coupling of another ring. This mecha-

nism would, of course, mean that there are two steps: first the cyclization and then the polymerization/coupling. This could be one argument why the other mechanism would be more probable. The proposed mechanism cannot explain through-plane polymerization because only a mono-layer is sublimed to the Au(III) surface.

8.4 Conclusion

This chapter investigates five porphyrinoids and one porphyrin-based MOF to understand the mechanism behind the self-conditioning process necessary for stabilizing the material used in battery applications. Several spectroscopic methods (FTIR, Raman) have been used to demonstrate the disappearance of the terminal ethynyl group and the formation of conjugated double bonds. The investigation of porphyrinoids without ethynyl functionality, namely CuDPP and CuTPP, showed that both compounds undergo irreversible oxidation above 3.5 V, as revealed in the CV analysis. As phenyl is not known to undergo electrochemically induced polymerization, the stabilization taking place must be due to another electrochemical process. The insertion of PF_6^- anions may be a plausible cause, as suggested by DFT calculations which revealed their immense influence on the structure of CuDEPP. Overall, bringing all investigations together, it becomes clear that the terminal ethynyl groups or other groups such as thiophen or 4-aminophenyl groups are undergoing electrochemically induced polymerization. The DFT calculations mentioned earlier provided a mechanism whereby the cationic radical is formed and leads to polymerization through the planes and not in-plane. This could explain the better performance of CuDEPP and CuTEP due to their through-plane conductivity which can enhance fast charge and discharge properties. In addition, the layered arrangement could facilitate ion diffusion. Furthermore, recent investigations suggest a mechanism involving cyclization with the formation of a five-membered ring in the periphery of the porphyrin, with a coupling reaction following and leading to the formation of a polymeric structure in-plane. Both provided mechanisms are possible, with the so far found indications as in IR spectroscopy or with the Os staining. The *post-mortem* analysis to solve the mechanism is challenging due to a slurry mixture containing many different components. The fact that the stabilization or self-conditioning is different for the porphyrinoids was

further indicated by evaluating their charge-discharge curves. The clear appearance of significant plateaus in the case of CuDPP and CuTPP demonstrates some difference in charge storage. Finally, with the study of the kinetic properties, it has been shown that CuTPyrP-MOF is the first porphyrinoid compound provide a battery-like charge storage mechanism that is more diffusion-controlled.

Chapter 9

Experimental Section

In the experimental section, the procedural approach is described. The first section outlines the synthesis protocols and evaluation of analytical methods.

9.1 Materials and Equipment

Chemicals

Commercially available chemicals were used as received.

Thin-layer chromatography (TLC)

Thin-layer chromatography was performed using silica gel-coated aluminum sheets received from MERCK (60 F₂₅₄). Detection was carried out using UV light in the wavelength range of 254 nm.

Column chromatography

The separation of the crude products was performed employing flash column chromatography. Silica gel Si 60 (<0.063 nm) from MERCK or activated basic alumina (MERCK90, 0.063-0.2 mm) was used as the stationary phase. The choice of the appropriate mobile phase is mentioned in experiment description.

¹H-NMR spectroscopy

The ¹H-NMR measurements were performed using a "BRUKER DRX 500" (BRUKER, 500 MHz) instrument. Deuterated chloroform (CDCl₃), dichloromethane (CD₂Cl₂)

or methanol (CD_3OD) was used as solvents. The measurements of G. R. FULMER *et al.*[283] were used as a reference. The coupling constants are reported in hertz [Hz]. The chemical shift is reported in ppm and referenced to tetramethylsilane as an internal standard. The multiplets are abbreviated as follows: s (singlet), d (doublet), t (triplet), q (quartet), and m (multiplet). The chemical shift values are given relative to the signal centroid, except for multiplets where the entire range is indicated. The data analysis was performed using "TopSpin 4.0.6" software from BRUKER. To further elucidate the structure, 2D-NMR spectra including ^1H - ^1H -COSY, HMBC, and HSQC were recorded.

^{13}C -NMR spectroscopy

The ^{13}C -NMR spectra were measured using the aforementioned instrument at 125 MHz. The distinction between primary, secondary, tertiary, and quaternary carbons was achieved through DEPT-135 and DEPT-90 experiments. The following abbreviations were used (-CH, - CH_3 = +, - CH_2 = -).

FT-IR

The substance under investigation was prepared as a KBr pellet. The IR spectra were recorded using the "Magna FTIR 750" instrument from NICOLET. The data analysis was performed using the "OPUS 7.0" software. The vibration frequencies were reported in wavenumbers (cm^{-1}), and the measurements were conducted in the range of 400-4000 cm^{-1} . The assignment of vibrational modes was performed using literature as a reference.[258] Abbreviations such as def (for deformation), sh (for sharp), str (for stretching), sym (for symmetric), and vib (for vibration) were utilized for characterization purposes.

ATR-IR

ATR-IR spectra were obtained using a Nicolet iS50 FTIR spectrometer, covering a range of 400-4000 cm^{-1} .

MALDI-ToF-MS

The MALDI-ToF mass spectra were recorded using the "WATERS Synapt" instrument from WATERS. No matrix or 2,5-dihydroxybenzoic acid (DHBA) was employed during the experiments. The mass values are reported as relative masses $[m/z]$, and the intensities are given as relative percentages [%] of the strongest signal.

ESI-MS

The ESI-MS spectra were recorded using the "BRUKER micrOTOF-Q II" instrument. The relative masses $[m/z]$ and relative intensities [%] of the most prominent signal are reported for each spectrum. Either methanol or dichloromethane (DCM) was employed as the solvent.

UV-Vis

The UV-Vis measurements were performed using the "Cary 500 Scan" instrument from VARIAN. Solutions with a concentration of approximately 10^{-5} M in dichloromethane (DCM) were used. However, an exact concentration could not be determined as the compound did not completely dissolve in most cases. Therefore, the extinction coefficient cannot be provided.

SEM/EDS

The SEM images were captured using a "ZEISS Leo Gemini 1530" System. EDS measurements were conducted using an Oxford Instruments X-MaxN 50 mm^2 Silicon Drift Detector within a Leo Gemini SEM.

Powder X-Ray diffraction

X-ray diffraction (XRD) patterns of the powders were obtained using a BRUKER D8 diffractometer. The measurements were conducted with Bragg-Brentano geometry

and Cu-K α radiation. The measurements were performed within the range of 0 to 50 degrees.

Elemental analysis

Elemental analyses were performed using a VARIO micro cube instrument in CHNS mode.

X-Ray photoelectron spectroscopy

The chemical state of the elements was analyzed using X-ray photoelectron spectroscopy (XPS) on a SPECS XPS system equipped with monochromatized Al K α radiation and a Phoibos 150 energy analyzer. The samples were handled under an argon atmosphere before being transferred to the XPS system. The binding energy calibration was performed using the main C1s peak set at 284.8 eV. Peak fitting was carried out using Casa XPS software, employing Shirley-type backgrounds and Gaussian-Lorentzian peak profiles.

TGA-DSC-MS

The measurements were conducted using a Setaram thermal analyzer SENSYS evo TGA-DSC, coupled with a "PFEIFFER OmniStar" mass spectrometer. The evolved gas during the analysis was analyzed using simultaneous thermogravimetric analysis, differential scanning calorimetry, and mass spectrometry (TGA-DSC-MS). The analyses were carried out under an argon atmosphere, with a heating rate of 10 °C/min.

Nitrogen adsorption

To determine the BET specific surface area and pore characteristics, nitrogen adsorption measurements were conducted. The measurements were carried out using a Micromeritics Instrument Corporation ASAP 2020 surface area and porosity analyzer apparatus. Prior to the measurements, powder samples were dried and degassed at 100 °C overnight until a pressure lower than 0.15 mbar was achieved. The specific surface area and micropore area were calculated using the standard instrument software, following the BET method.

FIB-SEM Tomography

FIB-SEM corss-sectioning and tomorgraphy was performed with a Strata 400 from FEI. The section thickness was 50nma and the cutting current was set to 0.92 nA (30 kV). The images were captured using the TLD (through-the-lens) detector at an image resolution of 2048x1768.

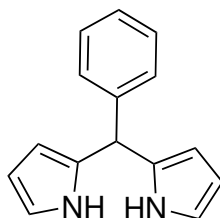
NanoCT

The 3D imaging were performed using the X-ray microscope Xradia 810 Ultra. This system uses a semi-monochromated X-ray beam from a Cr anode (energy of 5.4 keV) and a sequence of optics to achieve pixel size of 16 nm within a high resolution field of view setup corresponding to 16 μm , in absorption and Zernike phase contrast modes. The datasets were reconstructed using the proprietary software Zeiss Scout and Scan Reconstructor, which is based on filtered back projection algorithm. The 2D and 3D visualization, segmentation and statistics calculations were carried out using the software Dragonfly ORS [Dragonfly 2022.2 [Computer software]. Object Research Systems (ORS) Inc, Montreal, Canada, 2020; software available at <http://www.theobjects.com/dragonfly>].

9.2 xDEPP from Zn to Co and Free-base

9.2.1 Preparation of Complexes

5-phenyldipyrromethane (1)



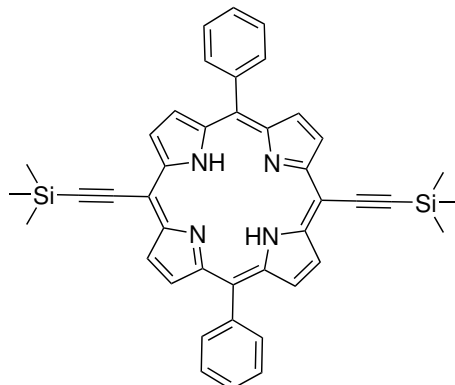
Compound (1) was synthesized following the procedures described in the literature.[284, 285] The reaction was conducted in an inert atmosphere. A mixture of (140 mL, 2 mol, 20 eq) pyrrole and (10.2 mL, 0.1 mol, 1 eq) of benzaldehyde was purged with argon for 15 minutes. The solution was then cooled in an ice bath, and a careful addition of (0.78 mL, 0.01 mol, 0.1 eq) of trifluoroacetic acid was made (note: significant heat generation during addition!). The resulting mixture was stirred for two hours. To quench the reaction, 30 mL of 0.1M NaOH solution was added. The mixture was subjected to three extractions with ethyl acetate (EA). The combined organic phases were washed with water and dried using sodium sulfate. The solvent was subsequently removed under reduced pressure. The crude product was initially purified using a flash column (2 hexane:1 EA) and further purified by column chromatography (SiO₂, 3 hexane:1 EA). A fraction containing the pure product was isolated, while the remaining fractions, which contained impurities, were discarded. The product obtained is a yellow solid. The NMR spectra obtained are in agreement with the literature.

Yield: 9% (2.00 g, 8.99 mmol)

¹H-NMR: (500 MHz, CDCl₃): δ = 7.95 (2H, s, NH), 7.27-7.39 (5H, m, Ph), 6.73-6.74 (2H, m, CH pyrrole), 6.22 (2H, q, J = 2.9 Hz, CH pyrrole), 5.96-5.98 (2H, m, CH pyrrole), 5.52 (1H, s, CH) ppm.

¹³C-NMR: (125 MHz, CDCl₃): δ = 142.1, 132.5, 128.7, 128.4, 127.0, 117.3, 108.4, 107.3, 44.0 ppm.

**5,15-bis(trimethylsilanylethynyl)-10,20-diphenyl-21*H*,23*H*-porphyrin
(DEPP-TMS) (2)**

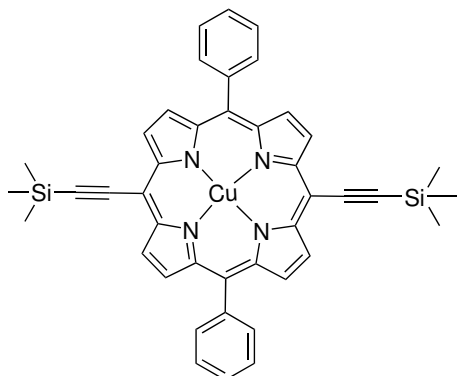


Compound (2) was synthesized following the procedures described in the literature.[152, 285, 286] Into a solution of (1 g, 4.5 mmol, 1 eq) of compound (1) and (0.69 mL, 4.7 mmol, 1.04 eq) of 3-(trimethylsilyl)-2-propynal in 500 mL of dried DCM, cooled in an ice bath, argon gas was passed for 15 min. Then, (0.08 mL, 0.68 mmol, 0.3 eq) of $\text{BF}_3 \cdot \text{OEt}_2$ was added dropwise. The ice bath was removed, and after reaching room temperature, (0.86 g, 3.8 mmol, 0.8 eq) of DDQ was added. The reaction mixture was stirred for one hour. The reaction was quenched with 1 mL of TEA. After filtration of the reaction mixture to remove side products, the excess solvent was removed under vacuum. The crude product was purified by column chromatography (SiO_2), using 1:1 DCM:hexane. Methanol was added to the fraction containing the product. DCM and hexane were removed under reduced pressure. The product precipitated in methanol and was filtered. The NMR spectra obtained are in agreement with the literature.

Yield: 45% (0.67 g, 1.02 mmol)

$^1\text{H-NMR}$: (500 MHz, CDCl_3): δ = 9.61 (4H, d, J = 4.5 Hz, CH pyrrole), 8.83 (4H, d, J = 4.45 Hz, CH pyrrole), 8.18 (4H, d, J = 7.45 Hz, Ph), 7.76-7.81 (6H, m, Ph), 0.60 (18H, s, TMS), -2.20 (2H, s, NH) ppm.

[5,15-bis(trimethylsilanylethynyl)-10,20-diphenylporphinato]copper(II)
(CuDEPP-TMS) (3)



Compound (3) was synthesized following the procedures described in the literature.[152] The free-base porphyrin (2) (0.52 g, 0.8 mmol, 1 eq) and $\text{Cu}(\text{OAc})_2 \cdot \text{H}_2\text{O}$ (0.52 g, 2.6 mmol, 3.2 eq) were dissolved in 70 mL of DCM and 7 mL of methanol, and the mixture was stirred overnight. The resulting reaction mixture was filtered through celite. After undergoing flash column chromatography using SiO_2 and DCM as the eluent, the product was obtained as a solid with a dark blue-purple color.

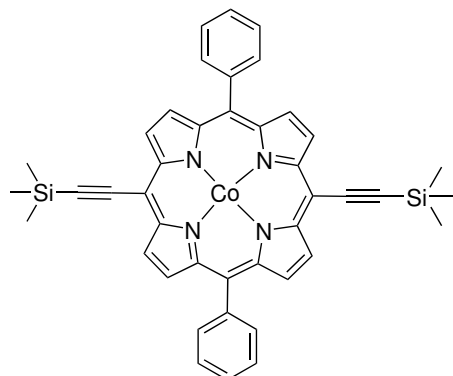
Yield: 64% (0.37 g, 0.55 mmol)

MALDI-ToF-MS: calculated for $\text{C}_{42}\text{H}_{36}\text{CuN}_4\text{Si}_2$ $[\text{M}]^-$: m/z : 714.17; found 715.28 (100%) $[\text{M}-\text{H}]^+$

Elemental analysis: calcd for $\text{C}_{42}\text{H}_{36}\text{CuN}_4\text{Si}_2$: C 70.41 H 5.06 N 7.82 found: C 72.85 H 4.75 N 7.84

$^1\text{H-NMR}$: paramagnetic compound

[5,15-bis(trimethylsilanylethynyl)-10,20-diphenylporphinato]cobalt(II)
(CoDEPP-TMS) (4)



Compound (4) was synthesized following the procedures described in the literature.[152, 285] The free-base porphyrin (2) (0.052 g, 0.08 mmol, 1 eq) was dissolved in a mixture of 10 mL chloroform and 10 mL acetic acid. To the solution, $\text{Co}(\text{OAc})_2 \cdot 4\text{H}_2\text{O}$ (0.2 g, 0.83 mmol, 10.4 eq) was added, and the resulting mixture was refluxed for 4 hours. The solvent was then evaporated under vacuum. After performing column chromatography using Al_2O_3 as the stationary phase and a gradient eluent system of 10% DCM in hexane to 100% DCM, the desired product was obtained as a blue solid.

Yield: 85% (0.048 g, 0.67 mmol)

$^1\text{H-NMR}$: paramagnetic compound

MALDI-ToF-MS: calculated for $\text{C}_{42}\text{H}_{36}\text{CoN}_4\text{Si}_2$ $[\text{M}]^-$: m/z : 711.2; found 711.0 (100%)

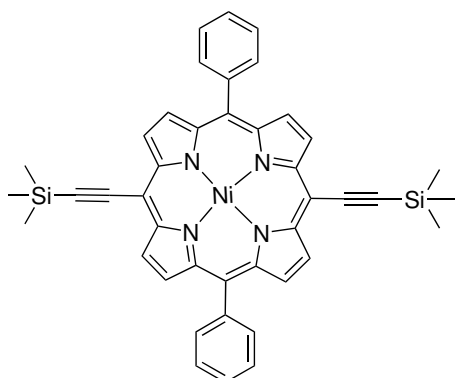
UV-Vis (CHCl_3): 428, 554, 589 nm.

IR (KBr): $\tilde{\nu}$ = 3436.01, 2924.02, 2142.49 ($\text{C}\equiv\text{C}$), 1623.01, 1347.46, 1246.49 ($\text{Si}(\text{CH}_3)_3$ sh sym. CH_3 def vib), 1210.95, 1167.12, 1068.64, 1004.21, 845.83 ($\text{Si}(\text{CH}_3)_3$ rocking vib), 796.00 (-Ph out of plane def vib), 752.87, 705.33 (ring out of plane def vib) cm^{-1} .

Table 9.1: Crystal data and structure refinement of CoDEPP-TMS.

CoDEPP-TMS	
Empirical Formula	C ₄₂ H ₃₆ N ₆ Si ₂ Co
Formula weight [g mol ⁻¹]	711.86
Temperature [K]	150
Crystal system	Triclinic
Space group	P $\bar{1}$
a [Å]	9.3678(4)
b [Å]	14.0547(7)
c [Å]	15.0024(7)
α [°]	66.824(5)
β [°]	82.406(4)
γ [°]	79.768(4)
Volume [Å ³]	1782.73(16)
Z	2
ρ_{calc} [g cm ⁻³]	1.326
μ [mm ⁻¹]	0.585
F(000)	742
Crystal size [mm ³]	0.228x0.205x0.156
Radiation	Mo K α ($\lambda = 71073$)
2 θ range for data collection [°]	4.4 to 54.2
Goodness-of-fit on F ²	1.065
Final R indexes [$I \geq 2\sigma(I)$]	R ₁ = 0.0423 wR ₂ = 0.1144
CCDC number	2143452

[5,15-bis(trimethylsilyl)ethynyl)-10,20-diphenylporphinato]nickel(II)
(NiDEPP-TMS) (5)



Compound (5) was synthesized following the procedures described in the literature.[152]

The free-base porphyrin (2) weighing (0.1 g, 0.15 mmol, 1 eq) and Ni(OAc)₂·4H₂O (0.35 g, 1.4 mmol, 9.3 eq) were dissolved in a mixture of 67 mL chloroform and 33 mL methanol. The resulting solution was heated under reflux for 3 days. Afterward, the mixture was allowed to cool to room temperature, and the solvent was removed under vacuum. The crude product was dissolved in chloroform and extracted twice with water. The organic phase was collected and dried using sodium sulfate. Chloroform was subsequently evaporated under vacuum. The product was then dissolved in THF, and water was added. THF was removed under vacuum, resulting in the precipitation of the product as a blue solid, which was then filtered.

Yield: 23% (0.025 g, 0.04 mmol)

¹H-NMR: paramagnetic compound

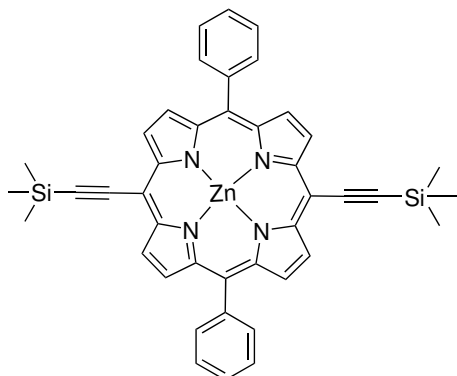
MALDI-ToF-MS: calculated for C₄₂H₃₆NiN₄Si₂ [M]⁺: m/z: 710.8; found 711.14 (100%) [M-H]⁺

UV-Vis (CHCl₃): 431, 552, 598 nm.

IR (KBr): $\tilde{\nu}$ = 3432.21, 2957.59, 2144.88 (C≡C), 1627.39, 1348.99, 1247.29 (Si(CH₃)₃ sh sym. CH₃ def vib), 1210.95, 1167.12, 1072.75, 1004.78, 844.93 (Si(CH₃)₃ rocking vib), 795.75 (-Ph out of plane def vib), 752.87, 705.47 (ring out of plane def vib) cm⁻¹.

Elemental analysis: calcd for C₄₂H₄₀NiN₄Si₂O₂: C 67.47 H 5.39 N 7.49 found: C 67.31 H 5.11 N 7.22

[5,15-bis(trimethylsilanylethynyl)-10,20-diphenylporphinato]zinc(II)
(ZnDEPP-TMS) (6)



Compound (6) was synthesized following the procedures described in the literature.[152, 287] The free-base porphyrin (0.23 g, 0.35 mmol, 1 eq) was dissolved in 125 mL of DCM, and Zn(OAc)₂·2H₂O (0.27 g, 1.23 mmol, 3.5 eq) in 3 mL of methanol was added. The resulting mixture was stirred at room temperature overnight. The solvent was then evaporated under reduced pressure, resulting in the formation of a dark green solid. The NMR spectra obtained are in agreement with the literature.

Yield: 74% (0.19 g, 0.26 mmol)

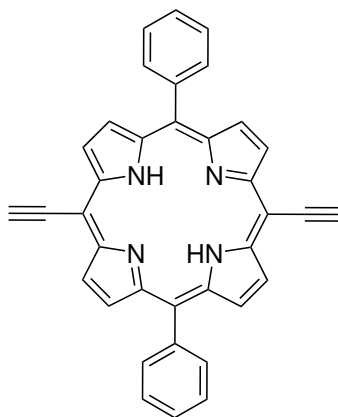
¹H-NMR (500 MHz, CDCl₃): δ = 0.60 (18H, s, TMS), 7.77-7.79 (6H, m, Ph), 8.18 (4H, d, J = 6.25 Hz, Ph), 8.92 (4H, d, J = 4.55 Hz, β-H), 9.70 (4H, d, J = 4.55 Hz, β-H) ppm.

MALDI-ToF-MS: calculated for C₄₂H₃₆ZnN₄Si₂ [M]⁻: m/z: 715.2; found 716.3 (100%) [M+H]⁻

Elemental analysis: calcd for C₄₂H₃₆ZnN₄Si₂: C 70.23 H 5.05 N 7.80 found: C 69.75 H 4.90 N 7.53

General procedure for deprotection of TMS-group (xDEPP) (7-11)

The deprotected compounds were prepared following the procedures described in the literature.[152, 288] The porphyrin (2-6) (0.05 mmol) was dissolved in 20 mL of anhydrous THF, and 1 mL (1 mmol) of a 1M solution of TBAF in THF was added. The resulting mixture was stirred overnight under an argon atmosphere. The reaction was stopped by adding 50 mL of water. THF was removed under reduced pressure. The precipitate was then filtered and dried overnight at 100 °C and at a reduced pressure of $2.0 \cdot 10^{-2}$ mbar.

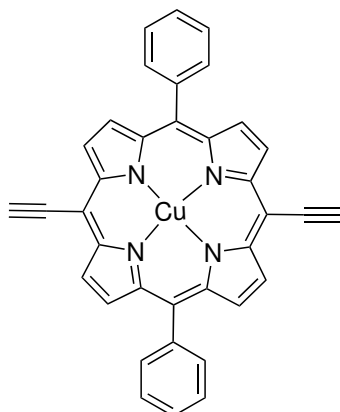
5,15-bis(ethynyl)-10,20-diphenylporphyrin (DEPP) (7)[152]

Yield: 98% (0.083 g, 0.16 mmol) based on (0.1097 g, 0.17 mmol) DEPP-TMS as starting material. Product appear as black solid.

MALDI-ToF-MS: calculated for $C_{36}H_{22}N_4$ $[M]^+$: m/z : 511.3; found 511.2 (100%) $[M]^+$

UV-Vis ($CHCl_3$): 424, 524, 561, 661 nm.

IR (KBr): $\tilde{\nu}$ = 3299.14, 3269.54 (-C≡C-H-CH str.), 3051.14, 2923.31, 2323.63, 2164.91, 2050.28, 1980.45, 1546.89 (C=C/N in plane vib), 1475.42, 1440.60, 1346.08 (-C≡C-H-CH wagging vib overtone), 1176.27, 1050.16, 1031.05, 1001.11, 970.37, 795.79 (-Ph out of plane def vib), 721.81, 699.19 (-Ph ring out of plane def vib) cm^{-2} .

[5,15-bis(ethynyl)-10,20-diphenylporphinato]copper(II) (CuDEPP) (8)

*Synthesized by Dr. Shagor Chowdry[148]

Product appears as blue solid.

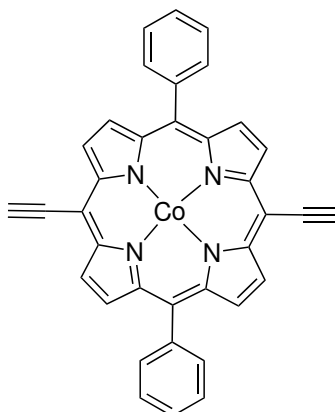
MALDI-ToF-MS: calculated for $C_{36}H_{20}CuN_4$ $[M]^+$: m/z: 511.3; found 511.2 (100%)

$[M]^+$

Elemental analysis: calcd for $C_{36}H_{20}CuN_4$: C 75.58 H 3.52 N 9.79 found: C 74.73

H 3.75 N 9.18

[5,15-bis(ethynyl)-10,20-diphenylporphinato]cobalt(II) (CoDEPP) (9)[152, 285]



Yield: 99% (0.028 g, 0.049 mmol) based on (0.033 g, 0.05 mmol) DEPP-TMS as starting material. Product appears as black solid.

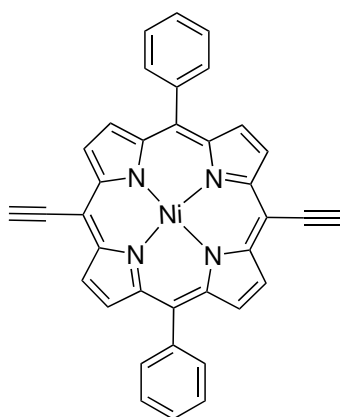
¹H-NMR: paramagnetic compound

MALDI-ToF-MS: calculated for C₃₆H₂₀CoN₄ [M]⁺: m/z: 568.1; found 567.1 (100%)
[M-H]⁺

UV-Vis (CHCl₃): 434, 580, 617 nm.

IR (KBr): $\tilde{\nu}$ = 3430.21, 3264.38 (-C≡C-H-CH str.), 2914.28, 2857.14, 2099.69, 1596.71, 1544.10 (C=C/N in plane vib), 1458.16, 1349.96 (-C≡C-H-CH wagging vib overtone), 1206.57, 1074.03, 1005.66, 795.83 (-Ph out of plane def vib) 752.98, 704.18 (-Ph Ring out of plane def vib), 667.39, 619.08 cm⁻¹.

Elemental analysis: calcd for C₄₀H₃₂CoN₄O₃: C 71.11 H 4.77 N 8.29 found: C 71.56 H 4.79 N 7.56

[5,15-bis(ethynyl)-10,20-diphenylporphinato]nickel(II) (NiDEPP) (10)[152]

Yield: 80% (0.020 g, 0.04 mmol) based on (0.033 g, 0.05 mmol) DEPP-TMS as starting material. Product appears as brownish solid

¹H-NMR: paramagnetic compound

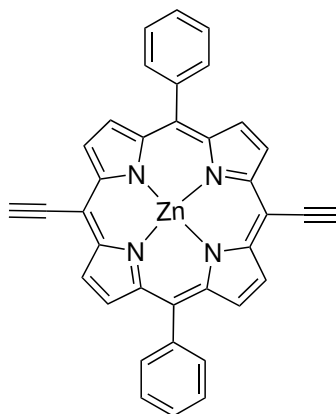
MALDI-ToF-MS: calculated for C₃₅H₂₁NiLiN₄ [(M+3H⁺-CH₃)³⁻+H⁺+Li⁺]⁻: m/z: 561.1; found 561.1 (100%) [(M+3H⁺-CH₃)³⁻+H⁺+Li⁺]⁻

UV-Vis (CHCl₃): 421, 535, 572, 639 nm.

IR (KBr): $\tilde{\nu}$ = 3442.80 (-C≡C-H-CH str.), 2958.69, 1566.02 (C=C/N in plane vib), 1484.93, 1352.43 (-C≡C-H-CH wagging vib overtone), 1206.57, 1160.83, 1072.00, 1004.93, 795.25 83 (-Ph out of plane def vib), 753.25, 701.85 (-Ph ring out of plane def vib) cm⁻¹.

Elemental analysis: calcd for C₄₅H₄₀NiN₄O₃: C 72.69 H 5.42 N 7.54 found: C 72.06 H 4.93 N 7.88

[5,15-bis(ethynyl)-10,20-diphenylporphinato]zinc(II) (ZnDEPP) (11)[152, 287]



Yield: 92% (0.1848 g, 0.32 mmol) based on (0.2569 g, 0.35 mmol) ZnDEPP-TMS as starting material. Product appears as blue solid.

MALDI-ToF-MS: calculated for $C_{36}H_{20}ZnN_4$ $[M]^+$: m/z : 573.1; found 573.0 (100%) $[M]^+$

Elemental analysis: calcd for $C_{36}H_{20}ZnN_4$: C 75.34 H 3.51 N 9.76 found: C 74.16 H 3.69 N 9.28

9.2.2 Computational

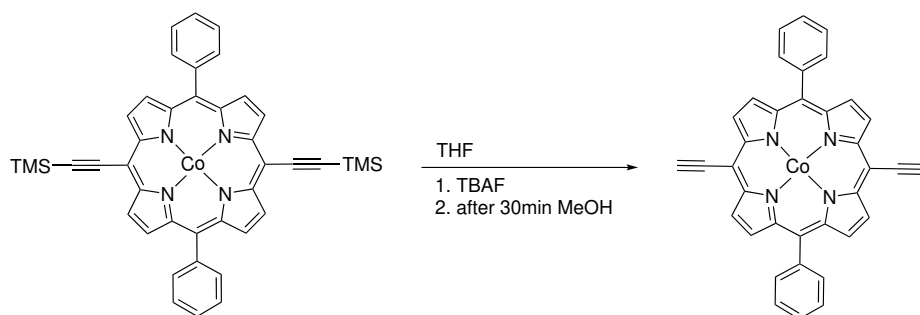
All computational calculations regarding xDEPPs were conducted using the Gaussian 16 software package. The geometry optimizations were carried out in the gas phase utilizing the B3LYP functional of the Density Functional Theory (DFT) method. For hydrogen, carbon, and nitrogen atoms, the 6-31G (d,p) basis set was employed, while the LANL2DZ basis set was used for metal atoms.

9.3 Microstructure of CoDEPP

9.3.1 Procedure

The CoDEPP-TMS (4) compound was synthesized according to the procedure described in the previous section. Different conditions were then employed to remove the TMS-group, aiming to achieve various microstructures of CoDEPP.

CoDEPP (12)



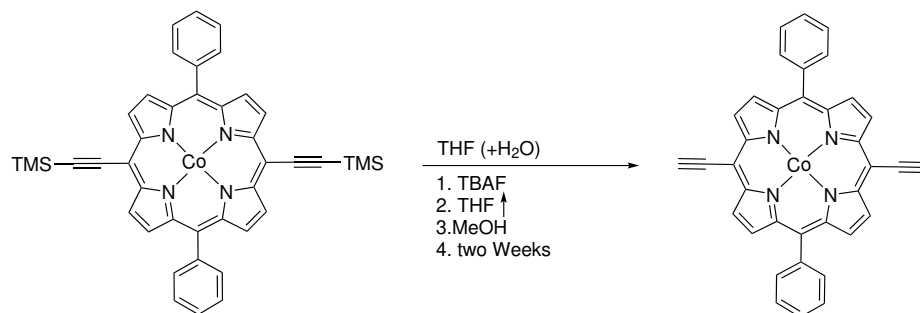
A mixture (0.4130 g, 0.58 mmol, 1 eq) of CoDEPP-TMS in 400 mL anhydrous THF was combined with a solution of (1.26 g, 4.8 mmol, 8.3 eq) of TBAF in 20 mL anhydrous THF under an argon atmosphere. The resulting reaction mixture was stirred for 3 hours under an argon atmosphere. Afterwards, 100 mL of MeOH were added to the reaction mixture. The THF solvent was then removed under reduced pressure. The resulting precipitate was filtered to obtain CoDEPP 12 as a dark blue/blackish solid.

Yield: 59% (0.1938 g, 0.35 mmol)

MALDI-ToF-MS: calculated for $C_{36}H_{20}CoN_4$ $[M]^+$: m/z: 568.1; found 567.1 (100%)
 $[M-H]^+$

Elemental analysis: calcd for $C_{54}H_{60}CoN_4O_4$: C 73.04 H 6.81 N 6.31 found: C 72.45 H 6.65 N 6.12

UV-Vis ($CHCl_3$): 415, 539, 589 nm.

CoDEPP (13)

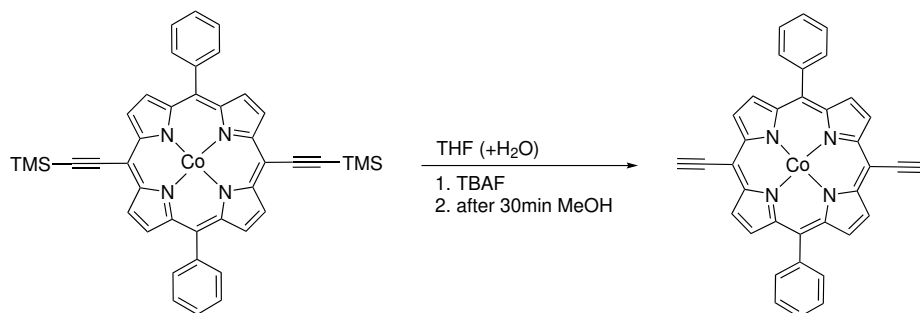
A mixture of (0.2997 g, 0.42 mmol, 1 eq) of CoDEPP-TMS in 100 mL THF and 1 mL dest. H_2O was combined with a solution of (0.63 g, 2.4 mmol, 5.71 eq) TBAF in 20 mL anhydrous THF. The resulting reaction mixture was stirred for 30 minutes. Subsequently, half of the THF was removed under reduced pressure. Afterwards, MeOH was added dropwise to the reaction mixture. Due to the absence of precipitation, more MeOH (150 mL) was added to the reaction solution. The reaction was left without stirring for two weeks. The resulting dark blue/blackish solid (CoDEPP 13) was obtained by filtration.

Yield: 36% (0.0867 g, 0.15 mmol)

MALDI-ToF-MS: calculated for $\text{C}_{36}\text{H}_{20}\text{CoN}_4$ $[\text{M}]^+$: m/z : 568.1; found 567.2 (100%)
 $[\text{M}-\text{H}]^+$

Elemental analysis: calcd for $\text{C}_{37}\text{H}_{32}\text{CoN}_4\text{O}_5$: C 66.17 H 4.80 N 8.34 found: C 66.67 H 3.80 N 8.75

UV-Vis (CHCl_3): 420, 545, 587 nm.

CoDEPP (14)

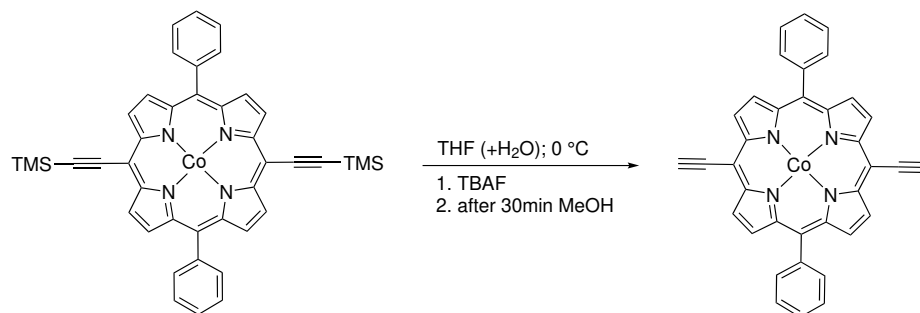
A mixture of (0.1000 g, 0.14 mmol, 1 eq) of CoDEPP-TMS in 100 mL THF and 1 mL dest. H₂O was combined with a solution of (0.3150 g, 1.2 mmol, 8.57 eq) of TBAF in 20 mL anhydrous THF. The resulting reaction mixture was stirred for 30 minutes. Afterwards, 50 mL MeOH were added to reaction mixture. The reaction was left without stirring for over night. The resulting dark blue/blackish solid (CoDEPP 14) was obtained by filtration.

Yield: 65% (0.0518 g, 0.09 mmol)

MALDI-ToF-MS: calculated for C₃₆H₂₀CoN₄ [M]⁺: m/z: 568.1; found 567.2 (100%)
[M-H]⁺

Elemental analysis: calcd for C₃₆H₂₂CoN₄O: C 73.85 H 3.79 N 9.57 found: C 73.44
H 3.58 N 9.65

UV-Vis (CHCl₃): 422, 540, 582 nm.

CoDEPP (15)

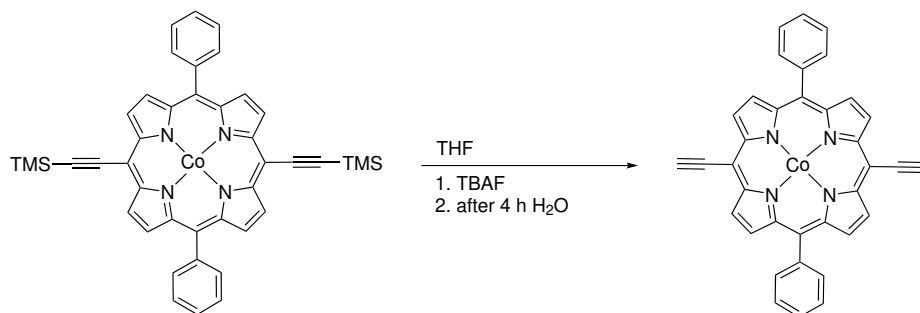
A mixture of (0.2371 g, 0.14 mmol, 1 eq) of CoDEPP-TMS in 100 mL THF and 1 mL dest. H₂O was combined with a solution of (0.3150 g, 1.2 mmol, 8.57 eq) of TBAF in 20 mL anhydrous THF at 0 °C. The resulting reaction mixture was stirred for 30 minutes. Afterwards, 50 mL MeOH were added to reaction mixture. The reaction was left without stirring over two nights in the refrigerator. Due to the absence of precipitate, half of the solvent was removed under reduced pressure. Since the boiling point of the solvents was close, it was not possible to remove only THF. The mixture was then left without stirring for 2 days. The resulting dark blue/blackish solid (CoDEPP 15) was obtained by filtration.

Yield: 64% (0.0503 g, 0.09 mmol)

MALDI-ToF-MS: calculated for C₃₆H₂₀CoN₄ [M]⁺: m/z: 568.1; found 567.2 (100%)
[M-H]⁺

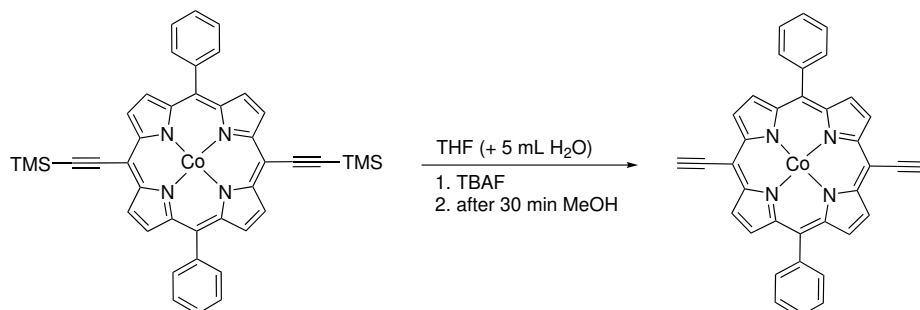
Elemental analysis: calcd for C₄₀H₂₈CoN₄O: C 75.11 H 4.41 N 8.76 found: C 76.89
H 4.60 N 8.12

UV-Vis (CHCl₃): 420, 546, 581 nm.

CoDEPP (16)

A mixture of (0.1867 g, 0.26 mmol, 1 eq) of CoDEPP-TMS in 225 mL THF was combined with a solution of (2 g, 7.6 mmol, 29.2 eq) of TBAF in 50 mL anhydrous THF. The resulting reaction mixture was stirred for 4 hours. Afterwards, 100 mL H₂O were added to reaction mixture. THF was removed under reduced pressure. The resulting dark blue/blackish solid (CoDEPP 16) was obtained by filtration.

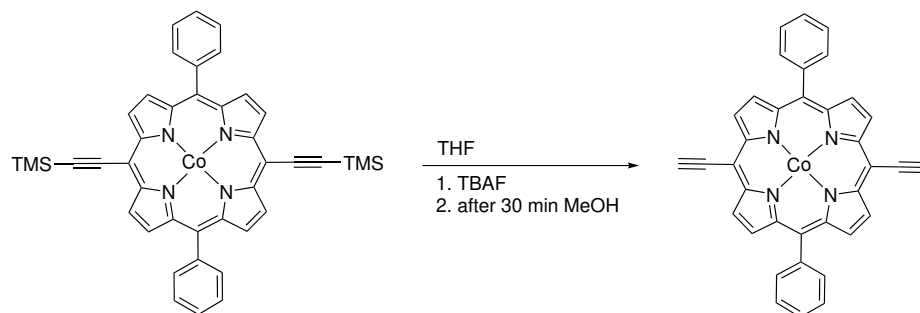
Yield: 17% (0.0249 g, 0.04 mmol)

CoDEPP (17)

A mixture of (0.0800 g, 0.11 mmol, 1 eq) of CoDEPP-TMS in 80 mL THF was combined with a solution of (0.2520 g, 0.96 mmol, 8.72 eq) of TBAF in 20 mL THF and 5 mL dest. H₂O. The resulting reaction mixture was stirred for 30 minutes. Afterwards, 40 mL MeOH were added to reaction mixture. The mixture was left without stirring overnight. The resulting dark blue/blackish solid (CoDEPP 17) was obtained by filtration.

Yield: 54% (0.0336 g, 0.06 mmol)

CoDEPP (18 (a-b))

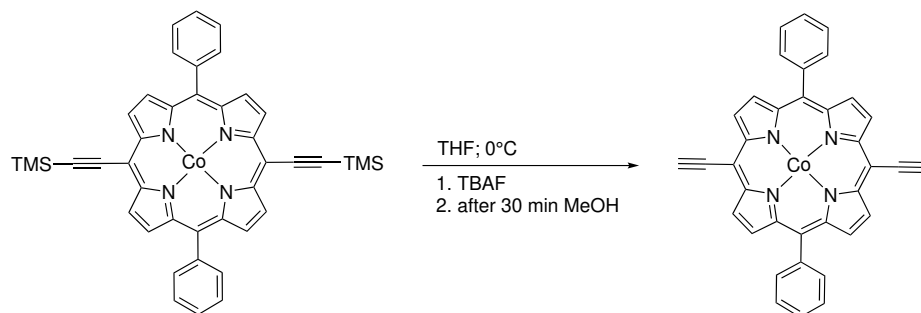


A mixture of (0.1000 g, 0.14 mmol, 1 eq) of CoDEPP-TMS in 100 mL anhydrous THF was combined with a solution of (0.3150 g, 1.2 mmol, 8.57 eq) of TBAF in 20 mL anhydrous THF under an argon atmosphere. The resulting reaction mixture was stirred for 30 minutes under an argon atmosphere. Afterwards, 50 mL of MeOH were added to the reaction mixture. The reaction mixture was left overnight to form precipitate. The mixture was then filtered to obtain CoDEPP (18(a)) in very low yields. The mother solution was further used and the THF was removed under reduced pressure, although it is not possible to avoid the loss of MeOH as well. Once visible precipitate formed, the solution was filtered to obtain a dark blue/blackish solid (18(b)).

Yield: 5% (0.0040 g, 0.007 mmol) 18(a)

Yield: 26% (0.0206 g, 0.04 mmol) 18(b)

CoDEPP (19 (a-b))



A mixture of (0.1000 g, 0.14 mmol, 1 eq) of CoDEPP-TMS in 100 mL anhydrous THF was combined with a solution of (0.3150 g, 1.2 mmol, 7.14 eq) of TBAF in 20 mL anhydrous THF under an argon atmosphere at 0 °C. The resulting reaction mixture was stirred for 30 minutes under an argon atmosphere. Afterwards, 50 mL of MeOH were added to the reaction mixture. The reaction mixture was left overnight to form precipitate. The mixture was then filtered to obtain CoDEPP (19(a)) in very low yields. The mother solution was further used and the THF was removed under reduced pressure, although it is not possible to avoid the loss of MeOH as well. Once visible precipitate formed, the solution was filtered to obtain a dark blue/blackish solid (19(b)).

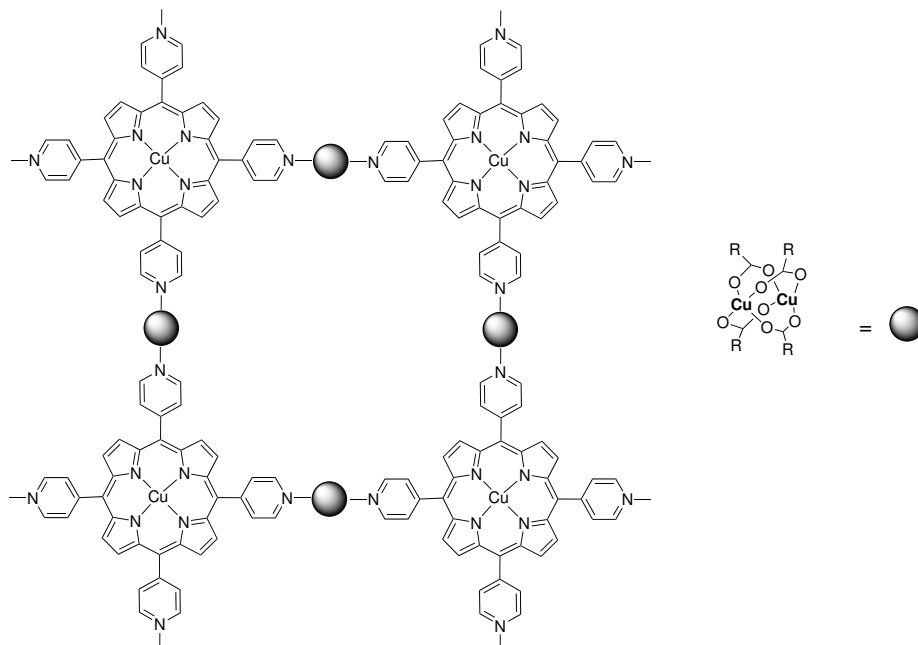
Yield: 2% (0.0016 g, 0.003 mmol) 19(a)

Yield: 86% (0.0687 g, 0.12 mmol) 19(b)

9.4 Pyridine-functionalized MOF

9.4.1 Preparation of CuTPyrP-MOF

[5,10,15,20-tetra(4-pyridyl)porphinato]copper(II)-metal organic framework (CuTPyrP-MOF) (20)



The free-base porphyrin (H_2TPyP) (PorphyChem SAS, France) (1 g, 1.61 mmol, 1 eq) and copper acetate $\text{Cu}(\text{OAc})_2 \cdot 4\text{H}_2\text{O}$ (4 g, 20.04 mmol, 12.45 eq) were dissolved in a mixture of 300 mL of chloroform and 100 mL of methanol. The resulting solution was stirred at room temperature for 24 hours. The solvent was then evaporated using vacuum. The resulting crude substance was subjected to washing using water and methanol to eliminate any remaining unreacted copper salt. The obtained product, appearing as a red solid, was subsequently dried using vacuum conditions (1×10^{-3} mbar).

Yield: 58% (1.3175 g, 0.94 mmol)

$^1\text{H-NMR}$: paramagnetic compound

MALDI-ToF-MS: calculated for $\text{C}_{40}\text{H}_{24}\text{CuN}_8[\text{M}]^-$: m/z : 679.1; found 679.0 (100%)

- (coordination bonds are breaking)

UV-Vis (CHCl_3): 418, 543 nm.

FTIR: $\tilde{\nu} = 1619$ (asym. CO_2^- str.), 1603 (asym. CO_2^- str.), 1422 (sym. CO_2^- str.), 1347 , 1222 , 1073 , 1000 (Pyr. ring str.), 799 , 679 cm^{-1} .

Elemental analysis: calcd for $C_{56}H_{48}Cu_5N_8O_{16}$: C 47.81 H 3.44 N 7.97 found: C 49.89 H 3.88 N 10.24.

[5,10,15,20-tetra(4-pyridyl)porphinato]copper(II)-metal organic framework (CuTPyrP-MOF) (21)[257]

A solution of copper acetate $Cu(OAc)_2 \cdot 4H_2O$ (4 g, 20.04 mmol, 12.45 eq) in 150 mL methanol was carefully layered on a solution of free-base porphyrin (H_2TPyP) (Porphy-Chem SAS, France) (1 g, 1.61 mmol, 1 eq) in 300 mL chloroform. The reaction was left for two weeks without further stirring. The formation of red dark solid precipitate could be observed. The product was not filtrated and kept in the solution.

9.4.2 Computational

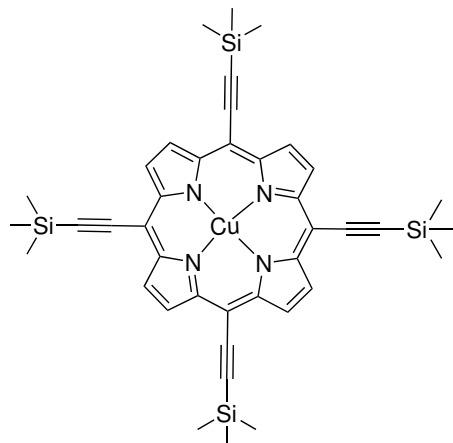
[260] Quantum chemical calculations were conducted on the bwForCluster JUSTUS 2 at the University of Ulm, employing Gaussian16 program package release C.01. Additionally, DFT calculations were executed using the B3LYP functional in conjunction with the def2-TZVP basis set within the implicit solvation model known as the Conductor-like Polarizable Continuum Model (CPCM) with chloroform as the chosen solvent. The achieved structures were confirmed as local energetic minima through frequency calculations. To elucidate the underlying cause of the Q-band red-shift observed in UV spectra upon Cu(II) insertion, we undertook time-dependent DFT (TD-DFT) calculations to ascertain electronic transitions and their connections to occupied and unoccupied molecular orbitals.

Molecular structure and electronic characteristics were calculated for both 5,10,15,20-tetrapyridyl porphyrin (H_2TPyP) and its Cu(II) complex, CuTPyP. In the case of neutral CuTPyP, which possesses a single unpaired electron, calculations were conducted in the doublet state. Conversely, for the anionic complex $[CuTPyP]^{-1}$, calculations were carried out in the singlet state. The M06-2X/TZVP method was employed for the anionic species, with the MDF10 pseudo-potential for copper, and solvent effects were considered using the PCM model with THF as the solvent.

9.5 Self-conditioning

9.5.1 Preparation of Complexes

[5,10,15,20-tetra(trimethylsilanylethynyl)porphinato]copper(II) (22)

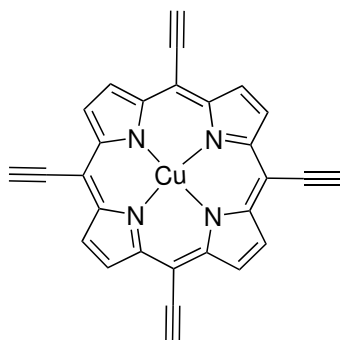


Compound (22) was synthesized following the procedures described in the literature.[156] 5,10,15,20-(tetra(trimethylsilanylethynyl)-21*H*,23*H*-porphin (0.2842 g, 0.4 mmol, 1 eq) (PorphyChem SAS, France), was dissolved in THF/DCM/Et₃N (200/200/40 mL). Cu(OAc)₂·4H₂O (0.4051 g, 2.2 mmol, 5.5 eq) was added under argon. After 48 h of stirring at room temperature, the green solution was filtered through celite, washed with 250 mL DCM, and concentrated. The residue was purified using SiO₂ column chromatography with Hexane:DCM (1:1) as eluent. The purple solid obtained was dissolved in DCM, methanol was added, DCM was evaporated, and the product was obtained as black solid from the filtered methanol phase.

Yield: 83% (0.25 g, 0.33 mmol)

MALDI-ToF-MS: calculated for C₄₀H₄₄CuN₄Si₄[M+H]⁺: m/z: 756.2; found 755.2 (100%) [M-H]⁻.

¹H-NMR: paramagnetic compound.

[5,10,15,20-tetra(ethynyl)porphinato]copper(II) (23)

Compound (23) was synthesized following the procedures described in the literature.[156] (tetra(trimethylsilyl)ethynyl)porphinato)copper(II) (22) (0.2522 g, 0.36 mmol, 1 eq), was dissolved in 200 mL dry THF and tetrabutylammonium fluoride (0.95 g, 3.6 mmol, 10 eq) were added under argon atmosphere. After 45 min of stirring 100 mL methanol were added. The reaction was left for 24 hours to form precipitate. The brownish solid was collect by filtration and was washed with methanol.

Yield: 38% (0.0649 g, 0.14 mmol)

MALDI-ToF-MS: calculated for $C_{28}H_{12}CuN_4[M]^+$: m/z: 466.0; found 467.1 (100%)
 $[M+H]^+$.

1H -NMR: paramagnetic compound.

Purchased chemicals from porphychem SAS, France.

CuDPP	[5,15-diphenylporphyrinato]copper(II)
CuTPP	[5,10,15,20-tetra(phenyl)porphyrinato]copper(II)
CuDPyrPP	[5,15-bis(4-pyridyl)-10,20-diphenylporphinato]copper(II)

9.6 Computational

Polymerization: All DFT calculations were performed in the Orca 5.0.1 package using the PBE-D3(BJ)/def2-SVP level of theory. This method involves GGA functional PBE, double- ζ quality basis set def2-SVP, and the third generation of Grimme's empirical dispersion correction (D3), with Becke-Johnson damping function (BJ). The converged structures were energetic minima, as established by frequency calculations.

Chapter 10

Concluding remarks

Organic electrode materials are promising alternatives to the widely used inorganic counterparts for battery applications. In order to develop novel organic materials, it is essential to gain a comprehensive understanding of their underlying operating principles and the extent to which they can be tuned. This understanding is crucial in order to tailor these materials to possess the specific properties required for their intended applications in electrochemical energy storage systems. In this study, various porphyrinoids have been investigated as cathode materials in different systems. Porphyrinoids, an emerging class of organic electrode materials, exhibit rich four-electron redox chemistry. These materials exhibit remarkable stability over numerous cycles, even at high current densities.

The initial focus of this study was to investigate the structure-performance relationship, delving into the impact of various metal centers using the DEPP ligand. A series of porphyrin derivatives were synthesized by metallating the free-base DEPP ligand with first-row transition metals ranging from Co to Zn. The subsequent electrochemical analyses shed light on the enhancement in both performance and stability resulting from metallation. Additionally, the choice of different metal centers exerted an immediate influence on chemical attributes such as solubility, crystalline packing, and crystallinity, all of which play a role in battery performance. Collectively, the copper complex exhibited the most promising performance, especially under high current densities and in terms of rate capability. This could potentially be attributed to the significantly higher diffusion coefficient of CuDEPP compared to the other metallated xDEPPs ($x = \text{Ni, Zn, Cu, Co and 2H}$). The ionic transport appears to be a product of

the material's porosity and surface area, while the rate capability correlates with the crystallinity. This research has effectively demonstrated that the metal center within porphyrin molecules provides a versatile avenue for tailoring material properties to suit various battery applications.

During the investigation of different metal centers, it was observed that CoDEPP exhibited a higher specific discharge capacity than CuDEPP in the initial cycles at low current densities. Building on this insight, considering the crucial role of crystallinity, a study was conducted to explore the morphological impact on CoDEPP when used as a cathode material in a lithium half-cell. Various synthetic routes were employed to manipulate the microstructure and morphology of the target product. Four distinctive morphologies—needle-shape, flower-shape, coral-shape, and popcorn-shape (amorphous)—were investigated electrochemically. The results highlighted the significance of crystallinity in yielding higher discharge capacities, whereas the particle size, surface area, and morphology significantly influenced the rate capability. Notably, the flower-shaped CoDEPP exhibited superior rate capability due to its optimized characteristics. Remarkably, all the investigated materials showcased remarkable stability over a span of more than 2000 cycles. In-depth 3D reconstructions unveiled that material porosity plays a pivotal role in ion diffusion coefficients. Additionally, the presence of self-conditioning, manifesting as electrochemically induced polymerization, was confirmed through Os staining, as evidenced by EDX mapping. This study successfully demonstrated that morphology serves as a versatile tool for designing materials tailored to specific battery applications, with particle size, surface area, and crystallinity playing pivotal roles in achieving desired characteristics.

In addition to single molecules, a pyridine-functionalized porphyrin-MOF was introduced, offering distinct advantages. The synthesis of symmetrical porphyrins is simplified in this case, and copper metallation is more straightforward compared to metals like cobalt or nickel, resulting in higher yields. The material exhibited intriguing characteristics, differing from the typical behavior of pseudocapacitive materials. After thorough material characterization and computational verification that Cu(II) tetraacetate linkers do not participate in the electrochemistry, the material's performance was initially explored in a lithium half-cell, showing promising outcomes with high rate capability and high discharge capacities. Subsequently, efforts were made to

implement the material in multivalent post-lithium systems. However, the material faced challenges in being adapted to aluminum batteries due to the corrosiveness of the electrolyte. Attempts to enhance performance by altering electrolyte composition or binder choice yielded only marginal improvements. Yet, when the material was employed as a cathode material in calcium batteries, coupled with a CaSn_3 alloy anode and $\text{Ca}[\text{B}(\text{hfp})_4]_2$ electrolyte, outstanding performance was demonstrated. The material exhibited remarkable stability over more than 3000 cycles, boasting excellent capacity retention. This study illustrated how modifying functionalities to form a MOF can lead to intriguing changes in the charge-storage mechanism while ensuring stability. Notably, this research marked the first presentation of a porphyrin-based material as a viable cathode material for calcium batteries. Moreover, the material demonstrated functionality even at extremely high rates.

Throughout the study of these materials, a recurring question emerged: what is the nature of self-conditioning, and is it indeed a result of electrochemically induced polymerization? To address this question, various functionalized porphyrins were introduced and examined under identical conditions. Surprisingly, even porphyrins containing functional groups, such as phenyl, which are not recognized to undergo specific polymerization, exhibited the phenomenon known as self-conditioning. This phenomenon is typified by an irreversible oxidation step in cyclic voltammetry (CV) at voltages exceeding 3.8 V. Multiple spectroscopic methods, as well as Os staining, were employed to confirm the formation of a polymer where the ethynyl functionality disappears and aliphatic double bonds emerge. All indications result in the validation of the hypothesis that polymerization occurs in the case of ethynyl, thiophene, or 4-aminophenyl functionalized porphyrins. However, it's important to note that other porphyrins, such as CuDPP, may undergo a distinct stabilization process that also manifests as an irreversible oxidation peak. This behavior could be linked to interactions with PF_6^- anions during charging. Furthermore, DFT calculations provided insights into the potential mechanism of electrochemically induced polymerization. These calculations suggested that the polymerization might not occur within the plane of the porphyrin but rather involve interactions between adjacent planes. Interestingly, PF_6^- anions appear to facilitate the reaction by inducing bending in the porphyrin structure, thus promoting the desired reaction pathways.

Looking forward, porphyrinoids hold immense potential as electrode materials, offering a versatile platform for tailoring properties to suit various battery applications. One of the goals is undoubtedly simplifying material synthesis to achieve higher yields, lower the costs, and a step in this direction has been taken with the development of CuTPyrP-MOF. Moreover, enhancing the properties of metal-free porphyrinoids could represent a substantial advancement towards more sustainable electrode materials.

The concept of self-conditioning remains as an intriguing area for further exploration. In instances where porphyrins do not undergo polymerization, a deeper investigation is warranted. In this context, efforts have been initiated to conduct solid-state NMR measurements on pristine CuDEPP and cycled CuDEPP to ascertain if the ethynyl group disappearance can be chemically validated. However, the paramagnetic nature of the material in its initial state has posed challenges to this approach. While the paramagnetic shift in solid-state NMR has been discussed in literature, its experimental realization remains complex. Alternative methods, such as *in situ* EPR measurements, could be introduced to validate the formation of the cationic radical as proposed in the polymerization process. Additionally, in the case of non-polymerizing stabilization steps, a more in-depth investigation into the interaction with the electrolyte anion is necessary to gain a comprehensive understanding of the underlying mechanism.

This study presents porphyrins as highly versatile materials with great promise for energy storage systems. Despite the existing designs, there is still a wealth of untapped potential in porphyrin research, offering exciting opportunities for further advances.

List of Figures

1.1	Classification of energy storage systems. Reproduced with permission[6], Copyright (2022) Elsevier.	2
1.2	Battery technology timeline. Reproduced with permission[16], Copyright (2022) American Chemical Society.	3
1.3	Comparison between potential and specific capacity of selected electrode materials. Reproduced with permission[18], Copyright (2018) Elsevier.	3
2.1	Working principle of a metal-based secondary battery. Reproduced with permission[22], Copyright (2016) American Chemical Society. . .	10
2.2	Three categories of oxide cathodes. Reproduced with permission[33], Copyright (2020) Springer Nature.	13
2.3	Positions of the redox energies relative to the top of the anion: p bands. Reproduced with permission[33], Copyright (2020) Springer Nature. .	14
2.4	Overview of different electrode materials in current LIBs. Reproduced with permission[39], Copyright (2013) Elsevier.	19
2.5	Overview of different electrode materials and future trend for Ca Batteries. Reproduced with permission[42], Copyright (2022) Wiley. . . .	21
2.6	Synthesis and single X-ray structure of $\text{Ca}[\text{B}(\text{hfp})_4]_2$. Reproduced with permission[45], Copyright (2019) The Royal Society of Chemistry. . .	24
2.7	Electrochemical transformation of the Ca-Sn alloy. Reproduced with permission[43], Copyright (2022) Springer Nature.	25

2.8	A comparative analysis of the gravimetric and volumetric capacities, cost, abundance, standard potentials, cation radius, and charge density of cations including Li, Na, K, Zn, and Al. Reproduced with permission[65], Copyright (2021) Springer Nature.	26
2.9	Typical configuration of an Aluminium-ion battery using room-temperature ionic liquid (RTIL) as electrolyte. Reproduced with permission[65], Copyright (2021) Springer Nature.	26
2.10	Charge Storage mechanism of an AIB with RTIL as electrolyte in A) discharged, B) medium charged and C) fully charged state. Reproduced with permission[64], Copyright (2020) Elsevier.	28
2.11	Formation of chloroaluminate species at varying ratios of AlCl ₃ -[EMIm]Cl electrolyte. Reprdouced with permission[64], Copyright (2020) Elsevier.	29
2.12	The progress in creating organic electrode materials for batteries. Reproduced with permission[78], Copyright (2020) Springer Nature.	31
2.13	Classification of the different organic electrode materials. Reproduced with permission[14], Copyright (2013) The Royal Society of Chemistry.	31
2.14	Possible cell configurations of organic electrode materials, where bipolar materials (B) can be employed between n-type and p-type materials. Cell configuration a) and b) represent the cases of Li ⁺ deposition/intercalation in anode and cathode. Configuration c) and d) are common for p-type materials, where the anions are transported from the electrode to the electrolyte or <i>vice versa</i> . Reproduced with permission[14], Copyright (2013) The Royal Society of Chemistry.	32
2.15	Key Parameters at Material and Device Levels for Practical Batteries. Reproduced with permission[78], Copyright (2020) Springer Nature.	35
2.16	Strategies to improve the performance of organic electrode materials. Reproduced with permission[98], Copyright (2018) Elsevier.	36
2.17	Weak intermolecular interactions in organic batteries. Reproduced with permission[111], Copyright (2020) Wiley.	37
2.18	Porphyrins and closely related structures: a) porphin b) chlorin c) corrin and d) isophlorin.	39
2.19	Possible positions for substitution.	39

2.20	Redox chemistry of NiNC with Mes = 2,4,6-trimethylphenyl. Reproduced with permission[133], Copyright (2014) Wiley.	42
2.21	Synthesis of Por-COF used as cathode material in Li-S batteries. Reproduced with permission[143], Copyright (2016) The Royal Society of Chemistry.	44
2.22	Molecular structure of [5,15-bis-(ethynyl)-10,20-diphenylporphinato]copper(II) (CuDEPP).	46
2.23	Redox reaction of CuDEPP forming dicationic and dianionic species.	46
2.24	Cyclic voltammograms (CVs) of CuDEPP: a) First cycle in a voltage range of 0.05-4.5 V b) 1st to 5th cycle in a voltage range of 1.8-4.5 V. Reproduced with permission[148], Copyright (2017) Wiley.	48
2.25	Rate performance of CuDEPP in a half-cell with different concentrations of the LiTFSI electrolyte 1, 3 and 6M. Reproduced with permission[157], Copyright (2022) The Royal Society of Chemistry.	49
2.26	Structures of porphyrins functionalized with thiophene and ethynyl groups. Reproduced with permission[151], Copyright (2022) Elsevier.	50
2.27	Mechanism[160] of electrochemically induced polymerization of Cu-TAPP. Reproduced with permission[159], Copyright (2023) Wiley. . .	52
3.1	$\pi \rightarrow \pi^*$ transition of ethane. Reproduced with permission[161], Copyright (2004) American Chemical Society.	54
3.2	Signals generated by the electron beam. [By Ponor - Own work, CC BY-SA 4.0, https://commons.wikimedia.org/w/index.php?curid=93635964][07.26.23].	
3.3	Working principle of FIB-SEM-Tomography. Reproduced with permission[163], Copyright 2019, Royal Society of chemistry.	56
3.4	Optical schematic of nanoCT. Reproduced with permission[165], Copyright (2022) Taylor& Francis group.	57
3.5	Typical discharge curves: (a) for different redox-system behavior; (b) at different discharge currents, and (c) for different discharge modes. (d) Typical charge/discharge curve. Reproduced with permission[22], Copyright (2016) American Chemical Society.	58

3.6	a) Voltage vs. time for linear sweep and CV b) typical CV. Reproduced with permission[167], Copyright (2020) The Korean Electrochemical Society.	59
3.7	a) A typical CV and parameters that can be derived from it and b) CV of reversible (a), quasi-reversible (b) and irreversible case (c). Reproduced with permission[167], Copyright (2020) The Korean Electrochemical Society.	60
3.8	a) Processes occurring at electrode surface b) theoretical impedance spectrum showing all processes separately c) practical example of EIS spectrum. Reproduced with permission[168], Copyright (2021) Springer Nature.	60
3.9	a) Randles circuit as an electrical equivalent circuit and b) Nyquist plot with semi circle representing kinetic control and diffusion controlled linear part. Reproduced with permission[22], Copyright (2016) American Chemical Society.	61
5.1	Coin cell assembly for half-cell measurements.	67
5.2	Synthesis of free-base DEPP and its metal complexes with M: Co ²⁺ , Cu ²⁺ , Ni ²⁺ and Zn ²⁺	68
5.3	Visual comparison of the solubility of xDEPPs and DEPP in dichloromethane after one day, confirming the limited solubility of CuDEPP and the more soluble NiDEPP (a). Comparison between the saturation concentrations of DEPP and xDEPPS in electrolyte (b).	69
5.4	Structures of porphyrin molecules xDEPPS used in this chapter (a) and CVs of DEPP (b), CoDEPP (c), NiDEPP (d), CuDEPP (e), and ZnDEPP (f) complexes in Li half-cell with LiPF ₆ electrolyte at the voltage range of 1-4.5 V.	72
5.5	Comparison of the electrochemical properties of the xDEPPs electrodes: (a) the first CV curves obtained at 0.1 mV s ⁻¹ and (b) discharge capacity and CE of xDEPPs in the initial 10 cycles based on the CV measurement in the potential range of 1-4.5 V (Fig. 5.4b-e).	73

5.6	Cycling performance (a) and first discharge curves (b) of xDEPPs at 100 mA g ⁻¹ in the potential range of 2.2-4.5 V.	74
5.7	The rate capability of xDEPP electrodes with an increase in the charge-discharge rate from 100 mA g ⁻¹ to 10 A g ⁻¹ and then a decrease to 500 mA g ⁻¹	75
5.8	XPS measurements in the Co 2p region for CoDEPP (a, b, c) and the Cu 2p region for CuDEPP (d, e, f) and CuDEPP (d, e, f) electrodes at OCV (a, d), charged (b, e), and discharge (c, f) states. UV-Vis absorption spectra of xDEPPs in the Q-band region between 480-680 nm (g).	76
5.9	Calculated frontier molecular energies in DEPP and its metal complexes (xDEPPS) (a) and (b) HOMO-LUMO and (c) HOMO-HOMO-1 energy gap of xDEPPs.	77
5.10	Rate performance of the xDEPPs (a) and selected voltage profile of CoDEPP (b), NiDEPP (c), ZnDEPP (d), and CuDEPP (e) at various current densities from 0.1 to 10 A g ⁻¹ in the potential range of 2.2-4.5 V.	78
5.11	SEM images of the different xDEPP electrode materials that have been used in this chapter.	79
5.12	Morphology of the as prepared metal DEPP electrodes (a, c, e, g), and after 100 cycles (b, d, f, h) for CuDEPP (a, b), CoDEPP (c, d), ZnDEPP (e, f), and NiDEPP (g, h).	79
5.13	The DFT-optimized structures of xDEPPs showing saddled distortion for NiDEPP and CoDEPP.	80
5.14	UV-Vis absorption spectra of DEPP and xDEPPs in DCM.	81
5.15	Comparison between the molecular structures of CoDEPP-TMS (top) and CuDEPP-TMS[148] (bottom). The structures were from single crystal XRD studies discussed in the text.	82

5.16	Crystal structures of CoDEPP-TMS and CuDEPP-TMS showing the top and side views of (a) ruffled Co-porphyrin and (b) planar Cu-porphyrin, and the packing of (c) Co-complex and (d) Cu-complex. Images were generated from CCDC Nos. 1506859[148] and 2143452. Powder XRD patterns (e) and pore size distribution curves (f) of the xDEPP active materials used in this study.	83
5.17	EIS of the xDEPP electrodes before (a) and after cycling at 100 mAh g ⁻¹ (c) with enlarged part of the high frequency region (b, d) and the equivalent circuit model (inset).	84
5.18	Comparison of Nyquist plots of xDEPP electrodes before cycling (a) and CuDEPP electrodes in fresh cells before cycling and after the 10th cycle (b). Estimated diffusion coefficient in fresh and cycled xDEPPs determined by EIS (c). (The equivalent circuit model and fitting results are shown in Fig. 5.17 and Table 5.4).	85
5.19	Nitrogen adsorption-desorption isotherms of the xDEPP active materials.	86
5.20	Molecular level stacking of CoDEPP (a) and CuDEPP (b).	87
5.21	Thermogravimetric analysis TGA (black signals), differential scanning calorimetry DCS (blue signals) and mass spectrometry MS of selected DEPP, CoDEPP and CuDEPP. The TGA and DSC profiles (a, c, e) and analysis of the evolved gases (b, d, f) of DEPP, CoDEPP and CuDEPP, respectively.	89
6.1	Coin cell assembly for half-cell measurements with GDL current collector.	93
6.2	Deprotection reaction of CoDEPP-TMS, leading to the formation of CoDEPP. Different reaction conditions have been utilized to prepare CoDEPP with different morphologies.	95
6.3	SEM Images of CoDEPP 12-15	97
6.4	Powder XRD patterns of CoDEPP 12-15	98
6.5	Cell configuration with CoDEPP in a lithium half-cell (in the charging state).	99
6.6	CV of CoDEPP 12-15 at 0.1 mV s ⁻¹ in a potential range of 2.2-4.5 V.	99

6.7	CVs of CoDEPP 12-15 (a-d) at 0.1 mV s ⁻¹ in a potential range 2.2-4.5 V - Cycles 1, 5, 10, 15 and 20.	100
6.8	a) Rate performance of CoDEPP 12-15 at different current densities between 0.1-4 A g ⁻¹ in a potential range of 2.2-4.5 V and b) 1st charge-discharge profiles.	101
6.9	a) Long-term cycling of CoDEPP 12-15 at 0.1 A g ⁻¹ for the first 20 cycles and 1 A g ⁻¹ at the further cycles in a voltage range of 2.2-4.5 V and b) zoom in to the first 100 cycles.	103
6.10	Charge-Discharge Profiles of morphological different CoDEPP 12-15 (a-d) after 100, 500, 1000, 1500 and 2000 cycles.	105
6.11	Nquist plots of CoDEPP 12-15 of non-cycled (a-d) and cycled (e-h) cells with their fit and the used equivalent circuit.	106
6.12	Nquist plots of CoDEPP 12-15 non-cycled cells in the high frequency regions.	107
6.13	Nquist plots of CoDEPP 12-15 (a-d) comparison of non-cycled and cycled cells.	108
6.14	Diffusion coefficient estimated by EIS of non-cycled and cycled CoDEPP cells.	109
6.15	2D slices of of the 3D reconstructed datasets, where the red dots represent the set pores within in the material.	113
6.16	3D visualization of the datasets with the pores highlighted in colors (similar color correspond to similar volume in the respective sample) of CoDEPP 12 (a), 13 (b) and 13 (embedded) (c). Right side: the reconstructed image was cropped in half for a better visualization of the pores distribution in the segmented volume. The distribution is better seen in the sample c) due to the higher density of pores in samples a) and b).	115
6.17	Instability of CoDEPP 12 in the electron beam, appearance of bubble in the scan 119 compared to scan 17.	117
6.18	(a) EDX layered image with element mapping (Os-red, C-turquoise, O-blue, Si-green, Co-purple) and (b) showing element distribution of cycled sample CoDEPP 12	118

6.19	Comparison Os mapping of cycled and non-cycled CoDEPP 12 electrode.	118
7.1	Synthetic route to obtain CuTPyrP-MOF.	123
7.2	(a) UV-Vis spectra of CuTPyrP and TPyrP and (b) IR spectrum of CuTPyrP-MOF and TPyrP.	124
7.3	Detailed XPS Cu2p3/2 spectrum of CuTPyrP-MOF. Reprduced with permission[260], Copyright 2023, Wiley.	125
7.4	Comparison of powder XRD diffraction pattern of batch 20 used in battery cells (blue), batch 21(a) freshly prepared sample from solution.	126
7.5	Comparison of SEM images of MOF 20 and 21.	127
7.6	Comparison of powder XRD diffraction pattern of batch 20 used in battery cells, batch 21(a) freshly measured, 21(b) dried before measured, simulated pattern (blue) and pattern from literature[262], reproduced with permission, Copyright (2016), American Chemical Society. . . .	128
7.7	Visualization of Frontier Molecular Orbitals (FMO) for the Tetraanion Model of CuTPyrP-MOF.	130
7.8	Cyclic Voltammogram of 20 in a lithium half-cell with a sweep rate of 0.1 mV s ⁻¹	132
7.9	(a) Rate test of 20 in lithium half-cell (b) initial charge-discharge curves in a voltage range of 1.8-4.5 V.	133
7.10	Charge-dischare curves of CuTPyrP-MOF visualizing disappearance of plateaus in cycle 8 and 80 compared to cycle 1 with a voltage range of 1.8-4.5 V.	134
7.11	Galvanstatic cycling of TPyrP and CuTPyrP-MOF in a voltage range of 0.3-2.3 V (vs. Al/Al ³⁺) at 50 mA g ⁻¹ using an electrolyte of 1.5:1 AlCl ₃ :EMImCl.	136
7.12	GCPL of TPyrP and CuTPyrP-MOF in a voltage range of 0.3-2.3 V (vs. Al/Al ³⁺) at 50 mA g ⁻¹ comparing electrolyte sof 1.5:1, 1.3:1 and 1.1:1 AlCl ₃ :EMImCl.	136
7.13	(a) Charge-discharge profile CuTPyrP-MOF with 1.3:1 AlCl ₃ :EMImCl and (b) GCPL in voltage range of 1-2.3 V (vs. Al/Al ³⁺) of CuTPyrP-MOF with 1.3:1 and 1.5:1 AlCl ₃ :EMImCl.	137

7.14	(a) CV of CuTPyrP-MOF between 1-2.3 V of cell with 1.3:1 electrolyte composition and (b) GCPL of CuTPyrP-MOF after observing in CV and using PVDF as binder.	138
7.15	CVs of (a) TPyrP and (b) CuTPyrP-MOF in the voltage range of 0.5-3.3 V with sweep rate of 1 mV s ⁻¹ and the charge discharge profiles (a) TPyrP and (b) CuTPyrP-MOF performed at a current density of 0.1 A g ⁻¹ . Reproduced with permission[260], Copyright (2023) Wiley.	140
7.16	Ex-situ XPS in Ca 2p region of discharged (0.5 V), charged (3.3 V) and pristine TPyrP (a) and CuTPyrP-MOF (b). Reproduced with permission[260], Copyright (2023) Wiley.	142
7.17	Cu 2p _{3/2} -XPS spectra of CuTPyrP-MOF in charged (at 3.3 V) and discharged (at 0.5 V) state. Reproduced with permission[260], Copyright (2023) Wiley.	143
7.18	(a) long-term cycling at 1 A g ⁻¹ , (b) Rate capability test with current densities between 0.2-2 A g ⁻¹ and charge discharge profiles of CuTPyrP-MOF at various current densities (c) and in long-term cycling at 1 A g ⁻¹ (d). Reproduced with permission[260], Copyright (2023) Wiley.	144
8.1	Selected porphyrinoids for this study.	151
8.2	Comparison of the first two cycles in CV in a voltage range of 1.8-4.5 V at a sweep rate of 0.1 mV s ⁻¹ (a) CuDEPP, (b) CuTEP (c) CuDPP (d) CuTPP (e) CuDPyrPP and (f) CuTPyrP-MOF.	152
8.3	Consecutive cycles in CV of CuDEPP, CuTEP, CuDPP, CuTPP, CuTPyrP-MOF and CuDPyrP in a voltage range of 1.8-4.5 V with sweep rate of 0.1 mV s ⁻¹	154
8.4	Comparison of the charge-discharge profile in a voltage range of 1.8-4.5 V at a current rate of 0.1 mV s ⁻¹ (a) all, (b) pyridine functionalized porphyrinoids (c) phenyl functionalized porphyrinoids and (d) porphyrinoids with ethynyl functionality.	156
8.5	Rate tests in a voltage range of 1.8-4.5 V at a current rates of 0.1, 0.2, 0.5, 1, 2, 4 and back to 1 A g ⁻¹	158

8.6	Long-term cycling in a voltage range of 1.8-4.5 V with initial 20 cycles at a current rate of 0.2 A g ⁻¹ , increasing to 1 A g ⁻¹ (b) zoom to the first 100 cycles.	158
8.7	Dissolution of CuDEPP, CuDPP, CuTEP, CuTPP, CuTPyrP-MOF and CuDPyrPP in DCM after one hour.	159
8.8	(a) CV curves of CuDPP obtained after various sweep rates in voltage range of 1.8-4.5 V (b) and (c) plot of $i/\nu^{1/2}$ vs. $\nu^{1/2}$ (d) visualized capacitive contribution at 1 mV s ⁻¹ and (e) contribution ratio of all sweep rates.	161
8.9	(a) CV curves of CuTPyrP-MOF obtained after various sweep rates in voltage range of 1.8-4.5 V (b) and (c) plot of $i/\nu^{1/2}$ vs. $\nu^{1/2}$ (d) visualized capacitive contribution at 1 mV s ⁻¹ and (e) contribution ratio of all sweep rates.	163
8.10	Contribution ratio of all compounds at sweep rates of (a) 0.2 mV s ⁻¹ and (b) 10 mV s ⁻¹	164
8.11	Possible Mechanism of the polyacetylene formation of CuDEPP and the arrangements in polyacetylene.	165
8.12	Polymerization through plane: (a) arrangement of CuDEPP and (b) polymerization product on example of dimer.	166
8.13	Bending of CuDEPP caused by PF ₆ ⁻ anion (a) top view and (b) side view.	167
8.14	Reported Cyclization reaction on Au(III) surface (a) formation of polymeric structure and (b) variation of the cis and trans formation. Reproduced with permission[282], Copyright (2023) Springer Nature. . .	167
A.1	The rate capability of the DEPP electrode was assessed by varying the charge-discharge rate, starting from 100 mA g ⁻¹ and gradually decreasing to 10 mA g ⁻¹ , and then increasing it to 500 mA g ⁻¹ (a). The selected voltage profile is depicted in (b).	234
A.2	The rate capability of the CoDEPP electrode was assessed by varying the charge-discharge rate, starting from 100 mA g ⁻¹ and gradually decreasing to 10 mA g ⁻¹ , and then increasing it to 500 mA g ⁻¹	234

A.3	The rate capability of the NiDEPP electrode was assessed by varying the charge-discharge rate, starting from 100 mA g ⁻¹ and gradually decreasing to 10 mA g ⁻¹ , and then increasing it to 500 mA g ⁻¹	235
A.4	The rate capability of the CuDEPP electrode was assessed by varying the charge-discharge rate, starting from 100 mA g ⁻¹ and gradually decreasing to 10 mA g ⁻¹ , and then increasing it to 500 mA g ⁻¹	235
A.5	The rate capability of the ZnDEPP electrode was assessed by varying the charge-discharge rate, starting from 100 mA g ⁻¹ and gradually decreasing to 10 mA g ⁻¹ , and then increasing it to 500 mA g ⁻¹	235
A.6	SEM Images of other CoDEPP morphologies 16-19.	237
A.7	Powder XRD pattern of all CoDEPP morphologies 12-19.	237
A.8	UV-Vis absorptions spectrum of CoDEPP 12-15.	238
A.9	IR spectra of CoDEPP 12-15.	238
A.10	Solubility of CoDEPP 12-15 in DCM after 1h.	239
A.11	UV-Vis absorptions spectrum of CuDPP, CuTPP, CuDEPP, CuTPyrP-MOF, CuDPyrPP.	239
A.12	Powder X-ray diffractograms of CuDPyrPP, CuDEPP, CuTEP, CuTPP, CuDPP and CuTPyrP-MOF.	240
A.13	SEM images of CuDPyrPP, CuDEPP, CuTEP, CuTPP, CuDPP and CuTPyrP-MOF.	241
A.14	Electronic properties of of CuDPyrPP, CuDEPP, CuTEP, CuTPP, CuDPP and CuTPyrP-MOF.	241
A.15	(a) CV curves of CuDEPP obtained after various sweep rates in voltage range of 1.8-4.5 V (b) visualized capacitive contribution at 1 mV s ⁻¹ (c) and (d) plot of i/v ^{1/2} vs. v ^{1/2} and (e) contribution ratio of all sweep rates.	242
A.16	(a) CV curves of CuDPyrPP obtained after various sweep rates in voltage range of 1.8-4.5 V (b) visualized capacitive contribution at 1 mV s ⁻¹ (c) and (d) plot of i/v ^{1/2} vs. v ^{1/2} and (e) contribution ratio of all sweep rates.	243

A.17 (a) CV curves of CuTEP obtained after various sweep rates in voltage range of 1.8-4.5 V (b) visualized capacitive contribution at 1 mV s ⁻¹ (c) and (d) plot of $i/\nu^{1/2}$ vs. $\nu^{1/2}$ and (e) contribution ratio of all sweep rates.	244
A.18 (a) CV curves of CuTPP obtained after various sweep rates in voltage range of 1.8-4.5 V (b) visualized capacitive contribution at 1 mV s ⁻¹ (c) and (d) plot of $i/\nu^{1/2}$ vs. $\nu^{1/2}$ and (e) contribution ratio of all sweep rates.	245

List of Tables

2.1	Defenition of cathode and anode.	6
2.2	Comparison between gravimetric capacity of lithiated metal oxides in LIBs.[23]	16
2.3	Comparison between material properties of different metal anodes.[42]	20
2.4	Different Types of organic electrode materials and their redox mechanism.[42]	34
5.1	Concentration and ϵ of saturated solutions of xDEPPs and DEPP in the electrolyte after 1 day confirm that CuDEPP has limited solubility, while NiDEPP is the more-soluble xDEPP in the series.	69
5.2	Frontier molecular orbitals HOMO and LUMO and LUMO+n ($n = 1$ and 2) orbitals of DEPP and xDEPP. LUMO+n denotes the orbitals lying energetically higher above the LUMO. For complexes containing unpaired electrons with a multiplicity $\neq 1$ the corresponding α and β orbitals are provided.	70
5.3	Calculated and experimental bond lengths (\AA) in xDEPPs.	71
5.4	EIS analyses results of the cell based on the xDEPP cathodes (fresh cell and after 10 cycles).	84
5.5	Thermal characterizations of xDEPPs with $T_{(5)}$ Temperature of 5% weight loss, $T_{(10)}$ temperature of 10% weight loss, and $W\%_{@800^{\circ}\text{C}}$ the percentage of solid residue after heating from room temperature to 800°C under argon.	87
6.1	Different reaction attempts to tune the morphology of CoDEPP with * samples employed in this study.	96

6.2	Rate capability factor CoDEPP 12-15	102
6.3	Stability factor CoDEPP 12-15	103
6.4	Capacity retention of CoDEPP 12-15 at 1 A g ⁻¹ for the first 1000 cycles and further 2000 cycles.	104
6.5	EIS analyses results of the cell based on CoDEPP 12-15 cathodes (non-cycled and after 10 cycles).	109
6.6	Pore volume of CoDEPP 12 , 13 and 13 (embedded).	114
7.1	Elemental Analysis results CuTPyrP-MOF.	124
8.1	Irreversible oxidation peaks observed during the initial charge cycle, potentially correlated with the self-conditioning process.	153
9.1	Crystal data and structure refinement of CoDEPP-TMS.	180
A.1	Frontier orbitals (HOMO and LUMO) of xDEPPs HOMO-2 and HOMO- 1 denote the molecule orbitals below the HOMO.	233
A.2	Frontier orbitals of (CuDEPP) ₃	236

Bibliography

- [1] Y. Zhao, O. Pohl, A. I. Bhatt, G. E. Collis, P. J. Mahon, T. R  ther, A. F. Hollenkamp, *Sustainable Chemistry* **2021**, *2*, 167–205.
- [2] N. Armaroli, V. Balzani, *Angewandte Chemie International Edition* **2007**, *46*, 52–66.
- [3] M. Fichtner, K. Edstr  m, E. Ayerbe, M. Berecibar, A. Bhowmik, I. E. Castelli, S. Clark, R. Dominko, M. Erakca, A. A. Franco, et al., *Advanced Energy Materials* **2022**, *12*, 2102904.
- [4] N. L. Panwar, S. C. Kaushik, S. Kothari, *Renewable and sustainable energy reviews* **2011**, *15*, 1513–1524.
- [5] A. A. Kebede, T. Kalogiannis, J. Van Mierlo, M. Berecibar, *Renewable and Sustainable Energy Reviews* **2022**, *159*, 112213.
- [6] J. Mitali, S. Dhinakaran, A. Mohamad, *Energy Storage and Saving* **2022**.
- [7] V. Z. Castillo, H.-S. De Boer, R. M. Mu  oz, D. E. Gernaat, R. Benders, D. van Vuuren, *Energy* **2022**, *258*, 124741.
- [8] H. Wang, C.-J. Yao, H.-J. Nie, K.-Z. Wang, Y.-W. Zhong, P. Chen, S. Mei, Q. Zhang, *Journal of Materials Chemistry A* **2020**, *8*, 11906–11922.
- [9] Y. Chen, K. Fan, Y. Gao, C. Wang, *Advanced Materials* **2022**, 2200662.
- [10] D. J. Min, F. Miomandre, P. Audebert, J. E. Kwon, S. Y. Park, *ChemSusChem* **2019**, *12*, 503–510.
- [11] A. Wild, M. Strumpf, B. H  upler, M. D. Hager, U. S. Schubert, *Advanced Energy Materials* **2017**, *7*, 1601415.
- [12] H. Kye, Y. Kang, D. Jang, J. E. Kwon, B.-G. Kim, *Advanced Energy and Sustainability Research* **2022**, *3*, 2200030.
- [13]   . Deunf, P. Moreau,   . Quarez, D. Guyomard, F. Dolhem, P. Poizot, *Journal of Materials Chemistry A* **2016**, *4*, 6131–6139.
- [14] Z. Song, H. Zhou, *Energy & Environmental Science* **2013**, *6*, 2280–2301.
- [15] T. Huang, M. Long, J. Xiao, H. Liu, G. Wang, *Energy Materials* **2021**.

- [16] S. Ponnada, M. S. Kiai, R. Krishnapriya, R. Singhal, R. K. Sharma, *Energy & Fuels* **2022**, *36*, 6013–6026.
- [17] M. R. Kaiser, Z. Han, J. Liang, S.-X. Dou, J. Wang, *Energy storage materials* **2019**, *19*, 1–15.
- [18] Y. Liang, Y. Yao, *Joule* **2018**, *2*, 1690–1706.
- [19] A. Vlad, J. Chen, Y. Yao, *Organic Electrode Materials and Engineering for Electrochemical Energy Storage*, **2023**.
- [20] D. Pribat, *Rechargeable Batteries—Materials, Technologies and New Trends*; Zhang, Z., Zhang, SS, Eds, **2015**.
- [21] S. Petrovic, *Cham: Springer International Publishing* **2021**.
- [22] S. Muench, A. Wild, C. Friebe, B. Haupler, T. Janoschka, U. S. Schubert, *Chemical reviews* **2016**, *116*, 9438–9484.
- [23] C. Glaize, S. Genies, *Lithium batteries and other electrochemical storage systems*, John Wiley & Sons, **2013**.
- [24] T. B. Reddy, *Linden's handbook of batteries*, McGraw-Hill Education, **2011**.
- [25] Ping Gao, PhD thesis, Universität Ulm, **18.11.2016**.
- [26] A. Nyman, T. G. Zavalis, R. Elger, M. Behm, G. Lindbergh, *Journal of The Electrochemical Society* **2010**, *157*, A1236.
- [27] M. Salado, E. Lizundia, I. Oyarzabal, D. Salazar, *physica status solidi (a)* **2022**, *219*, 2100710.
- [28] Z. Zhang, S. S. Zhang, *Nature Communications* **2015**, *4*.
- [29] L. J. Hounjet, *Energy Storage* **2022**, *4*, e309.
- [30] A. Thompson, M. Whittingham, *Materials Research Bulletin* **1977**, *12*, 741–744.
- [31] K. Mizushima, P. Jones, P. Wiseman, J. B. Goodenough, *Materials Research Bulletin* **1980**, *15*, 783–789.
- [32] A. Yoshino, *Angewandte Chemie International Edition* **2012**, *51*, 5798–5800.
- [33] A. Manthiram, *Nature communications* **2020**, *11*, 1550.
- [34] R. Korthauer, *Handbuch lithium-ionen-batterien*, Springer, **2013**.
- [35] B. K. Sovacool, *The Extractive Industries and Society* **2021**, *8*, 271–293.
- [36] B. Lung-Hao Hu, F.-Y. Wu, C.-T. Lin, A. N. Khlobystov, L.-J. Li, *Nature communications* **2013**, *4*, 1687.
- [37] X.-B. Cheng, R. Zhang, C.-Z. Zhao, Q. Zhang, *Chemical reviews* **2017**, *117*, 10403–10473.
- [38] S.-H. Yu, X. Feng, N. Zhang, J. Seok, H. D. Abruña, *Accounts of chemical research* **2018**, *51*, 273–281.
- [39] J. Xu, S. Dou, H. Liu, L. Dai, *Nano Energy* **2013**, *2*, 439–442.

- [40] M. E. Arroyo-de Dompablo, A. Ponrouch, P. Johansson, M. R. Palacín, *Chemical Reviews* **2019**, *120*, 6331–6357.
- [41] I. D. Hosein, *ACS Energy Letters* **2021**, *6*, 1560–1565.
- [42] H. Song, C. Wang, *Advanced Energy and Sustainability Research* **2022**, *3*, 2100192.
- [43] Z. Zhao-Karger, Y. Xiu, Z. Li, A. Reupert, T. Smok, M. Fichtner, *nature communications* **2022**, *13*, 3849.
- [44] D. Wang, X. Gao, Y. Chen, L. Jin, C. Kuss, P. G. Bruce, *Nature materials* **2018**, *17*, 16–20.
- [45] Z. Li, O. Fuhr, M. Fichtner, Z. Zhao-Karger, *Energy & Environmental Science* **2019**, *12*, 3496–3501.
- [46] A. Ponrouch, J. Bitenc, R. Dominko, N. Lindahl, P. Johansson, M. R. Palacín, *Energy Storage Materials* **2019**, *20*, 253–262.
- [47] X. Yu, M. J. Boyer, G. S. Hwang, A. Manthiram, *Advanced Energy Materials* **2019**, *9*, 1803794.
- [48] W. Ren, F. Xiong, Y. Fan, Y. Xiong, Z. Jian, *ACS applied materials & interfaces* **2020**, *12*, 10471–10478.
- [49] A. L. Lipson, D. L. Proffit, B. Pan, T. T. Fister, C. Liao, A. K. Burrell, J. T. Vaughey, B. J. Ingram, *Journal of The Electrochemical Society* **2015**, *162*, A1574.
- [50] M. Cabello, F. Nacimiento, J. R. González, G. Ortiz, R. Alcántara, P. Lavela, C. Perez-Vicente, J. L. Tirado, *Electrochemistry Communications* **2016**, *67*, 59–64.
- [51] Y. Jie, Y. Tan, L. Li, Y. Han, S. Xu, Z. Zhao, R. Cao, X. Ren, F. Huang, Z. Lei, et al., *Angewandte Chemie International Edition* **2020**, *59*, 12689–12693.
- [52] X. Tang, D. Zhou, B. Zhang, S. Wang, P. Li, H. Liu, X. Guo, P. Jaumaux, X. Gao, Y. Fu, et al., *Nature Communications* **2021**, *12*, 2857.
- [53] S. Hou, X. Ji, K. Gaskell, P.-f. Wang, L. Wang, J. Xu, R. Sun, O. Borodin, C. Wang, *Science* **2021**, *374*, 172–178.
- [54] A. L. Lipson, S. Kim, B. Pan, C. Liao, T. T. Fister, B. J. Ingram, *Journal of Power Sources* **2017**, *369*, 133–137.
- [55] A. Ponrouch, C. Frontera, F. Bardé, M. R. Palacín, *Nature materials* **2016**, *15*, 169–172.
- [56] D. Aurbach, R. Skaletsky, Y. Gofer, *Journal of The Electrochemical Society* **1991**, *138*, 3536.
- [57] C. Derrington, A. Lindner, M. O’keeffe, *Journal of Solid State Chemistry* **1975**, *15*, 171–174.
- [58] J. Muldoon, C. B. Bucur, T. Gregory, *Chemical reviews* **2014**, *114*, 11683–11720.
- [59] H. Matzke, *Journal of Materials Science* **1970**, *5*, 831–836.
- [60] A. Shyamsunder, L. E. Blanc, A. Assoud, L. F. Nazar, *ACS Energy Letters* **2019**, *4*, 2271–2276.

- [61] K. Ta, R. Zhang, M. Shin, R. T. Rooney, E. K. Neumann, A. A. Gewirth, *ACS applied materials & interfaces* **2019**, *11*, 21536–21542.
- [62] S. D. Pu, C. Gong, X. Gao, Z. Ning, S. Yang, J.-J. Marie, B. Liu, R. A. House, G. O. Hartley, J. Luo, et al., *ACS Energy Letters* **2020**, *5*, 2283–2290.
- [63] J. Park, Z.-L. Xu, G. Yoon, S. K. Park, J. Wang, H. Hyun, H. Park, J. Lim, Y.-J. Ko, Y. S. Yun, et al., *Advanced materials* **2020**, *32*, 1904411.
- [64] B. Craig, T. Schoetz, A. Cruden, C. P. de Leon, *Renewable and Sustainable Energy Reviews* **2020**, *133*, 110100.
- [65] E. Faegh, B. Ng, D. Hayman, W. E. Mustain, *Nature Energy* **2021**, *6*, 21–29.
- [66] P. Gifford, J. Palmisano, *Journal of the Electrochemical Society* **1988**, *135*, 650.
- [67] K. V. Kravchyk, S. Wang, L. Piveteau, M. V. Kovalenko, *Chemistry of Materials* **2017**, *29*, 4484–4492.
- [68] N. P. Stadie, S. Wang, K. V. Kravchyk, M. V. Kovalenko, *ACS nano* **2017**, *11*, 1911–1919.
- [69] L. D. Reed, E. Menke, *Journal of the Electrochemical Society* **2013**, *160*, A915.
- [70] N. S. Hudak, *The Journal of Physical Chemistry C* **2014**, *118*, 5203–5215.
- [71] Y. Liu, S. Sang, Q. Wu, Z. Lu, K. Liu, H. Liu, *Electrochimica Acta* **2014**, *143*, 340–346.
- [72] A. Holland, R. Mckerracher, A. Cruden, R. Wills, *Journal of Applied Electrochemistry* **2018**, *48*, 243–250.
- [73] G. A. Elia, K. Marquardt, K. Hoepfner, S. Fantini, R. Lin, E. Knipping, W. Peters, J.-F. Drillet, S. Passerini, R. Hahn, *Advanced Materials* **2016**, *28*, 7564–7579.
- [74] D. Xu, M. Liang, S. Qi, W. Sun, L.-P. Lv, F.-H. Du, B. Wang, S. Chen, Y. Wang, Y. Yu, *ACS nano* **2020**, *15*, 47–80.
- [75] D. Williams, J. Byrne, J. Driscoll, *Journal of The Electrochemical Society* **1969**, *116*, 2.
- [76] P. Novák, K. Müller, K. Santhanam, O. Haas, *Chemical Reviews* **1997**, *97*, 207–282.
- [77] Y. Liang, Z. Tao, J. Chen, *Advanced Energy Materials* **2012**, *2*, 742–769.
- [78] Y. Lu, J. Chen, *Nature Reviews Chemistry* **2020**, *4*, 127–142.
- [79] Y. Lu, Q. Zhang, F. Li, J. Chen, *Angewandte Chemie* **2023**, *135*, e202216047.
- [80] B. Esser, F. Dolhem, M. Becuwe, P. Poizot, A. Vlad, D. Brandell, *Journal of Power Sources* **2021**, *482*, 228814.
- [81] S.-R. Deng, L.-B. Kong, G.-Q. Hu, T. Wu, D. Li, Y.-H. Zhou, Z.-Y. Li, *Electrochimica acta* **2006**, *51*, 2589–2593.
- [82] N. Oyama, T. Tatsuma, T. Sato, T. Sotomura, *Nature* **1995**, *373*, 598–600.

- [83] X.-y. Han, C.-x. Chang, L.-j. Yuan, T.-l. Sun, J. Sun, *Advanced materials* **2007**, *19*, 1616–1621.
- [84] N. Oyama, T. Sarukawa, Y. Mochizuki, T. Shimomura, S. Yamaguchi, *Journal of Power Sources* **2009**, *189*, 230–239.
- [85] A. G. MacDiarmid, L. Yang, W. Huang, B. Humphrey, *Synthetic metals* **1987**, *18*, 393–398.
- [86] N. Mermilliod, J. Tanguy, F. Petiot, *Journal of the Electrochemical Society* **1986**, *133*, 1073.
- [87] M. Zhou, J. Qian, X. Ai, H. Yang, *Advanced Materials* **2011**, *23*, 4913–4917.
- [88] K. Kaneto, K. Yoshino, Y. Inuishi, *Japanese journal of applied physics* **1983**, *22*, L567.
- [89] L. Liu, F. Tian, X. Wang, Z. Yang, M. Zhou, X. Wang, *Reactive and Functional Polymers* **2012**, *72*, 45–49.
- [90] K. Sakaushi, E. Hosono, G. Nickerl, T. Gemming, H. Zhou, S. Kaskel, J. Eckert, *Nature communications* **2013**, *4*, 1485.
- [91] P. J. Nigrey, D. MacInnes, D. P. Nairns, A. G. MacDiarmid, A. J. Heeger, *Journal of The Electrochemical Society* **1981**, *128*, 1651.
- [92] L. Shacklette, J. Toth, N. Murthy, R. Baughman, *Journal of the Electrochemical Society* **1985**, *132*, 1529.
- [93] L. Zhu, A. Lei, Y. Cao, X. Ai, H. Yang, *Chemical Communications* **2013**, *49*, 567–569.
- [94] K. Oyaizu, H. Nishide, *Advanced Materials* **2009**, *21*, 2339–2344.
- [95] K. Nakahara, K. Oyaizu, H. Nishide, *Chemistry Letters* **2011**, *40*, 222–227.
- [96] T. Janoschka, M. D. Hager, U. S. Schubert, *Advanced Materials* **2012**, *24*, 6397–6409.
- [97] L. Zhan, Z. Song, N. Shan, J. Zhang, J. Tang, H. Zhan, Y. Zhou, Z. Li, C. Zhan, *Journal of Power Sources* **2009**, *193*, 859–863.
- [98] Y. Lu, Q. Zhang, L. Li, Z. Niu, J. Chen, *Chem* **2018**, *4*, 2786–2813.
- [99] C. N. Gannett, L. Melecio-Zambrano, M. J. Theibault, B. M. Peterson, B. P. Fors, H. D. Abruña, *Materials Reports: Energy* **2021**, *1*, 100008.
- [100] Y. Lu, Q. Zhao, L. Miao, Z. Tao, Z. Niu, J. Chen, *The Journal of Physical Chemistry C* **2017**, *121*, 14498–14506.
- [101] A. Iordache, D. Bresser, S. Solan, M. Retegan, M. Bardet, J. Skrzypski, L. Picard, L. Dubois, T. Gutel, *Advanced Sustainable Systems* **2017**, *1*, 1600032.
- [102] S. Gottis, A.-L. Barrès, F. Dolhem, P. Poizot, *ACS Applied Materials & Interfaces* **2014**, *6*, 10870–10876.
- [103] Y. Liang, Z. Chen, Y. Jing, Y. Rong, A. Facchetti, Y. Yao, *Journal of the American Chemical Society* **2015**, *137*, 4956–4959.

- [104] Z. Zhu, J. Chen, *Journal of the Electrochemical Society* **2015**, *162*, A2393.
- [105] T. Ma, Q. Zhao, J. Wang, Z. Pan, J. Chen, *Angewandte Chemie International Edition* **2016**, *55*, 6428–6432.
- [106] T. Matsunaga, T. Kubota, T. Sugimoto, M. Satoh, *Chemistry letters* **2011**, *40*, 750–752.
- [107] Z. Song, Y. Qian, M. L. Gordin, D. Tang, T. Xu, M. Otani, H. Zhan, H. Zhou, D. Wang, *Angewandte Chemie* **2015**, *127*, 14153–14157.
- [108] Y. Wang, Y. Ding, L. Pan, Y. Shi, Z. Yue, Y. Shi, G. Yu, *Nano Letters* **2016**, *16*, 3329–3334.
- [109] T. B. Schon, B. T. McAllister, P.-F. Li, D. S. Seferos, *Chemical Society Reviews* **2016**, *45*, 6345–6404.
- [110] J. J. Shea, C. Luo, *ACS applied materials & interfaces* **2020**, *12*, 5361–5380.
- [111] C. Wang, *Energy & Environmental Materials* **2020**, *3*, 441–452.
- [112] C. Wang, H. Dong, L. Jiang, W. Hu, *Chemical Society Reviews* **2018**, *47*, 422–500.
- [113] A. Shimizu, H. Kuramoto, Y. Tsujii, T. Nokami, Y. Inatomi, N. Hojo, H. Suzuki, J.-i. Yoshida, *Journal of Power Sources* **2014**, *260*, 211–217.
- [114] Z. Luo, L. Liu, J. Ning, K. Lei, Y. Lu, F. Li, J. Chen, *Angewandte Chemie International Edition* **2018**, *57*, 9443–9446.
- [115] C. Wang, Y. Fang, Y. Xu, L. Liang, M. Zhou, H. Zhao, Y. Lei, *Advanced Functional Materials* **2016**, *26*, 1777–1786.
- [116] T. Kakui, S. Sugawara, Y. Hirata, S. Kojima, Y. Yamamoto, *Chemistry—A European Journal* **2011**, *17*, 7768–7771.
- [117] E. B. Fleischer, *Accounts of Chemical Research* **1970**, *3*, 105–112.
- [118] K. M. Kadish, E. Van Caemelbecke, *Journal of Solid State Electrochemistry* **2003**, *7*, 254–258.
- [119] A. Osuka, E. Tsurumaki, T. Tanaka, *Bulletin of the Chemical Society of Japan* **2011**, *84*, 679–697.
- [120] M. Imran, M. Ramzan, A. K. Qureshi, M. A. Khan, M. Tariq, *Biosensors* **2018**, *8*, 95.
- [121] D. Wróbel, A. Siejak, P. Siejak, *Solar Energy Materials and Solar Cells* **2010**, *94*, 492–500.
- [122] M. Gouterman, G. H. Wagnière, L. C. Snyder, *Journal of Molecular Spectroscopy* **1963**, *11*, 108–127.
- [123] N. J. Hestand, F. C. Spano, *Chemical reviews* **2018**, *118*, 7069–7163.
- [124] M. Gouterman, *Journal of Molecular Spectroscopy* **1961**, *6*, 138–163.
- [125] G. Zamborlini, D. Lüftner, Z. Feng, B. Kollmann, P. Puschnig, C. Dri, M. Panighel, G. Di Santo, A. Goldoni, G. Comelli, et al., *Nature communications* **2017**, *8*, 335.
- [126] W. Zheng, N. Shan, L. Yu, X. Wang, *Dyes and Pigments* **2008**, *77*, 153–157.

- [127] A. Dudkowiak, E. Tešlak, J. Habdas, *Journal of molecular structure* **2006**, *792*, 93–98.
- [128] M. Kawao, H. Ozawa, H. Tanaka, T. Ogawa, *Thin Solid Films* **2006**, *499*, 23–28.
- [129] D. Gerster, J. Reichert, H. Bi, J. V. Barth, S. M. Kaniber, A. W. Holleitner, I. Visoly-Fisher, S. Sergani, I. Carmeli, *Nature nanotechnology* **2012**, *7*, 673–676.
- [130] S. Saito, A. Osuka, *Angewandte Chemie International Edition* **2011**, *50*, 4342–4373.
- [131] M.-S. Liao, S. Scheiner, *The Journal of chemical physics* **2002**, *117*, 205–219.
- [132] H.-g. Wang, Q. Wu, L. Cheng, L. Chen, M. Li, G. Zhu, *Energy Storage Materials* **2022**.
- [133] J.-Y. Shin, T. Yamada, H. Yoshikawa, K. Awaga, H. Shinokubo, *Angewandte Chemie* **2014**, *126*, 3160–3165.
- [134] H. Wu, J. Zhang, X. Du, M. Zhang, J. Yang, J. Zhang, T. Luo, H. Liu, H. Xu, G. Cui, *Chemical Communications* **2019**, *55*, 11370–11373.
- [135] K. Jeong, J.-M. Kim, S. H. Kim, G. Y. Jung, J. Yoo, S.-H. Kim, S. K. Kwak, S.-Y. Lee, *Advanced Functional Materials* **2019**, *29*, 1806937.
- [136] H. Yang, S. Zhang, L. Han, Z. Zhang, Z. Xue, J. Gao, Y. Li, C. Huang, Y. Yi, H. Liu, et al., *ACS applied materials & interfaces* **2016**, *8*, 5366–5375.
- [137] L. Shu, J. Yu, Y. Cui, Y. Ma, Y. Li, B. Gao, H.-g. Wang, *International Journal of Hydrogen Energy* **2022**, *47*, 10902–10910.
- [138] N. A. Kumar, R. R. Gaddam, M. Suresh, S. R. Varanasi, D. Yang, S. K. Bhatia, X. Zhao, *Journal of Materials Chemistry A* **2017**, *5*, 13204–13211.
- [139] X. Han, S. Li, W.-L. Song, N. Chen, H. Chen, S. Huang, S. Jiao, *Advanced Energy Materials* **2021**, *11*, 2101446.
- [140] L. Zhou, D. L. Danilov, R.-A. Eichel, P. H. Notten, *Advanced Energy Materials* **2021**, *11*, 2001304.
- [141] S. Dörfler, H. Althues, P. Härtel, T. Abendroth, B. Schumm, S. Kaskel, *Joule* **2020**, *4*, 539–554.
- [142] Z. Wang, B. Wang, Y. Yang, Y. Cui, Z. Wang, B. Chen, G. Qian, *ACS applied materials & interfaces* **2015**, *7*, 20999–21004.
- [143] H. Liao, H. Wang, H. Ding, X. Meng, H. Xu, B. Wang, X. Ai, C. Wang, *Journal of Materials Chemistry A* **2016**, *4*, 7416–7421.
- [144] H.-D. Lim, B. Lee, Y. Bae, H. Park, Y. Ko, H. Kim, J. Kim, K. Kang, *Chemical Society Reviews* **2017**, *46*, 2873–2888.
- [145] L. Majidi, A. Ahmadiparidari, N. Shan, S. Kumar Singh, C. Zhang, Z. Huang, S. Rastegar, K. Kumar, Z. Hemmat, A. T. Ngo, et al., *Small* **2022**, *18*, 2102902.

- [146] W.-H. Ryu, F. S. Gittleson, J. M. Thomsen, J. Li, M. J. Schwab, G. W. Brudvig, A. D. Taylor, *Nature communications* **2016**, *7*, 12925.
- [147] Y. Zhang, R.-L. Zhong, M. Lu, J.-H. Wang, C. Jiang, G.-K. Gao, L.-Z. Dong, Y. Chen, S.-L. Li, Y.-Q. Lan, *ACS Central Science* **2020**, *7*, 175–182.
- [148] P. Gao, Z. Chen, Z. Zhao-Karger, J. E. Mueller, C. Jung, S. Klyatskaya, T. Diemant, O. Fuhr, T. Jacob, R. J. Behm, M. Ruben, M. Fichtner, *Angewandte Chemie (International ed. in English)* **2017**, *56*, 10341–10346.
- [149] Y. Sun, F. He, X. Huang, B. Ren, J. Peng, D. Chen, X. Hu, X. Sun, P. Gao, *Chemical Engineering Journal* **2023**, *451*, 138734.
- [150] Y. Zhou, X. Huang, X. Chen, F. He, D. Chen, X. Sun, S. Tan, P. Gao, *ACS Applied Materials & Interfaces* **2022**, *14*, 40862–40870.
- [151] X. Wu, X. Feng, J. Yuan, X. Yang, H. Shu, C. Yang, J. Peng, E. Liu, S. Tan, P. Gao, et al., *Energy Storage Materials* **2022**, *46*, 252–258.
- [152] S. Shakouri, E. Abouzari-Lotf, J. Chen, T. Diemant, S. Klyatskaya, F. D. Pammer, A. Mizuno, M. Fichtner, M. Ruben, *ChemSusChem* **2023**, *16*, e202202090.
- [153] X. Chen, X. Feng, B. Ren, L. Jiang, H. Shu, X. Yang, Z. Chen, X. Sun, E. Liu, P. Gao, *Nano-Micro Letters* **2021**, *13*, 1–16.
- [154] S. Lv, J. Yuan, Z. Chen, P. Gao, H. Shu, X. Yang, E. Liu, S. Tan, M. Ruben, Z. Zhao-Karger, et al., *ChemSusChem* **2020**, *13*, 2286–2294.
- [155] E. Abouzari-Lotf, R. Azmi, Z. Li, S. Shakouri, Z. Chen, Z. Zhao-Karger, S. Klyatskaya, J. Maibach, M. Ruben, M. Fichtner, *ChemSusChem* **2021**, *14*, 1840–1846.
- [156] Z. Chen, P. Gao, W. Wang, S. Klyatskaya, Z. Zhao-Karger, D. Wang, C. Kübel, O. Fuhr, M. Fichtner, M. Ruben, *ChemSusChem* **2019**, *12*, 3737–3741.
- [157] B. Ren, Y. Sun, X. Feng, J. Peng, R. Ding, X. Sun, E. Liu, P. Gao, *Sustainable Energy & Fuels* **2022**, *6*, 361–370.
- [158] X. Feng, X. Chen, B. Ren, X. Wu, X. Huang, R. Ding, X. Sun, S. Tan, E. Liu, P. Gao, *ACS Applied Materials & Interfaces* **2021**, *13*, 7178–7187.
- [159] T. Smok, E. Abouzari-Lotf, S. Frentzen, T. Diemant, M. Fichtner, *Batteries & Supercaps* **2023**, *6*, e202300026.
- [160] H.-g. Wang, H. Wang, Z. Si, Q. Li, Q. Wu, Q. Shao, L. Wu, Y. Liu, Y. Wang, S. Song, et al., *Angewandte Chemie* **2019**, *131*, 10310–10314.
- [161] R. J. Anderson, D. J. Bendell, P. W. Groundwater, *Organic spectroscopic analysis, Vol. 22*, Royal Society of Chemistry, **2004**.

- [162] W. Zhou, R. Apkarian, Z. L. Wang, D. Joy, *Scanning Microscopy for Nanotechnology: Techniques and Applications* **2007**, 1–40.
- [163] J. E. Van Der Hoeven, E. B. Van Der Wee, D. M. De Winter, M. Hermes, Y. Liu, J. Fokkema, M. Bransen, M. A. Van Huis, H. C. Gerritsen, P. E. De Jongh, et al., *Nanoscale* **2019**, *11*, 5304–5316.
- [164] E. Drioli, L. Giorno, *Encyclopedia of membranes*, Springer, **2018**.
- [165] H. Villarraga-Gómez, D. L. Begun, P. Bhattad, K. Mo, M. Norouzi Rad, R. T. White, S. T. Kelly, *Nondestructive Testing and Evaluation* **2022**, *37*, 519–535.
- [166] N. Hussain, T. Scherer, C. Das, J. Heuer, R. Debastiani, P. Gumbsch, J. Aghassi-Hagmann, M. Hirtz, *Small* **2022**, *18*, 2202987.
- [167] T. Kim, W. Choi, H.-C. Shin, J.-Y. Choi, J. M. Kim, M.-S. Park, W.-S. Yoon, *Journal of Electrochemical Science and Technology* **2020**, *11*, 14–25.
- [168] M. Gaberšček, *Nature Communications* **2021**, *12*, 6513.
- [169] J. H. Furhop, K. M. Kadish, D. G. Davis, *Journal of the American Chemical Society* **1973**, *95*, 5140–5147.
- [170] M. Noori, A. C. Aragonès, G. Di Palma, N. Darwish, S. W. Bailey, Q. Al-Galiby, I. Grace, D. B. Amabilino, A. González-Campo, I. Díez-Pérez, et al., *Scientific reports* **2016**, *6*, 37352.
- [171] F. Ghani, J. Kristen, H. Riegler, *Journal of Chemical & Engineering Data* **2012**, *57*, 439–449.
- [172] C. Julien, A. Mauger, A. Vijn, K. Zaghbi, C. Julien, A. Mauger, A. Vijn, K. Zaghbi, *Lithium batteries*, Springer, **2016**.
- [173] D. H. Freeman, I. D. Swahn, P. Hambright, *Energy & fuels* **1990**, *4*, 699–704.
- [174] R. H. Felton, H. Linschitz, *Journal of the American Chemical Society* **1966**, *88*, 1113–1116.
- [175] Y. Chen, M. Tang, Y. Wu, X. Su, X. Li, S. Xu, S. Zhuo, J. Ma, D. Yuan, C. Wang, et al., *Angewandte Chemie International Edition* **2019**, *58*, 14731–14739.
- [176] Y. Niwa, *The Journal of Chemical Physics* **1975**, *62*, 737–738.
- [177] T. Liu, K. C. Kim, B. Lee, Z. Chen, S. Noda, S. S. Jang, S. W. Lee, *Energy & Environmental Science* **2017**, *10*, 205–215.
- [178] P. Jiménez, E. Levillain, O. Alévêque, D. Guyomard, B. Lestriez, J. Gaubicher, *Angewandte Chemie International Edition* **2017**, *56*, 1553–1556.
- [179] J. C. Bachman, R. Kaviani, D. J. Graham, D. Y. Kim, S. Noda, D. G. Nocera, Y. Shao-Horn, S. W. Lee, *Nature communications* **2015**, *6*, 7040.
- [180] R. D. Shannon, *Acta crystallographica section A: crystal physics diffraction theoretical and general crystallography* **1976**, *32*, 751–767.

- [181] S. Ukai, Y. H. Koo, N. Fukui, S. Seki, H. Shinokubo, *Dalton Transactions* **2020**, *49*, 14383–14387.
- [182] L. R. Dinelli, G. Von Poelhsitz, E. E. Castellano, J. Ellena, S. E. Galembeck, A. A. Batista, *Inorganic chemistry* **2009**, *48*, 4692–4700.
- [183] Y. Le Mest, M. L’Her, J. Courtot-Coupez, J. Collman, E. Evitt, C. Bencosme, *Journal of electroanalytical chemistry and interfacial electrochemistry* **1985**, *184*, 331–346.
- [184] W. R. Scheidt, K. E. Buentello, N. Ehlinger, A. Cinquantini, M. Fontani, F. Laschi, *Inorganica chimica acta* **2008**, *361*, 1722–1727.
- [185] S.-J. Kim, K. Onishi, M. Matsumoto, K. Shigehara, *Journal of Porphyrins and Phthalocyanines* **2001**, *5*, 397–404.
- [186] Y. Asai, K. Onishi, T. Arai, M. Matsumoto, S. Miyata, K. Shigehara, *Polymers for Advanced Technologies* **2001**, *12*, 259–265.
- [187] L. P. Cook, G. Brewer, W. Wong-Ng, *Crystals* **2017**, *7*, 223.
- [188] M. Zhao, J. C. Jimenez, C. Wang, G. Rui, T. Ma, C. Lu, A. L. Rheingold, R. Li, L. Zhu, G. Sauvé, *The Journal of Physical Chemistry C* **2022**, *126*, 6543–6555.
- [189] I. Cojocariu, F. Feyersinger, P. Puschnig, L. Schio, L. Floreano, V. Feyer, C. M. Schneider, *Chemical Communications* **2021**, *57*, 3050–3053.
- [190] Z. Parsa, S. S. Naghavi, N. Safari, *The Journal of Physical Chemistry A* **2018**, *122*, 5870–5877.
- [191] Q. Liu, X. Zhang, W. Zeng, J. Wang, Z. Zhou, *Chinese Journal of Chemistry* **2016**, *34*, 910–918.
- [192] R. Giovannetti, *Macro to nano spectroscopy* **2012**, 87–108.
- [193] J. Shelmutt, C. Medforth, et al., *Chemical Society Reviews* **1998**, *27*, 31–42.
- [194] Z. Zhou, M. Shen, C. Cao, Q. Liu, Z. Yan, *Chemistry—A European Journal* **2012**, *18*, 7675–7679.
- [195] Z. Zhou, C. Cao, Q. Liu, R. Jiang, *Organic letters* **2010**, *12*, 1780–1783.
- [196] R. E. Haddad, S. Gazeau, J. Pécaut, J.-C. Marchon, C. J. Medforth, J. A. Shelmutt, *Journal of the American Chemical Society* **2003**, *125*, 1253–1268.
- [197] H. Ryeng, A. Ghosh, *Journal of the American Chemical Society* **2002**, *124*, 8099–8103.
- [198] M. Stepien, E. Gonka, M. Żyła, N. Sprutta, *Chemical reviews* **2017**, *117*, 3479–3716.
- [199] A. Borissov, Y. K. Maurya, L. Moshniaha, W.-S. Wong, M. Żyła-Karwowska, M. Stepien, *Chemical Reviews* **2021**, *122*, 565–788.
- [200] Z.-D. Huang, X.-M. Liu, S.-W. Oh, B. Zhang, P.-C. Ma, J.-K. Kim, *Journal of Materials Chemistry* **2011**, *21*, 10777–10784.

- [201] V. Bhat, *Nano Select* **2020**, *1*, 226.
- [202] K. Zou, P. Cai, B. Wang, C. Liu, J. Li, T. Qiu, G. Zou, H. Hou, X. Ji, *Nano-micro letters* **2020**, *12*, 1–19.
- [203] B. E. Gurkan, Z. Qiang, Y.-M. Chen, Y. Zhu, B. D. Vogt, *Journal of The Electrochemical Society* **2017**, *164*, H5093.
- [204] J. Yang, Z. Wang, Y. Shi, P. Sun, Y. Xu, *ACS applied materials & interfaces* **2020**, *12*, 7179–7185.
- [205] I. Gomez, O. Leonet, J. Alberto Blazquez, H.-J. Grande, D. Mecerreyes, *ACS Macro Letters* **2018**, *7*, 419–424.
- [206] S. Zhang, S. Ren, D. Han, M. Xiao, S. Wang, L. Sun, Y. Meng, *ACS applied materials & interfaces* **2020**, *12*, 36237–36246.
- [207] S. Yesilot, N. Kılıç, S. Sariyer, S. Kucukkoçulu, A. Kılıç, R. Demir-Cakan, *ACS Applied Energy Materials* **2021**, *4*, 12487–12498.
- [208] K. B. Labasan, H.-J. Lin, F. Baskoro, J. J. H. Togonon, H. Q. Wong, C.-W. Chang, S. D. Arco, H.-J. Yen, *ACS Applied Materials & Interfaces* **2021**, *13*, 17467–17477.
- [209] K. Liu, Y. Liu, D. Lin, A. Pei, Y. Cui, Materials for lithium-ion battery safety. *Sci Adv* *4* (6): eaas9820, **2018**.
- [210] Z. Li, M. Dadsetan, J. Gao, S. Zhang, L. Cai, A. Naseri, M. E. Jimenez-Castaneda, T. Filley, J. T. Miller, M. J. Thomson, et al., *Advanced Energy Materials* **2021**, *11*, 2101764.
- [211] M. Wu, Y. Zhao, R. Zhao, J. Zhu, J. Liu, Y. Zhang, C. Li, Y. Ma, H. Zhang, Y. Chen, *Advanced Functional Materials* **2022**, *32*, 2107703.
- [212] Z. Ma, G. Shao, Y. Fan, G. Wang, J. Song, T. Liu, *ACS Applied Materials & Interfaces* **2014**, *6*, 9236–9244.
- [213] J. Zhang, J. Qiao, K. Sun, Z. Wang, *Particuology* **2022**, *61*, 18–29.
- [214] J. C. Garcia, J. Bareño, J. Yan, G. Chen, A. Hauser, J. R. Croy, H. Iddir, *The Journal of Physical Chemistry C* **2017**, *121*, 8290–8299.
- [215] L. Xiao, Y. Guo, D. Qu, B. Deng, H. Liu, D. Tang, *Journal of Power Sources* **2013**, *225*, 286–292.
- [216] S. T. Taleghani, B. Marcos, K. Zaghbi, G. Lantagne, *Journal of The Electrochemical Society* **2017**, *164*, E3179.
- [217] J. Jamnik, J. Maier, *Physical Chemistry Chemical Physics* **2003**, *5*, 5215–5220.
- [218] D.-W. Chung, P. R. Shearing, N. P. Brandon, S. J. Harris, R. E. Garcia, *Journal of The Electrochemical Society* **2014**, *161*, A422.
- [219] C.-C. Lin, J.-M. Ho, M.-S. Wu, *Powder Technology* **2015**, *274*, 441–445.

- [220] K. Tao, H. Dou, K. Sun, *Colloids and Surfaces A: Physicochemical and Engineering Aspects* **2008**, *320*, 115–122.
- [221] A. Barna, B. Pécz, M. Menyhard, *Micron* **1999**, *30*, 267–276.
- [222] W.-B. Hua, X.-D. Guo, Z. Zheng, Y.-J. Wang, B.-H. Zhong, B. Fang, J.-Z. Wang, S.-L. Chou, H. Liu, *Journal of Power Sources* **2015**, *275*, 200–206.
- [223] A. Mohanty, N. Garg, R. Jin, *Angewandte Chemie* **2010**, *122*, 5082–5086.
- [224] F. Cao, F. Zhang, R. Deng, W. Hu, D. Liu, S. Song, H. Zhang, *CrystEngComm* **2011**, *13*, 4903–4908.
- [225] J. Ge, J. Lei, R. N. Zare, *Nature nanotechnology* **2012**, *7*, 428–432.
- [226] H. Zhang, G. Cao, Z. Wang, Y. Yang, Z. Shi, Z. Gu, *Nano letters* **2008**, *8*, 2664–2668.
- [227] Z. Zhu, X. Li, Y. Zeng, W. Sun, W. Zhu, X. Huang, *The Journal of Physical Chemistry C* **2011**, *115*, 12547–12553.
- [228] J. Ning, Q. Dai, T. Jiang, K. Men, D. Liu, N. Xiao, C. Li, D. Li, B. Liu, B. Zou, et al., *Langmuir* **2009**, *25*, 1818–1821.
- [229] A. Shirazi, M. Azadi Kakavand, T. Rabczuk, *Journal of Nanotechnology in Engineering and Medicine* **2015**, *6*, 041003.
- [230] B. Kang, G. Ceder, *Nature* **2009**, *458*, 190–193.
- [231] W.-J. Zhang, *Journal of Power Sources* **2011**, *196*, 2962–2970.
- [232] F. Hasan, J. Kim, H. Song, S. H. Lee, J. H. Sung, J. Kim, H. D. Yoo, *Journal of Electrochemical Science and Technology* **2020**, *11*, 352–360.
- [233] L. Wei, Y. Wang, Y. Wang, M. Xu, G. Zheng, *Journal of colloid and interface science* **2014**, *432*, 297–301.
- [234] J.-M. Song, Y.-Z. Lin, H.-B. Yao, F.-J. Fan, X.-G. Li, S.-H. Yu, *ACS nano* **2009**, *3*, 653–660.
- [235] C. Chen, T. Tao, W. Qi, H. Zeng, Y. Wu, B. Liang, Y. Yao, S. Lu, Y. Chen, *Journal of Alloys and Compounds* **2017**, *709*, 708–716.
- [236] S. I. Abdul Halim, C. H. Chan, J. Apotheker, *Chemistry Teacher International* **2021**, *3*, 105–115.
- [237] N. Meddings, M. Heinrich, F. Overney, J.-S. Lee, V. Ruiz, E. Napolitano, S. Seitz, G. Hinds, R. Raccichini, M. Gaberšček, et al., *Journal of Power Sources* **2020**, *480*, 228742.
- [238] Z. Chen, W. Zhang, Z. Yang, *Nanotechnology* **2019**, *31*, 012001.
- [239] M. Ender, J. Joos, T. Carraro, E. Ivers-Tiffée, *Journal of the electrochemical society* **2012**, *159*, A972.
- [240] B. Song, T. Sui, S. Ying, L. Li, L. Lu, A. M. Korsunsky, *Journal of Materials Chemistry A* **2015**, *3*, 18171–18179.

- [241] T. Philipp, G. Neusser, E. Abouzari-Lotf, S. Shakouri, F. D. Wilke, M. Fichtner, M. Ruben, M. Mundszinger, J. Biskupek, U. Kaiser, et al., *Journal of Power Sources* **2022**, *522*, 231002.
- [242] Z. Su, V. De Andrade, S. Cretu, Y. Yin, M. J. Wojcik, A. A. Franco, A. Demortière, *ACS Applied Energy Materials* **2020**, *3*, 4093–4102.
- [243] M. Parker, D. Vesely, *Microscopy research and technique* **1993**, *24*, 333–339.
- [244] G. H. Michler, W. Lebek, *Polymer Morphology: Principles Characterization and Processing* **2016**, 37–53.
- [245] L. Sun, J. Xie, Z. Chen, J. Wu, L. Li, *Dalton Transactions* **2018**, *47*, 9989–9993.
- [246] G. Song, Y. Shi, S. Jiang, H. Pang, *Advanced Functional Materials* **2023**, 2303121.
- [247] X. Tan, Y. Wu, X. Lin, A. Zeb, X. Xu, Y. Luo, J. Liu, *Inorganic Chemistry Frontiers* **2020**, *7*, 4939–4955.
- [248] Z. Parviz, P. Salimi, S. Javadian, H. Gharibi, A. Morsali, E. Bayat, L. Leoncino, S. Lauciello, R. Proietti Zaccaria, *ACS Applied Energy Materials* **2022**, *5*, 15155–15165.
- [249] Y. Xu, H. Gong, H. Ren, X. Fan, P. Li, T. Zhang, K. Chang, T. Wang, J. He, *Small* **2022**, *18*, 2203917.
- [250] Y. Han, Z. Liu, F. Zheng, Y. Bai, Z. Zhang, X. Li, W. Xiong, J. Zhang, A. Yuan, *Journal of Alloys and Compounds* **2021**, *881*, 160531.
- [251] C. Dong, L. Xu, *ACS Applied Materials & Interfaces* **2017**, *9*, 7160–7168.
- [252] J. Lin, R. C. K. Reddy, C. Zeng, X. Lin, A. Zeb, C.-Y. Su, *Coordination Chemistry Reviews* **2021**, *446*, 214118.
- [253] Z. Ye, Y. Jiang, L. Li, F. Wu, R. Chen, *Nano-Micro Letters* **2021**, *13*, 1–37.
- [254] F. He, Y. Zhou, X. Chen, T. Wang, Y. Zeng, J. Zhang, Z. Chen, W. Liu, P. Gao, *Chemical Communications* **2023**, *59*, 2787–2790.
- [255] F.-H. Wang, Z.-Y. Liu, S. Yang, L. Shi, D.-Z. Lin, H.-Y. Liu, G.-Q. Yuan, *Synthetic Communications* **2021**, *51*, 2053–2062.
- [256] Q. Lin, C. Mao, A. Kong, X. Bu, X. Zhao, P. Feng, *Journal of Materials Chemistry A* **2017**, *5*, 21189–21195.
- [257] T. Ohmura, N. Setoyama, Y. Mukae, A. Usuki, S. Senda, T. Matsumoto, K. Tatsumi, *CrytEngComm* **2017**, *19*, 5173–5177.
- [258] G. Socrates, *Infrared and Raman characteristic group frequencies: tables and charts*, John Wiley & Sons, **2004**.
- [259] A. S. Duke, E. A. Dolgoplova, R. P. Gallenage, S. C. Ammal, A. Heyden, M. D. Smith, D. A. Chen, N. B. Shustova, *The Journal of Physical Chemistry C* **2015**, *119*, 27457–27466.

- [260] T. Smok, S. Shakouri, E. Abouzari-Lotf, F. D. Pammer, T. Diemant, S. Jana, A. Roy, Y. Xiu, S. Klyatskaya, M. Ruben, Z. Zhao-Karger, M. Fichtner, *Batteries & Supercaps* **2023**.
- [261] P. St. Petkov, G. N. Vayssilov, J. Liu, O. Shekhah, Y. Wang, C. Wöll, T. Heine, *ChemPhysChem* **2012**, *13*, 2025–2029.
- [262] T. Ohmura, A. Usuki, K. Fukumori, T. Ohta, M. Ito, K. Tatsumi, *Inorganic chemistry* **2006**, *45*, 7988–7990.
- [263] M. Sajjadnejad, S. Saleh-Haghshenas, *Adv J Chem A* **2023**, *6*, 172–187.
- [264] R. Haldar, N. Sikdar, T. K. Maji, *Materials Today* **2015**, *18*, 97–116.
- [265] F. Gandara, V. A. de la Peña-O'Shea, F. Illas, N. Snejko, D. M. Proserpio, E. Gutierrez-Puebla, M. A. Monge, *Inorganic chemistry* **2009**, *48*, 4707–4713.
- [266] A. Llinàs, J. M. Goodman, *Drug Discovery Today* **2008**, *13*, 198–210.
- [267] R. C. Evans, Z. Nilsson, B. Balch, L. Wang, J. R. Neilson, C. R. Weinberger, J. B. Sambur, *ChemElectroChem* **2020**, *7*, 753–760.
- [268] Y. Jiang, J. Liu, *Energy & Environmental Materials* **2019**, *2*, 30–37.
- [269] X.-M. Lin, D.-Y. Wu, P. Gao, Z. Chen, M. Ruben, M. Fichtner, *Chemistry of Materials* **2019**, *31*, 3239–3247.
- [270] X. Huang, Y. Zhou, Y. Zeng, X. Chen, F. He, T. Wang, D. Lan, W. Liu, S. Tan, P. Gao, *Chemical Engineering Journal* **2023**, *470*, 144248.
- [271] Y. Zeng, J. Zhou, J. Zhang, Y. Liao, C. Sun, Y. Su, P. Gao, S. Tan, *Chemical Communications* **2023**, *59*, 4962–4965.
- [272] S. Bai, Q. Hu, Q. Zeng, M. Wang, L. Wang, *ACS applied materials & interfaces* **2018**, *10*, 11319–11327.
- [273] A. Bettelheim, B. White, S. Raybuck, R. W. Murray, *Inorganic Chemistry* **1987**, *26*, 1009–1017.
- [274] W. Sassi, R. Msaadi, J.-Y. Hihn, R. Zrelli, *Polymer Bulletin* **2021**, *78*, 4261–4280.
- [275] L. Li, Y.-J. Hong, D.-Y. Chen, W.-C. Xiao, M.-J. Lin, *Chemical Communications* **2019**, *55*, 2364–2367.
- [276] T. R. Ferguson, M. Z. Bazant, *Electrochimica Acta* **2014**, *146*, 89–97.
- [277] V. Augustyn, J. Come, M. A. Lowe, J. W. Kim, P.-L. Taberna, S. H. Tolbert, H. D. Abruña, P. Simon, B. Dunn, *Nature materials* **2013**, *12*, 518–522.
- [278] J. Wang, J. Polleux, J. Lim, B. Dunn, *The Journal of Physical Chemistry C* **2007**, *111*, 14925–14931.
- [279] A. Eftekhari, *ACS Sustainable Chemistry & Engineering* **2017**, *5*, 2799–2816.

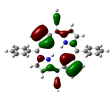
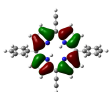
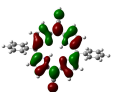
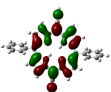
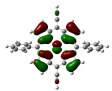
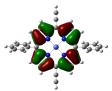
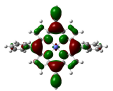
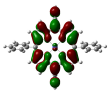
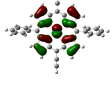
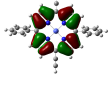
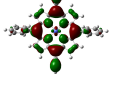
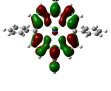
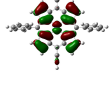

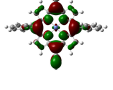
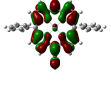
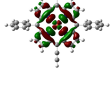
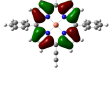
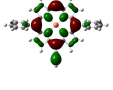
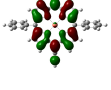
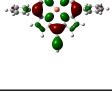
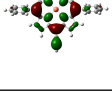
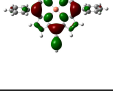
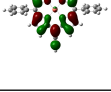
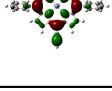
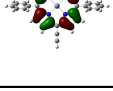
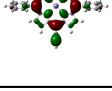
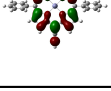
- [280] X. Zhao, Y. Zhang, Y. Wang, H. Wei, *Batteries & Supercaps* **2019**, *2*, 899–917.
- [281] C. K. Jung, D. Stottmeister, T. Jacob, *Energy Technology* **2020**, *8*, 2000388.
- [282] N. Cao, J. Björk, E. Corral-Rascon, Z. Chen, M. Ruben, M. O. Senge, J. V. Barth, A. Riss, *nature chemistry* **2023**.
- [283] G. R. Fulmer, A. J. Miller, N. H. Sherden, H. E. Gottlieb, A. Nudelman, B. M. Stoltz, J. E. Bercaw, K. I. Goldberg, *Organometallics* **2010**, *29*, 2176–2179.
- [284] S.-L. Lai, L. Wang, C. Yang, M.-Y. Chan, X. Guan, C.-C. Kwok, C.-M. Che, *Advanced Functional Materials* **2014**, *24*, 4655–4665.
- [285] Shirin Shakouri, Master 's, **2018**.
- [286] E. H. Cho, S. H. Chae, K. Kim, S. J. Lee, J. Joo, *Synthetic metals* **2012**, *162*, 813–819.
- [287] P. K. Goldberg, T. J. Pundsack, K. E. Splan, *The Journal of Physical Chemistry A* **2011**, *115*, 10452–10460.
- [288] I. Hijazi, T. Bourgeteau, R. Cornut, A. Morozan, A. Filoramo, J. Leroy, V. Derycke, B. Jousset, S. Campidelli, *Journal of the American Chemical Society* **2014**, *136*, 6348–6354.

Appendix A

Appendix

A.1 Chapter 5

Table A.1: Frontier orbitals (HOMO and LUMO) of xDEPPs HOMO-2 and HOMO-1 denote the molecule orbitals below the HOMO.

	HOMO-2	HOMO-1	HOMO	LUMO
DEPP				
CoDEPP α				
CoDEPP β				
NiDEPP				
CuDEPP α				
CuDEPP β				
ZnDEPP				

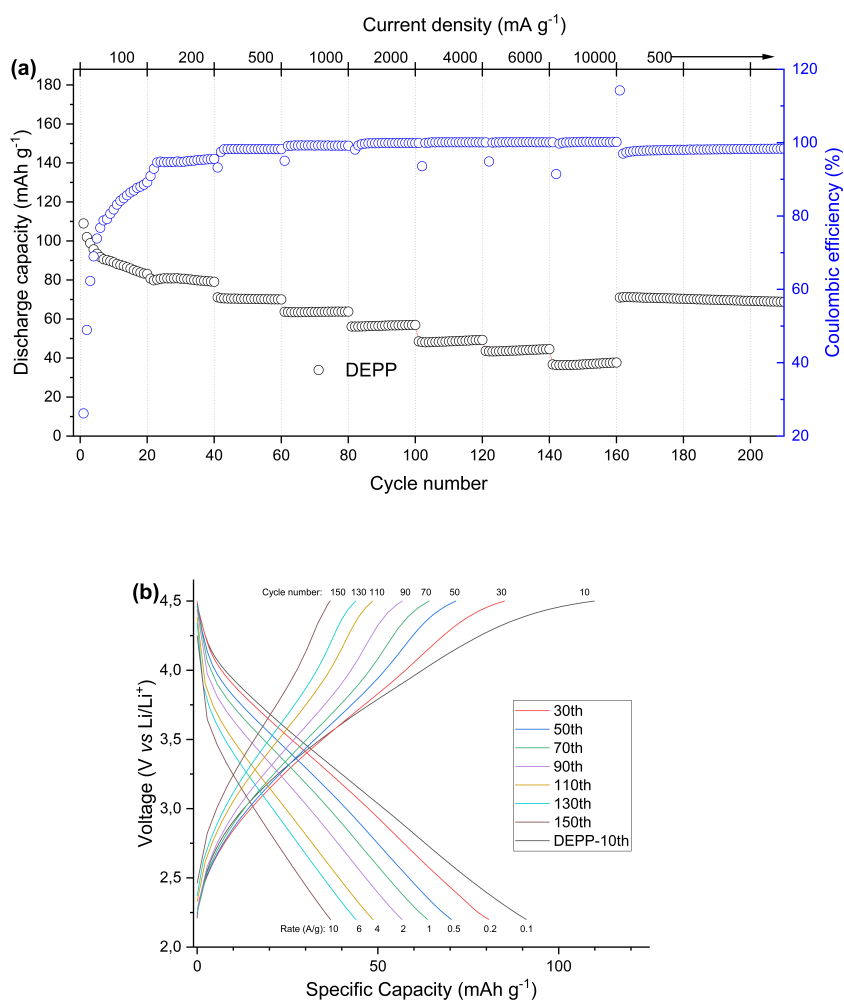


Figure A.1: The rate capability of the DEPP electrode was assessed by varying the charge-discharge rate, starting from 100 mA g⁻¹ and gradually decreasing to 10 mA g⁻¹, and then increasing it to 500 mA g⁻¹ (a). The selected voltage profile is depicted in (b).

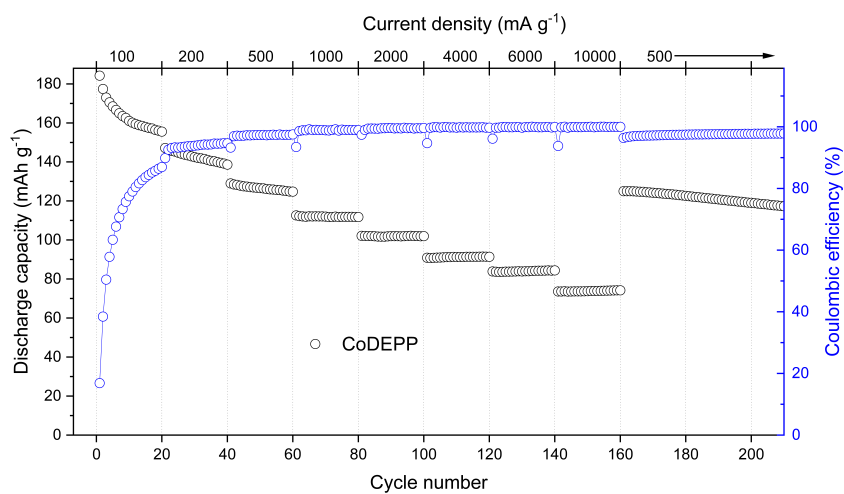


Figure A.2: The rate capability of the CoDEPP electrode was assessed by varying the charge-discharge rate, starting from 100 mA g⁻¹ and gradually decreasing to 10 mA g⁻¹, and then increasing it to 500 mA g⁻¹.

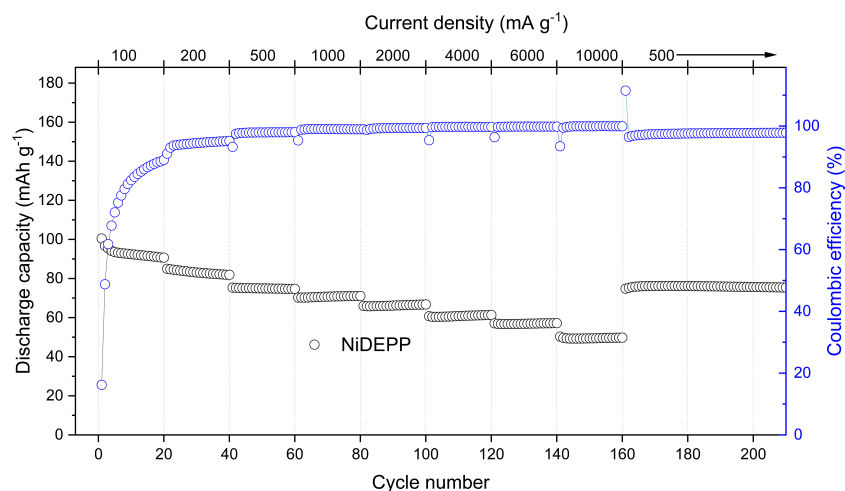


Figure A.3: The rate capability of the NiDEPP electrode was assessed by varying the charge-discharge rate, starting from 100 mA g⁻¹ and gradually decreasing to 10 mA g⁻¹, and then increasing it to 500 mA g⁻¹.

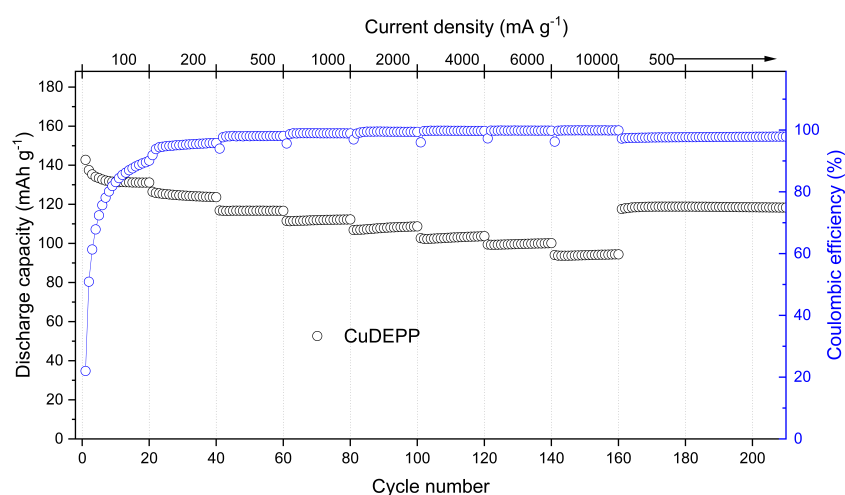


Figure A.4: The rate capability of the CuDEPP electrode was assessed by varying the charge-discharge rate, starting from 100 mA g⁻¹ and gradually decreasing to 10 mA g⁻¹, and then increasing it to 500 mA g⁻¹.

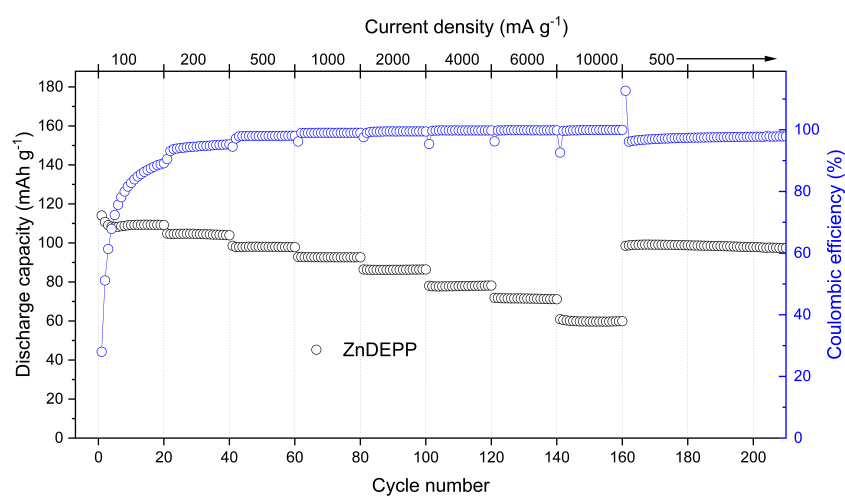
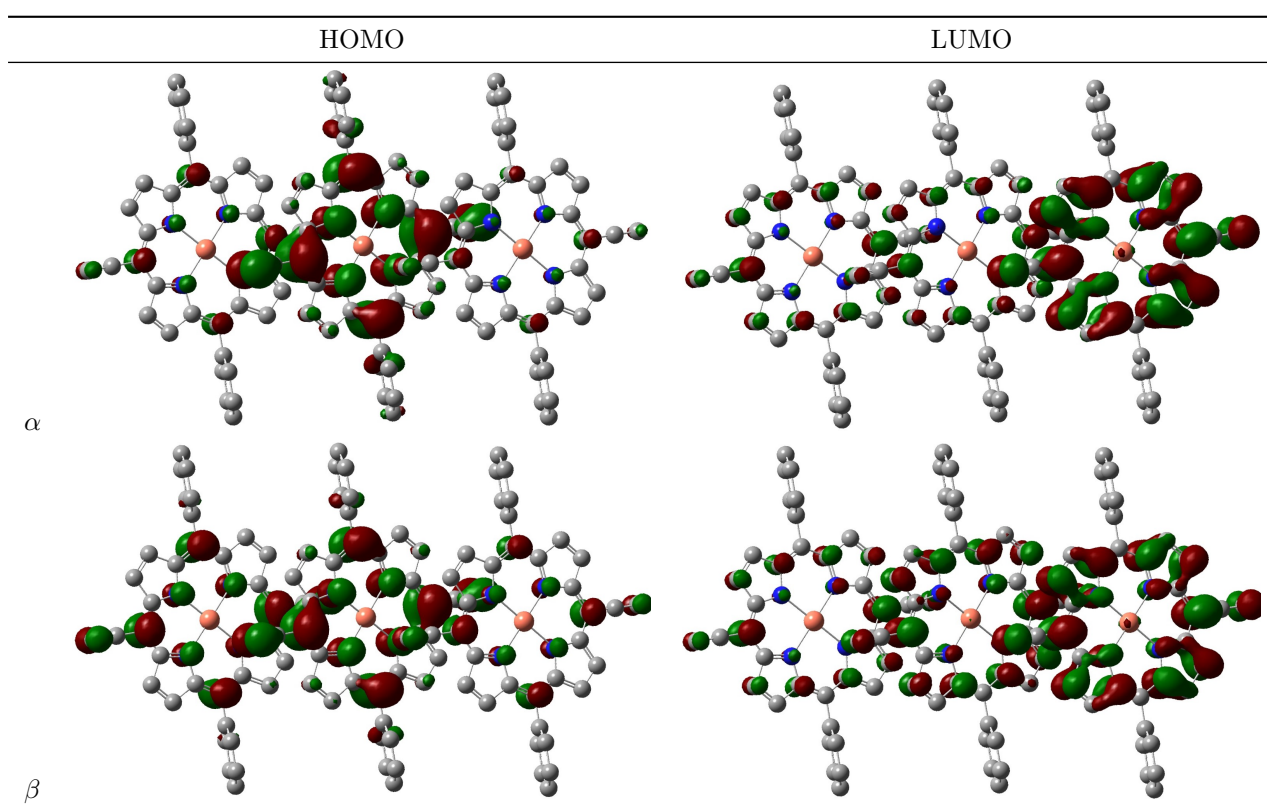


Figure A.5: The rate capability of the ZnDEPP electrode was assessed by varying the charge-discharge rate, starting from 100 mA g⁻¹ and gradually decreasing to 10 mA g⁻¹, and then increasing it to 500 mA g⁻¹.

Table A.2: Frontier orbitals of $(\text{CuDEPP})_3$.



A.2 Chapter 6

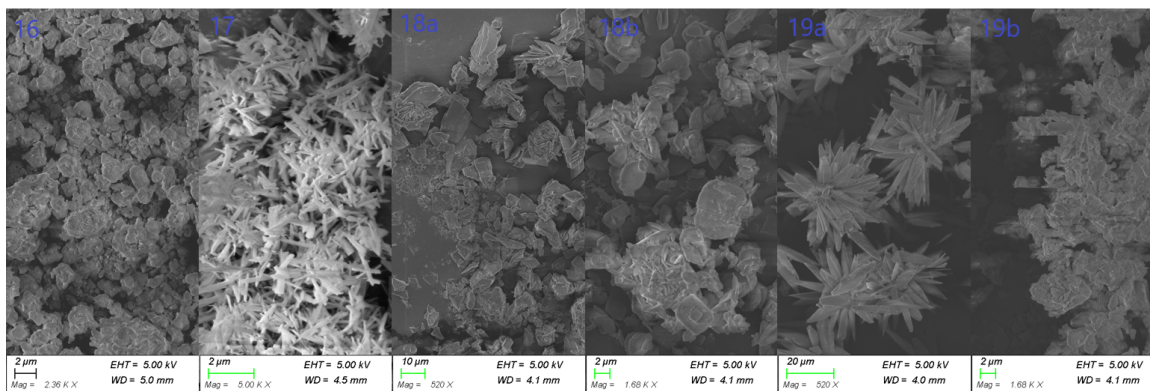


Figure A.6: SEM Images of other CoDEPP morphologies 16-19.

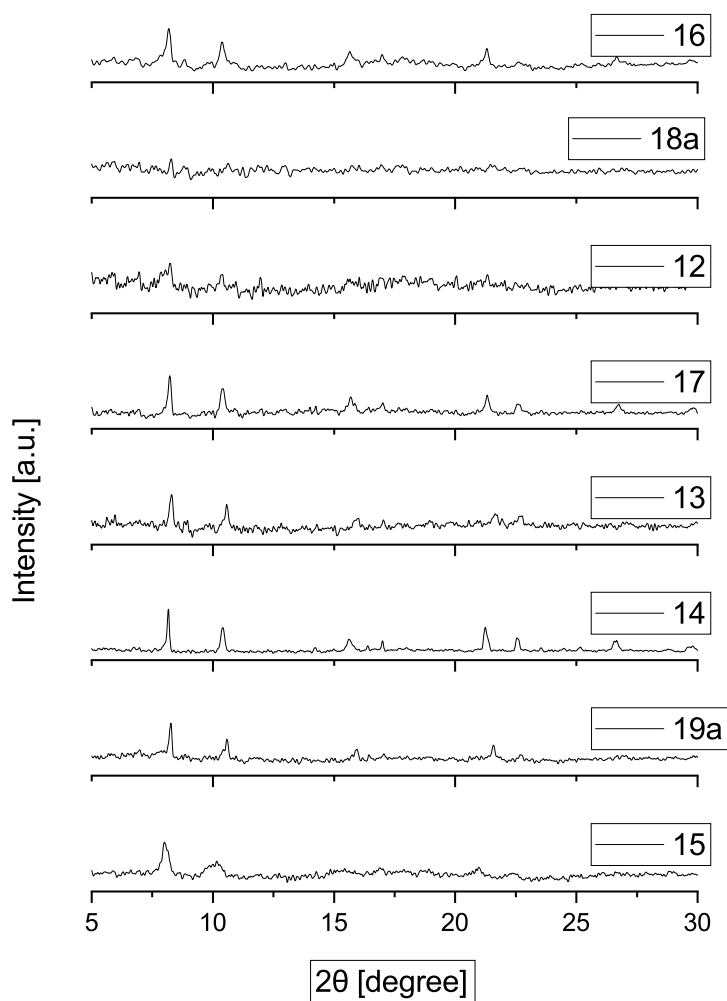


Figure A.7: Powder XRD pattern of all CoDEPP morphologies 12-19.

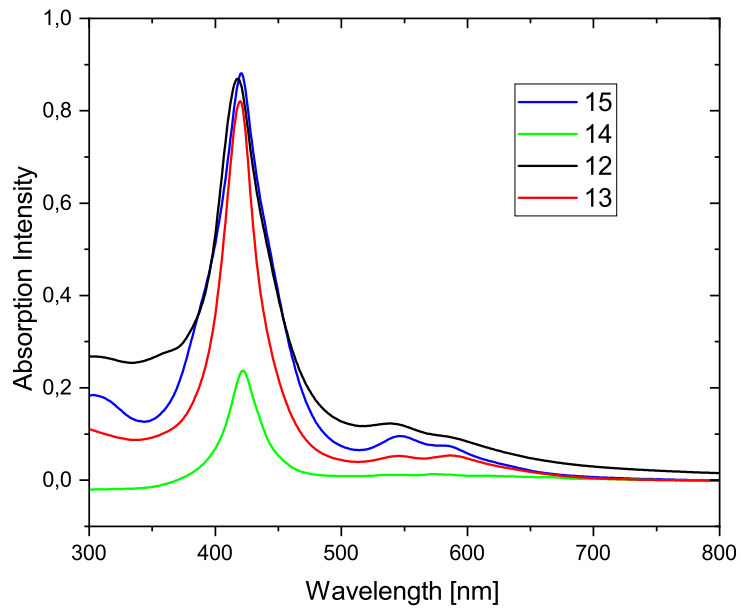


Figure A.8: UV-Vis absorptions spectrum of CoDEPP 12-15.

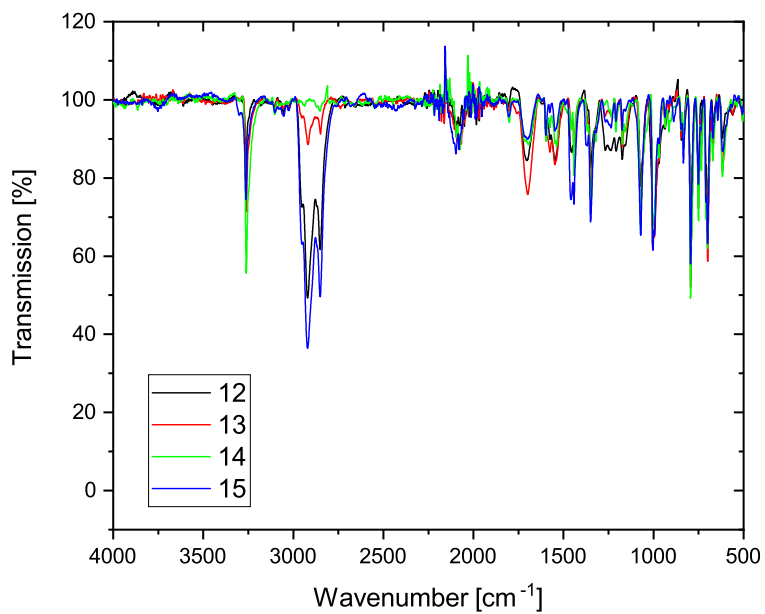


Figure A.9: IR spectra of CoDEPP 12-15.

A.3 Chapter 8

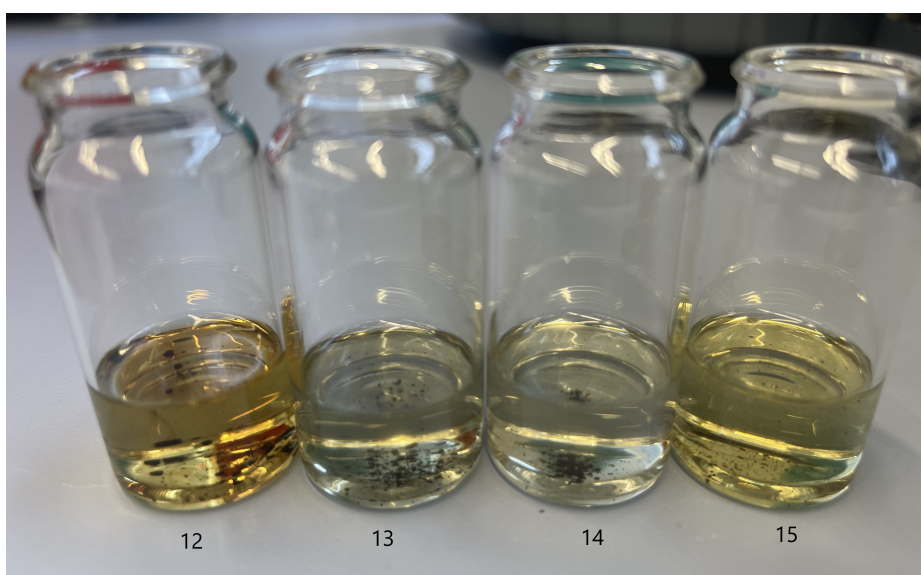


Figure A.10: Solubility of CoDEPP 12-15 in DCM after 1h.

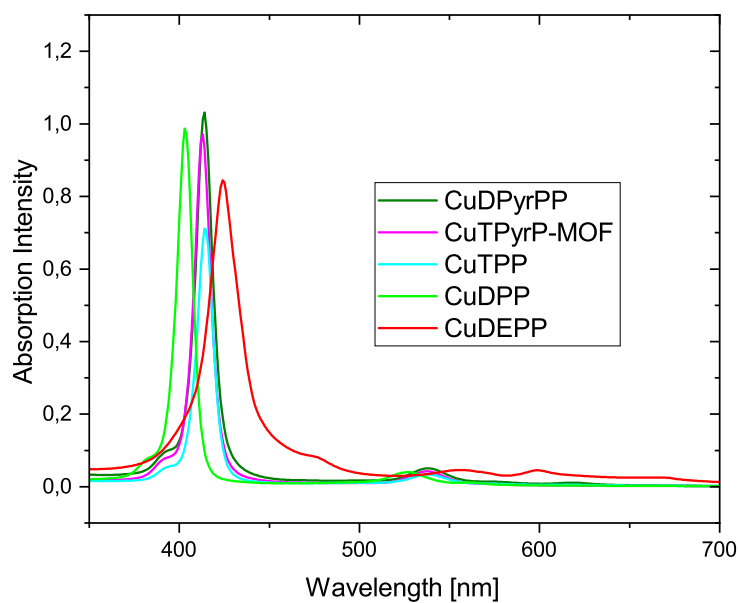


Figure A.11: UV-Vis absorptions spectrum of CuDPP, CuTPP, CuDEPP, CuTPyrP-MOF, CuDPyrPP.

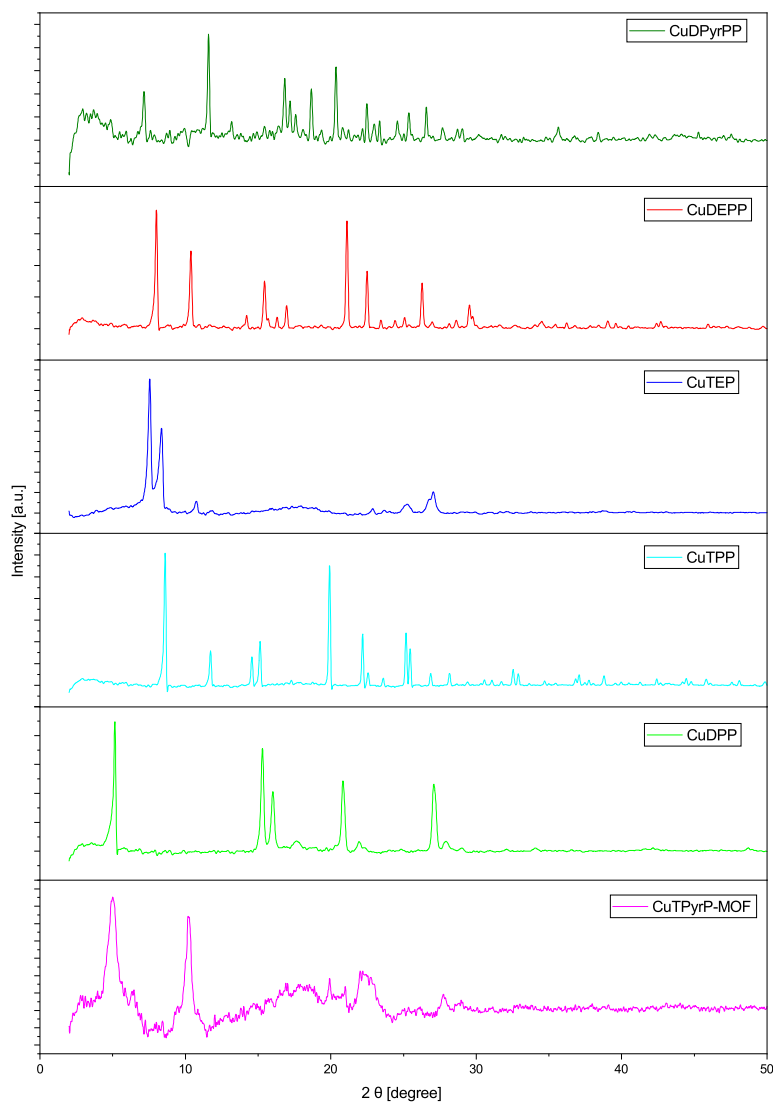


Figure A.12: Powder X-ray diffractograms of CuDPyrPP, CuDEPP, CuTEP, CuTPP, CuDPP and CuTPyrP-MOF.

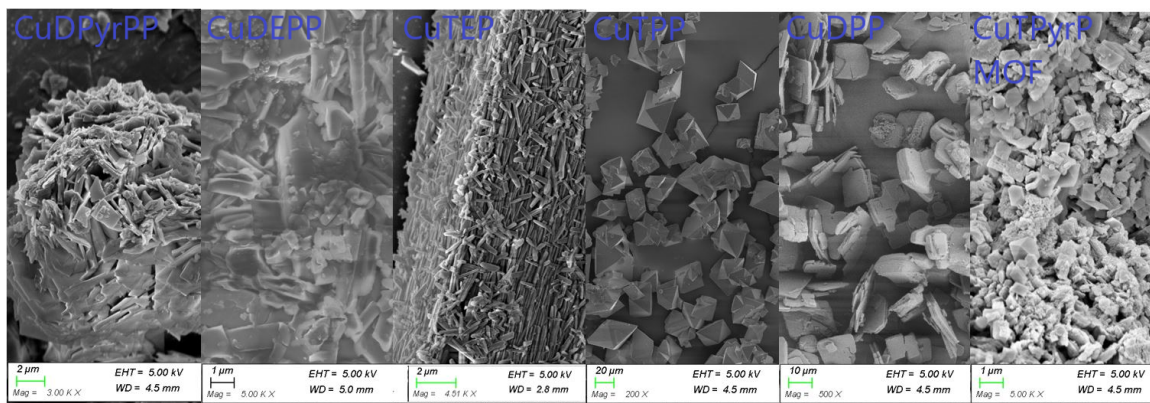


Figure A.13: SEM images of CuDPyrPP, CuDEPP, CuTEP, CuTPP, CuDPP and CuTPyrP-MOF.

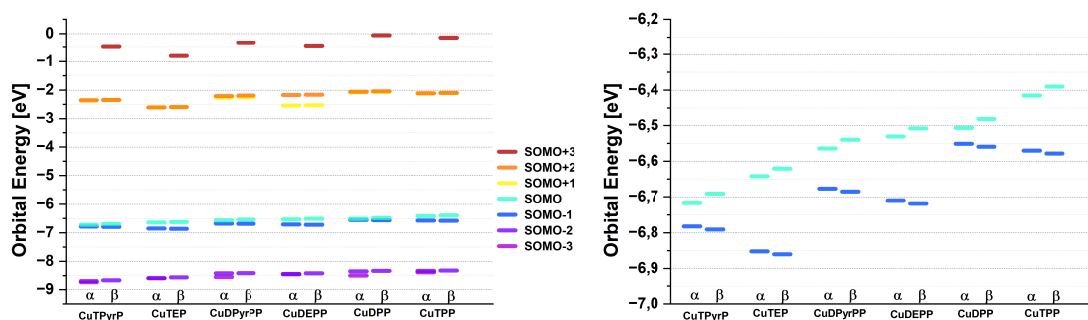


Figure A.14: Electronic properties of CuDPyrPP, CuDEPP, CuTEP, CuTPP, CuDPP and CuTPyrP-MOF.

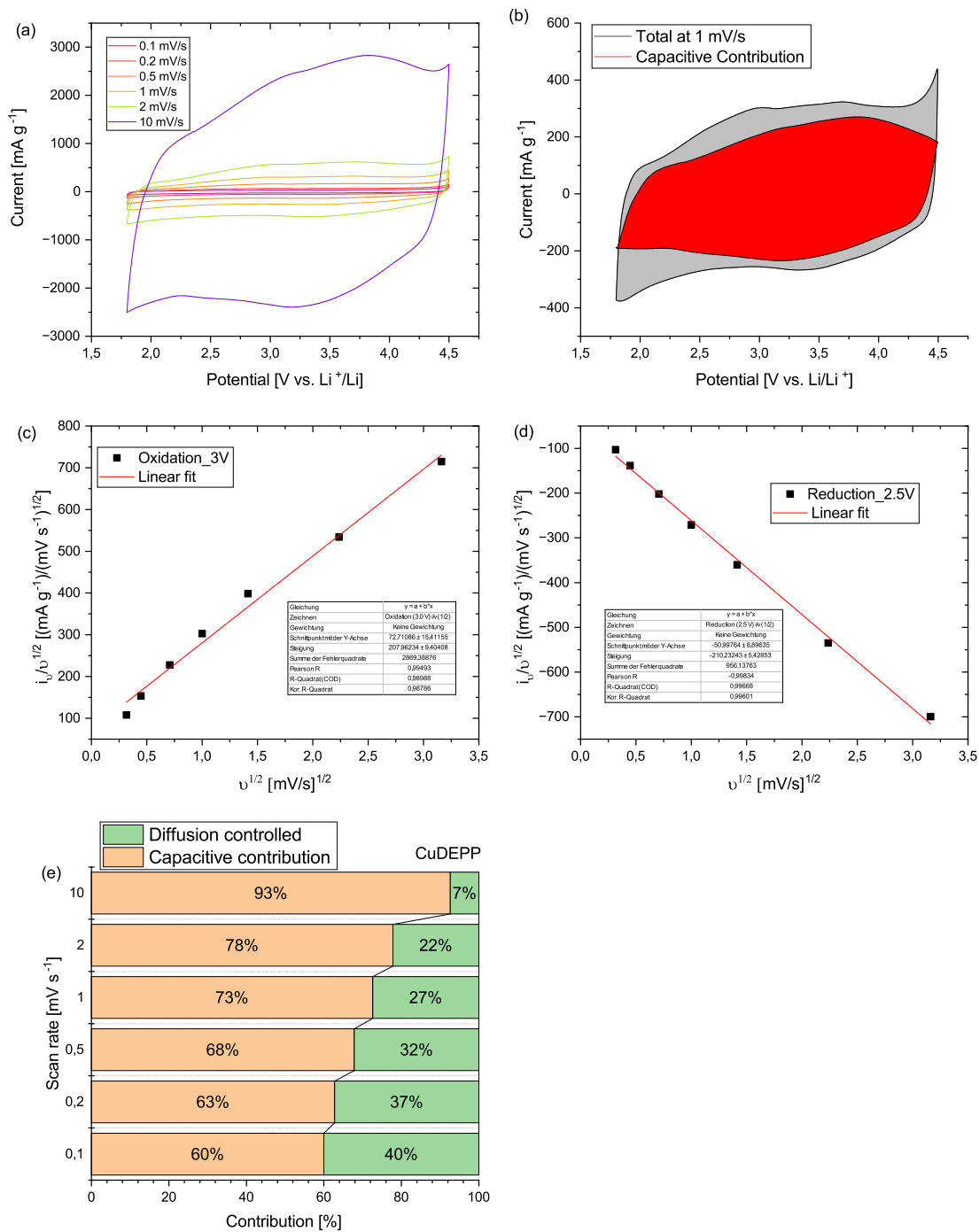


Figure A.15: (a) CV curves of CuDEPP obtained after various sweep rates in voltage range of 1.8-4.5 V (b) visualized capacitive contribution at 1 mV s⁻¹ (c) and (d) plot of $i_p/v^{1/2}$ vs. $v^{1/2}$ and (e) contribution ratio of all sweep rates.

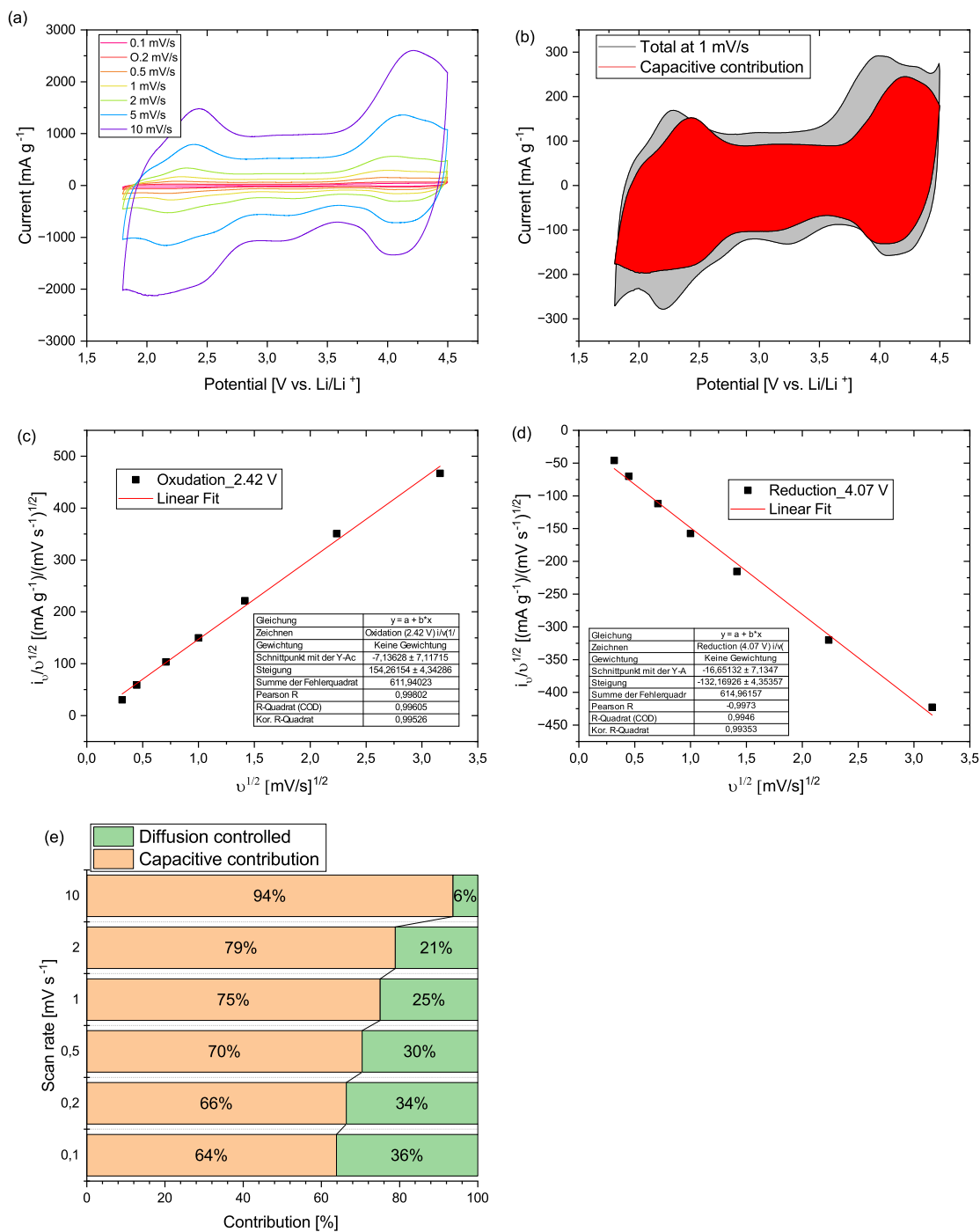


Figure A.16: (a) CV curves of CuDPyrPP obtained after various sweep rates in voltage range of 1.8-4.5 V (b) visualized capacitive contribution at 1 mV s⁻¹ (c) and (d) plot of $i_p/v^{1/2}$ vs. $v^{1/2}$ and (e) contribution ratio of all sweep rates.

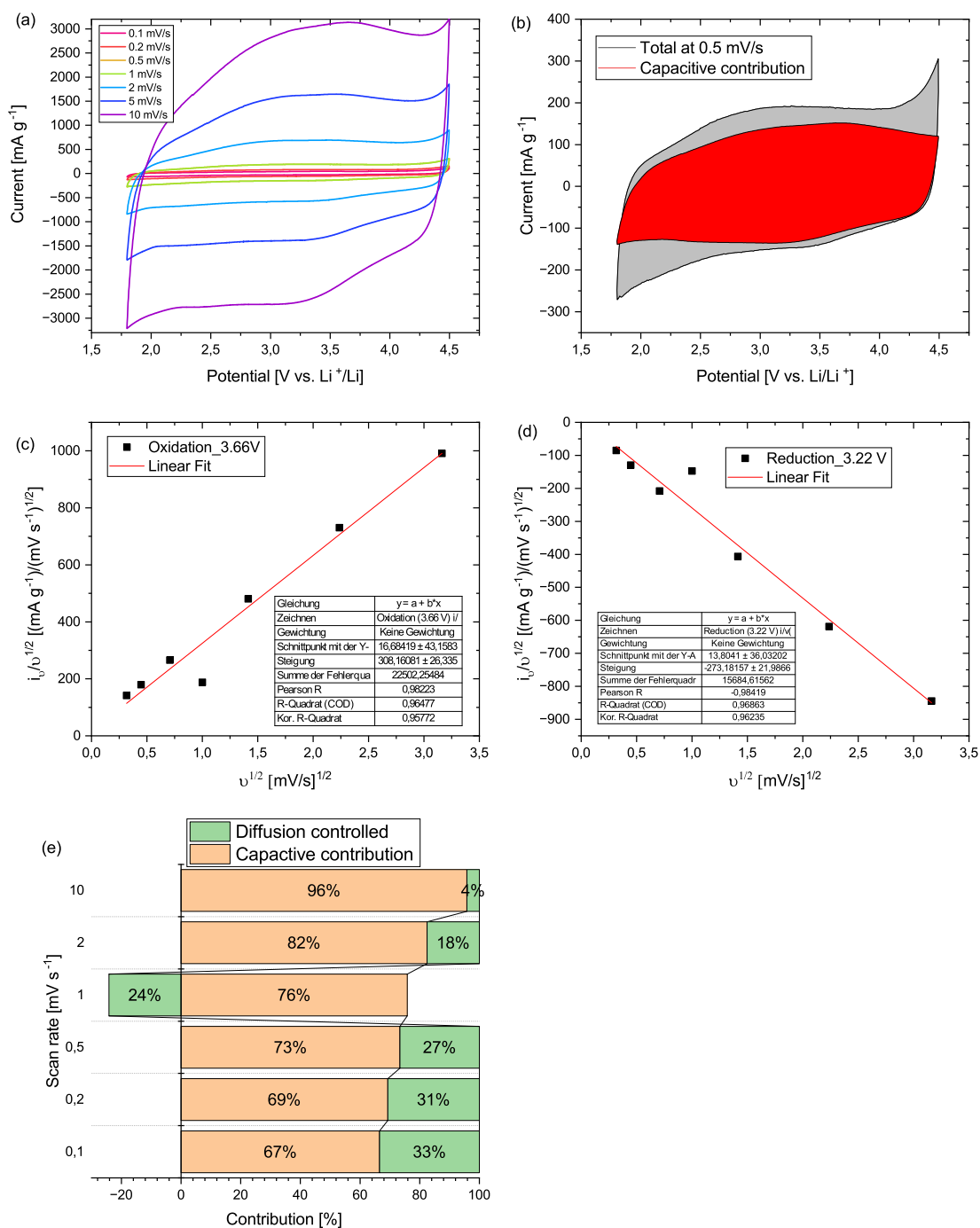


Figure A.17: (a) CV curves of CuTEP obtained after various sweep rates in voltage range of 1.8-4.5 V (b) visualized capacitive contribution at 1 mV s⁻¹ (c) and (d) plot of $i_a/v^{1/2}$ vs. $v^{1/2}$ and (e) contribution ratio of all sweep rates.

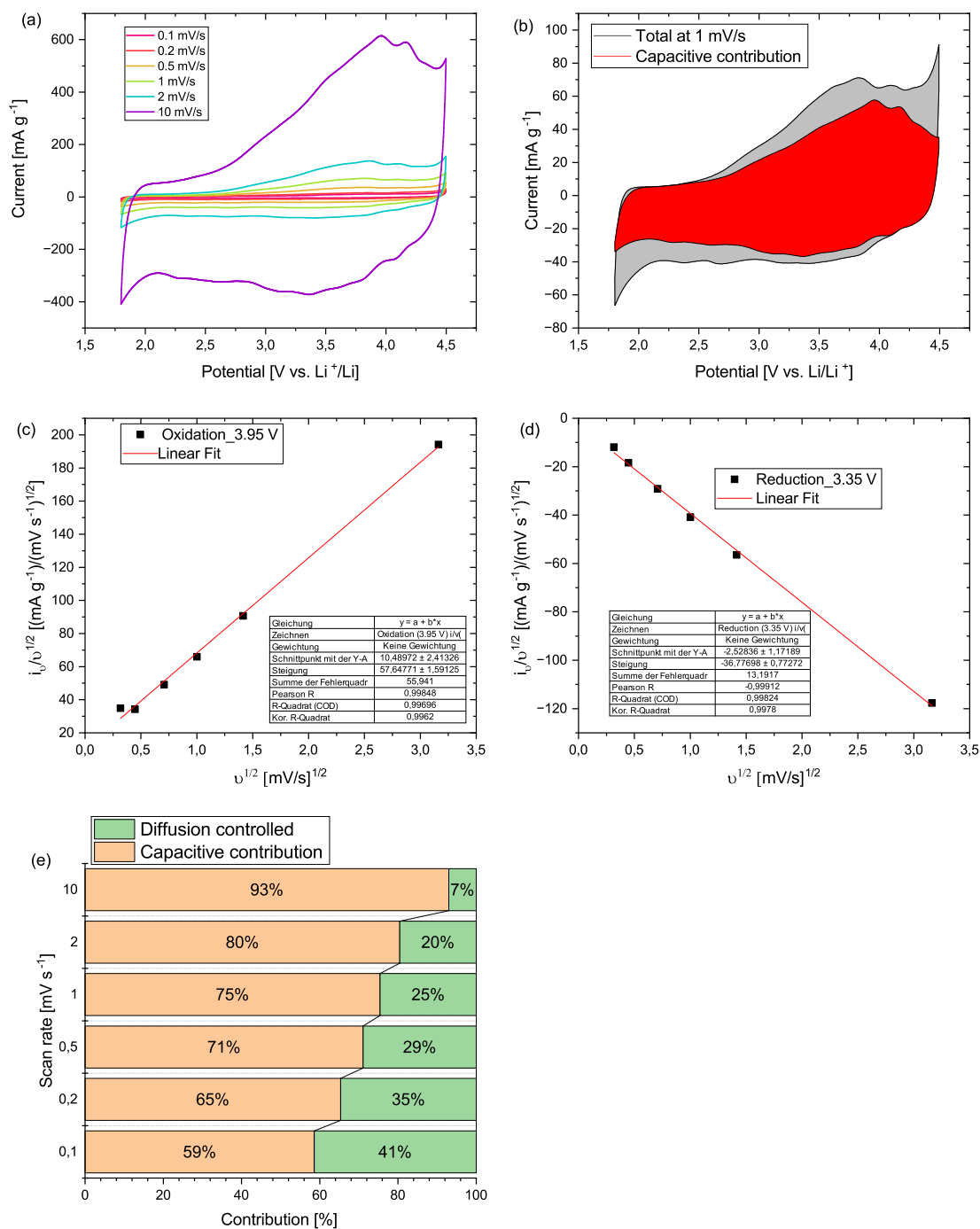


Figure A.18: (a) CV curves of CuTPP obtained after various sweep rates in voltage range of 1.8-4.5 V (b) visualized capacitive contribution at 1 mV s⁻¹ (c) and (d) plot of $i_p/v^{1/2}$ vs. $v^{1/2}$ and (e) contribution ratio of all sweep rates.